frontiers | Research Topics

The integration of clinical veterinary anatomy and diagnostic imaging

Edited by
Sokol Duro, Tomasz Szara and Ozan Gündemir

Published in
Frontiers in Veterinary Science

ISSN 1664-8714
ISBN 978-2-8325-6411-0
DOI 10.3389/978-2-8325-6411-0

About Frontiers

Frontiers is more than just an open access publisher of scholarly articles: it is a pioneering approach to the world of academia, radically improving the way scholarly research is managed. The grand vision of Frontiers is a world where all people have an equal opportunity to seek, share and generate knowledge. Frontiers provides immediate and permanent online open access to all its publications, but this alone is not enough to realize our grand goals.

Frontiers journal series

The Frontiers journal series is a multi-tier and interdisciplinary set of open-access, online journals, promising a paradigm shift from the current review, selection and dissemination processes in academic publishing. All Frontiers journals are driven by researchers for researchers; therefore, they constitute a service to the scholarly community. At the same time, the *Frontiers journal series* operates on a revolutionary invention, the tiered publishing system, initially addressing specific communities of scholars, and gradually climbing up to broader public understanding, thus serving the interests of the lay society, too.

Dedication to quality

Each Frontiers article is a landmark of the highest quality, thanks to genuinely collaborative interactions between authors and review editors, who include some of the world's best academicians. Research must be certified by peers before entering a stream of knowledge that may eventually reach the public - and shape society; therefore, Frontiers only applies the most rigorous and unbiased reviews. Frontiers revolutionizes research publishing by freely delivering the most outstanding research, evaluated with no bias from both the academic and social point of view. By applying the most advanced information technologies, Frontiers is catapulting scholarly publishing into a new generation.

What are Frontiers Research Topics?

Frontiers Research Topics are very popular trademarks of the *Frontiers journals series*: they are collections of at least ten articles, all centered on a particular subject. With their unique mix of varied contributions from Original Research to Review Articles, Frontiers Research Topics unify the most influential researchers, the latest key findings and historical advances in a hot research area.

Find out more on how to host your own Frontiers Research Topic or contribute to one as an author by contacting the Frontiers editorial office: frontiersin.org/about/contact

The integration of clinical veterinary anatomy and diagnostic imaging

Topic editors

Sokol Duro — Agricultural University of Tirana, Albania

Tomasz Szara — Warsaw University of Life Sciences, Poland

Ozan Gündemir — Istanbul University Cerrahpasa, Türkiye

Citation

Duro, S., Szara, T., Gündemir, O., eds. (2025). *The integration of clinical veterinary anatomy and diagnostic imaging*. Lausanne: Frontiers Media SA.

doi: 10.3389/978-2-8325-6411-0

Table of contents

frontiers | Frontiers in Veterinary Science

TYPE Editorial
PUBLISHED 20 May 2025
DOI 10.3389/fvets.2025.1602545

OPEN ACCESS

EDITED AND REVIEWED BY
Hussein M. El-Husseiny,
Tokyo University of Agriculture and Technology, Japan

*CORRESPONDENCE
Sokol Duro
durosokol@ubt.edu.al

RECEIVED 29 March 2025
ACCEPTED 02 May 2025
PUBLISHED 20 May 2025

CITATION
Duro S, Gündemir O and Szara T (2025) Editorial: The integration of clinical veterinary anatomy and diagnostic imaging.
Front. Vet. Sci. 12:1602545.
doi: 10.3389/fvets.2025.1602545

Editorial: The integration of clinical veterinary anatomy and diagnostic imaging

Sokol Duro [1]*, Ozan Gündemir[2] and Tomasz Szara[3]

[1]Department of Morphofunctional Modules, Faculty of Veterinary Medicine, Agricultural University, Tirana, Albania, [2]Department of Anatomy, Faculty of Veterinary Medicine, Istanbul University—Cerrahpaşa, Istanbul, Türkiye, [3]Department of Morphological Sciences, Institute of Veterinary Medicine, Warsaw University of Life Sciences, Warsaw, Poland

KEYWORDS

anatomical structures, diagnostic imaging, innovative MRI techniques, spectral CT, shear wave elastography, vascular anatomy

Editorial on the Research Topic
The integration of clinical veterinary anatomy and diagnostic imaging

The integration of clinical veterinary anatomy and diagnostic imaging has significantly advanced veterinary medicine, enhancing diagnostic precision, surgical planning, and therapeutic strategies. Veterinary anatomy provides the fundamental framework for understanding the structure and function of animal bodies. At the same time, imaging modalities offer non-invasive tools to visualize these structures in both normal and pathological states. The synergy between these fields has improved the accuracy of disease diagnosis and paved the way for more refined interventional procedures. With continuous advancements in imaging technologies, including higher-resolution imaging, three-dimensional reconstructions, and quantitative analysis, veterinary medicine is experiencing an unprecedented transformation. The Research Topic, "*The integration of clinical veterinary anatomy and diagnostic imaging*," presents a collection of 14 studies that exemplify this interdisciplinary approach, contributing to a deeper understanding of anatomical variations, pathological conditions, and novel diagnostic methodologies.

The evolution of imaging technologies has been instrumental in veterinary diagnostics. Techniques such as computed tomography (CT), magnetic resonance imaging (MRI), and ultrasonography have become indispensable tools, providing detailed anatomical insights that facilitate the identification of pathologies challenging to detect through traditional methods. These modalities have expanded the diagnostic capabilities of veterinarians, allowing for early disease detection, improved treatment monitoring, and more precise therapeutic interventions. Several studies within this Research Topic highlight the practical applications of integrating anatomy and imaging:

Magnetic resonance imaging (MRI) is an exceptionally valuable tool in veterinary medicine, providing detailed visualization of musculoskeletal, nervous, and lymphatic structures. Several studies in this collection explore innovative MRI techniques and their potential applications in diagnosing and monitoring various conditions. They offer new approaches for early detection, disease characterization, and improved treatment planning.

Bunzendahl et al. investigated the magnetic properties of canine menisci using *ex vivo* MRI techniques to explore age-related joint degeneration. Their study assessed magnetization transfer, T1, and T2* relaxation times as potential cartilage and meniscal health biomarkers. By analyzing meniscal tissue's structural and biochemical composition,

the researchers identified patterns associated with degenerative changes, which could serve as early indicators of osteoarthritis. Their findings provide a foundation for developing non-invasive diagnostic techniques that allow veterinarians to track joint deterioration over time. The study's results emphasize the potential of MRI-based biomarkers in guiding therapeutic interventions to preserve joint function and mitigate osteoarthritic progression in aging dogs.

Lee et al. applied two-point and six-point Dixon MRI for fat fraction analysis in healthy dogs' lumbar vertebral bodies and paraspinal muscles, comparing the results with magnetic resonance spectroscopy. The study demonstrated that Dixon MRI provides a reliable and non-invasive method for quantifying fat infiltration in muscle tissue. It is a valuable tool for assessing muscle health and detecting early signs of atrophy. Their research suggests that this imaging technique could be beneficial for monitoring metabolic disorders and neuromuscular conditions that affect muscle composition. By eliminating the need for invasive biopsies, Dixon MRI offers a practical alternative for routine veterinary assessments and long-term health monitoring. The study further validates Dixon MRI as a faster, clinically feasible alternative to traditional magnetic resonance spectroscopy, increasing its applicability in veterinary practice.

DuPont and Boudreau measured canine medial retropharyngeal lymph nodes using T2 spin-echo sequences at 3T MRI to establish baseline values for normal lymph node size and texture. The study provides critical reference data for distinguishing between physiological variations and pathological enlargement due to lymphoma, infection, or metastatic disease. By defining normal morphometric parameters, this research improves the diagnostic utility of MRI in clinical settings, allowing for more accurate assessments of lymphadenopathy. Their findings highlight the importance of advanced imaging techniques in early disease detection, ultimately aiding in timely therapeutic decision-making. The study also explores the potential correlation between lymph node size and systemic disease, further expanding the role of MRI in clinical veterinary oncology.

Kim et al. detailed the MRI characteristics of an atypical cervical glioma with a predominant extramedullary distribution in a dog. The case study underscored the importance of MRI in differentiating spinal tumors based on their location, extent, and tissue characteristics, which directly influence treatment planning. Their imaging findings provided crucial insights into the compressive effects of the tumor on surrounding neural structures, guiding the surgical approach and postoperative management. The study further demonstrated the potential for significant neurological recovery following the intervention, even in severe spinal cord compression cases, emphasizing the importance of early and accurate imaging for optimizing treatment outcomes. By combining advanced MRI findings with histopathological confirmation, this case highlights the evolving role of MRI in diagnosing and managing complex spinal tumors in veterinary patients.

In addition to MRI, CT remains a highly effective tool in veterinary diagnostic imaging. By utilizing advanced computed tomography (CT) modalities—including spectral CT, cone beam CT (CBCT), multidetector CT (MDCT), and CT angiography—researchers are enhancing diagnostic accuracy, refining treatment strategies, and improving non-invasive assessment techniques. These innovations provide a more precise understanding of anatomical and pathological variations, ultimately optimizing clinical decision-making in veterinary medicine.

Ji et al. examined the echocardiographic and CT features of congenital bronchoesophageal artery hypertrophy and fistula in a dog. Their study highlighted the complementary roles of echocardiography and CT angiography in diagnosing complex vascular anomalies, which are often challenging to detect using a single imaging modality. A 4-year-old beagle underwent routine medical screening, revealing a right-sided continuous murmur. Further imaging identified multiple systemic-to-pulmonary shunts, which were surgically ligated. Postoperative imaging confirmed reduced ventricular overload and decreased shunt flow. This study provides valuable insight into the imaging features and surgical management of multi-origin systemic-to-pulmonary shunts, emphasizing the role of multimodal imaging in diagnosis and intervention.

Umh et al. conducted a detailed morphologic study of PDA in 25 dogs using computed tomography imaging, providing an in-depth characterization of anatomical variations in this congenital defect. By evaluating differences in PDA morphology, the study helps refine surgical and catheter-based closure techniques, ensuring better procedural outcomes. Their findings revealed three distinct PDA morphologies, with significant correlations between anatomical dimensions and body weight. The distinctive cross-sectional configuration observed via CT imaging offers valuable pre-procedural planning insights, potentially aiding the design of new occlusion devices. This research enhances interventional cardiology approaches, allowing for more tailored and effective treatment strategies.

Hagenbach et al. compared cone beam computed tomography (CBCT) with multidetector computed tomography (MDCT) for imaging the equine carpal region. Their study demonstrated that CBCT provides detailed visualization of bone and soft tissue structures with reduced radiation exposure compared to MDCT. In a study of 28 forelimbs from 15 horses, CBCT was effective for assessing osseous structures and some intraarticular ligaments, particularly after contrast enhancement. However, MDCT provided superior imaging of soft tissue structures and cartilage. These findings position CBCT as a reliable diagnostic tool for equine orthopedic evaluations, particularly useful in detecting early-stage musculoskeletal injuries such as stress fractures and osteoarthritis.

Mikić et al. evaluated virtual non-contrast spectral CT images compared to accurate unenhanced images in rabbits, demonstrating that spectral CT offers a viable alternative to conventional imaging with potentially lower radiation doses. By analyzing 219 regions of interest in 20 rabbits, the study confirmed that attenuation values between virtual and accurate non-contrast images were highly comparable, particularly in the spleen, liver, musculature, and renal cortices. Additionally, the elimination of motion artifacts and reduction in radiation exposure make this method particularly beneficial for fragile or repeatedly imaged patients. While the technique has shown promise for normal

tissues, further research is needed to validate its applicability in diseased organs, paving the way for broader veterinary applications.

Shear Wave Elastography (SWE) has emerged as a valuable non-invasive diagnostic tool for assessing reproductive organ health in veterinary medicine. Zappone et al. investigated testicular stiffness in healthy and fertile male dogs using qualitative (2D-SWE) and quantitative (pSWE, 2D-SWE) techniques. Their study established baseline values for normal testicular stiffness in medium-to-large breed dogs, finding relatively uniform stiffness with minor variations across anatomical regions but no significant differences between testes, breeds, or age groups. Additionally, body weight showed a correlation with stiffness in 2D-SWE measurements. These findings highlight the potential of SWE for detecting early testicular abnormalities, improving reproductive management, and aiding in diagnosing subclinical infertility in breeding dogs. Further research with larger and more diverse canine populations will help refine its clinical applications.

Similarly, Uçmak et al. explored the use of SWE in monitoring postpartum reproductive organ recovery in Kivircik ewes. Their study quantified shear wave speed (SWS) and stiffness in the uterine cervix, caruncles, and vulvar labia, alongside Power Doppler ultrasonography to assess blood flow changes in caruncles. They observed significant time-dependent differences in cervical stiffness and caruncular regression, providing key insights into uterine involution. The findings demonstrate the potential of SWE in tracking postpartum recovery and fertility status in livestock, offering a new non-invasive approach to reproductive health assessment in ewes.

Together, these studies underscore the growing role of elastography in veterinary reproductive medicine. By enabling precise, real-time evaluation of tissue stiffness in different reproductive structures, SWE is promising to improve breeding management, early disease detection, and overall reproductive efficiency in companion animals and livestock.

Kleiner et al. and Wolf et al. investigated advanced techniques for sacroiliac luxation repair in feline cadaveric models. Both studies utilized CT-based neuronavigation to enhance surgical accuracy and safety. Kleiner et al. compared fluoroscopy-controlled freehand drilling to computer-assisted navigation, demonstrating improved screw placement precision with neuronavigation. Similarly, Wolf et al. assessed the feasibility of minimally invasive computer-assisted drilling (MICA) compared to the traditional fluoroscopy-controlled approach. Their study highlighted a steep learning curve but showed that computer-assisted techniques reduced surgical inaccuracies over time, improving accuracy deviations from 4.2 mm to 0.9 mm after five procedures. Moreover, Wolf et al. introduced a new patient reference array placement method, which improved safety by preventing violations of vital structures. These findings emphasize the role of CT-based image guidance in orthopedic procedures, enhancing surgical precision while minimizing neurovascular risks.

Godlewska et al. presented a case report on a nodular lesion in the ventral neck of a rat, utilizing radiography, ultrasound, and echocardiography alongside histopathology to establish a differential diagnosis. The study highlighted the challenges of assessing subcutaneous tumors in small mammals due to their rapid growth and varied etiologies. Their comprehensive multimodal imaging approach facilitated a more accurate lesion characterization, enabling targeted biopsy and subsequent therapeutic planning. The case emphasizes the importance of combining different imaging modalities in diagnosing rare or ambiguous masses in exotic animal practice.

Reinitz et al. utilized CT-based angiography with a barium contrast agent to generate a 3D reconstruction of the vascular anatomy in an African elephant's hindfoot. This study provides crucial insights into the unique blood supply to the digital cushion, supporting in the diagnosis, treatment, and prevention of foot diseases, which are a leading cause of morbidity in captive and wild elephants.

In conclusion, this Research Topic of studies underscores the pivotal role of advanced imaging techniques in modern veterinary medicine. By integrating detailed anatomical knowledge with cutting-edge imaging modalities, veterinary professionals can achieve more accurate diagnoses, refine surgical techniques, and improve patient outcomes across various species and conditions. The studies within this Research Topic illustrate how imaging is essential for diagnosing diseases and advancing anatomical knowledge, surgical precision, and therapeutic approaches in veterinary science.

Author contributions

SD: Writing – original draft, Writing – review & editing, Conceptualization. OG: Writing – original draft, Writing – review & editing. TS: Writing – review & editing, Writing – original draft, Conceptualization, Supervision.

Acknowledgments

The Topic Editors appreciate the contributions of all authors to this Research Topic.

Conflict of interest

The authors declare that the research was conducted in the absence of any commercial or financial relationships that could be construed as a potential conflict of interest.

Publisher's note

frontiers | Frontiers in Veterinary Science

TYPE Original Research
PUBLISHED 02 May 2024
DOI 10.3389/fvets.2024.1397347

OPEN ACCESS

EDITED BY
Ozan Gündemir,
Istanbul University Cerrahpasa, Türkiye

REVIEWED BY
Silvia Burti,
University of Padua, Italy
Zeynep Günay Uçmak,
Istanbul University-Cerrahpasa, Türkiye
Muzaffer Onur Şeran,
Independent Researcher, Istanbul, Türkiye

*CORRESPONDENCE
Letizia Sinagra
✉ letizia.sinagra@gmail.com
Viola Zappone
✉ viola.zappone@unime.it

RECEIVED 07 March 2024
ACCEPTED 12 April 2024
PUBLISHED 02 May 2024

CITATION
Zappone V, Iannelli NM, Sinagra L, Donato G, Quartuccio M, Cristarella S, De Majo M and Caspanello T (2024) Assessment of testicular stiffness in fertile dogs with shear wave elastography techniques: a pilot study. *Front. Vet. Sci.* 11:1397347. doi: 10.3389/fvets.2024.1397347

Assessment of testicular stiffness in fertile dogs with shear wave elastography techniques: a pilot study

Viola Zappone[1]*, Nicola Maria Iannelli[1,2], Letizia Sinagra[1]*, Giulia Donato[1], Marco Quartuccio[1], Santo Cristarella[1], Massimo De Majo[1] and Tiziana Caspanello[1]

[1]Department of Veterinary Sciences, University of Messina, Messina, Italy, [2]Clinica Veterinaria Camagna–VetPartners, Reggio di Calabria, Italy

Ultrasound of the testes is important in the evaluation of breeding dogs, and recently advanced techniques such as Shear Wave Elastography (SWE) have been developed. This study focused on evaluation of normal testicular stiffness in healthy and fertile male dogs, employing both qualitative (2D-SWE) and quantitative (pSWE, 2D-SWE) techniques. Nineteen dogs of various medium-large breeds aged 3.39 ± 2.15 years, and with a history of successful reproduction were included after clinical, B-mode and Doppler ultrasound of testes and prostate, and semen macro and microscopic evaluations. pSWE involved square regions of interest (ROIs) placed at six different points in the testicular parenchyma, while 2D-SWE depicted stiffness with a color scale ranging from blue (soft) to red (stiff), allowing a subsequent quantification of stiffness by the application of 4 round ROIs. The results showed a mean Shear Wave Speed (SWS) of 2.15 ± 0.39 m/s using pSWE, with lower values above the mediastinum compared to below, and in the center of the testis compared to the cranial and caudal poles. 2D-SWE demonstrated a uniform blue pattern in the parenchyma, and a mean SWS of 1.65 ± 0.15 m/s. No significant differences were found between left and right testes, above and below the mediastinum, or among breeds. No correlations were observed between mean SWS and body condition score, age, testicular and prostatic volume. Weight was positively correlated with mean SWS only by 2D-SWE. By performing semen analysis and enrolling only healthy and fertile adult dogs, we ensured both structural and functional integrity of the testes. This pilot study represents a valuable baseline data for testicular stiffness by both pSWE and 2D-SWE with a Mindray US machine in medium-large sized healthy and fertile dogs, pointing out the potential role of SWE in the non-invasive fertility assessment and management of breeding dogs.

KEYWORDS

shear wave elastography, ultrasound, dog, testis, fertility

Introduction

The ultrasonographic evaluation of the testes is an important step in assessing the reproductive potential of a male dog, along with clinical examination of the genitalia, assessment of libido and examination of semen (1). Ultrasonography is a reliable imaging technique that allows real-time assessment of the reproductive tract and is the gold standard

for testicular evaluation due to its high resolution, ability to assess flow, availability, and safety (2, 3). To improve the accuracy of bidimensional ultrasound, several advanced ultrasound techniques have been developed, such as Doppler, contrast-enhanced ultrasonography (CEUS), 3D/4D ultrasonography, and elastography (3).

Elastography is an ultrasound technique for measuring tissue stiffness. Currently, there are two main categories, Strain elastography (SE) techniques, which measure the elastic recovery of tissue after the application of external mechanical compression with a probe, and Shear wave elastography (SWE) techniques, which are based on the measurement of shear wave speed (SWS). Shear waves are generated in the tissue in response to focused acoustic pulses from the probe, and their speed is positively correlated with tissue stiffness. Moreover, SWE techniques can be divided into point shear-wave elastography (pSWE) and multidimensional SWE (2D-SWE, and 3D-SWE). The former measures the SWS in a focal point in the tissue (called region of interest, ROI), while 2D-SWE measures the SWSs in several points within a larger field of view (FOV) and depicts them in a color-coded map (called elastogram), superimposed to the gray-scale image (4–7). In 3D-SWE, the images are reconstructed in three dimensions (i.e., the axial, sagittal, and coronal planes), using a single sweep of the ultrasound beam across the entire area of interest. Thus, 3D-SWE has the capability to generate volumetric images and to effectively show the stiffest point within a mass (8, 9). Results of SWE can be expressed both in m/s (as shear wave speed) or be converted to Young's modulus (in kPa) (6).

In human medicine, testicular stiffness has been investigated by elastography in both physiological (10) and pathological testes (11–18). Elastography has been applied for the evaluation of undescended testes, infertility, testicular torsion, tumors, microlithiasis, varicocele and segmental testicular infarction (18), and has shown efficacy in the diagnosis of varicocele (19) and in discriminating focal non-neoplastic lesions from neoplasms, and benign from malignant testicular tumors (20). This technique also showed to be useful in predicting the postoperative improvement in some sperm parameters in patients subjected to varicelectomy (21).

In veterinary medicine, studies on the application of elastography to canine testes have demonstrated its utility in differentiating Leydigomas from non-neoplastic testicular lesions by 2D-SWE (22), in assessing normal testicular values by pSWE (23), in describing pSWE characteristics of pathological testicular tissue (24), and in evaluating epididymal spermatogenesis by SE (25).

The aim of this study was to assess normal testicular stiffness using pSWE and 2D-SWE in dogs with established fertility. This would allow this ultrasound technique to be used as a diagnostic support in course of testicular disorders that may interfere with normal fertility in dogs.

Materials and methods

Ethical approval

All treatments, housing and animal care followed EU Directive 2010/63/EU on the protection of animals used for scientific purposes. The Ethics Committee of the Department of Veterinary Medicine and Animal Productions at the University of Messina, Italy (protocol n. 051/2021), approved the protocol and procedures. Informed consent was obtained from each dog owner before its inclusion in the study.

Animals and inclusion criteria

A total of 19 client-owned healthy male dogs, heterogeneous in breed and age, were included in the study, which took place between April and October 2023. The subjects were presented to a veterinary practice (Clinica Veterinaria Camagna – VetPartners, Reggio Calabria, Italy) for an evaluation of their reproductive potential. To be included in the study, subjects had to be in good general health, have at least one litter in their reproductive history, and have prostatic and testicular echotexture and sizes within the physiological range the animal's weight and size (26, 27). They also had to be free of clinical and ultrasound abnormalities of the reproductive system and have sperm with minimum characteristics according to the World Health Organization standard methods (28).

For each dog, a remote and recent medical history was acquired, and general clinical examinations and blood analysis were performed. Blood tests included a complete blood count (CBC), and a baseline serum biochemistry assessment of albumin (ALB), globulin (GLOB), ALB/GLOB ratio, alkaline phosphatase (ALKP), Alanine transaminase (ALT), blood urea nitrogen (BUN), creatinine (CREA), glucose (GLU), and total proteins (TP). Finally, a complete reproductive health examination was performed, including a clinical examination of the reproductive system, ultrasound of the testes and prostate, and semen analysis.

Ultrasound procedures

Ultrasonography was performed by the same operator (MQ), who had 15 years of experience in this field, to avoid interobserver variability. All the procedures on the dogs were performed without sedation or anesthesia. Scrotal sac hair was clipped, and gel was applied to the surface.

B-mode ultrasound was performed by a 3–12 MHz linear transducer (L12-3E) using a Mindray DC-80A ultrasound equipment (Mindray Medical Italy S.R.L. Via Leonardo da Vinci, 158–20,090 Trezzano sul Naviglio, Italia). Qualitative analysis of blood flow by Color and power Doppler was performed in testes, epididymis, and spermatic cord.

Testicular volume was calculated using the electronic calipers of the device, applying the formula for an ellipse: volume = length × width × height × 0.5236. The volume of each testicle was added to give the total testicular volume (TTV). Prostatic volume (PV) was calculated using the formula: [1/2.6 (L × W × D)] + 1.8 (29). Both testes and prostate were assessed for size, margins (regular or irregular) and echotexture of the parenchyma (homogeneous and heterogeneous, hypoechoic, hyperechoic or mixed in relation to the surrounding tissue). Elastography was performed using a linear transducer (L12-3E) to obtain pSWE and 2D-SWE data. To minimize the external pressure of the probe, a thick layer of coupling gel was applied to the scrotal surface and the transducer was gently positioned in order to obtain a longitudinal scan of the testis. The shape of contact surface displayed on the screen was used as a quality criterion for the degree of manual pressure. pSWE was performed using square ROIs

of 0.5 × 0.5 cm, positioned in six points of the testicular parenchyma (i.e., cranial, middle, and caudal portions, above and below the mediastinum line, respectively) where there was no vascularization signal. The machine gave real-time median SWS values within the ROI and quality indexes, such as the Motion-stability index (MST-B) and Interquartile range/median (IQR/M) ratio. The first index is represented by a 5-point star-shaped scale that turns green when the object is perfectly still, while the IQR/M ratio is an index of variability of the measurements within the ROI. The criteria for frame acquisition were at least 4 green stars for the MST-B index and an IQR/M ratio < 15% (7, 30). A mean value for each of the six ROI was calculated in m/s.

For the 2D-SWE ultrasound, the FOV was set to include the whole testis in longitudinal scan. When the elastography mode was on, the machine provided a dual image representing the B-mode ultrasound on the left, and the elastogram on the right. The color scale of the elastogram ranged from blue to red (0–70 kPa – 0.0–4.8 m/s), with blue areas representing the softest tissue and red areas representing the stiffest tissue. The criterion for the acquisition of the frames was a MST-B index of at least 4 green stars. Subsequently, in post-processing of the saved image, focal mean SWSs could be assessed by placing round ROIs within the FOV. The operator placed two pairs of ROIs of 0.5 cm diameter on each testis, two ROIs being above the mediastinum line, and two beneath it. Also in this case, the ROIs were positioned in areas without vascularity. Then the average SWSs between the two ROIs of each couple were calculated.

Semen analysis

Sperm collection was performed in a quiet and appropriate environment with a non-slip floor, by manual collection and in the presence of a teasing bitch, and after removal of the extragonadal reserve to minimize defects in sperm stored in the epididymis, such as reduced motility and increased debris. Macroscopically, the volume, color and appearance of the ejaculate were assessed. Sperm concentration was assessed using an SDM1 photometer (MiniTube™), calibrated for dogs by prior validation with a Makler chamber (Sefi-Medical Instruments, Haifa, Israel), by placing 10 µL of ejaculate in the appropriate loggia of the instrument's analysis microscope. Motility was assessed using the CASA software. The analysis was performed with the following parameters: number of frames acquired 30, frame rate 60 Hz, minimum cell contrast 75, minimum cell size 4 pixels, straightness threshold 75%, path velocity threshold 100 µm/s-1, mean path velocity (VAP) cut-off 9.0 µm/s-1, mean VAP cut-off 20 µm/s-1, non-motile head size 4 pixels, non-motile head intensity 80, static head size 0.44–4.98, static head intensity 0.49–1.68 and static elongation 17–96%. After staining with eosin/nigrosin, cell morphology was assessed by examining a minimum of 200 spermatozoa per slide. For the evaluation of the semen parameters, we applied the threshold values reported by Tesi et al. (31).

Statistical analysis

The statistical analysis was performed using software *Jamovi* (Version 2.3.28.0 for MacOS) (32). Descriptive statistics were expressed in mean ± standard deviation, and median values. Shear wave speed (SWS) values were expressed in m/s, in mean values ± standard deviation, 95% confidence interval for the mean, and minimum and maximum values. Shapiro–Wilk test was performed to assess normality of data. Data obtained by 2D-SWE were normally distributed, while data from pSWE did not follow normality; hence, for the analysis of these data sets, parametric and non-parametric tests were employed, respectively.

For pSWE measurements, Mann–Whitney's U test was performed to evaluate differences between measurements in left and right testicle, and above and below the mediastinum line. Friedman's test was used for the analysis of variance between the six measurement points. If the test was positive and statistically significant, *post-hoc* Paired Comparisons (Durbin-Conover) were performed.

For 2D-SWE evaluations, Student's T test was applied to evaluate differences between measurements taken in left and right testis, above and below the mediastinal line.

For both pSWE and 2D-SWE measurements, a Spearman Rho test was applied to search for correlation between of mean SWS with weight, body condition score (BCS), age, testicular volume, and prostatic volume of the dogs. Kruskall-Wallis test was used for the analysis of variance of pSWE and 2D-SWE values between breeds.

For correlations between total testicular volume (TTV) and total sperm count (TSC), TTV and sperm motility percentages, prostatic volume (PV) and TSC, and between ejaculate volume and sperm motility percentages, Rho Spearman's test was performed.

For all the tests, results with p values <0.05 were considered statistically significant.

Results

Animals

Nineteen male dogs were included in the study (Table 1), of which seven were English Setters, six Pointers, four Italian Pointing dogs, one German Wirehaired Pointer and one Italian Spinone. The age of the dogs ranged from 1 to 9 years, with a mean of 3.39 ± 2.15 years and a median of 3 years. Their weight ranged from 15.5 to 31 kg, with a mean of 23.19 ± 4.90 kg and a median of 23 kg. Body condition score (BCS) showed a mean score of 4.29 ± 0.75 on a scale of 1 to 9 points. None of the dogs showed alterations of the blood parameters examined. Due to lack of compliance, dogs n.17 and n.18 were only assessed with pSWE and 2D-SWE, respectively.

B-mode and Doppler ultrasound

By B-mode ultrasound, the testes and the prostate of all the dogs included were normal in size, margins, and parenchyma echotexture. The testes were ovoid in shape, with regular margins characterized by a thin and hyperechoic line (tunica albuginea). Testicular parenchyma presented medium echogenicity with a fine and homogeneous echotexture, interrupted by the presence of the mediastinum in the central part of the testis, which appeared as a hyperechoic line or spot, in the longitudinal and transverse scans, respectively. The prostate showed a rounded shape, with smooth margins and a homogeneous fine-coarse, medium-echoic texture. Color and power-Doppler examinations of testicles, prostate and

TABLE 1 Characteristics of subjects enrolled in the study: breed, body weight, body condition score.

Dog	Breed	Body Weight (kg)	Age (Years)	BCS (1–9)
1	Pointer	21	8	4.5
2	Pointer	23	1.5	3.5
3	English Setter	19	9	4
4	Pointer	20	5	4
5	English Setter	18.5	2	3.5
6	English Setter	20	4	4
7	English Setter	24	4	4
8	English Setter	21	4	4
9	Pointer	21	5	5
10	Pointer	23	1.5	4.5
11	Pointer	24	1.5	5
12	Italian Spinone	25	1	6
13	English Setter	15.5	2.5	5
14	English Setter	15.7	2.5	5.5
15	Italian Pointing dog	31	2	4
16	Italian Pointing dog	30	2	4.5
17	Italian Pointing dog	31	3	3.5
18	Italian Pointing dog	30	3	3
19	German Wirehaired Pointer	28	3	4

BCS = Body condition score.

spermatic cord showed the presence of widely distributed arterial and venous blood flows (Figure 1). Quantitative testicular and prostatic ultrasound evaluations showed a mean total testicular volume (TTV) of 16.62 ± 4.36 cm^3 and a mean prostatic volume (PV) of 10.88 ± 4.18 cm^3 (Table 2).

pSWE

Eighteen pairs of testes were evaluated by pSWE and 216 measurements were obtained (Figure 2). Mean SWS was 2.15 ± 0.39 m/s (95%CI = 2.10–2.21 m/s). Mean ± Standard deviation (SD), 95% confidence interval (CI) for the mean, minimum and maximum SWSs obtained in the six different points of the testes, are reported in Table 3.

No statistical differences were found between left and right testicles ($p = 0.189$), while the mean values obtained below the mediastinum (2.30 ± 0.41 m/s) were significantly higher than the ones taken above the mediastinum (2.01 ± 0.31 m/s) ($p < 0.001$). Friedman's test showed significant differences between the measurements taken in the three points of the testicular parenchyma (cranial, middle, caudal portion) ($p < 0.001$). *Post-hoc* comparisons showed that measurements taken in the middle of the testicular parenchyma were significantly lower than measures obtained in the cranial ($p < 0.001$) and caudal ($p = 0.008$) poles. These differences remained when measurements above ($p = 0.003$) and below ($p < 0.001$) the mediastinum were considered separately.

No significant differences were found in mean SWS values between different breeds ($p = 0.159$). No correlation was found between pSWE measurements and weight, BCS, age, testicular volume, prostatic volume (Table 4).

2D-SWE

Eighteen pairs of testes were evaluated by 2D-SWE and 72 SWS measurements were obtained.

Qualitative analysis showed a uniform blue pattern in the testicular parenchyma, while the surrounding structures (testicular involutes) appeared as a colored border from green to red, following the gradient of the scale, from the internal to the external part of the FOV (Figure 3). Results of quantitative analysis, Mean, with the respective 95% confidence interval (CI), standard deviation (SD), minimum and maximum values, expressed m/s, are reported in Table 5.

No significant differences were found between left and right testicles ($p = 0.061$), and between measurement taken above (1.64 ± 0.15 m/s) and below (1.66 ± 0.15 m/s) the mediastinum line ($p = 0.486$). There were no significant differences also in measurements between breeds ($p = 0.249$).

A significant positive correlation was found between testicular stiffness and weight of dogs. No correlation was found between 2D-SWE values and age, BCS, testicular volume, and prostatic volume of the evaluated patients (Table 6).

Semen analysis

The results of the evaluation of the ejaculate of the 19 dogs included in the study are reported in Table 2. The analysis of quantitative parameters showed an average volume of 8.92 ± 4.96 mL of ejaculate, an average concentration of spermatozoa of 103.15 ± 63.26 $\times 10^6$/ml and a mean total sperm count of 859.23 ± 328.44 $\times 10^6$ spermatozoa. The evaluation of motility of the spermatozoa showed average percentage values of 71.38 ± 12.57%, 27.37 ± 12.01%, and 1.28 ± 2.66% of progressive, non-progressive, and immobile spermatozoa, respectively. The percentage of spermatozoa with abnormalities was lower than 10%. The values of the semen parameters were in the physiological range for the species, breed and size of each animal, demonstrating their fertility.

Spearman's Rho test showed absence of correlations between TTV and TSC ($p = 0.769$), between TTV and sperm motility percentages ($p = 0.656$), and between PV and TSC ($p = 0.542$). Ejaculate volume was positively correlated to the percentage of progressive spermatozoa (Rho: 0.498; $p = 0.035$), and negatively correlated to the percentage of non-progressive spermatozoa (Rho: −0.499; $p = 0.035$).

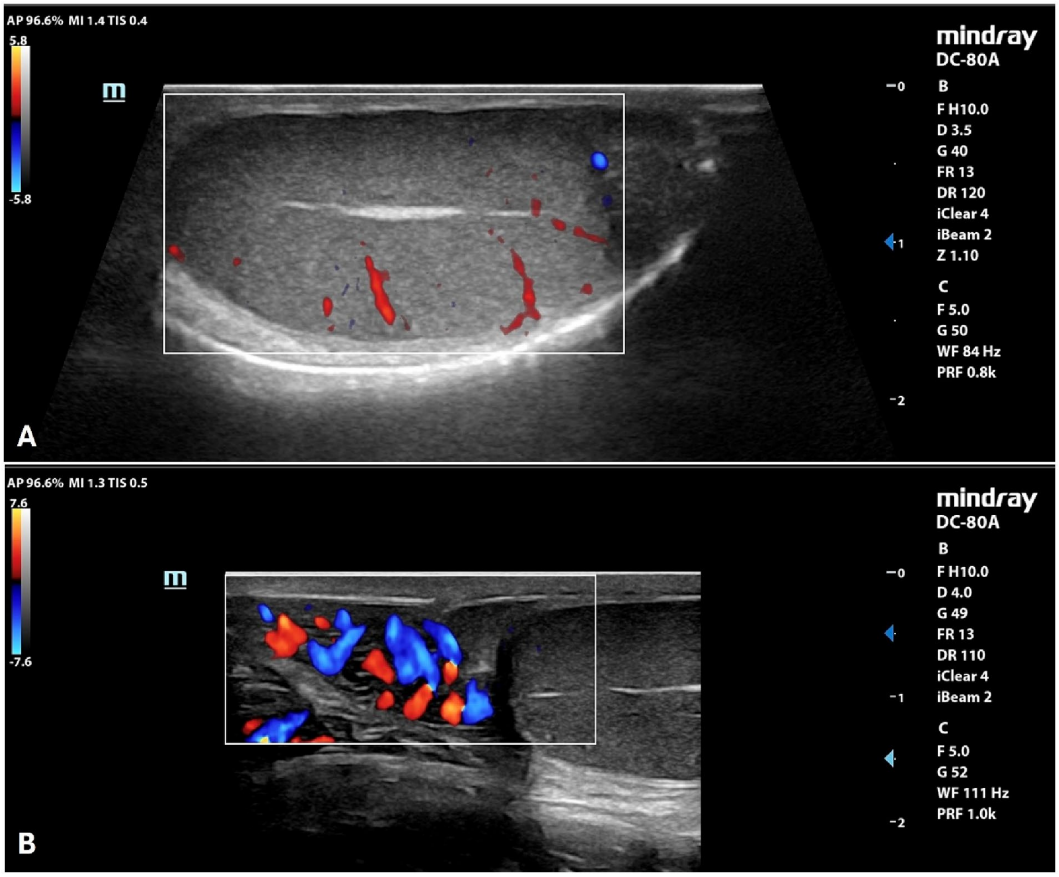

FIGURE 1
Color Doppler examination of the testicle **(A)** and spermatic cord **(B)** of a normal canine testicle.

Discussion

Elastography is a safe and harmless ultrasound technique that allows the depiction of mechanical properties of tissues, and the assessment of tissue stiffness, adding diagnostic power to conventional ultrasound techniques. This technique found important applications in human medicine, being highly predictive of hepatic fibrosis and helpful in the characterization of breast and thyroid nodules (33, 34).

In veterinary medicine, several studies evaluated the performance of elastography in discriminating healthy from abnormal tissue, and in characterizing tissue alterations (35, 36). The application of elastography to canine reproductive tract was reported for the first time in 2015, with the assessment of prostatic strain values in healthy beagle dogs (37); in 2016, SE was used to assess canine testicular, epididymal, and prostatic physiological strain values (38). Compared to SE techniques, SWE techniques showed higher sensitivity (39, 40) and better inter-operator agreement (41, 42). On the other hand, the repeatability of SWE becomes an issue when comparing measurements obtained from different machines. In fact, ultrasound manufacturers use their own software for elastography, whose measurements differ significantly from each other. For this reason, the guidelines for the application of SWE suggest that each manufacturer should have its own reference values (6, 7, 33). To the best of our knowledge, our is the first study that evaluates the performance of both focal and bidimensional SWE techniques in canine testes with normal semen analysis and in absence of ultrasonographic abnormalities of testes and prostate, using Mindray equipment. Therefore, this work establishes the baseline for standard values, useful for further comparisons with pathological findings.

In our study, dogs that could be considered healthy and fertile were selected to assess their testicular SWS. As the dogs enrolled were breeding dogs, it was not possible to perform cytologic and/or histopathologic evaluation of the testicles to assess their integrity. In fact, these traumatic procedures can cause testicular damage, with complications that may also become evident only in the long term (43, 44). Hence, we applied strict inclusion criteria as evidence of both structural and functional integrity of the testicles; good health and fertility were assessed by the absence of clinical and laboratory alterations, the presence of at least one litter in dogs' history, and a thorough breeding soundness examination, including B-mode and Doppler ultrasound evaluations and semen analysis.

Although correlations between semen parameters and prostatic and testicular volumes were previously reported (45–47), in our study there were no correlations between testicular volume and total sperm count, between testicular volume and sperm motility, or between prostatic volume and total sperm count. However, this discrepancy could be due to the limited number of dogs evaluated, that could have affected the power of the statistical analysis. Furthermore, ejaculate volume showed correlation with sperm motility, being positively correlated to the percentage of progressive spermatozoa, and

10.3389/fvets.2024.1397347

TABLE 2 Total testicular and prostate volume and semen parameters of the ejaculate of the 19 dogs included in the study.

Subjects	Measurements		Quantitative parameters			Motility		
Dog	TTV (cm^3)	PV (cm^3)	Volume (ml)	Count ($x10^6$/ml)	TSC ($x10^6$)	Progr. %	N-Progr. %	Immobile %
1	11.24	14.09	13	53.92	700.96	74	25.46	0.54
2	20.6	11.32	14	38.55	999.04	82	17.89	0.11
3	20.55	8.47	5	133.45	667.25	69.45	27.8	2.75
4	16.42	10.22	5	124.65	623.25	69.19	27.54	3.27
5	12.21	10.9	10	57.84	630.45	59.7	37.72	2.58
6	11.63	5.28	9	161.35	1452.15	28.9	69.85	1.24
7	21.58	6.06	7	22.57	157.99	62.2	26.42	11.38
8	15.73	10.32	3.5	273.18	956.13	65.56	34.44	0
9	10.35	16.54	12	104.03	1248.36	69.36	30.54	0.1
10	20.06	12.68	5	165.76	828.8	74.54	25.46	0
11	19.8	5.6	10	128.17	1281.7	82.77	17.23	0
12	9.23	13.24	4	169.89	679.56	70.63	29.37	0
13	13.77	6.07	9	121.76	1095.84	76.23	23.68	0.09
14	17.05	5.39	8	109.44	875.52	76.61	23.14	0.25
15	21.73	11.78	9	100.33	902.97	71.4	28.83	0.23
16	23.39	20.19	19	87.28	903.42	80.66	19.01	0.33
17	15.61	16.25	20	35.57	1323.36	73	25.82	1.18
18	20.1	12.68	3	36.05	529.98	86	13.85	0.15
19	14.8	9.62	4	36.05	468.65	84	15.93	0.07

US = Ultrasound; TTV = Total testicular volume; PV = Prostatic volume; TSC = Total Sperm count; Progr = Progressive; N-Progr = Non-Progressive.

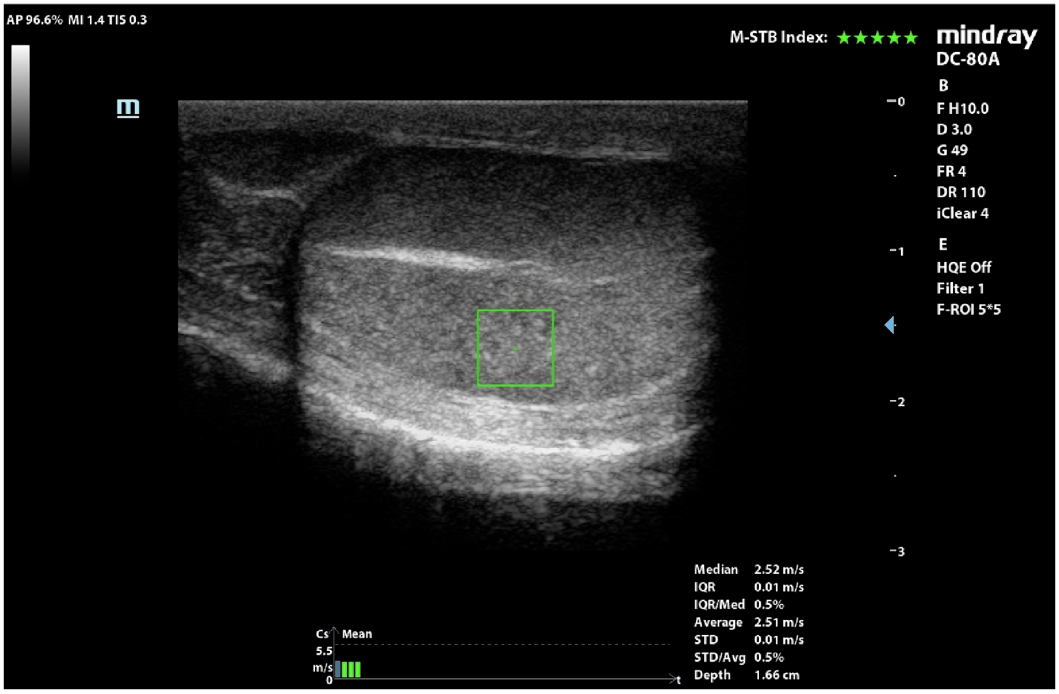

FIGURE 2
pSWE of a normal dog's testicle. ROI was positioned in the middle portion and below the mediastinum.

TABLE 3 Shear wave speeds (SWSs) obtained by pSWE in the six points of measurement (cranial, middle, and caudal portions of the parenchyma, above and under the mediastinum).

	Above mediastinum			Below mediastinum		
	Cranial	Middle	Caudal	Cranial	Middle	Caudal
Mean ± SD (m/s)	2.15 ± 0.32	1.86 ± 0.23	2.01 ± 0.32	2.41 ± 0.37	2.14 ± 0.44	2.36 ± 0.40
95% CI for the mean (m/s)	2.04–2.26	1.79–1.94	1.9–2.11	2.28–2.53	1.99–2.29	2.22–2.49
Min (m/s)	1.62	1.56	1.42	1.53	1.54	1.51
Max (m/s)	2.81	2.46	3.04	3.07	3.07	3.21

TABLE 4 Analysis of correlation between mean SWS and weight, age, body condition score (BCS), testicular and prostatic volume of the dogs examined by pSWE.

		Weight	Age	BCS	Testicular volume	Prostatic volume
Mean SWS	Spearman's Rho	0.065	−0.394	0.327	−0.122	0.284
	DoF	16	16	16	16	16
	p value	0.797	0.106	0.185	0.631	0.253

BCS, Body condition score; DoF, Degrees of freedom.

negatively correlated to the percentage of immobile spermatozoa. To the best of our knowledge, this is the first report of this finding in dogs. Although it was not the aim of our study, this topic is worth of further investigations involving a lager sample size, to ensure a robust statistical analysis of the factors influencing semen quality.

With pSWE evaluation, by measuring in six points of the testicular parenchyma, we obtained an average SWS of 2.15 ± 0.39 m/s. Noteworthy, we found that measurements taken above the mediastinum showed lower values than the ones taken below, and that the central portion of the parenchyma was softer than the cranial and caudal poles, regardless of the depth of the measurement. Although there is no previous report of this finding in veterinary medicine, it has been previously described in human testes (10, 42), and has been explained as a reflection of the different structural anatomy in the testicular portions examined; in fact, the central part of the testis is characterized by more seminiferous tubules and greater lymphatic and blood vascularization, opposed to a higher tissue density in the rete testis area (42). Considering these differences, it may be practical to assess the stiffness in several points on the testis, which should include at least the central portion and one of the extreme portions (cranial or caudal) of the parenchyma, both above and below the mediastinum. This will allow the operator to perform a thorough and reliable pSWE evaluation, and to avoid biases related to the point of measurement.

In veterinary medicine, the reference values for a healthy testis according to pSWE have been reported in two studies by Feliciano et al. (23, 24). The first was a preliminary study, which found a mean SWS of 1.28 m/s in juvenile dogs, and 1.26 m/s in adult and senior dogs. In that study no semen analysis, nor cytology or histopathology were performed to confirm the healthy status of the testes (23). In the second study, the same authors evaluated both healthy and abnormal testes, histopathology was performed, and an average SWS of 1.30 ± 0.12 m/s for healthy testes was reported (24). Furthermore, the authors described testicular disorders in 36 testes, defining the values for degeneration, atrophy, hypoplasia, orchitis, interstitial cell tumors, Sertoliomas and Leydigomas, and finding that the benign lesions were softer than malignant ones (24). In both their studies, the shear velocities obtained for normal healthy canine testes higher than those observed in humans (0.62–1.01 m/s) (48), probably due to a major presence of fibrous tissue in the testes of dogs compared to those of humans (23, 24). Despite we performed the same acquisition procedure (i.e., six ROIs in the longitudinal scan), higher SWSs than reported by Feliciano et al. were measured (23, 24). Unfortunately, as the authors used an Acuson S2000/Siemens ultrasound machine, we cannot establish whether the nature of this difference is due only to the different ultrasound machines used or there might be other influencing factors.

Glińska-Suchocka et al. (22) evaluated the performance of 2D-SWE in assessing testicular lesions in 9 dogs with non-neoplastic testicular lesions and Leydigomas, reporting that Leydigomas showed a stiffness of 91.85 kPa (corresponding to 5.53 m/s) compared to 11.25 kPa (corresponding to 1.93 m/s) of nonneoplastic lesions. The authors then suggested elastography for the screening of testicular lesions. However, the authors did not include a healthy control group with which to compare our results. Although, also in this case, the ultrasound machine was different than ours, so the value of a comparison would be low (22).

In our study, the 2D-SWE evaluation showed a mean SWS of 1.65 ± 0.15 m/s. SWS by 2D-SWE showed a significant correlation with weight of the dogs. However, the relatively low strength of the correlation, with a borderline *p* value, and the small population sample consisting of medium-large sized dogs, must be taken into account when considering this result. Mean SWSs obtained by pSWE and 2D-SWE differed from each other, the former being higher than the latter. It has previously been reported that these techniques give different values in human testes, since they rely on different sampling techniques, with greater slowing of shear waves in larger FOV/ROIs than in smaller ones (42). Furthermore, 2D-SWE is characterized by better resolution but lower precision at each image pixel than pSWE (5). However, since this kind of comparison has not been made in other studies using Mindray machines, and was not the aim of our study, it should be further assessed with the appropriate accurate analysis.

In a recent study, Gloria et al. (25) performed strain elastography in dogs to assess testicular stiffness in association with seminal

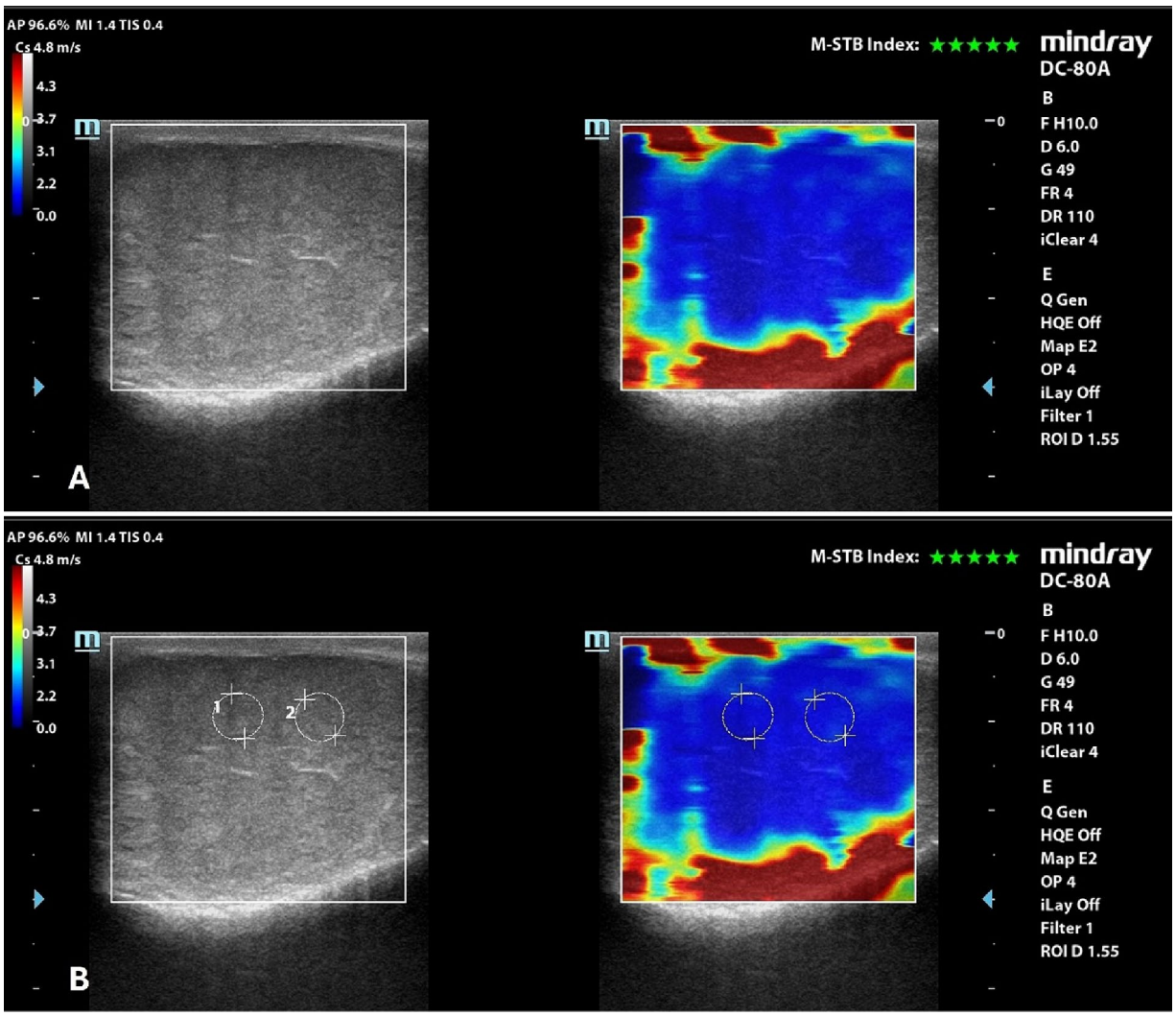

FIGURE 3
2D-SWE of a normal dog's testicle, with a dual image showing the B-mode on the left and the elastogram on the right; **(A)** qualitative assessment; **(B)** quantitative assessment obtained by placing 2 round ROIs in the testicular parenchyma above the mediastinum line.

TABLE 5 Quantitative values obtained by 2D-SWE of testes.

	SWS (m/s)
Mean ± SD	1.65 ± 0.15
95% CI for the mean	1.62–1.69
Minimum	1.35
Maximum	2.03

TABLE 6 Spearman's Rho correlation test between mean SWS obtained by 2D-SWE and weight, age, body condition score, total testicular volume, and prostatic volume of the dogs examined.

		Weight	Age	BCS	TTV	PV
mean SWS	Spearman's Rho	0.498*	−0.17	−0.166	0.034	0.076
	DoF	16	16	16	16	16
	p value	0.035	0.5	0.512	0.893	0.764

*$p < 0.05$: DoF = degrees of freedom.

parameters of spermatozoa collected from epididymis after orchiectomy, and with histological quantification of fibrous connective tissue. They found that increased testicular stiffness was associated to functional alterations, rather than to connective tissue deposition (25). In human medicine, a correlation of SWS with testicular parenchymal damage and quantitative sperm abnormality was found (49), and elastography has shown good predictive potential for recovery of semen quality after varicocelectomy (21). A similar evaluation with SWE techniques is worth to be done also in dogs. In fact, being SWE quantitative techniques, it would be possible to correlate quantitative parameters of elastography and semen analysis. As our sample was only made of healthy dogs, we could not perform this assessment. A wider sample, including dogs with semen abnormalities, and with different sizes and weights, should be further evaluated; this would provide a thorough characterization of the standard features of testicular SWE, as well as the assessment of the potential predictive value of SWE also for canine semen quality, and perhaps the definition of thresholds values. If a predictive potential for semen quality will

be found, SWE could play an essential role as a complementary step to breeding soundness examination in male dogs.

Lack of compliance is one limitation in the use of SWE in animals. In fact, the subject should remain perfectly still during the evaluation in order to obtain the most reliable results (50). This requirement is difficult to achieve in veterinary medicine, unless performing the exam under general anesthesia and with controlled ventilation, to avoid respiratory motion artifacts. Thanks to its extra-abdominal location, SWE of the testes is not affected by respiratory movements. Furthermore, the application of several quality criteria for the acquisition of the images ensured the reliability of our results. Nevertheless, two of the nineteen dogs enrolled became extremely uncompliant and allowed us to perform only half of the examination.

As mentioned above, our is a pilot study whose sample was mainly composed of medium-large sized dogs; thus, the next crucial step is to extend the research also to small, toy and giant sizes, with the same procedures and equipment, in order to create a database of reference values of testicular stiffness in fertile breeding dogs.

Conclusion

In conclusion, this pilot study provides a valuable baseline data for testicular stiffness using both pSWE and 2D-SWE with a Mindray ultrasound machine in medium-large size dogs with established fertility. The ability to accurately assess testicular health and functionality in a non-invasive manner provides veterinarians with a valuable supplement to their diagnostic approach, contributing to a better reproductive management of canine patients. Further research on a larger sample of dogs of different size are required to fully realize the potential of this innovative approach to improve fertility assessment and management in breeding dogs.

Data availability statement

The original contributions presented in the study are included in the article/supplementary material, further inquiries can be directed to the corresponding authors.

Ethics statement

The animal studies were approved by University of Messina, Italy (protocol n. 051/2021). The studies were conducted in accordance with the local legislation and institutional requirements. Written informed consent was obtained from the owners for the participation of their animals in this study.

Author contributions

VZ: Methodology, Writing – original draft, Writing – review & editing. NMI: Resources, Supervision, Validation, Writing – review & editing. LS: Investigation, Methodology, Writing – original draft. GD: Formal analysis, Writing – review & editing. MQ: Conceptualization, Methodology, Supervision, Writing – review & editing. SC: Supervision, Validation, Writing – review & editing. MDM: Conceptualization, Methodology, Writing – review & editing. TC: Conceptualization, Methodology, Writing – original draft.

Funding

The author(s) declare that no financial support was received for the research and/or authorship.

Acknowledgments

The authors acknowledge the University of Messina for supporting the publication of this paper through the APC initiative.

Conflict of interest

The authors declare that the research was conducted in the absence of any commercial or financial relationships that could be construed as a potential conflict of interest.

Publisher's note

References

1. England G, Bright L, Pritchard B, Bowen I, De Souza M, Silva L, et al. Canine reproductive ultrasound examination for predicting future sperm quality. *Reprod Domest Anim*. (2017) 52:202–7. doi: 10.1111/rda.12825

2. Rebik K, Wagner JM, Middleton W. Scrotal ultrasound. *Radiol Clin North Am*. (2019) 57:635–48. doi: 10.1016/j.rcl.2019.01.007

3. Mantziaras G, Luvoni GC. Advanced ultrasound techniques in small animal reproduction imaging. *Reprod Dom Anim*. (2020) 55:17–25. doi: 10.1111/rda.13587

4. Bamber J, Cosgrove D, Dietrich C, Fromageau J, Bojunga J, Calliada F, et al. EFSUMB guidelines and recommendations on the clinical use of ultrasound Elastography. Part 1: basic principles and technology. *Ultraschall Med*. (2013) 34:169–84. doi: 10.1055/s-0033-1335205

5. Shiina T, Nightingale KR, Palmeri ML, Hall TJ, Bamber JC, Barr RG, et al. WFUMB guidelines and recommendations for clinical use of ultrasound Elastography: part 1: basic principles and terminology. *Ultrasound Med Biol*. (2015) 41:1126–47. doi: 10.1016/j.ultrasmedbio.2015.03.009

6. Ferraioli G, Barr RG, Farrokh A, Radzina M, Cui XW, Dong Y, et al. How to perform shear wave elastography Part I. *Med Ultrason*. (2022) 24:95–106. doi: 10.11152/mu-3217

7. Ferraioli G, Barr RG, Farrokh A, Radzina M, Cui XW, Dong Y, et al. How to perform shear wave elastography Part II. *Med Ultrason*. (2022) 24:196–210. doi: 10.11152/mu-3342

8. Choi HY, Sohn Y-M, Seo M. Comparison of 3D and 2D shear-wave elastography for differentiating benign and malignant breast masses: focus on the diagnostic performance. *Clin Radiol*. (2017) 72:878–86. doi: 10.1016/j.crad.2017.04.009

9. Tian J, Liu Q, Wang X, Xing P, Yang Z, Wu C. Application of 3D and 2D quantitative shear wave elastography (SWE) to differentiate between benign and malignant breast masses. *Sci Rep*. (2017) 7:41216. doi: 10.1038/srep41216

10. Trottmann M, Marcon J, D'Anastasi M, Bruce MF, Stief CG, Reiser MF, et al. Shear-wave elastography of the testis in the healthy man – determination of standard values. *Clin Hemorheol Microcirc*. (2016) 62:273–81. doi: 10.3233/CH-162046

11. Yüzkan S, Çilengir A. Shear wave elastography for assessment of testicular stiffness in patients with varicocele: a prospective comparative study. *J Med Ultrasound*. (2022) 30:277–81. doi: 10.4103/jmu.jmu_218_21

12. Cao W, Han H, Guan X, Lyu C, Zhou Q, Tian L, et al. Elastography and CONTRAST-ENHANCED ultrasound to assess the effect of varicocelectomy: a CASE-CONTROLLED study. *Andrologia*. (2022) 54:e14586. doi: 10.1111/and.14586

13. Alperen K, Ayca S, Unal T, Han GK, Sadik G. Testes parenchymal shear wave Elastography findings in varicocele. *J Coll Physicians Surg Pak*. (2022) 32:855–9. doi: 10.29271/jcpsp.2022.07.855

14. Mulati Y, Li X, Maimaitiming A, Apizi A, Wang Y. Is there any predictive value of testicular shear wave elastic modulus in testicular functions for varicocele patients? *Andrologia*. (2022) 54:e14393. doi: 10.1111/and.14393

15. Beşler MS, Gökhan MB, Ölçücüoğlu E, Özdemir FAE. Shear wave elastography for the evaluation of testicular salvage after testicular torsion. *Andrologia*. (2022) 54:e14565. doi: 10.1111/and.14565

16. Ladke P, Dhok A, Phatak S, Mitra K, Jakhotia Y. Diagnostic and imaging features of a non-seminomatous germ cell tumor of the testis: a case report and review of the literature. *Cureus*. (2022) 14:e32305. doi: 10.7759/cureus.32305

17. Bhansali PJ, Phatak SV, Mishra GV, Nagendra V. Elastographic imaging of anaplastic seminoma of testis with its ultrasound and Doppler correlation: a case report. *Cureus*. (2022) 14:e32813. doi: 10.7759/cureus.32813

18. Simon V, Dudea S, Crisan N, Stanca V, Dudea-Simon M, Andras I, et al. Elastography in the urological practice: urinary and male genital tract, prostate excluded—review. *Diagnostics*. (2022) 12:1727. doi: 10.3390/diagnostics12071727

19. Baleato-Gonzalez S, Osorio-Vazquez I, Flores-Ríos E, Santiago-Pérez MI, Laguna-Reyes JP, Garcia-Figueiras R. Testicular evaluation using shear wave Elastography (SWE) in patients with varicocele. *J Imaging*. (2023) 9:166. doi: 10.3390/jimaging9090166

20. Cantisani V, Di Leo N, Bertolotto M, Fresilli D, Granata A, Polti G, et al. Role of multiparametric ultrasound in testicular focal lesions and diffuse pathology evaluation, with particular regard to elastography: review of literature. *Andrology*. (2021) 9:1356–68. doi: 10.1111/andr.13067

21. Abdelwahab K, Eliwa AM, Seleem MM, El Galaly H, Ragab A, Desoky EA, et al. Role of preoperative testicular shear wave Elastography in predicting improvement of semen parameters after Varicocelectomy for male patients with primary infertility. *Urology*. (2017) 107:103–6. doi: 10.1016/j.urology.2017.04.026

22. Glińska-Suchocka K, Jankowski M, Kubiak K, Spużak J, Dzimira S. Sonoelastography in differentiation of benign and malignant testicular lesion in dogs. *Pol J Vet Sci*. (2014) 17:487–91. doi: 10.2478/pjvs-2014-0070

23. Feliciano MAR, Maronezi MC, Simões APR, Uscategui RR, Maciel GS, Carvalho CF, et al. Acoustic radiation force impulse elastography of prostate and testes of healthy dogs: preliminary results. *J Small Anim Pract*. (2015) 56:320–4. doi: 10.1111/jsap.12323

24. Feliciano MAR, Maronezi MC, Simões APR, Maciel GS, Pavan L, Gasser B, et al. Acoustic radiation force impulse (ARFI) elastography of testicular disorders in dogs: preliminary results. *Arq Bras Med Vet Zootec*. (2016) 68:283–91. doi: 10.1590/1678-4162-8284

25. Gloria A, Bracco C, Di Francesco L, Marruchella G, Contri A. Stiffness estimated by strain elastography reflects canine testicular spermatogenesis and histology. *Theriogenology*. (2023) 209:1–8. doi: 10.1016/j.theriogenology.2023.06.011

26. Eilts BE, Williams DB, Moser EB. Ultrasonic measurement of canine testes. *Theriogenology*. (1993) 40:819–28. doi: 10.1016/0093-691X(93)90217-S

27. Atalan G, Holt PE, Barr FJ. Ultrasonographic estimation of prostate size in normal dogs and relationship to bodyweight and age. *J Small Anim Pract*. (1999) 40:119–22. doi: 10.1111/j.1748-5827.1999.tb03052.x

28. England GCW. Relationship between ultrasonographic appearance, testicular size, spermatozoal output and testicular lesions in the dog. *J Small Anim Pract*. (1991) 32:306–11. doi: 10.1111/j.1748-5827.1991.tb00936.x

29. Kamolpatana K, Johnston GR, Johnston SD. Determination of canine prostatic volume using transabdominal ultrasonography. *Vet Radiol Ultrasound*. (2000) 41:73–7. doi: 10.1111/j.1740-8261.2000.tb00430.x

30. Ferraioli G, Maiocchi L, Filice C, Kendy C. C. (2020). Shear wave elastography for the assessment of diffuse liver disease: protocol and case studies. Available at:https://www.mindray.com/content/dam/xpace/en/resources/clinical-paper/Shear_Wave_Elastography.pdf (Accessed October 1, 2023).

31. Tesi M, Sabatini C, Vannozzi I, Di Petta G, Panzani D, Camillo F, et al. Variables affecting semen quality and its relation to fertility in the dog: a retrospective study. *Theriogenology*. (2018) 118:34–9. doi: 10.1016/j.theriogenology.2018.05.018

32. The Jamovi project. (2024). jamovi (Version 2.5) [Computer Software]. Available at: https://www.jamovi.org

33. Săftoiu A, Gilja OH, Sidhu PS, Dietrich CF, Cantisani V, Amy D, et al. The EFSUMB guidelines and recommendations for the clinical practice of Elastography in non-hepatic applications: update 2018. *Ultraschall in Med*. (2019) 40:425–53. doi: 10.1055/a-0838-9937

34. Zaleska-Dorobisz U, Kaczorowski K, Pawluś A, Puchalska A, Inglot M. Ultrasound Elastography – review of techniques and its clinical applications. *Adv Clin Exp Med*. (2014) 23:645–55. doi: 10.17219/acem/26301

35. Ercolin ACM, Uchôa AS, Aires LPN, Gomes DR, Tinto ST, Feliciano GSM, et al. Use of new ultrasonography methods for detecting neoplasms in dogs and cats: a review. *Animals*. (2024) 14:312. doi: 10.3390/ani14020312

36. Şeran MO, Uçmak ZG, Tek Ç. Strain elastography is a useful tool in the evaluation of canine mammary neoplasms. *Vet Arhiv*. (2024) 94:55–66. doi: 10.24099/vet.arhiv.2115

37. Jeon S, Lee G, Lee S, Kim H, Yu D, Choi J. Ultrasonographic elastography of the liver, spleen, kidneys, and prostate in clinically normal beagle dogs. *Vet Radiol Ultrasound*. (2015) 56:425–31. doi: 10.1111/vru.12238

38. Mantziaras G, Luvoni GC. Ultrasound elastography of the normal canine prostate and testicles. *Proceedings of the 8th Quadrennial International Symposium on Canine and Feline Reproduction which is a Joint Meeting with the 19th EVSSAR Congress, 22-25 June*. Paris, (2016).

39. Tyloch DJ, Tyloch JF, Adamowicz J, Neska-Długosz I, Grzanka D, Van Breda S, et al. Comparison of strain and shear wave Elastography in prostate Cancer detection. *Ultrasound Med Biol*. (2023) 49:889–900. doi: 10.1016/j.ultrasmedbio.2022.11.015

40. Ogino Y, Wakui N, Nagai H, Matsuda T. Comparison of strain elastography and shear wave elastography in diagnosis of fibrosis in nonalcoholic fatty liver disease. *J Med Ultrasonics*. (2023) 50:187–95. doi: 10.1007/s10396-023-01293-z

41. Chang JM, Won J-K, Lee K-B, Park IA, Yi A, Moon WK. Comparison of shear-wave and strain ultrasound Elastography in the differentiation of benign and malignant breast lesions. *Am J Roentgenol*. (2013) 201:W347–56. doi: 10.2214/AJR.12.10416

42. Marcon J, Trottmann M, Rübenthaler J, Stief CG, Reiser MF, Clevert DA. Shear wave elastography of the testes in a healthy study collective – differences in standard values between ARFI and VTIQ techniques. *Clin Hemorheol Microcirc*. (2017) 64:721–8. doi: 10.3233/CH-168052

43. Jequier AM. *Male infertility: A clinical guide*. *2nd* ed. Cambridge, United Kingdom: Cambridge University Press (2011).

44. Dohle GR, Elzanaty S, Van Casteren NJ. Testicular biopsy: clinical practice and interpretation. *Asian J Androl*. (2012) 14:88–93. doi: 10.1038/aja.2011.57

45. Paltiel HJ, Diamond DA, Di Canzio J, Zurakowski D, Borer JG, Atala A. Testicular volume: comparison of Orchidometer and US measurements in dogs. *Radiology*. (2002) 222:114–9. doi: 10.1148/radiol.2221001385

46. Gouletsou PG, Galatos AD, Leontides LS. Comparison between ultrasonographic and caliper measurements of testicular volume in the dog. *Anim Reprod Sci*. (2008) 108:1–12. doi: 10.1016/j.anireprosci.2007.06.020

47. Bracco C, Gloria A, Contri A. Ultrasound-based Technologies for the Evaluation of testicles in the dog: keystones and breakthroughs. *Vet Sci*. (2023) 10:683. doi: 10.3390/vetsci10120683

48. D'Anastasi M, Schneevoigt BS, Trottmann M, Crispin A, Stief C, Reiser MF, et al. Acoustic radiation force impulse imaging of the testes: a preliminary experience. *Clin Hemorheol Microcirc*. (2011) 49:105–14. doi: 10.3233/CH-2011-1461

49. Erdoğan H, Durmaz MS, Özbakır B, Cebeci H, Özkan D, Gökmen İE. Experience of using shear wave elastography in evaluation of testicular stiffness in cases of male infertility. *J Ultrasound*. (2020) 23:529–34. doi: 10.1007/s40477-020-00430-5

50. Holdsworth A, Bradley K, Birch S, Browne WJ, Barberet V. Elastography of the normal canine liver, spleen and kidneys: canine elastography. *Vet Radiol Ultrasound*. (2014) 55:620–7. doi: 10.1111/vru.12169

frontiers | Frontiers in Veterinary Science

TYPE Original Research
PUBLISHED 13 May 2024
DOI 10.3389/fvets.2024.1399392

OPEN ACCESS

EDITED BY
Sokol Duro,
Agricultural University of Tirana, Albania

REVIEWED BY
Mohamed A. M. Alsafy,
Alexandria University, Egypt
Juan Alberto Corbera,
University of Las Palmas de Gran Canaria, Spain

*CORRESPONDENCE
László Zoltán Reinitz
✉ reinitz.laszlo.zoltan@univet.hu

RECEIVED 19 March 2024
ACCEPTED 23 April 2024
PUBLISHED 13 May 2024

CITATION
Reinitz LZ, Lenzing F, Papp E, Biácsi A, Fajtai D and Petneházy Ö (2024) CT reconstruction based 3D model of the digital cushion's blood supply in the hind foot of an African savanna elephant (*Loxodonta africana*).
Front. Vet. Sci. 11:1399392.
doi: 10.3389/fvets.2024.1399392

CT reconstruction based 3D model of the digital cushion's blood supply in the hind foot of an African savanna elephant (*Loxodonta africana*)

László Zoltán Reinitz[1]*, Franka Lenzing[1], Endre Papp[2], Alexandra Biácsi[2], Dániel Fajtai[3,4] and Örs Petneházy[3,4]

[1]Department of Anatomy and Histology, University of Veterinary Medicine Budapest, Budapest, Hungary, [2]Nyíregyházi Állatpark Nonprofit Kft. (Sosto Zoo), Nyíregyháza, Hungary, [3]Medicopus Nonprofit Ltd., Kaposvár, Hungary, [4]Institute of Animal Physiology and Nutrition, Department of Physiology and Animal Health, Hungarian University of Agriculture and Life Sciences, Kaposvár, Hungary

Introduction: Foot health is crucial for elephants, as pathological lesions of the feet are a leading cause of euthanasia in captive elephants, which are endangered species. Proper treatment of the feet, particularly in conditions affecting the digits and the digital cushion, requires a thorough understanding of the underlying anatomy. However, only limited literature exists due to the small population and the epidemiological foot diseases which often precludes many deceased elephants from scientific study. The aim of this study was to provide a detailed anatomical description of the blood supply to the African elephant's hindfoot.

Methods: The healthy right hindlimb of a 19-year-old deceased female African savanna elephant was examined using computed tomography. Following a native sequence, 48 mL of barium-based contrast agent was injected into the caudal and cranial tibial arteries, and a subsequent scan was performed. The images were processed with 3D Slicer software.

Results: The medial and lateral plantar arteries run in a symmetrical pattern. They each have a dorsal and a plantar branch, which reach the plantar skin before turning toward the axial plane of the sole to reach the digital cushion from the proximal direction. An accurate 3D model of the arteries and the bones of the foot, a set of labeled images and an animation of the blood supply have been created for ease of understanding.

Discussion: In contrast to domestic ungulates, the digital cushion of the hindlimb is supplied differently from that of the forelimb. The lack of large vessels in its deeper layers indicates a slow regeneration time. This novel anatomical information may be useful in the planning of surgical interventions and in emergency medical procedures.

KEYWORDS

African savanna elephant, CT reconstruction, hindfoot, blood supply, anatomy, 3D

1 Introduction

Elephants, belonging to the family *Elephantidae* and to the order *Proboscidea*, hold a symbolic place in the annals of human history, representing strength, grace, wisdom, and peace (1). The African savanna elephant (*Loxodonta africana*) is the largest terrestrial animal, with an average shoulder height:body weight ratio of 3.2 m:6000 kg for males and 2.6 m:3000 kg for females (2), and has been classified as endangered on the Red List of the International Union for Conservation of Nature since 2001 (3).

Wild elephants only lie down to sleep for about an hour every 3 to 4 days; otherwise they only sleep in a standing position for 1 to 2 h per day (4). While captive individuals may have slightly different sleeping habits, the legs and feet are critically important to their health. The limbs of the elephant are columnar, and, as in most quadruped animals, the forelimbs carry a greater weight (5–7). The limbs remain columnar during slow-paced movement, with a limited flexion appearing at higher speeds (8). The primary function of the hindlimb is to initiate movement and transmit thrust to the trunk, as in all quadrupeds. However, the elephant hindlimb shares many similarities with the human hindlimb in morphology (e.g., elongated femur) and movement pattern (no significant rotation or abduction/adduction in the stifle) (7, 8). This stiffness of movement, the poor limb configuration (9, 10) an walking on hard surfaces, often in cold, damp conditions with limited space (6, 10, 11) result in widespread occurrence of foot diseases in captive elephants.

Approximately 50% of captive elephants experience foot-related diseases at some point in their lives (12). In a recent paper, only 26% of the United Kingdom's captive elephant population showed normal locomotion (9). Another study found that only 1.2% of the elephants examined had no visible lesions on their nails and pads (13). Among the varieties of diseases, chronic unresponsive foot infections stand out as a leading cause for euthanasia in captive elephants (14). While certain external lesions such as nail cracks, foreign bodies, and visible infections can be identified without the need for diagnostic imaging (15), these superficial lesions can also lead to more severe diseases, particularly those affecting the underlying bones, such as osteomyelitis, ascending soft tissue infections, and infectious arthritis. These conditions are challenging to diagnose and treat, as the elephants spend most of their time standing; this outlook could however be improved with a better understanding of the underlying anatomical structures (8, 16).

The anatomy of the feet in the different elephant species is remarkably similar despite the significant differences in their habitat (17). Their hindfoot is generally smaller than the forefoot as it bears less weight, with the forelegs bearing up to 60%, and the hindlegs bearing about 40%. Its shape is ovoid in character due to a lateral (17) or mediolateral (18) compression, which is pronounced in African savanna elephants. The African savanna elephant has no phalangeal bones distal to the first metatarsal bone, and the digit is only evidenced by a single, axial sesamoid bone. Smuts and Bezuidenhout (19) excluded this structure from the digits and view the African elephant as having only four digits, whilst Ramsay and Henry (17) accepted and counted this rudiment as the first digit. Digits three and four are the largest and therefore carry the greatest weight.

A significant digital cushion is located behind the slanted digits, under the tarsus. It is composed of fibrous connective tissue containing collagen, reticulin, and elastic fibers. Through the ability to compress and expand during locomotion, the digital cushion can be counted as a dynamic feature which makes the movements of the feet more active than previously assumed (18). The compression and relaxation mechanism work like a pump as the digital cushion facilitates the return of venous blood toward the central venous system against gravity (14), which is a critical function given the size and the constant movement of the elephant. While digital cushions are also described in many other mammalian species, such as horses (20, 21), their significance in locomotion is extraordinary in elephants due to the absence of the weight-bearing suspensory apparatus of the distal phalanx, which is the chief weight-bearing structure in horses (22).

The available literature for the vasculature of the elephant's hindlimb is scarce. Ramsay and Henry (17), much like Smuts and Bezuidenhout (19), focus on the locomotive system. Ramsay and Henry found that the cranial tibial artery (*arteria (a.) tibialis cranialis*), which provides the dorsal blood supply of the pes in equines and ruminants (21, 23), became small at the level of the tarsus (11). The same paper reported that the caudal tibial artery provided the majority of the plantar blood supply (17); it divided into a medial and a lateral branch at the calcaneus, with the medial branch running through the *canalis tarsi*. Both the medial and the lateral branches were shown to extend into the digital cushion on their respective sides (17, 24), but the paper does not give any further description about the exact location or further branching of these arteries. There are no diagrams or photos available about the foot's blood supply to improve understanding.

Petneházy et al. described the blood supply of the digital cushion in the forelimb of an Asian elephant using computed tomography (CT)-based reconstruction (25). They found that the metacarpal artery gave rise to a short trunk, which divided into a palmar and a dorsal branch, both of which supply the digital cushion from their respective directions; the short trunk also gave off a branch running toward the first digit. Given the similarities in the foot anatomy between the two species, a similar arrangement of vessels can be hypothesized to exist in the forelimb of the African savanna elephant as well.

To date, externally visible landmarks have been used in surgical procedures (26) to guide incisions. This approach leads to complications in procedures such as phalangeal removal (27), because the course and size of the vessels are unpredictable. In addition, diseases such as osteomyelitis and osteitis are currently treated with antibiotics injected locally into the vessels without knowing their exact course. Such treatment is done by looking for superficial veins with ultrasound (28). A detailed understanding of the systemic circulation and blood supply is of great necessity to form the basis of surgical treatments of the limbs, while avoiding vascular complications, and to effectively deliver drugs locally via specific vessels that supply a targeted tissue area. The aim of this study is to improve the current state of knowledge by providing a detailed description of the blood supply of the digital cushion and the digits in the African elephant, supported by images and 3D animation.

2 Materials and methods

The right hindfoot of a deceased African savanna elephant at the Sosto Zoo (Nyíregyházi Állatpark Nonprofit Kft. (Sosto Zoo), HRSz15010/2, Sóstói út, H-4431 Nyíregyháza, Hungary) was used for

the study. The 19-year-old female specimen was parent-reared in a peer group and kept on 1 hectare of landscaped forest soil with mounds and ditches. In addition, there was an indoor facility with 400 square meters of floor area covered with synthetic resin. Use of the outdoor area was limited to 6 h per day during winter conditions. The female died of Clostridium enterotoxemia, but her foot was clinically assessed as healthy. The leg was cut at the tibiotarsal joint (*articulatio (art.) tibiotarsale*) with a bone saw and was frozen at −4°C. The leg was then placed in a room temperature environment for 48 h and the cranial and the caudal tibial arteries were cannulated (16G intravenous catheter, B. Braun AG., Melsungen, Germany) before the examination was performed.

Three CT series were produced at the Kaposi Somogy County Teaching Hospital Dr. József Baka Diagnostic, Radiation Oncology, Research and Teaching Center (Kaposvár, Hungary) with a SIEMENS SOMATOM Sensation Cardiac CT (Multislice scanner, Siemens AG, Erlangen, Germany). A native series was taken, resulting in 2144 slices (Exposure Time: 16.04 s; Scanning Length: 493 mm; Exposed Range: 464 mm; Nominal Single Collimation Width: 0.6 mm; Nominal Total Collimation Width: 38.4 mm; Pitch Factor: 0.8 ratio; Number of X-Ray Sources: 1; KVP: 120 kV; Maximum X-Ray Tube Current: 240 mA; X-Ray Tube Current: 239 mA; Exposure Time per Rotation: 1 s).

Following the native series, a total of 20 milliliters (ml) of barium sulfate-containing Micropaque contrast agent (Micropaque/ Microtrast, Guerbet Inc., Villepinte, France) was administered over 3 min into the cannulated vessels, and a second series of CT scans was performed with similar settings as in the previous scan (Figure 1), directly after injecting the contrast agent. This was followed by an additional 3 min' long injection of 28 mL contrast agent and a subsequent immediate third scan. Injection of further contrast agent became difficult at this point, and the process was ceased. The obtained material was saved in a DICOM format.

The sequences were evaluated by two veterinary surgeons with experience in elephant care and were found to be free of pathological lesions. The toenails possessed good shape and constitution which corresponded with the assessment that this elephant did not have foot-related disease. The skeletal maturation of the elephant was found to be complete, as the growth plates were completely closed. This observation was again in line with the documented age of the investigated animal, as this is a process typically occurring at the age of 9 to 10 years (29, 30).

FIGURE 1
Contrast filled Computed Tomography image of the African savanna elephant's right hindfoot. Mid-sagittal plane.

The first series was selected to be used for the bone reconstruction process. The vessels in the 2nd series were not adequately filled, and the contrast agent did not reach the sole, but the vessels in the 3rd series were much more visible, so it was selected for reconstruction of the blood supply.

The chosen datasets were loaded into the open-source, free 3D Slicer software (31, 32). The current version at the time of use was version 5.2.2. The 3D Slicer is constantly being optimized with the help of the National Institutes of Health. The program for computerized image analysis is characterized by being freely available and not tied to specific hardware, which makes it easily accessible and user-friendly. It is intended for both medical and veterinary clinical research purposes in the realm of image processing, medical image informatics, and visualization using 3D models (31, 32).

The "Paint" effect in the "Segment editor" module of the software was used to segment the bones. The voxels of each bone were manually stained one by one in the selected color to get clear borders and to visualize the different bone groups as thoroughly and realistically as possible (Figure 2). The software lacks a standard setting for each bone of the region and there is no generally accepted color code. Therefore, we selected colors from the available options that were readily distinguished from each other. Every bone group and every individual bone was colored in one slice. After finishing the coloration, the segments were converted to models through the "Segment editor / Models" effect to create a multicolored 3D reconstruction of the elephant's foot.

The "Threshold" effect as an automatic segmentation, which can be found in the "Segment editor" module, was used for the vessel's reconstruction. The "Threshold" effect identifies the density of the different tissues shown in the CT images. Through the "Threshold range," the densities which will be colored can be determined (31, 32). For the vessels, the "Threshold range" was 2,800–3,070. This marked the basic structures of the main vessels without marking the other tissues. Afterwards an anatomist traced and verified every vessel and their smaller branches slice by slice and manually revised the segmentation using the "Segment editor / Paint" effect.

Once these models were saved, the "Threshold" effect was set to a wide range (99–3,071) on the same CT sequence, and every tissue was segmented into one block. This model was used to reconstruct the external view, the skin, and its features.

All models were merged to get the comprehensive connection between bones and arteries and to identify the arteries and branches in the following step. The vessels, individual bones, and skin features may be turned on and off or their opacity may be changed in order to get a better perspective (Figure 3).

3 Results

The finalized model enabled us to view a composite representation of all reconstructed tissues and examine the connection between

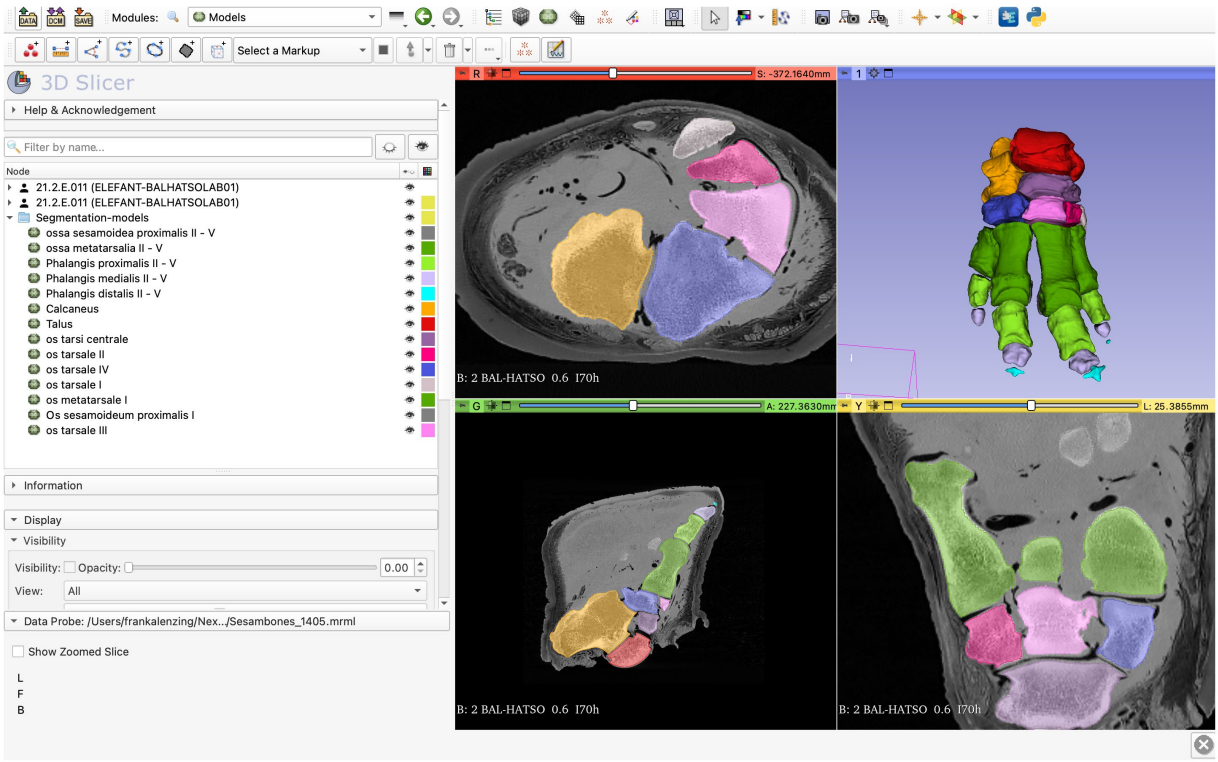

FIGURE 2
Screenshot of the 3D Slicer; completed process of transforming segments to models through the "Segment editor / Models" effect.

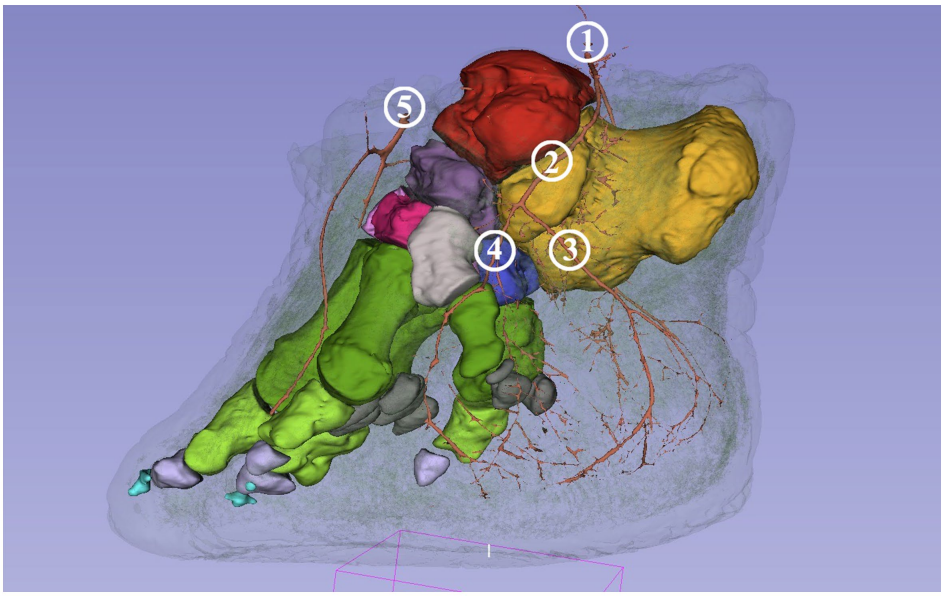

FIGURE 3
Screenshot of the 3D Slicer; composed 3D model of the African savanna elephant's right hindfoot with bones and the arteries. The opacity of the neighboring soft tissue is reduced to 10%. Medial view. Red: talus, yellow: calcaneus, dark purple: os tali centrale, light gray: os tarsale I., violet: os tarsale II, light pink: os tarsale III, blue: os tarsale IV, dark green: ossa metatarsalia I-V, light green: phalanx proximalis I-V, light purple: phalanx media I-V, cyan:: phalanx distale I-V, dark gray: ossa sesamoidea proximalia, **1**: a. tibialis caudalis; **2**: a. plantaris medialis; **3**: a. plantaris medialis r. plantaris; **4**: a. plantaris medialis r. dorsalis; **5**: a. dorsalis pedis.

bones, arteries, and skin. Identified vessels not previously described in the elephant are named according to the homologous vessels in the Illustrated Veterinary Anatomical Nomenclature (21).

The oval-shaped sole formed by mediolateral compression was seen, and the three toenails could be identified. The lack of pathological lesions in the foot indicates appropriate housing conditions and husbandry techniques. The reconstruction of the bones revealed comparatively small nutritional openings clustered on the *calcaneus* (especially on the *sustentaculum tali*), *talus,* and on the dorsal surface of the metatarsal bones. The plantar surface of the metatarsal bones remained smooth. The *prehallux* was visible in the CT images, but it was not stained together with the bones.

The detailed study of the 3D bone models confirmed that the *calcaneus* and the *talus* of African elephants form a *sinus tarsi.* The first digit had no phalanges, and the first metatarsus was the most distal bone, which was supported by a single proximal sesamoid bone at its distal epiphysis. The fifth digit lacked the distal phalange. All other digits had all three phalanges present with a pair of proximal sesamoid bones for each.

On the dorsal aspect of the foot, we saw a descending *a. dorsalis pedis* which divided into two well-visible arteries. The *a. digitalis dorsalis communis II* ran in a mediodistal direction over the third tarsal bone and then between the second and the third metatarsal bones. It gave off *a. digitalis dorsalis propria III abaxialis*, which was only traceable to the first phalanx (Figure 4).

The *a. digitalis dorsalis communis III* ran distally over the dorsal aspect of the third tarsal bone and could be traced to the height of the basis of metatarsal bones three and four. From both common digital dorsal arteries, a branch (*a. tarsea lateralis et medialis*) was visible coursing in the abaxial direction of the respective side over the proximal row of the tarsus.

On the plantar aspect proximal to the *calcaneus,* the caudal branch of the caudal tibial artery divided into a medial (*a. plantaris medialis*) and a lateral branch (*a. plantaris lateralis*) which ran in a mediodistal and laterodistal direction, respectively.

The medial plantar artery gave rise to small branches running toward the nutritional holes on the caudomedial aspect of the *calcaneus.*

Both the lateral and the medial plantar arteries divided into a dorsal and a plantar branch (*ramus (r.) dorsalis et r. plantaris*). The *a. plantaris medialis* divided at the level of the central tarsal bone while the *a. plantaris lateralis* divided slightly more distally at the level of the fourth tarsal bone. The dorsal branch of the medial plantar artery vascularized the middle and distal row of the tarsus and ran on the medial aspect of the first metatarsal bone before giving off a medial branch to the dorsomedial side of the digital cushion. The remaining portion ran around the distal phalange of the first digit (*a. digitalis dorsalis propria I abaxialis*), descended until the sole, and finally turned in the plantar direction to supply the digital cushion. The plantar branch of both plantar arteries divided into a similarly strong lateral and medial

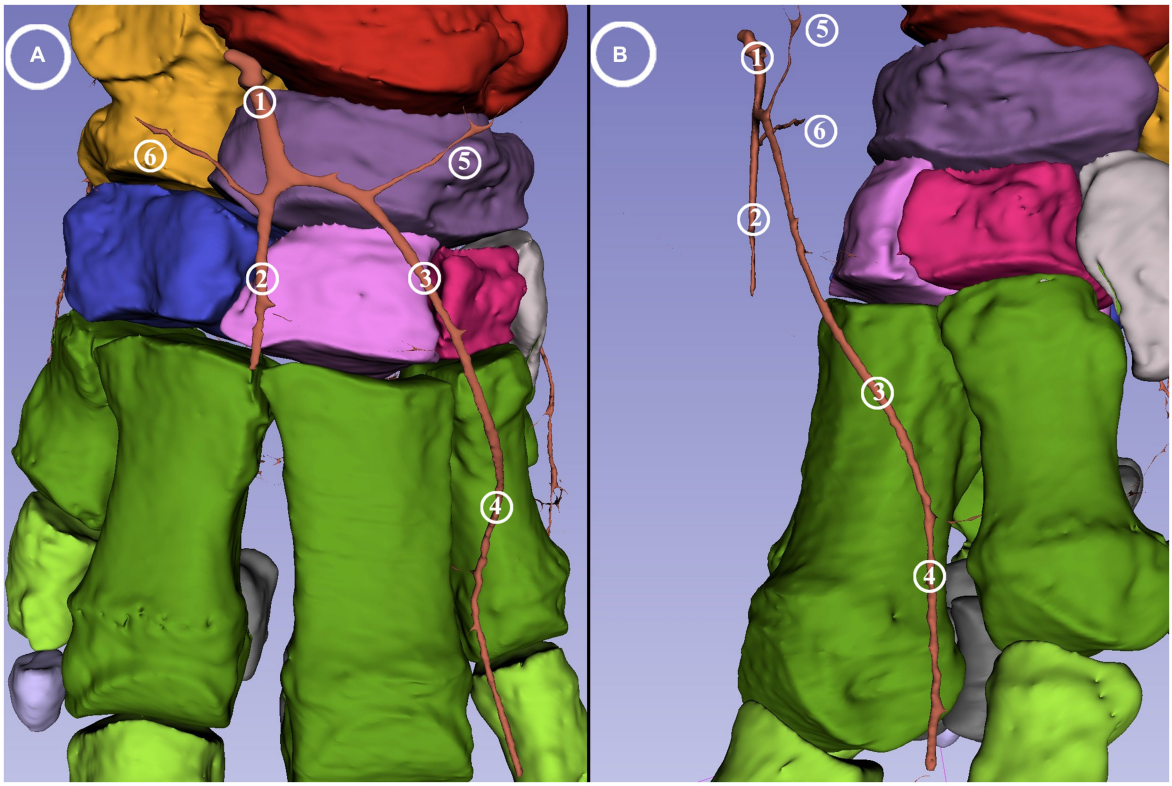

FIGURE 4
Dorsal blood supply of the African savanna elephant's right hindfoot. Screenshot of the 3D Slicer. **(A)** Dorsal view. **(B)** Mediodorsal view. Red: talus, yellow: calcaneus, dark purple: os tali centrale, light gray: os tarsale I., violet: os tarsale II, light pink: os tarsale III, blue: os tarsale IV, dark green: ossa metatarsalia I-V, light green: phalanx proximalis I-V, light purple: phalanx media I-V, cyan:: phalanx distale I-V, dark gray: ossa sesamoidea proximalia, **1**: a. dorsalis pedis; **2**: a. digitalis dorsalis communis III; **3**: a. digitalis dorsalis communis II; **4**: a. digitalis dorsalis propria III abaxialis; **5**: a. tarsea medialis; **6**: a. tarsea lateralis.

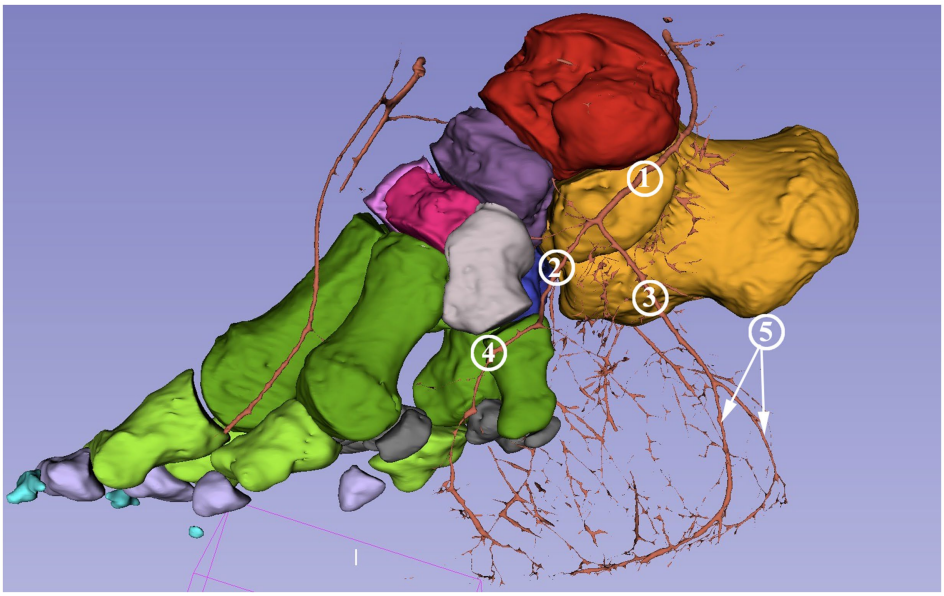

FIGURE 5
Blood supply of the digital cushion of the African savanna elephant's right hindfoot. Screenshot of the 3D Slicer. Medial view. Red: talus, yellow: calcaneus, dark purple: os tali centrale, light gray: os tarsale I., violet: os tarsale II, light pink: os tarsale III, blue: os tarsale IV, dark green: ossa metatarsalia I-V, light green: phalanx proximalis I-V, light purple: phalanx media I-V, cyan:: phalanx distale I-V, dark gray: ossa sesamoidea proximalia, **1**: a. plantaris medialis; **2**: a. plantaris medialis r. dorsalis; **3**: a. plantaris medialis r. plantaris; **4**: a. digitalis dorsalis propria I abaxialis; **5**: rr. tori digitalis.

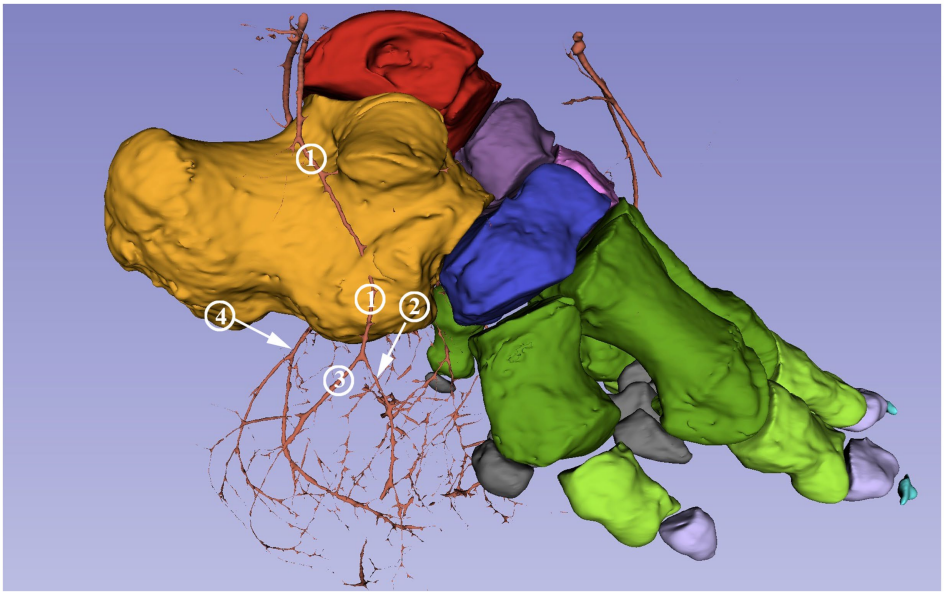

FIGURE 6
Blood supply of the digital cushion of the African savanna elephant's right hindfoot. Screenshot of the 3D Slicer. Lateral view. Red: talus, yellow: calcaneus, dark purple: os tali centrale, light gray: os tarsale I., violet: os tarsale II, light pink: os tarsale III, blue: os tarsale IV, dark green: ossa metatarsalia I-V, light green: phalanx proximalis I-V, light purple: phalanx media I-V, cyan:: phalanx distale I-V, dark gray: ossa sesamoidea proximalia, **1**: a. plantaris lateralis; **2**: a. plantaris lateralis r. dorsalis; **3**: a. plantaris lateralis r. plantaris; **4**: a. plantaris medialis r. plantaris.

branches (*rr. tori digitalis*) at level of the middle of the first phalanges. These supplied the digital cushion and the caudal portion of the sole from the medioplantar and lateroplantar directions, respectively (Figure 5); they bent toward the plantar direction, with the arch almost reaching the plantar skin and the terminal portion located 0.5 cm from the sole skin.

The dorsal branch of the lateral plantar artery did not have any direct branch for the digits. Its main portion supplied the dorsolateral side of the digital cushion (Figure 6). It had a branch running horizontally in the medial direction behind the proximal epiphysis of the fifth metatarsal bone. This built an arch toward the medial plantar artery under the calcaneus, but the reconstruction is incomplete at this

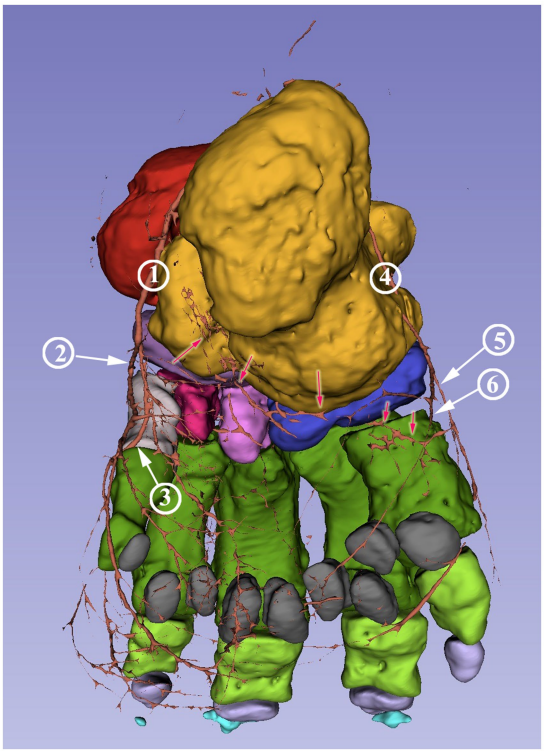

FIGURE 7
Blood supply of the African savanna elephant's right hindfoot. Screenshot of the 3D Slicer. Plantar view. Red: talus, yellow: calcaneus, dark purple: os tali centrale, light gray: os tarsale I., violet: os tarsale II, light pink: os tarsale III, blue: os tarsale IV, dark green: ossa metatarsalia I-V, light green: phalanx proximalis I-V, light purple: phalanx media I-V, cyan:: phalanx distale I-V, dark gray: ossa sesamoidea proximalia, **1**: a. plantaris medialis; **2**: a. plantaris medialis r. plantaris; **3**: a. plantaris medialis r. dorsalis; **4**: a. plantaris lateralis; **5**: a. plantaris lateralis r. plantaris; **6**: a. plantaris lateralis r. dorsalis; the red arrows mark the visible portions of the arcus plantaris profundus.

section (Figure 7). The plantar branch of the lateral plantar artery mirrored the path of the plantar branch of the medial plantar artery; thus, it supplied the digital cushion from a lateroplantar direction.

4 Discussion

The aim of this study was to identify and visualize the blood supply of the African elephant's hindfoot and to present it in an approachable way. 3D models are highly beneficial for spatial representation as they are realistic and facilitate the imagination of complex structures.

The animal's death was unexpected due to its rapidly progressive disease. The necessary pathological necropsy and post-mortem administrative paperwork, as well as coordination between the three institutes, took significant time. As a result, the team had to freeze the limb in order to preserve it.

Gross dissection, cryosectioning, and standard & CT angiography are alternative methods to obtain morphological data on the blood supply. Gross dissection and cryosectioning require a fresh cadaver however (33). Dissection of the specimen following the CT examinations would not have provided additional information. It is unlikely that tracing the branches that the contrast agent did not fill would have been feasible.

Basic angiography on this specimen would provide much less information than a CT and would not permit reconstruction. CT angiography (or positive contrast imaging) in a living elephant could lead to better results as the perfusion of the tissue would better distribute the contrast agent. However, as there is no literature on contrast imaging in live elephants, this option is likely precluded by the current technical limitations. CT scanners are located indoors in conditions that are inaccessible for adult elephants. While some specially trained dogs can remain motionless for the duration of a CT scan (34, 35) this is not realistic for elephants, whose slightest movement could seriously damage the equipment. Therefore, full anesthesia would be required; however current patient tables of the CT scanners cannot move the animal.

Reconstructive anatomical methods offer a more detailed assessment and significantly improve visualization compared to traditional techniques (36). Due to the change in permeability of the vascular wall, iodine-based contrast agents (such as those used in angiography) would rapidly penetrate into adjacent tissues. Although this technique is frequently used in certain studies (37) to increase tissue contrast, it would limit the visibility of the vessels that this study aimed to examine. No such effects of barium sulfate have been reported, even with an extended time period between injection and CT scans. However, during this period, due to its high viscosity, contrast can leak into small and insignificant vessels, leading to a decreased signal-to-noise ratio (38).

There are options in 3D Slicer to automate the segmentation process (31, 32), but that requires the subject to be in the exact same position for the different scans. During the injection of the contrast agent, the position of the limb was slightly altered, resulting in this method being inapplicable for our study. Therefore, we elected to proceed with manual segmentation.

This study is subject to certain limitations, mainly the utilization of only one specimen for the research. Anatomical studies of rare, endangered species often use only one (25, 39–42) or two (43) subjects. In addition, the possibility to use imaging techniques such as CT and MRI are also limited by the size, weight, and transport issues of this species (16) and the cost of such examinations. Greater collaboration among zoos would be necessary to include multiple healthy limbs in an extensive anatomical study.

No evidence of a correlation between body size or gender and foot morphology has been found in elephants (17, 19) or domesticated species (21, 23). Thus, individual anatomical differences, which would not have a clinical impact, may appear in our model, but the major structures are typically identical within the healthy members of the same species (21, 23). The vessels approaching the digital cushion are smaller in diameter then those supplying the digits, although the pad itself is much bigger in volume. They are well visible close to the skin but become scarce deeper. This supports the histological findings of Weissengruber et al. (18) and indicates limited healing capabilities for deep lesions.

Grouped nutritional holes were found on the *calcaneus*, *talus*, and dorsal surface of the metatarsal bones. Previously, nutritive openings were only described on the dorsal surface of the first phalangeal bones (17). Our study is the first to report the *sinus tarsi* in an African elephant. Although previously unreported in this species, it is in line with the anatomy of domestic mammals (20, 21) and the Asian elephant (25).

The filling of the specimen with contrast agent was stopped when the counterpressure became significant and the contrast agent started to appear on the cut surface of the limb. This indicated that the approachable vessels were full, and forcing more contrast agent could damage the arteries or create artifacts during the CT scans (38). Despite this, the reconstruction showed that the filling of the vessels

was not complete. The plantar blood supply of the digits is not visible, either due to the collapse of the vessels during the process or blood clots already present at outset. Freezing could also have such an effect, but based on the authors' experience with such specimens, the thawing time was sufficient to prevent residual frozen bodies from blocking the flow of the contrast agent. The visible vessels still provide valuable, novel information on the blood supply of the foot.

On the dorsal aspect of the foot in horses, cattle, sheeps & dogs, the *a. dorsalis pedis* descends until the distal third of the metatarsal bones where the dorsal common digital arteries would branch off, which make the *a. tarsea medialis et lateralis* well distinguishable branches of the *a. dorsalis pedis* at the height of the *art. centrodistalis* (23). In our study, the second and the third dorsal common digital arteries separate from the main vessel proximal to the distal row of the tarsus, making the medial and lateral tarsal arteries their subbranches on the respective sides. No further dorsal digital arteries were found. This can be the result of insufficient filling of the vessels, but in such cases, traces or short stumps are usually present (44). Therefore, it is more likely that digits I and V are fully supplied from the plantar direction just like the abaxial sides of digits II and IV.

On the plantar side the blood supply of the digital cushion is visible. Both the medial and lateral plantar arteries approach the pad from both the dorsal and the plantar directions and create many anastomoses close to the sole between the medial and lateral sides and the plantar and dorsal approaches as well. Ramsey & Henry did not report the division on the proximal portion of both the medial and the lateral plantar arteries or the anastomoses near the sole, indicating that their dissection stopped at the level of the tarsus (17). This setup is very different from the one described in the forelimb of the Asian elephant (25), where a single trunk arising from the *arcus palmaris profundus* would serve as the major vessel, and its direct branches reach the digital cushion close to the median plane of the limb. Previous studies state that the anatomy of the hindfoot in the different elephant species are similar (17, 18). Based on this, the blood supply to the digital cushion in the forelimb and hindlimb of elephants appears to differ significantly. This is a novel finding, as species with existing descriptions of this region, such as horses, cattle, and sheep, have similar blood supply to the digital cushion in each hoof. In those species the r*r. tori digitales* of the medial and lateral sides arise from the plantar digital arteries of the corresponding side on both the forelimb and the hindlimb (21, 23). However, the aforementioned studies about African elephants, as well as Asian elephants, focus on the locomotive apparatus rather than the vessels (17, 18). It is possible that the blood supply differs significantly despite the commonalities in the muscles and joints.

The incomplete arch connecting the medial and lateral plantar arteries distal to the calcaneus is probably the deep plantar arch (*arcus plantaris profundus*), which serves as the origin for the plantar blood supply of the digits in domestic mammals. As the arch itself is already fragmented, its branches are not distinguishable. The *a. tarsea perforans*, which runs through the canalis tarsi, was described in African savanna elephants (17) but we were unable to locate any sign of the vessel despite the presence of the canal. This could be the result of the insufficient filling of the contrast agent or an individual difference as this artery is reported to be inconstant in some species (21). For the contrast agent to sufficiently reach every major branch, including the mostly horizontally-oriented perforating tarsal artery and the deep plantar arch, a fresh carcass is needed, the limb should be severed more proximally and the blood should be flushed out before the contrast agent is injected.

5 Conclusion

The study provides novel information about the blood supply of the digital cushion in an African elephant. The previously described medial and lateral plantar arteries on each side of the tarsus divide into dorsal and plantar branches to supply the digital cushion and the caudal portion of the sole. The plantar branches are more dominant and running directly under the skin. The distribution of the arteries and their location compared to the skeleton and the skin are accessible through high quality images and 3D models, which are the first such to be presented of the region. The size and distribution of the vessels explain the slow healing of the digital cushion.

This anatomical description of the region will help caretakers and veterinarians execute treatment in the best possible way, which is especially important considering the vital role the condition of the foot and the digital cushion have in the general health of elephants.

While the forefeet and the hindfeet look very similar and have many similarities in their skeleton and dynamics, the blood supply of their digits and digital cushion are very different.

The 3D printable model can be used to educate students, caregivers, and veterinarians to help keep captive elephants healthy in the future, protecting the endangered species.

Data availability statement

The datasets presented in this study can be found in online repositories. The names of the repository/repositories and accession number(s) can be found at: https://figshare.com/s/638488f9efbd1d75ede3.

Ethics statement

Ethical approval was not required for the study involving animals in accordance with the local legislation and institutional requirements because we used the limb of a deceased elephant. The animal died due to natural causes before the study began. As the study only focuses on a limb of an already deceased animal, no ethical approval is necessary.

Author contributions

LR: Conceptualization, Formal analysis, Funding acquisition, Investigation, Project administration, Software, Supervision, Writing – original draft, Writing – review & editing. FL: Formal analysis, Investigation, Software, Visualization, Writing – review & editing. EP: Investigation, Resources, Supervision, Validation, Writing – review & editing. AB: Resources, Supervision, Validation, Writing – review & editing. DF: Data curation, Resources, Visualization, Writing – review & editing. ÖP: Conceptualization, Investigation, Methodology, Resources, Software, Supervision, Visualization, Writing – review & editing.

Funding

The author(s) declare financial support was received for the research, authorship, and/or publication of this article. This study was co-funded by the University of Veterinary Medicine Budapest, the Medicopus Nonprofit Kft., and the Hungarian University of Agriculture and Life Sciences.

Acknowledgments

The authors would like to thank Mr. David Gamba, BSc and Dr. David James Hotchkiss, DVM, PhD for their expertise and assistance in our study, particularly in the English language review.

Conflict of interest

DF and ÖP were employed by Medicopus Nonprofit Ltd.

The remaining authors declare that the research was conducted in the absence of any commercial or financial relationships that could be construed as a potential conflict of interest.

Publisher's note

References

1. Larramendi A. Shoulder height, body mass, and shape of proboscideans. *Acta Palaeontol Pol*. (2016) 61:537–74. doi: 10.4202/app.00136.2014

2. Clemente CJ, Dick TJM. How scaling approaches can reveal fundamental principles in physiology and biomechanics. *J Exp Biol*. (2023) 226:jeb245310. doi: 10.1242/jeb.245310

3. Gobush KS, Edwards CTT, Balfour D, Wittemyer G, Maisels F, Taylor RD. *Loxodonta africana* (amended version of 2021 assessment). *IUCN Red List of Threatened Species 2022*. (2022). doi: 10.2305/IUCN.UK.2022-2.RLTS.T181008073A223031019.en

4. Gravett N, Bhagwandin A, Sutcliffe R, Landen K, Chase MJ, Lyamin OI, et al. Inactivity/sleep in two wild free-roaming African elephants matriarchs – does large body size make elephants the shortest mammalian sleepers? *PLos One*. (2017) 12:e0171903. doi: 10.1371/journal.pone.0171903

5. Houck R. Veterinary care of performing elephants In: ME Fowler, editor. *Zoo and wild animal medicine. Current therapy 3*. Philadelphia, PA: WB Saunders (1993). 453454.

6. Hutchinson JR, Schwerda D, Famini DJ, Dale RH, Fischer MS, Kram R. The locomotor kinematics of Asian and African elephants: changes with speed and size. *J Exp Biol*. (2006) 209:3812–27. doi: 10.1242/jeb.02443

7. Schwerda D. *Analyse Kinematischer parameter der Lokomotion Von Loxodonta Africana (Proboscidea: Elephantidae). [Master's thesis]*. Jena: Institut für spezielle Zoologie und Evolutionsbiologie mit Phyletischem Museum der Friedrich-Schiller-Universität (2003).

8. Weissengruber GE, Fuss FK, Egger G, Stanek G, Hittmair KM, Forstenpointner G. The elephant knee joint: morphological and biomechanical considerations. *J Anat*. (2006) 208:59–72. doi: 10.1111/j.1469-7580.2006.00508.x

9. Turner A, Masters N, Pfau T, Hutchinson JR, Weller R. Development and evaluation of a standardized system for the assessment of locomotor health in elephants under human care. *J Zoo Wildl Med*. (2023) 54:529–37. doi: 10.1638/2022-0110

10. Hittmair KM, Vielgrader HD. Radiographic diagnosis of lameness in African elephants (*Loxodonta africana*). *Vet Radiol Ultrasound*. (2000) 41:511–5. doi: 10.1111/j.1740-8261.2000.tb01879.x

11. Schmidt M, Elephants (Proboscidea). Disease description In: ME Fowler, editor. *Zoo and wild animal medicine. 2nd* ed. Philadelphia, PA: WB Saunders (1986). 901–16.

12. Mikota SK, Sargaent EL, Ranglack G. *Medical management of of the elephant*. West Bloomfield, MI: Indira Publishing House (1994). p. 65–67.

13. Wendler P, Ertl N, Flügger M, Sós E, Schiffmann C, Clauss M, et al. Foot health of Asian elephants (*Elephas maximus*) in European zoos. *J Zoo Wildl Med*. (2019) 50:513–27. doi: 10.1638/2018-0228

14. Murray E, Fowler ME. An overview of foot conditions in Asian and African elephants In: B Csuti, EL Sargent and US Bechert, editors. *The elephant's foot*. Ames, IA: Iowa State University Press (2001). 3–9.

15. Lewis KD, Shepherdson DJ, Owens TM. A survey of elephant husbandry and foot health in north American zoos. *Zoo Biol*. (2009) 29:221–36. doi: 10.1002/zoo.20291

16. Regnault S, Dixon J, Warren-Smith CMR, Hutchinson JR, Weller R. Skeletal pathology and variable anatomy in elephant feet assessed using computed tomography. *PeerJ*. (2017) 5:e2877. doi: 10.7717/peerj.2877

17. Ramsay EC, Henry RW. Anatomy of the elephant foot In: B Csuti, EL Sargent and US Bechert, editors. *The elephant's foot*. Ames, IA: Iowa State University Press (2001). 9–12.

18. Weissengruber GE, Egger GF, Hutchinson JR, Groenewald HB, Elsässer L, Famini D, et al. The structure of the cushions in African elephants (*Loxodonta africana*). *J Anat*. (2006) 209:781–92. doi: 10.1111/j.1469-7580.2006.00648.x

19. Smuts MMS, Bezuidenhout AJ. Osteology of the pelvic limb of the African elephant (*Loxodonta africana*). *Onderstepoort J Vet Res*. (1994) 61:51–66.

20. Nickel R, Schummer A, Seiferle E. *Lehrbuch der Anatomie der Haustiere. Band I: Bewegungsapparat*. Stuttgart, Germany: F. Enke. (2005) p. 112–127.

21. Constantinescu G, Habel R, Hillebrand A, Sack W, Schaller O, Simoens P, et al. *Illustrated veterinary anatomical nomenclature. 3rd edition*. Stuttgart, GFermany: F. Enke (2012). p. 332–333.

22. Pollitt CC, Collins SN. The suspensory apparatus of the distal phalanx in normal horses. *Equine Vet J*. (2016) 48:496–501. doi: 10.1111/evj.12459

23. Nickel R, Schummer A, Seiferle E. *Lehrbuch der Anatomie der Haustiere. Band III: Kreislaufsystem, Haut und Hautorgane*. Stuttgart, Germany: F. Enke. (2005). p. 154–156.

24. Mariappa D. *Anatomy and histology of the Indian elephant*. Oak Park, IL: Indira Publishing House (1986).

25. Petneházy Ö, Rück S, Sós E, Reinitz LZ. 3D reconstruction of the blood supply of an Elephant's forefoot using fused CT and MRI sequences. *Animals*. (2023) 13:1789. doi: 10.3390/ani13111789

26. Guanghao L, Liming C, Youfeng X, Peng W. Treatment of hoof disease in an Asian elephant (*Elephas maximus*) using creative surgery: a successful case report. *Iran J Vet Surg*. (2020) 15:168–72. doi: 10.30500/ivsa.2020.224068.1211

27. Gage LJ, Fowler ME, Pascoe JR, Blasko D. Surgical removal of infected phalanges from an Asian elephant (*Elephas maximus*). *J Zoo Wildl Med*. (1997) 28:208–11.

28. Dutton CJ, Delnatte PG, Hollamby SR, Crawshaw GJ. Successful treatment of digital osteitis by intravenous regional perfusion of ceftiofur in an African elephant (*Loxodonta africana*). *J Zoo Wildl Med*. (2017) 48:554–8. doi: 10.1638/2015-0292R1.1

29. Siegal-Willott J, Isaza R, Johnson R, Blaik M. Distal limb radiography, ossification, and growth plate closure in the juvenile Asian elephant (*Elephas maximus*). *J Zoo Wildl Med*. (2008) 39:320–34. doi: 10.1638/2007-0031.1

30. Whitaker JM, Rousseau L, Williams T, Rowan RA, Hartwig CW. Scoring system for estimating age in the foot skeleton. *Am J Phys Anthropol*. (2002) 118:385–92. doi: 10.1002/ajpa.10109

31. Fedorov A, Beichel R, Kalpathy-Cramer J, Finet J, Fillion-Robin JC, Pujol S, et al. 3D slicer as an image computing platform for the quantitative imaging network. *J Magn Reson Imaging*. (2012) 30:1323–41. doi: 10.1016/j.mri.2012.05.001

32. Kapur T, Pieper S, Fedorov A, Fillion-Robin JC, Halle M, O'Donnell L. Increasing the impact of medical image computing using community-based open-access hackathons: the NA-MIC and 3D slicer experience. *Med Image Anal*. (2016) 33:176–80. doi: 10.1016/j.media.2016.06.035

33. Czeibert K, Baksa G, Grimm A, Nagy SA, Kubinyi E, Petneházy Ö. MRI CT and high resolution macro-anatomical images with cyrosectioning of a beagle brain: creating the base of a multimodal imaging atlas. *PLos One*. (2019) 14:e0213458. doi: 10.1371/journal.pone.0213458

34. Berns GS, Brooks AM, Spivak M. Functional MRI in awake unrestrained dogs. *PLoS One*. (2012) 7:e38027. doi: 10.1371/journal.pone.0038027

35. Andics A, Gacsi M, Farago T, Kis A, Miklosi A. Voice-sensitive regions in the dog and human brain are revealed by comparative fMRI. *Curr Biol*. (2014) 24:574–8. doi: 10.1016/j.cub.2014.01.058

36. Nitzsche B, Boltze J, Ludewig E, Flegel T, Schmidt MJ, Seeger J. A stereotaxic breed-averaged, symmetric T2w canine brain atlas including detailed morphological and volumetrical data sets. *Neuroimage*. (2019) 187:93–103. doi: 10.1016/j.neuroimage.2018.01.066

37. Callahan S, Crowe-Riddell JM, Nagesan RS, Gray JA, Rabosky ARD. A guide for optimal iodine staining and 400 high-throughput diceCT scanning in snakes. *Ecol Evol*. (2021) 11:11587–603. doi: 10.1002/ece3.7467

38. Chabior M, Donath T, David C, Bunk O, Schuster M, Schroer C, et al. Beam hardening effects in grating-based x-ray phase-contrast imaging. *Med Phys*. (2011) 38:1189–95. doi: 10.1118/1.3553408

39. Tefera M. Kinematics and comparative anatomy of some limb bones of the African elephant (*Loxodonta africana*) and large domestic animals. *J Vet Anat*. (2012) 5:15–31. doi: 10.21608/jva.2012.44872

40. Eales N. XXV.—the anatomy of a foetal African elephant, Elephas Africanus (*Loxodonta africana*). Part II. The body muscles. *Earth Environ Sci Trans Royal Soc Edinb*. (1928) 55:609–42. doi: 10.1017/S0080456800013338

41. Dunn RH, Beresheim A, Gubatina A, Bitterman K, Butaric L, Bejes K, et al. Muscular anatomy of the forelimb of tiger (*Panthera tigris*). *J Anat*. (2022) 241:119–44. doi: 10.1111/joa.13636

42. Reinitz LZ, Cerny C, Papp E, Biácsi A, Fajtai D, Petneházy Ö. CT based 3D reconstruction of the forefoot's blood supply in a white rhinoceros. *Acta Vet Scand*. (2024) 66:10. doi: 10.1186/s13028-024-00732-2

43. Hubbard C, Naples V, Ross E, Carlon B. Comparative analysis of paw pad structure in the clouded leopard (*Neofelis nebulosa*) and domestic cat (*Felis catus*). *Anat Rec*. (2009) 292:1213–28. doi: 10.1002/ar.20930

44. El-Gendy SAA, Kamal BM, Alsafy MAM. 3D render volume CT reconstruction of the bones and arteries of the hind digit of the dromedary camel (*Camelus dromedarius*). *BMC Zool*. (2022) 7:49. doi: 10.1186/s40850-022-00151-8

frontiers | Frontiers in Veterinary Science

TYPE Case Report
PUBLISHED 22 May 2024
DOI 10.3389/fvets.2024.1400139

OPEN ACCESS

EDITED BY
Sokol Duro,
Agricultural University of Tirana, Albania

REVIEWED BY
Sam Long,
Veterinary Referral Hospital, Australia
Murat Kabak,
Ondokuz Mayıs University, Türkiye

*CORRESPONDENCE
Junghee Yoon
✉ heeyoon@snu.ac.kr

†These authors have contributed equally to this work and share first authorship

RECEIVED 19 March 2024
ACCEPTED 09 May 2024
PUBLISHED 22 May 2024

CITATION
Kim J, Kim K, Chung DJ, Kim Y, Kim K, Oh D, Lee N, Choi J and Yoon J (2024) Case report: Magnetic resonance imaging features with postoperative improvement of atypical cervical glioma characterized by predominant extramedullary distribution in a dog. *Front. Vet. Sci.* 11:1400139. doi: 10.3389/fvets.2024.1400139

Case report: Magnetic resonance imaging features with postoperative improvement of atypical cervical glioma characterized by predominant extramedullary distribution in a dog

Junyoung Kim[1,2†], Kihoon Kim[3†], Dai Jung Chung[1], Yebeen Kim[1], Kitae Kim[4], Dayoung Oh[5], Namsoon Lee[6], Jihye Choi[2] and Junghee Yoon[2*]

[1]N Animal Medical Center, Seoul, Republic of Korea, [2]College of Veterinary Medicine and the Research Institute for Veterinary Science, Seoul National University, Seoul, Republic of Korea, [3]Jeil Referral Animal Medical Center, Busan, Republic of Korea, [4]Veterinary Health Center, University of Missouri, Colombia, MO, United States, [5]Department of Environmental and Radiological Health Sciences, College of Veterinary Medicine and Bio-medical Sciences, Colorado State University, Fort Collins, CO, United States, [6]College of Veterinary Medicine, Chungbuk National University, Cheongju, Republic of Korea

Introduction: Intramedullary cord tumors present diagnostic and therapeutic challenges. Furthermore, spinal cord tumors can move across compartments, making antemortem diagnosis difficult, even with advanced imaging. This report presents a rare case of a cranial cervical spinal glioma, confirmed by surgical histopathology, with postoperative improvement in a dog.

Case description: A 9-year-old female Maltese dog presented with kyphotic posture, progressive left hemiparesis, and decreased appetite. Neurological examination revealed neck pain and decreased proprioception in the left limbs along with intact deep pain perception. Two days later, the patient developed non-ambulatory tetraparesis. Magnetic resonance imaging (MRI) revealed an ovoid, well-defined mass with homogeneously marked contrast enhancement in the second cervical spinal cord that severely compressed the spinal cord. This mass was heterogeneously hyperintense on T2-weighted images and iso-to-hypointense on T1-weighted images, showing an appearance resembling the "golf-tee" and "dural tail" signs. The MRI findings suggested an intradural extramedullary tumor. Intraoperatively, a well-demarcated mass which was locally adherent to the spinal meninges was removed. Both histopathological and genomic tumor tests were indicative of a glioma. Approximately 2 weeks postoperatively, the patient's neurological signs returned to normal.

Conclusion: This case report describes an atypical cervical glioma with complicated MR characteristics in a dog, where MRI helped guide surgical intervention.

KEYWORDS

canine, histopathology, laminotomy, oligodendroglioma, spinal tumors

1 Introduction

Spinal neoplasia can result in clinical signs of spinal cord dysfunction (1). Spinal cord tumors are classified as intramedullary (accounting for ~15% of such tumors) (1–8), extradural (~50%) (1, 4, 5, 8), and intradural extramedullary tumors (35%). Intramedullary tumors include astrocytomas, oligodendrogliomas, and ependymomas (1, 5–7). Some neoplasms, including nephroblastomas and peripheral nerve sheath tumors, can occupy both intradural extramedullary and intramedullary locations (2, 5, 6).

Magnetic resonance imaging (MRI) has excellent contrast resolution and is essential for the diagnosis of spinal cord neoplasms (6, 9). Signal intensity, degree of contrast enhancement, and presence of fluid-filled compartments are used to differentiate spinal cord neoplasms (5). Moreover, the location of a spinal cord neoplasm with respect to the meninges helps predict the histological type (1, 5). However, intramedullary cord tumors present diagnostic and therapeutic challenges (9). Spinal cord tumors can move across compartments, making antemortem diagnosis difficult, even with advanced imaging (8). Although successful surgical removal has been described, intramedullary spinal cord tumors may not be generally amenable to surgery (1, 5, 8).

Treatment options for spinal tumors include surgical removal, radiotherapy, and chemotherapy (1). The prognosis depends on the tumor type, degree of spinal infiltration, spinal cord damage pre-and intraoperatively, degree of local resection, and surgeon's experience (1, 2, 5). Cytoreductive surgery, the primary treatment for patients with spinal cord neoplasia, may be used with or without radio-and chemotherapy (1, 5). It is commonly performed for extradural and intradural extramedullary neoplasms but rarely for intramedullary neoplasms (1, 2, 5). This reflects the technical expertise required to resect neoplasms within the spinal cord without iatrogenic injuries. Therefore, the preoperative distinction between intradural extramedullary and intramedullary neoplasms may be useful. Although MRI has excellent contrast resolution, its relatively low spatial resolution may negatively affect differentiation between intradural extramedullary and intramedullary neoplasms (5). A previous canine study reported a case of confirmed intramedullary cervical glioma exhibiting characteristics of intradural extramedullary lesions on MRI. In humans, MRI has a sensitivity of ~83% for the diagnosis of intradural extramedullary tumors, with 31 of 187 of these tumors misdiagnosed as intramedullary tumors (5). The present report describes a rare case of postoperative improvement in a cranial cervical glioma in a dog characterized by a predominant intradural extramedullary lesion distribution on MRI findings regarding the origin of the mass.

2 Case description

A 9-year-old intact female Maltese dog weighing 1.9 kg was presented with a kyphotic posture and decreased appetite for 3 days. Neurological examination revealed no abnormalities other than mild neck pain. A nonsteroidal anti-inflammatory drug was administered for pain control. However, 2 days later, the patient was returned to the hospital with deteriorating neurological symptoms and left hemiparesis. The dog was ambulatory with mild-to-moderate neck pain and decreased proprioceptive reactions in the left limbs, along with intact deep pain perception. Physical examination revealed a grade II heart murmur with no other abnormalities. Laboratory findings were mostly normal, except for mildly elevated levels of alkaline phosphatase (405 U/L; reference range, 47–254 U/L) and alanine aminotransferase (95 U/L; reference range, 17–78 U/L). Radiography revealed marked ventral spondylosis deformans with intervertebral disc space narrowing in the 6th–7th cervical vertebrae, with no other abnormalities. Echocardiography and abdominal ultrasonography showed myxomatous mitral valve disease stage B1 and small bilateral renal calculi. Based on clinical and neurological signs, the main differential diagnoses were cervical intervertebral disc disease, degenerative myelopathy, neoplasia or inflammatory diseases, and vascular disorders of the brain or cervical spine. Therefore, an MRI of the brain and cervical spinal cord was planned. Two days before the MRI examination, the patient's clinical signs progressively deteriorated, presenting as non-ambulatory tetraparesis with normal deep pain responses in all four limbs.

MR images of the brain and cervical spine were acquired using a 1.5-Tesla scanner (MAGNETOM AVANTO, Siemens, Germany) with head and neck knee coils, respectively. The MRI sequences of the brain and cervical spine used in the present case are shown in Table 1. On T2-weighted images, ill-defined, heterogeneously hyperintense areas in the spinal cord were identified eccentrically in the central-to-left dorsal aspect of the second cervical (C2) spinal cord, leading to focal spinal cord swelling showing a loss of normal parenchymal architecture and circumferential attenuation of the cerebrospinal fluid (CSF) line on T2-weighted half-Fourier acquisition single-shot turbo spin-echo sequence (Figures 1A,C,D). The lesion appeared iso-to-hypointense on T1-weighted images and iso-to-hyperintense on T2-weighted multi-echo data image combination sequence images (Figures 1B,E,F). Post-contrast T1-weighted images revealed an ovoid, well-defined mass with homogeneously marked contrast enhancement (size: 10.9 × 7.2 × 8.3 mm, length/height/width; Figures 1G–I). The mass contained multiple small cavitary lesions suggestive of cystic or necrotic areas, causing severe left-sided compression of the spinal cord (Figure 1G). In the dorsal subarachnoid space just caudal to the C2 mass, although not typical, a structure resembling the "golf-tee" sign, a characteristic sign of an intradural extramedullary lesion (4, 6, 10, 11), and syringomyelia were noted (Figure 1A). Additionally, an appearance mimicking the "dural tail sign" in the meninges adjacent to the thickened C2 left nerve root with contrast enhancement, mild atrophy with contrast enhancement of the paraspinal muscle adjacent to the lesion, and ventral meningeal enhancement were identified (Figures 1H,I). However, broad-based dural attachment of the mass was not evident in any sequence. Other MRI findings included multiple cervical intervertebral disc degeneration with protrusion, bilateral ventriculomegaly, and Chiari-like malformations. Based on MRI findings, we concluded that the C2 spinal mass was the cause of the patient's symptoms. Considering the MRI characteristics of the mass (single, well-defined, marked contrast enhancement, and mass effect), a spinal tumor concurrent with gliosis, left-sided neuritis, and myositis was strongly suspected rather than inflammatory or vascular diseases. However, the origin of the C2 mass could not be determined because of its extensive distribution throughout the spinal parenchyma in all

TABLE 1 MRI sequences of the brain and cervical spine used in the present case.

	Sequences	TR (ms)	TE (ms)	FOV (mm)	Slice thickness (mm)
Brain	T1 sagittal	560	12	130×130	3.0
	T2 sagittal	3,860	120	130×130	3.0
	T1 transverse	599	11	130×130	3.0
	T2 transverse	4,000	89	130×130	3.0
	FLAIR transverse	7,290	88	130×130	3.0
	T2* GE transverse	572	15	130×130	3.0
	DWI transverse	4,500	91	130×130	3.0
Cervical	T1 sagittal	524	13	160×160	2.5
	T2 sagittal	3,000	91	160×160	2.5
	T1 transverse	550	15	100×100	3.0
	T2 transverse	3,360	82	100×100	3.0
	T2 MEDIC transverse	600	23	120×120	3.0
	3D T2 SPACE sagittal	1730	193	160×160	0.9
	T2 HASTE myelography sagittal	8,000	1,200	160×160	
Post-contrast	T1 sagittal	524	13	160×160	2.5
	T1 transverse	550	15	100×100	3.0
	T1 dorsal	400	12	180×180	3.0
	3D T1[a] sagittal	21	7	180×180	0.8

DWI, diffusion-weighted images; FLAIR, fluid-attenuated inversion recovery; FOV, field of view; HASTE, half-Fourier acquisition single-shot turbo spin-echo; MRI, magnetic resonance imaging; MEDIC, multi-echo data image combination; SPACE, sampling perfection with application-optimized contrast using different flip angle evolution; T2* GE, T2*-weighted gradient-recalled echo; TE, echo time; TR, repetition time; 3D T1[a], three-dimensional T1-weighted spoiled gradient-echo water excitation.

images. An intradural extramedullary tumor (e.g., meningioma, nerve sheath tumor, or nephroblastoma) was considered a primary differential diagnosis, and other possibilities were an intramedullary tumor or intramedullary invasion by an extramedullary tumor. Given its clear margins, location, size, and the progression of clinical signs, surgical removal of the mass was planned via dorsal laminectomy of C2 combined with durotomy. A high-speed burr and bone-cutting forceps were used to create a hinged osteotomy of the C2 dorsal arch involving the cranial 75% of the C2 spinous process (Figure 2). The bone flap was rotated dorsally and cranially on the preserved attachment of the cranial aspect of the C2 spinous process to the dorsal arch of C1 to visualize the dorsal dura. A midline durotomy revealed a capsulated mass. Most tumor parts were easily separated and removed from the adjacent spinal cord parenchyma; however, the ventral part adhered locally to the spinal cord meninges adjacent to the left nerve root with fibrotic tissues (Figure 2). After careful removal of these ventral tumor tissues, mild hemorrhage occurred but was promptly controlled. No abnormalities were observed in the spinal cord. A biological, absorbable dura substitute (Lyoplant Onlay; B Braun Co., Germany) was used to cover the dural defect and sutured to the adjacent dura before the spinous process was returned to its normal position. Subsequently, the dorsal arch of the axis was rotated back over the exposed vertebral canal, and the spinous process was stabilized with 2–0 non-absorbable sutures (PROLENE Polypropylene Suture; ETHICON Co., United States) through one predrilled hole. The excised mass, characterized by a red, well-circumscribed, and elastic appearance (Figure 3), was histopathologically examined (hematoxylin and eosin staining). Spindle round-to-polygonal cells containing small-to-moderate amounts of pale, eosinophilic, wispy-to-granular cytoplasm were observed. The nuclei were heterochromatic, with one or two variably distinct nucleoli, along with moderate anisocytosis and anisokaryosis (Figure 3). These findings were most consistent with glioma, in which oligodendroglioma may be the most consistent. The histopathological identification of an intramedullary tumor did not match the MRI or surgical findings. Thus, a genomic tumor test was performed using the same tissue sample as the histopathology; immunohistochemical staining for glial cell tumor markers could not be performed because of the owner's financial constraints. This genomic tumor test is a tumor-only, next-generation sequencing, hybrid-capture test involving canine gene panel covering 482,000 base pairs of 120 genes associated with canine or human cancer. Genetic data revealed copy number loss of *CDKN2N* and gain of *MYC*, supporting the diagnosis of a canine glioma. Three days postoperatively, the dog was able to stand up and walk in the cage, and its appetite returned to normal. Approximately 2 weeks postoperatively, all neurological signs returned to normal. Although postoperative MRI and computed tomography (CT) examinations were recommended to confirm the residual tissue of the glioma and assess metastasis, including "CSF drop metastasis" from the glioma (12–14), only a 16-channel multi-detector CT (Emotion 16, Siemens Healthcare, Forchheim, Germany) scan was performed due to the owner's financial constraints. On postoperative CT images, regional bone defects in the C2 lamina due to surgery were identified. However, no significant CT findings were identified in the whole body, including tumor metastasis, lymph node enlargement, or contrast-enhanced lesions around the surgical site. Although chemotherapy was recommended based on the genetic data and considering possible recurrence and local adhesion or invasion of the tumor, the owner rejected this

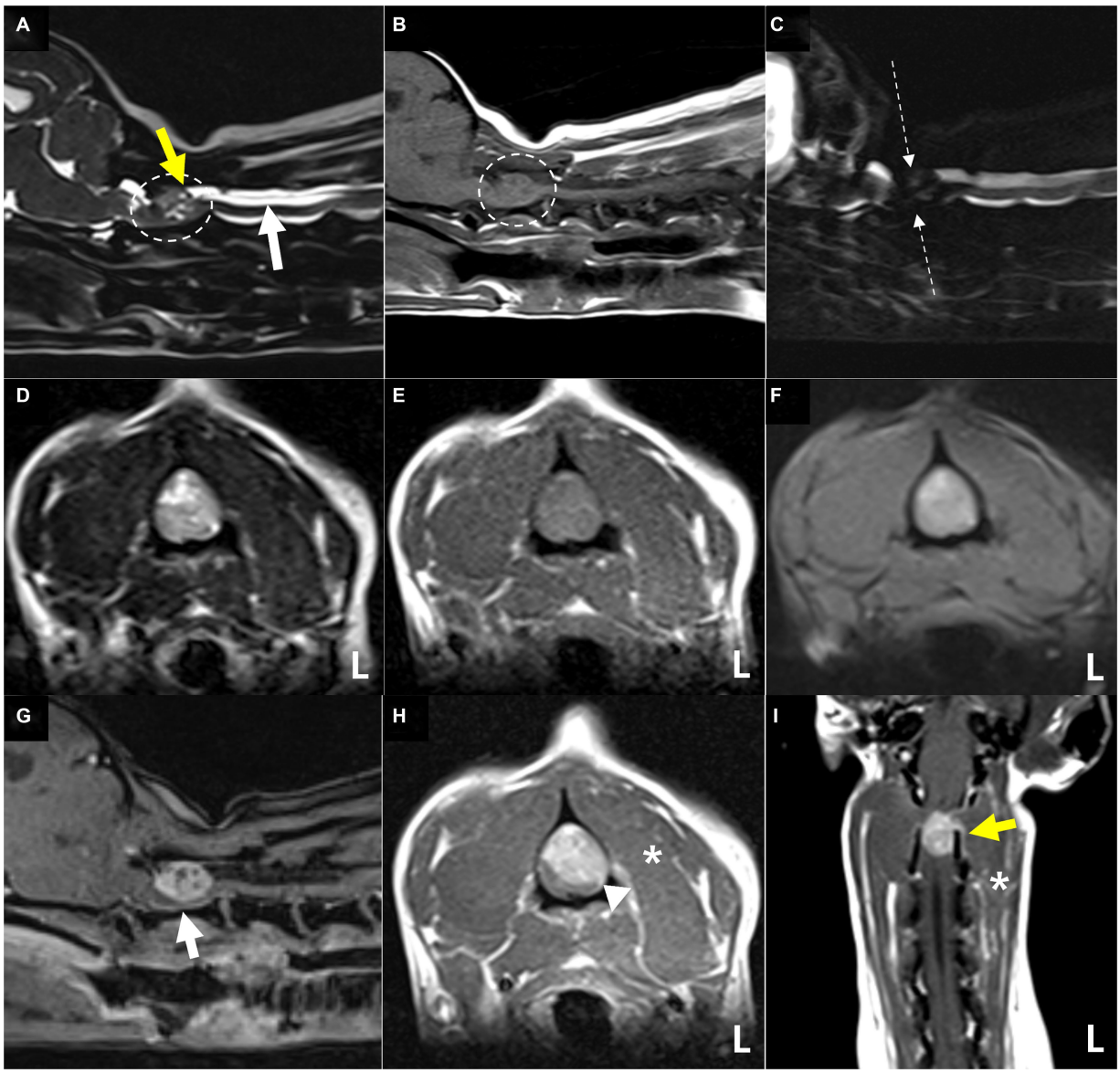

FIGURE 1
Magnetic resonance images showing the cervical spinal cord of the present case. The extensive lesion in the second cervical (C2) spinal cord **(A,B)** (dotted circles) is ill-defined and heterogeneously hyperintense with loss of normal intraparenchymal architecture on sagittal **(A)** and transverse **(D)** T2-weighted images. The lesion appears iso-to-hypointense on sagittal **(B)** and transverse **(E)** T1-weighted images and iso-to-hyperintense on T2-weighted multi-echo data image combination sequence images **(F)**. The origin of this C2 lesion cannot be determined due to its extensive distribution throughout the spinal parenchyma on all images. The lesion leads to focal spinal cord swelling and attenuation of the cerebrospinal fluid line on T2-weighted half-Fourier acquisition single-shot turbo spin-echo myelography **(C)**, accompanied by the presence of a structure resembling the "golf-tee" sign **(A)** (yellow arrow) in the dorsal subarachnoid space and diffuse syringomyelia **(A)** (white arrow) just caudal to the lesion. Post-contrast T1-weighted sagittal **(G)**, transverse **(H)**, and dorsal **(I)** images of the cervical spinal cord. Post-contrast T1-weighted images reveal an ovoid, well-defined mass with homogeneously marked contrast enhancement. The mass contains multiple small cavities **(G)**, suggestive of cystic or necrotic areas, leading to severe left-sided compression of the spinal cord and an appearance mimicking the "dural tail sign" of the adjacent meninges **(H)** (arrowhead) **(H)**. A thickened left C2 nerve root with contrast enhancement (**I**) (yellow arrow), mild atrophy and contrast enhancement of the paraspinal muscle **(H,I)** (asterisks) adjacent to the lesion, and ventral meningeal enhancement **(G)** (white arrow) are also present. These findings strongly suggest a spinal tumor concurrent with gliosis and left-sided neuritis and myositis rather than inflammatory or vascular diseases. Based on these MRI findings, the mass is considered to be of intradural extramedullary rather than of intramedullary origin.

suggestion. Ten months after discharge, no recurrence of neurological signs had been reported.

The authors declare that no Institutional Animal Care and Use Committee or other approval was needed. Written informed consent was obtained from the owner prior to any procedures being performed.

3 Discussion

This report presents a rare case of a cranial cervical spinal glioma, confirmed by surgical histopathology, with postoperative improvement in a dog. Gliomas arise from glial cells in the brain or spinal cord and are grouped as astrocytic, oligodendroglial, and

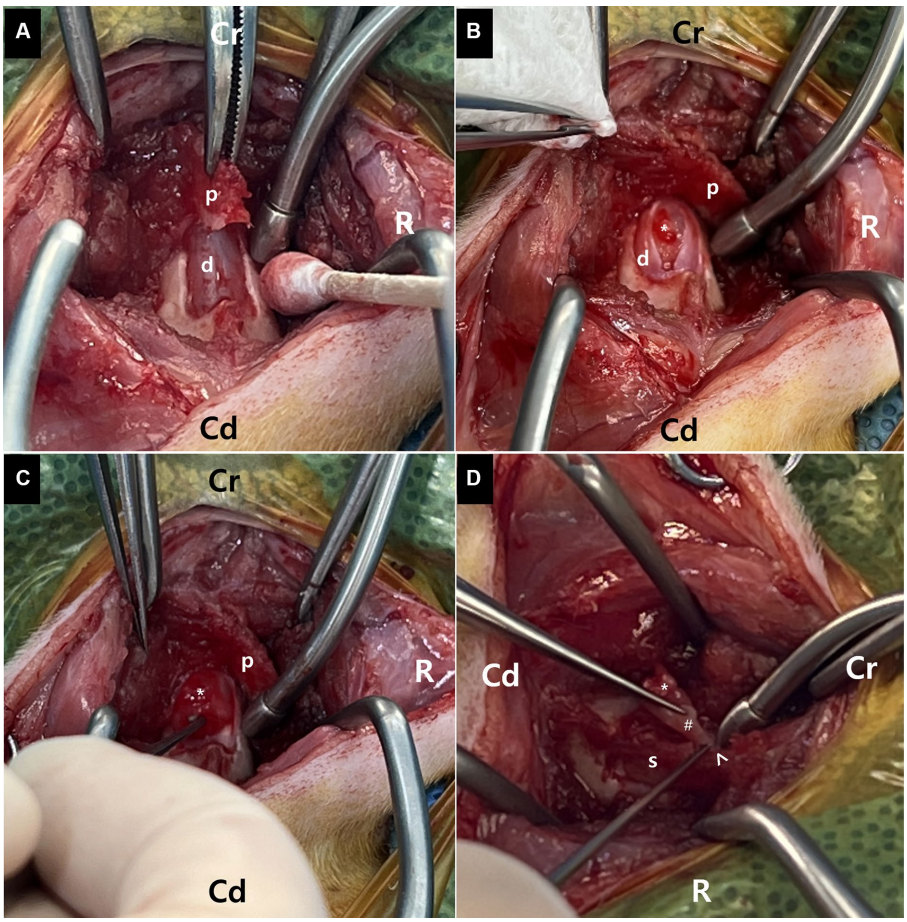

FIGURE 2
Surgical removal of the mass following dorsal laminotomy of the axis combined with durotomy at the second cervical vertebra. **(A)** A bone flap (p) of the C2 axis spinous process is created with laminotomy of the C2 axis. The bone flap (p) is rotated dorsally and cranially to visualize the dorsal dura **(D)**. **(B,C)** Following the laminotomy, a midline durotomy reveals a capsulated mass (asterisk). Most parts of this tumor are easily removed from the adjacent spinal cord (s) parenchyma. **(D)** The ventral part of the mass (asterisk) regionally adheres to the spinal cord (S) meninges (arrowhead) adjacent to the left nerve root with fibrotic tissues (hash). The ventral tumor tissues are carefully removed.

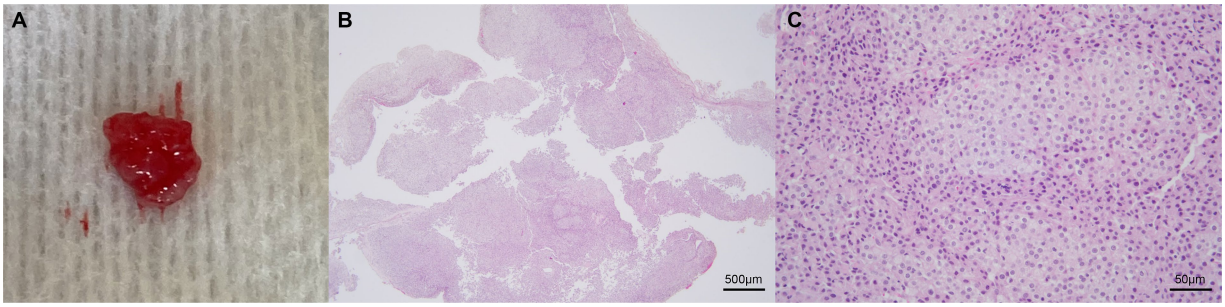

FIGURE 3
Representative images of the excised mass. Gross appearance **(A)** and photomicrographs of histopathological evaluation **(B,C)**. The mass is characterized by a red, well-circumscribed, and elastic appearance **(A)**. The poorly demarcated mass is composed of neoplastic cells arranged in sheets and occasional short streams (**B**: 40×). The spindled, round, or polygonal cells contain small-to-moderate amounts of pale eosinophilic, wispy-to-granular cytoplasm, and heterochromatic nuclei with one or two variably distinct nucleoli (**C**: 400×). Anisocytosis and anisokaryosis are moderate **(C)**. These findings are consistent with glioma, in which oligodendroglioma may be the most consistent. Scale bars in **(B)**: 500 μm and in **(C)**: 50 μm.

ependymal tumors. Canine gliomas typically affect older individuals, especially those of brachycephalic breeds, and occur mainly in the frontal, parietal, or temporal telencephalic lobes and less frequently in the brainstem and spinal cord (3, 7). The most common type of canine spinal cord glioma is ependymoma, followed by astrocytoma, oligodendroglial tumors, gliomatosis cerebri, and unclassified glioma

(3, 8). In a recent report of seven canine spinal gliomas, the affected spinal cord segments were, in decreasing order of frequency, thoracic (three cases), lumbar (three cases), and cervical (one case); the most common spinal cord glioma was oligodendroglioma (3). In another canine report of 53 intramedullary spinal tumor cases, thoracolumbar segments were the most frequently affected, although primary intramedullary tumors were more common in the cervical spinal cord in young dogs. Furthermore, intramedullary masses were identified in all dogs in which MRI was performed (8). However, intramedullary spinal tumors can expand and infiltrate other sites, although intramedullary spinal lesions may initially be intraparenchymal (3, 8). Clinical diagnosis and treatment of intramedullary neoplasms may be challenging because of the rapidly progressive clinical course and neuroanatomical location of these tumors. On MRI, both astrocytomas and oligodendrogliomas appear as ovoid-to-elliptical mass lesions that are well-marginated, located eccentrically in the spinal cord, and associated with variable degrees of spinal cord expansion. Astrocytomas and oligodendrogliomas are iso-to-hypointense on T1-weighted images and hyperintense on T2-weighted and short-tau inversion recovery images with moderate contrast enhancement. In contrast, ependymomas appear as focal to multi-segmental, fusiform, centrally located lesions that are heterogeneously iso-to-hypointense on T1-weighted images and hyperintense on T2-weighted images, with marked contrast enhancement (8). Nevertheless, there have been reports of one dog diagnosed with oligodendroglioma showing hyperintensity on T1-weighted images and another dog with diffuse leptomeningeal oligodendroglioma accompanied by the "dural tail sign" (15, 16). In a recent study evaluating the MRI characteristics of inflammatory, neoplastic, and vascular diseases of the canine spinal cord, the diagnostic sensitivity was excellent for intradural spinal diseases but poor for intramedullary tumors. Published descriptions of the imaging features of intramedullary tumors are sparse, their predilection sites are poorly understood and variable, and their MRI features overlap with those of inflammatory and vascular diseases (9). Therefore, the present case, which included MRI and surgical resection with histopathological examination of the spinal mass, has significant clinical value. The MRI characteristics included a well-defined, homogenously marked contrast-enhancing, single-mass lesion with extensive, eccentric distribution throughout the spinal parenchyma. The origin of the lesion was difficult to establish because of the extensive involvement of the spinal cord parenchyma without broad-based dural contact and findings mimicking the "golf-tee" and "dural tail" signs, further complicating the evaluation. This case suggests that an intramedullary glioma should be considered when the lesion is widely distributed throughout the spinal parenchyma, even if it is located eccentrically rather than centrally. The authors considered the present case to be a glioma originating from the spinal cord parenchyma, exhibiting extensive expansion in the extramedullary space. Ultimately, the mass was relatively well removed, significantly contributing to the improvement of the neurological symptoms. Intraoperatively, the mass was observed in the extramedullary region, facilitating its identification and resection after durotomy. The left ventral area of the mass adhered to the meninges around the left intervertebral foramen. To date, such canine spinal gliomas attached to the meninges with a pedunculated pattern have not been reported. Additionally, the mass exhibited a well-circumscribed red-colored and elastic appearance, differing in characteristics from those in previously reported soft grayish masses in oligodendroglioma or oligodendrogliomatosis (14–16). Consequently, the surgeons suspected, even postoperatively, the extension of an intradural extramedullary tumor into the intramedullary parenchyma rather than an intramedullary origin. Considering the craniocervical location and elastic appearance of the mass, the surgeons suspected a meningioma (17, 18). Following the histopathological results, a genomic tumor test was performed, which strongly supported the diagnosis of a spinal glioma. Indeed, it has been reported that the MYC gene is overexpressed in glioma, and the deletion of the CDKN gene is considered a clinically important molecular alteration in glioma (19, 20). This case provided additional evidence against drawing a conclusion regarding a presumptive histologic diagnosis and making decisions based solely on MRI findings to classify the lesion location relative to the meninges (5).

To the best of our knowledge, this is the only reported case of a canine spinal glioma with remarkable postoperative improvement. Most reported canine spinal gliomas or intramedullary tumors were diagnosed postmortem or were associated with a short survival time due to rapid deterioration postoperatively (3, 8, 13–16, 21). This may be primarily due to the challenge of diagnosing spinal glioma antemortem and implementing surgical treatment owing to the intramedullary tumor location.

This report had several limitations, including a lack of immunohistochemical data, CSF analysis, and various MRI sequences. Although differentiating among glioma types based on histopathological results was necessary, immunohistochemistry could not be performed. Therefore, the definitive glioma type could not be confirmed. Nevertheless, we considered the mass to be an oligodendroglioma or astrocytoma with higher potential, based on MRI features and histopathological findings. Considering the size, distribution, and pronounced contrast enhancement, the mass leaned more toward a high-grade tumor than a low-grade tumor, indicating the necessity for ongoing monitoring to detect any potential recurrence (16). The lack of CSF analyses might not have substantially impacted the patient's evaluation and diagnosis because spinal gliomas have no specific CSF characteristics (3, 7, 9, 14, 22). The inclusion of post-contrast fat saturation and diffusion tensor imaging may have provided additional information on the mass distribution and location and may have proven beneficial in determining the type of spinal tumors on MRI for future reference (23, 24).

Despite numerous reports detailing the MRI features of canine spinal tumors, the present case indicated the existence of additional types not yet reported. Although histopathological examination is typically required for a definitive diagnosis, MRI provided detailed information on the location, distribution, and margination of spinal cord lesions, facilitating surgical decision-making. Additional information regarding spinal tumor characteristics on MRI may contribute to the advancement of antemortem diagnosis. Furthermore, surgical treatment may benefit patients with spinal cord tumors that are considered removable based on MRI findings.

Data availability statement

The original contributions presented in the study are included in the article/supplementary material, further inquiries can be directed to the corresponding author/s.

Ethics statement

Ethics review and approval was not required as per local legislation and institutional requirements. Written informed consent was obtained from the owner prior to any procedures being performed. Written informed consent was obtained from the owners for the participation of their animals in this study.

Author contributions

JK: Conceptualization, Data curation, Formal analysis, Investigation, Writing – original draft, Writing – review & editing. KihK: Conceptualization, Data curation, Formal analysis, Investigation, Writing – review & editing. DC: Data curation, Formal analysis, Investigation, Writing – review & editing. YK: Data curation, Formal analysis, Investigation, Writing – review & editing. KitK: Data curation, Formal analysis, Investigation, Writing – review & editing. DO: Data curation, Formal analysis, Investigation, Writing – review & editing. NL: Data curation, Formal analysis, Investigation, Writing – review & editing. JC: Data curation, Formal analysis, Investigation, Writing – review & editing. JY: Investigation, Resources, Supervision, Validation, Writing – review & editing.

Funding

The author(s) declare that no financial support was received for the research, authorship, and/or publication of this article.

Acknowledgments

The authors would like to thank Editage (www.editage.co.kr) for English language editing.

Conflict of interest

The authors declare that the research was conducted in the absence of any commercial or financial relationships that could be construed as a potential conflict of interest.

Publisher's note

All claims expressed in this article are solely those of the authors and do not necessarily represent those of their affiliated organizations, or those of the publisher, the editors and the reviewers. Any product that may be evaluated in this article, or claim that may be made by its manufacturer, is not guaranteed or endorsed by the publisher.

References

1. Besalti O, Caliskan M, Can P, Vural SA, Algin O, Ahlat O. Imaging and surgical outcomes of spinal tumors in 18 dogs and one cat. *J Vet Sci*. (2016) 17:225–34. doi: 10.4142/jvs.2016.17.2.225

2. Auger M, Hecht S, Springer CM. Magnetic resonance imaging features of extradural spinal neoplasia in 60 dogs and seven cats. *Front Vet Sci*. (2021) 7:610490. doi: 10.3389/fvets.2020.610490

3. Rissi DR, Barber R, Burnum A, Miller AD. Canine spinal cord glioma: a case series and review of the literature. *J Vet Diagn Invest*. (2017) 29:126–32. doi: 10.1177/1040638716673127

4. Kutara K, Maeta N, Kanda T, Ohnishi A, Mitsui I, Miyabe M, et al. Magnetic resonance imaging findings of an intradural extramedullary hemangiosarcoma in a dog. *J Vet Med Sci*. (2019) 81:1527–32. doi: 10.1292/jvms.19-0260

5. Krasnow MS, Griffin JF IV, Levine JM, Mai W, Pancotto TE, Kent M, et al. Agreement and differentiation of intradural spinal cord lesions in dogs using magnetic resonance imaging. *J Vet Intern Med*. (2022) 36:171–8. doi: 10.1111/jvim.16327

6. Mai W. *Diagnostic MRI in dogs and cats. 1st* ed Broken Sound Parkway NW, Suite: CRC Press (2018).

7. Mamom T, Meyer-Lindenberg A, Hewicker-Trautwein M, Baumgärtner W. Oligodendroglioma in the cervical spinal cord of a dog. *Vet Pathol*. (2004) 41:524–6. doi: 10.1354/vp.41-5-524

8. Pancotto TE, Rossmeisl JH Jr, Zimmerman K, Robertson JL, Werre SR. Intramedullary spinal cord neoplasia in 53 dogs (1990–2010): distribution, clinicopathologic characteristics, and clinical behavior. *J Vet Intern Med*. (2013) 27:1500–8. doi: 10.1111/jvim.12182

9. Masciarelli AE, Griffin JF, Fosgate GT, Hecht S, Mankin JM, Holmes SP, et al. Evaluation of magnetic resonance imaging for the differentiation of inflammatory, neoplastic, and vascular intradural spinal cord diseases in the dog. *Vet Radiol Ultrasound*. (2017) 58:444–53. doi: 10.1111/vru.12501

10. Kippenes H, Gavin PR, Bagley RS, Silver GM, Tucker RL, Sande RD. Magnetic resonance imaging features of tumors of the spine and spinal cord in dogs. *Vet Radiol Ultrasound*. (1999) 40:627–33. doi: 10.1111/j.1740-8261.1999.tb00890.x

11. Casado D, Fernandes R, Lourinho F, Gonçalves R, Clark R, Violini F, et al. Magnetic resonance imaging features of canine intradural/extramedullary intervertebral disc extrusion in seven cases. *Front Vet Sci*. (2022) 9:1003042. doi: 10.3389/fvets.2022.1003042

12. Bentley RT, Yanke AB, Miller MA, Heng HG, Cohen-Gadol A, Rossmeisl JH. Cerebrospinal fluid drop metastases of canine glioma: magnetic resonance imaging classification. *Front Vet Sci*. (2021) 8:650320. doi: 10.3389/fvets.2021.650320

13. Vigeral M, Bentley RT, Rancilio NJ, Miller MA, Heng HG. Imaging diagnosis-antemortem detection of oligodendroglioma "cerebrospinal fluid drop metastases" in a dog by serial magnetic resonance imaging. *Vet Radiol Ultrasound*. (2018) 59:E32–7. doi: 10.1111/vru.12474

14. Koch MW, Sánchez MD, Long S. Multifocal oligodendroglioma in three dogs. *J Am Anim Hosp Assoc*. (2011) 47:e77–85. doi: 10.5326/JAAHA-MS-5551

15. Lobacz MA, Serra F, Hammond G, Oevermann A, Haley AC. Imaging diagnosis-magnetic resonance imaging of diffuse leptomeningeal oligodendrogliomatosis in a dog with dural tail sign. *Vet Radiol Ultrasound*. (2018) 59:E1–6. doi: 10.1111/vru.12441

16. Schkeeper AE, Moon R, Shrader S, Koehler JW, Linden D, Taylor AR. Imaging diagnosis-magnetic resonance imaging features of a multifocal oligodendroglioma in the spinal cord and brain of a dog. *Vet Radiol Ultrasound*. (2017) 58:E49–54. doi: 10.1111/vru.12401

17. McDonnell JJ, Tidwell AS, Faissler D, Keating J. Magnetic resonance imaging features of cervical spinal cord meningiomas. *Vet Radiol Ultrasound*. (2005) 46:368–74. doi: 10.1111/j.1740-8261.2005.00067.x

18. Petersen SA, Sturges BK, Dickinson PJ, Pollard RE, Kass PH, Kent M, et al. Canine intraspinal meningiomas: imaging features, histopathologic classification, and long-term outcome in 34 dogs. *J Vet Intern Med*. (2008) 22:946–53. doi: 10.1111/j.1939-1676.2008.0106.x

19. Wang J, Wang H, Li Z, Wu Q, Lathia JD, McLendon RE, et al. C-Myc is required for maintenance of glioma cancer stem cells. *PLoS One*. (2008) 3:e3769. doi: 10.1371/journal.pone.0003769

20. Lu VM, O'Connor KP, Shah AH, Eichberg DG, Luther EM, Komotar RJ, et al. The prognostic significance of CDKN2A homozygous deletion in IDH-mutant lower-grade glioma and glioblastoma: a systematic review of the contemporary literature. *J Neuro-Oncol*. (2020) 148:221–9. doi: 10.1007/s11060-020-03528-2

21. Giron C, Paquette D, Culang D, Doré M, Masseau I. Diffuse meningeal oligodendrogliomatosis characterized by spinal intra-parenchymal nodules on magnetic resonance imaging in a dog. *Can Vet J*. (2020) 61:1312–8.

22. Korff CP, Chu SA, Percival AJ, Nelissen S, Wood JH, Davies E, et al. Unique cytologic and imaging features of a lumbosacral oligodendroglioma in a cat. *J Vet Diagn Invest*. (2023) 35:289–94. doi: 10.1177/10406387231166132

23. Yoon H, Park NW, Ha YM, Kim J, Moon WJ, Eom K. Diffusion tensor imaging of white and grey matter within the spinal cord of normal beagle dogs: sub-regional differences of the various diffusion parameters. *Vet J*. (2016) 215:110–7. doi: 10.1016/j.tvjl.2016.03.018

24. Allett B, Hecht S. Magnetic resonance imaging findings in the spine of six dogs diagnosed with lymphoma. *Vet Radiol Ultrasound*. (2016) 57:154–61. doi: 10.1111/vru.12340

frontiers | Frontiers in Veterinary Science

TYPE Case Report
PUBLISHED 22 May 2024
DOI 10.3389/fvets.2024.1400076

OPEN ACCESS

EDITED BY
Sokol Duro,
Agricultural University of Tirana, Albania

REVIEWED BY
Noelia Vazquez Odo,
Facultad de veterinaria UdelaR, Uruguay
Howard Dobson,
Invicro, United States

*CORRESPONDENCE
Hakyoung Yoon
✉ hyyoon@jbnu.ac.kr

RECEIVED 19 March 2024
ACCEPTED 30 April 2024
PUBLISHED 22 May 2024

CITATION
Ji Y, Kang J, Heo S, Lee K and Yoon H (2024) Case report: Echocardiographic and computed tomographic features of congenital bronchoesophageal artery hypertrophy and fistula in a dog. *Front. Vet. Sci.* 11:1400076. doi: 10.3389/fvets.2024.1400076

Case report: Echocardiographic and computed tomographic features of congenital bronchoesophageal artery hypertrophy and fistula in a dog

Yewon Ji[1], Jinsu Kang[2], Suyoung Heo[3], Kichang Lee[1] and Hakyoung Yoon[1,4]*

[1]Department of Veterinary Medical Imaging, College of Veterinary Medicine, Jeonbuk National University, Iksan, Republic of Korea, [2]Department of Veterinary Surgery, College of Veterinary Medicine, Kyungpook National University, Daegu, Republic of Korea, [3]Department of Surgery, College of Veterinary Medicine, Jeonbuk National University, Iksan, Republic of Korea, [4]Biosafety Research Institute and College of Veterinary Medicine, Jeonbuk National University, Iksan, Republic of Korea

Introduction: Studies on aberrant bronchoesophageal arteries are limited. Herein, we report a case of a multi-origin systemic-to-pulmonary shunt with suspected bronchoesophageal artery hypertrophy and fistula in a dog.

Case report: A 4-year-old castrated male beagle weighing 11 kg underwent routine medical screening. Physical examination revealed a right-sided continuous murmur of grades 1–2. Thoracic radiography revealed a mild cardiomegaly. Echocardiography revealed a continuous turbulent shunt flow distal to the right pulmonary artery (RPA) branch from the right parasternal short axis pulmonary artery view. Computed tomography demonstrated systemic-to-pulmonary shunts originating from the descending aorta at the level of T7–8, the right 5th and 6th dorsal intercostal arteries, and the right brachiocephalic trunk, which formed anomalous networks around the trachea and esophagus that anastomosed into a large tortuous vessel at the level of T6–7 and entered the RPA. Surgical ligation of multiple shunting vessels was performed. Postoperative echocardiography and computed tomography showed decreased left ventricular volume overload and markedly decreased size of the varices. Additionally, most of the shunting vessels were without residual shunt flow.

Conclusion: The present study provides information regarding imaging features and the successful surgical management of multiple systemic-to-pulmonary shunts originating from the descending aorta, right brachiocephalic trunk, and intercostal arteries and terminating at the RPA. Multimodal imaging features after surgical ligation have also been described.

KEYWORDS

aortopulmonary shunt, aberrant bronchoesophageal artery, esophageal varices, cardiovascular anomaly, canine

1 Introduction

Various cardiovascular malformations associated with systemic-to-pulmonary (L-to-R) shunts have been reported in the veterinary literature. L-to-R shunts can progress to heart failure due to volume overload. The clinical significance of L-to-R shunts depends on their size and the blood flowing through them (1). The types of L-to-R shunts include patent ductus arteriosus (PDA) (2, 3), aortopulmonary window (APW) (4–7), L-to-R arteriovenous fistulae (8), arteriovenous shunts (9), and various atypical L-to-R shunts (10–17). Bronchoesophageal artery (BEA) hypertrophy, also referred to as an aberrant BEA, is a relatively rare type of L-to-R shunt in dogs (10, 11, 14, 15, 17). The BEA usually arises from the fifth right dorsal intercostal artery and courses next to the esophagus, which is known to play a major role in supplying oxygen to the airways and supporting pulmonary structures (18). Normal bronchial arteries from the BEA communicate with the pulmonary artery only through a capillary bed, resulting in a physiologically small amount of L-to-R shunting flow that is hemodynamically insignificant (19). Although aberrant BEAs are known to be abnormal bronchial-to-pulmonary artery communications, the underlying etiology is still not fully understood; however, these anomalies of BEA can result in a significant L-to-R shunt, which can present as similar features on physical and radiographic examinations. Therefore, advanced imaging examinations, such as echocardiography and computed tomography (CT), are essential in distinguishing BEA anomalies from other L-to-R shunts.

To date, five studies on aberrant BEA, BEA hypertrophy, and anomalous BEA have been reported in dogs (10, 11, 14, 15, 17); additionally, there is a lack of reports on BEA anomalies in other animals. However, these cases have differences in the locations of shunt insertion, and there are no reports of cases with right-sided murmurs. In these reports, the echocardiographic and CT characteristics of anomalous BEA have been described; however, to our knowledge, no study in the veterinary literature has described the related postoperative CT features.

Herein, we report a case of a multi-origin systemic-to-pulmonary shunt with suspected BEA hypertrophy and fistula. This report aimed to describe in detail the echocardiographic and CT features of the multiple shunts and changes in postoperative echocardiographic and CT findings.

2 Case description

A 4-year-old castrated male beagle weighing 11 kg underwent routine medical screening. The patient had no history of diseases other than chronic otitis externa and no clinical signs indicative of cardiovascular diseases. On physical examination, no abnormalities were observed (temperature, 38°C; heart rate, 110 beats/min; and systolic blood pressure, 150 mmHg); however, a mild right-sided basal continuous murmur of grades 1–2 was noted. Laboratory examinations revealed mildly elevated alanine aminotransferase levels. Thoracic radiography (HF-525 PLUS, ECORAY, Seoul, Korea; kVP 70, mA 200, exposure time 0.03 s) was performed, which revealed an increased vertebral heart score of 11.7 (reference range, 8.7–10.7) and a sternal contact of 3.5 (reference range, 2.5–3.0) on the right lateral view. Generalized cardiomegaly and a slight bulge at the 1–3 o'clock of the cardiac silhouette were identified in the ventrodorsal view. The diameters of the caudal vena cava and pulmonary vessels were within normal ranges.

Two-dimensional transthoracic echocardiographic examination was performed using a 5-MHz 72 phased array transducer (Aplio 300; Canon Medical System, Europe B.V., Zoetermeer, 73 Netherlands), which revealed the following measurements: left ventricular end-diastolic internal diameter corrected for body weight (LVIDDn), 1.74 (upper limit; <1.7) (20); left ventricular end-systolic internal diameter corrected for body weight (LVIDSn), 1.14 (reference range, 0.74–1.33) (21); end-diastolic volume index (EDVI), 103.11 (upper limit;>100) (22); end-systolic volume index (ESVI), 40.87 (lower limit;<30) (22). These measurements were calculated using the Teichholz method. Additionally, the following were noted: E peak velocity, 91.3 cm/s, 58-117cm/s. (23); E/E', 10.49 (reference range, 7.3–9.5) (24); and LA:Ao, 0.97 (upper limit <1.6) (20). Collectively, these observations suggested mild left ventricular eccentric hypertrophy. No significant mitral, tricuspid, aortic, or pulmonic regurgitations were observed. From the right parasternal short axis pulmonary artery view, a continuous L-to-R turbulent shunt flow distal to the right pulmonary artery (RPA) showing a mosaic pattern was identified on color Doppler, with a peak velocity of 4.18 m/s and a pressure gradient of 69.89 mmHg on continuous wave Doppler (Figures 1A,B). However, the orifice of the shunt at the typical location of the PDA or the orientation of the shunt could not be identified on echocardiography.

CT (Alexion, TSX-034A, Toshiba Medical Systems, Tochigi, Japan) was performed to further assess the orientation and anatomical features of the suspected shunting vessel. The CT scan was performed under general anesthesia induced using butorphanol 0.2 mg/kg (Butophan; Myungmoon Pharm Co., Ltd., Seoul, Korea) and propofol 6 mg/kg (MCT/LCT 1%, Freefol-MCT; Daewon Pharm Co., Ltd., Seoul, Korea) and maintained with 1.5% isoflurane (Isoflurane; Hana Pharm Co., Ltd., Hwaseong, Korea). The CT parameters were as follows: helical scan mode, 100 kVp, 150 mA, 256 × 256 matrix, rotation time of 0.75 s, and slice thickness of 1 mm. Pre- and post-contrast CT images were acquired. For the contrast medium, 900 mg iodine/kg of iohexol in a total volume of 28 mL (Omnipaque, GE Healthcare, United States) was injected intravenously at a rate of 3 mL/s using a power injector. Post-contrast CT scans were performed when the ascending aorta started to show contrast enhancement and 120 s after the first injection.

CT tomography revealed multiple L-to-R shunts (Figure 2). The first shunt (shunt 1) identified was a tortuous vessel originating from the brachiocephalic trunk that ran caudally and anastomosed with the peritracheal network (Figures 2E,G). The second shunt (shunt 2) was caudal to the first one, originated from the thoracic descending aorta at the T8 level, and formed tortuous vessels that eventually connected to the periesophageal network (Figures 2A,B,F). Regarding the third shunt (shunt 3), the vessels arising from the right fifth and sixth dorsal intercostal arteries joined and formed a tortuous shunting vessel that ran cranially and connected to the peritracheal network (Figures 2B–D,F,G). These three shunts were connected to either the peritracheal or periesophageal dense network and eventually anastomosed to a large tortuous vessel connected to the RPA. The measured size of the orifice was 4.1 mm at insertion (Figures 2D,G).

After imaging, the shunts were surgically ligated. Midazolam 0.2 mg/kg (Midazolam, Bukwang Pharm Co., Seoul, Korea) and

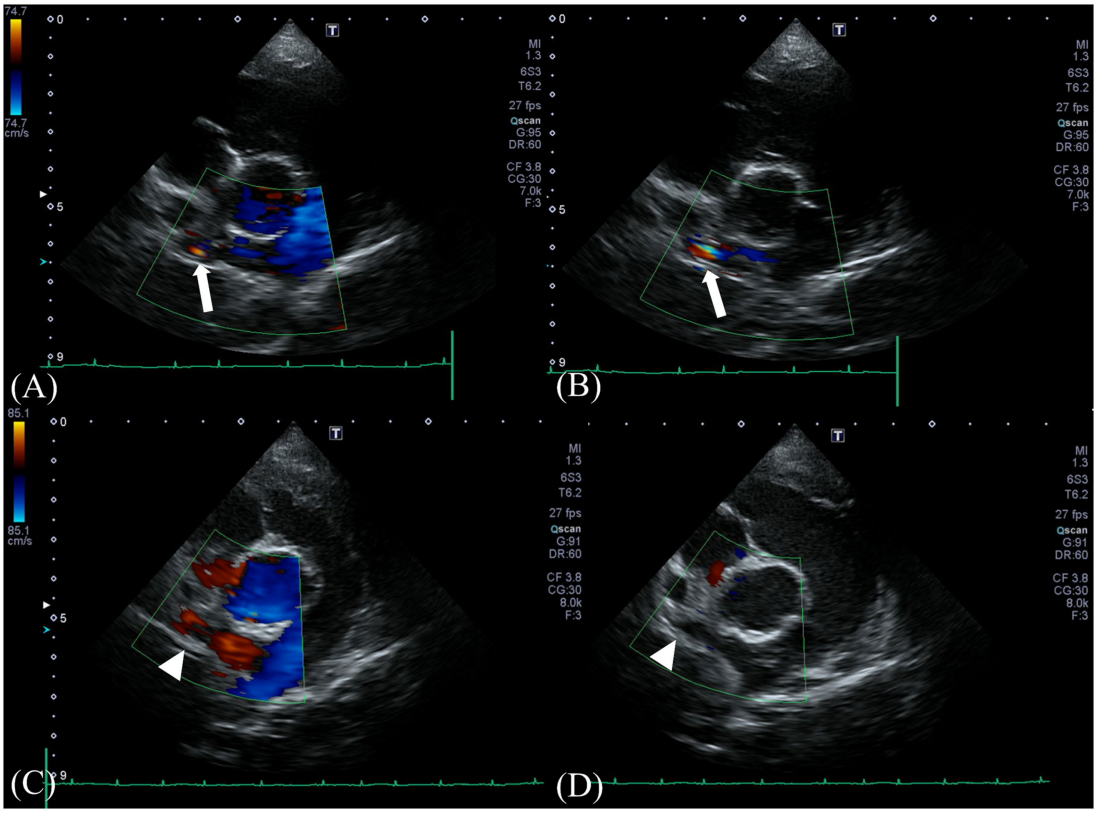

FIGURE 1
Preoperative Doppler echocardiography at the shunt insertion. Color-flow Doppler examination from a right parasternal short-axis view **(A,B)** reveals a turbulent positive continuous shunt flow entering the distal right pulmonary artery (white arrow) (systolic, 4.18 m/s; diastolic, 2.56 m/s). Postoperative Doppler echocardiography at the preoperative location of the shunt. No residual flow was seen at the location (white arrowhead) **(C,D)**.

butorphanol 0.2 mg/kg (Butophan, Myungmoon Pharm Co., Seoul, Korea) were administered intravenously. Intravenous cefazolin 25 mg/kg (cefazolin sodium, Korus Pharm Co., Chuncheon, Korea) was administered as premedication, and general anesthesia was induced with intravenous propofol 6 mg/kg (Provive 1%; Myungmoon Pharm Co., Seoul, Korea) and maintained with sevoflurane (Sevofran, Hana Pharm Co., Seoul, Korea). The dog was positioned in left lateral recumbency, and the right thorax was prepared for aseptic surgery. An intercostal thoracotomy was performed at the 5th right intercostal space, and a shunt entering the right pulmonary artery branch was identified (Figure 3A). The shunt was bluntly separated and ligated using a surgical clip (Hemoclip, Teleflex, Pennsylvania, USA) and 5-0 polypropylene (PROLENE, Ethicon, New Jersey, USA) (Figures 3B,C). Next, the shunts connected to the brachiocephalic trunk and the right 5th-6th dorsal intercostal arteries supplying the periesophageal network were identified, and ligation was performed (Figures 3D–F). Sutures were performed using a routine method, and the dog recovered from anesthesia without any complications. For postoperative analgesia, butorphanol–lidocaine–ketamine was administered (butorphanol at a dosage of 0.02 mg/kg/h, lidocaine [lidocaine hydrochloride, Jeil Pharm Co., Daegu, Korea] at a dosage of 1.5 mg/kg/h, and ketamine [ketamine hydrochloride, Yuhan Corp., Seoul, Korea] at a dosage of 0.6 mg/kg/h) via constant rate infusion.

Follow-up echocardiography and CT were performed at 3 weeks and 12 weeks postoperatively. On postoperative echocardiography at 3 weeks and 12 weeks after surgical ligation, no residual shunting of the right pulmonary artery was observed (Figures 1C,D). Additionally, echocardiographic parameters showed a diminution of the left ventricular volume overload (preoperative LVIDDn 1.74 to postoperative LVIDDn 1.46; preoperative EDVI 103.11 to postoperative EDVI 67.41). Moreover, decreases in E peak velocity from 91.3 cm/s to 44.70 cm/s, and E/E' from 10.49 to 6.67 cm/s were observed, which indicated a decrease in left atrial pressure. CT at 3 weeks postoperatively showed no residual enhancement caudal to the ligation site of shunt 1 originating from the brachiocephalic trunk or shunt 2 originating from the descending aorta. Shunt 3 originating from the fifth and sixth right dorsal intercostal arteries, showed no cranial or caudal residual flow to the clip at the two ligation sites; however, mild residual enhancement of the vessel connected to the peritracheal network was observed. The shunting vessel anastomosed from the three shunts and the peritracheal–periesophageal network were observed; however, no connection between the aorta and the RPA was identified (Figure 4). No remarkable changes or aneurysms were observed on the follow-up CT at 12 weeks postoperatively.

3 Discussion

An L-to-R shunt can result in left ventricular volume overload, and treatment options vary according to shunt type; thus, a definitive diagnosis of the shunt is important. To date, several anomalous

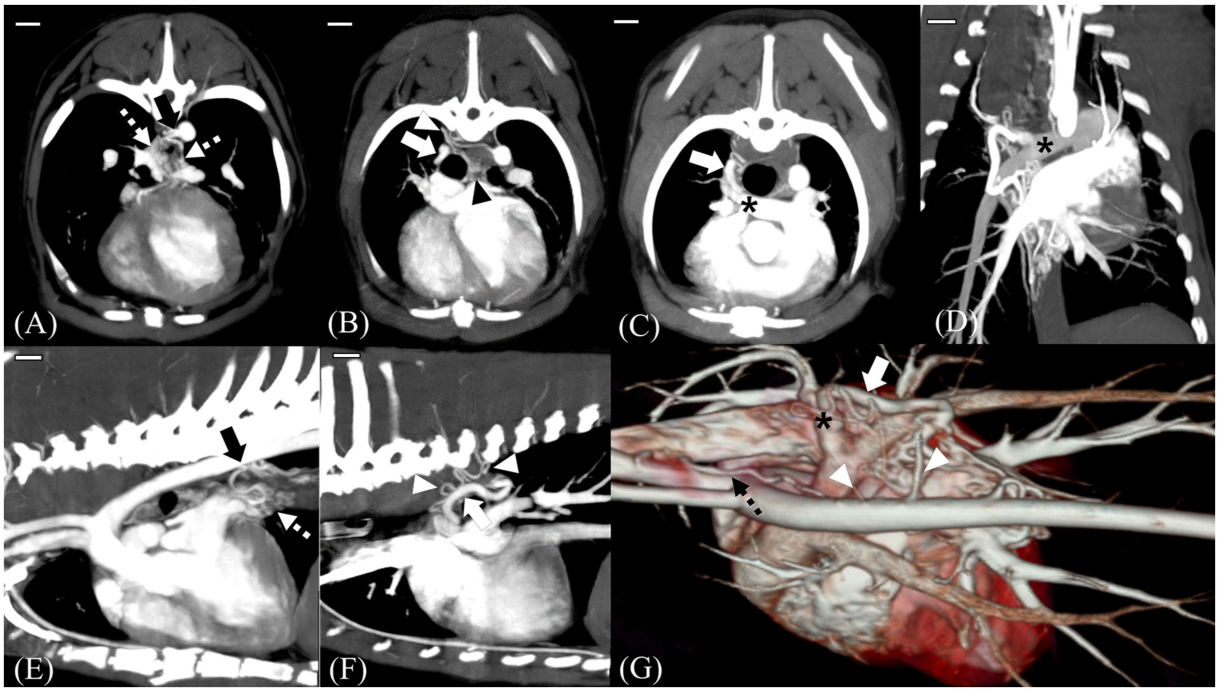

FIGURE 2
MIP images and a 3D reconstructed image of preoperative computed tomography scans. Scale bars equal 10 mm. Transverse 5-mm-thick slab MIP **(A–C)**, dorsal 10-mm-thick slab MIP **(D)**, sagittal 7.5-mm-thick slab MIP **(E,F)**, and 3D reconstructed images of the heart and adjacent vessels **(G)**. Shunt (black arrow) from the descending aorta at T8 level, which was considered the enlarged left bronchoesophageal artery (BEA) **(A,E)**. Note that in **(E)**, the shunt is supplying the periesophageal network (white dotted arrow). Tortuous vessels (white arrowhead) arising from the fifth and sixth dorsal intercostal arteries course forward and connect to the peritracheal network (black arrowhead) **(B,F,G)**. On dorsal and transverse MIP images, the main shunt (white arrow) entering the distal right pulmonary artery (RPA) (black asterisk) is seen **(C,D)**. 3D reconstructed image showing multiple tortuous vessels (white arrowhead), a network, and the main shunt vessel (white arrow) connected to the distal RPA (black asterisk). Note the aberrant tortuous vessel from the brachiocephalic trunk, which was considered the aberrant right BEA (black dotted arrow) **(G)**.

aortopulmonary shunts that differ from typical PDA or APW, which comprise the majority of L-to-R shunts in dogs, have been reported in the veterinary literature (10–16). Herein, the physical, radiographic, echocardiographic, and CT characteristics of BEA hypertrophy compared to other L-to-R shunts are discussed.

Few reports have described the features of BEA (25, 26) and anomalous L-to-R communication associated with aberrant BEA in dogs (9–11, 14, 15). Previous reports have demonstrated shunts between the BEA and the pulmonary artery or branches suspected to be aberrant branches of the BEA connected to the main pulmonary artery (MPA) (10, 11, 15). In one study, all cases of aberrant BEA coexisted with a network of closely related tortuous vessels. Additionally, it described the features and patterns of congenital and acquired BEA hypertrophy and concurrent L-to-R artery communications (14). A recent study described the imaging features of anomalous bronchial and non-bronchial arterial blood supply to the lungs in dogs and proposed a classification of BEA hypertrophy. The imaging features of congenital BEA hypertrophy include an enlarged left BEA from an enlarged intercostal artery between T5 and T8; an aberrant origin of the right BEA from the right brachiocephalic trunk; the presence of a large and tortuous vessel between the dense peritracheal–periesophageal network and the MPA through an orifice; and no evidence of lung or pleural diseases (14).

Herein, one physical characteristic was a mild continuous murmur heard at the basal level of the right heart. Continuous murmurs are usually heard in PDA and APW (2, 4), generally at the base and apex (4, 27). All previous cases of BEA hypertrophy had various grades of left-sided murmur, either apical or basal (11, 14, 15, 17); however, no study has reported BEA hypertrophy with a right basal murmur. In previous reports regarding BEA hypertrophy, shunt insertion locations were the proximal left pulmonary artery, between the aorta and the pulmonary artery, and the proximal RPA. Herein, the location of the main shunt entering the RPA was distal rather than proximal; this may be a reason for the different murmur locations. These findings indicate that BEA hypertrophy can have various shunt insertion locations, and murmur locations can vary according to the location. In addition to relatively common congenital anomalies with right-sided murmurs, such as ventricular septal defects (VSDs) (28), rare cardiovascular anomalies such as the aorta-right atrial tunnel (29) can present with a right-sided continuous murmur. Therefore, the differential diagnosis, in the case of a continuous right-sided murmur, should include BEA hypertrophy, aorto-right atrial tunnel, and VSD. However, murmur alone is insufficient to diagnose BEA hypertrophy; echocardiography and CT should be performed for a definite diagnosis.

Herein, distinct echocardiography and CT features enabled the differentiation of the condition from other cardiovascular anomalies. Because the location of the main shunt entering the distal RPA was different from the level of the ligamentum arteriosum, it could be distinguished from PDA. Tortuous communicating vessels were also identified. Because APW is characterized by an opening or

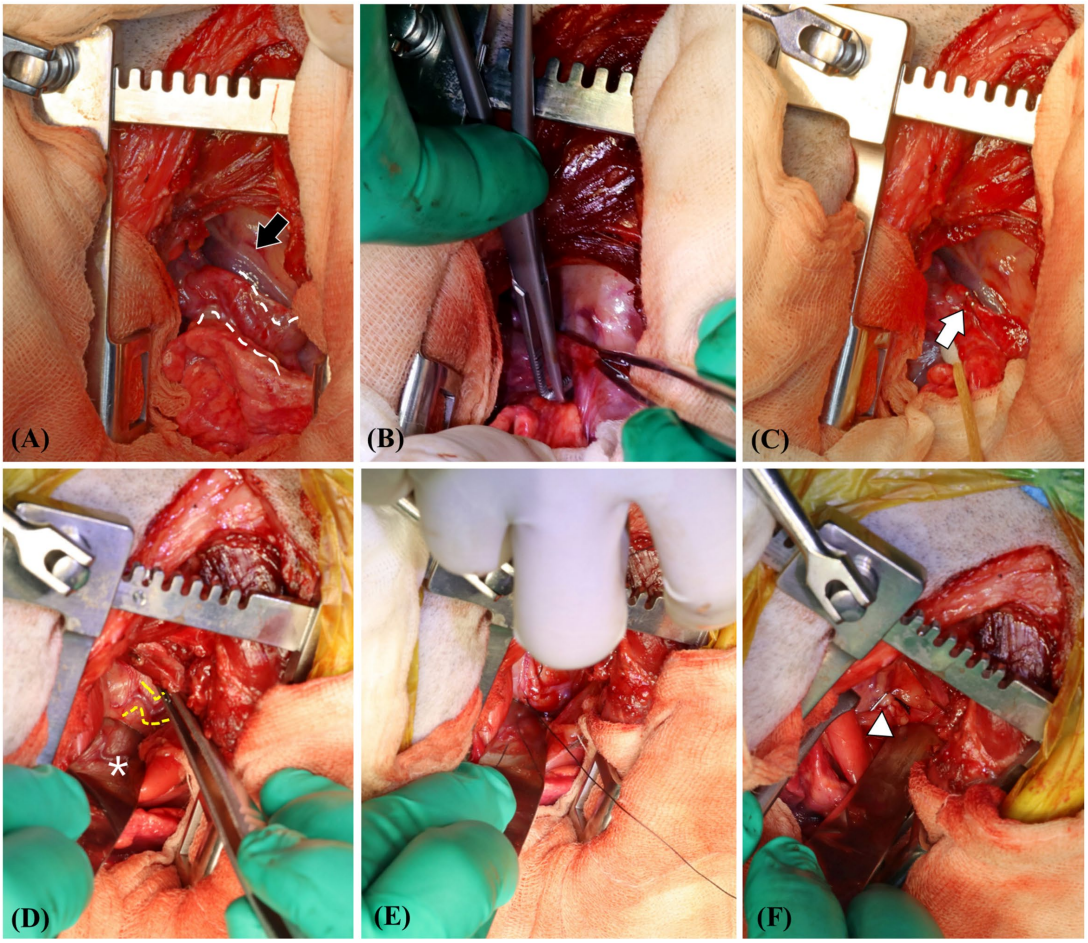

FIGURE 3
View at the time of surgical ligation of the shunting vessels. The main shunt entering the right pulmonary artery (white dotted line) is identified **(A)**. The caudal vena cava is indicated by the black arrow. Blunt separation and ligation of the shunt are performed using a surgical clip (white arrow) and 5–0 polypropylene **(B,C)**. Identification and ligation of the shunting vessel (yellow dotted line) from the brachiocephalic trunk—which was considered the aberrant form of the right bronchoesophageal artery and right fifth–sixth dorsal intercostal arteries—is performed, and a surgical clip (white arrowhead) is observed. The white asterisk indicates the reflection of the esophagus on the malleable retractor **(D–F)**.

window without tortuous vessels or significant length of communication (30), it could be differentiated from APW. This case also showed three tortuous vessels originating from different locations entering the dense peritracheal and periesophageal networks, which eventually formed a large tortuous vessel that entered the RPA. One of the tortuous vessels was connected to the suspected aberrant BEA originating from the fifth and sixth intercostal arteries and entered the peritracheal network. Our findings were similar to those of a previous report on congenital BEA hypertrophy; therefore, the present case was considered to have congenital BEA hypertrophy.

However, herein, as the main shunt entered distal to the RPA, there were some differences compared with previous reports. In a review of BEA hypertrophy and aberrant BEA, only two dogs had shunts entering the RPA, while others had shunts entering the left pulmonary artery, usually at the proximal part or between the aorta and the pulmonary artery caudal to the ligamentum arteriosum (11, 14, 15). In both cases, shunts entering the RPA were proximal, not distal (14, 15).

Shunt insertion location can be critical when L-to-R shunt identification is based solely on echocardiography, especially when the patient is asymptomatic. Because the efficacy and accuracy of the diagnosis from echocardiography are affected by the experience of the clinician performing echocardiography (31), uncommon shunts with atypical origins may be neglected and remain unidentified. It is relatively easier to identify shunts entering the MPA or proximal branches on the echocardiography on the basic right parasternal short-axis view at the level of the MPA, but they can be missed when shunts with a small amount of flow enter the distal branches. Therefore, it is important to check for anomalous shunt flows not only at the location of typical shunts but also distal to them from modified views, if needed.

Herein, subsidiary anomalies were observed compared to typical BEA hypertrophy alone. On CT examination, a slight difference was identified cranially, where the enlarged left BEA arose. The fifth and sixth dorsal intercostal arteries did not course directly but tortuously from the aorta, from which two tortuous arteries arose. These two tortuous vessels coursed and eventually connected as a tortuous vessel and entered the peritracheal network. Despite the unknown etiopathology of BEA hypertrophy and concurrent peritracheal–periesophageal network, the left BEA and fifth, sixth, and eighth dorsal intercostal arteries develop as branches of the dorsal intersegmental arteries or their ventral branches during the

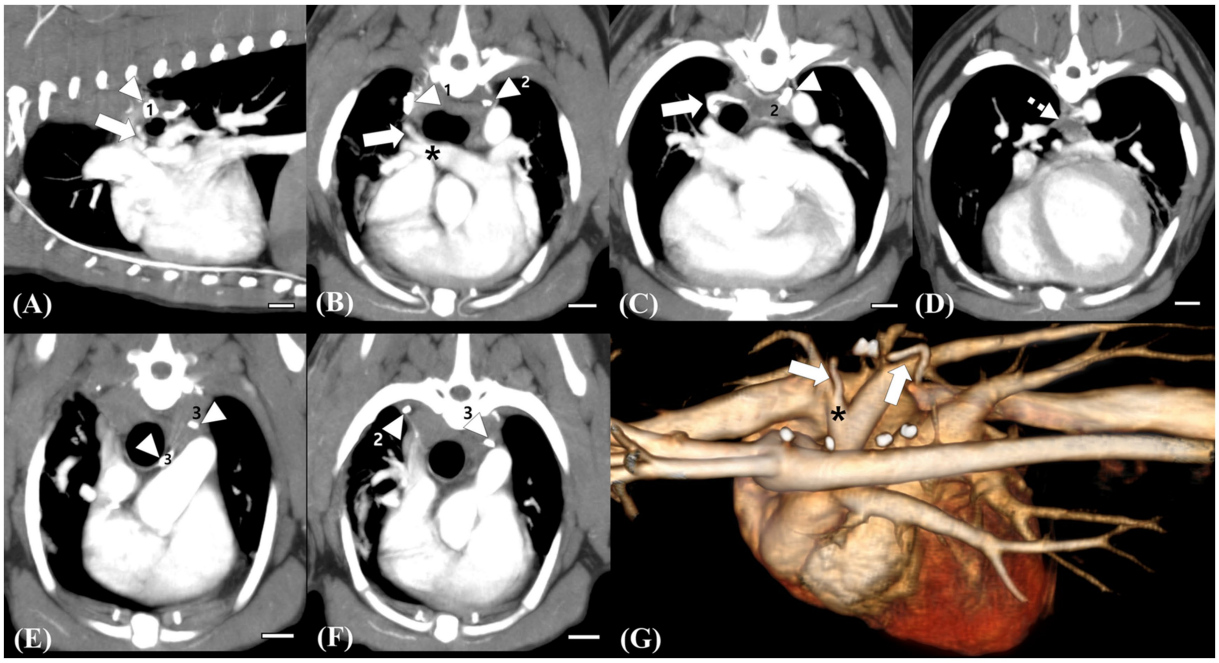

FIGURE 4
Follow-up computed tomography (CT) images at 12 weeks postoperatively **(A–F)** and a reconstructed 3D image **(G)** for comparison. Scale bars equal 10 mm. The remaining trunk of the ligated vessel (white arrow) connected to the right pulmonary artery, which is supplied by the peritracheal network (white dotted arrow), is identified, but no connection cranial to the surgical clip (white arrowhead, 1) is observed **(A,B,C,G)**. Note the remarkable decrease in the flow of the peritracheal network (white dotted arrow) and the ligated vessel compared with those observed in preoperative CT **(D,G)**. Surgical clip for the ligation of the small tortuous vessel originating from the fifth and sixth intercostal arteries, which were supplying the peritracheal network (white arrowhead, 2) **(C)**. Ligation of the shunting vessel from the brachiocephalic trunk, which was considered the aberrant right bronchoesophageal artery (BEA) supplying the peritracheal network. No remaining flow after the ligation is observed. Surgical clips for the ligation of the suspected aberrant right BEA (white arrowhead, 3) and of the small shunting vessel originating from the fifth dorsal intercostal artery (white arrow, 2) **(C–F)**.

development of the vascular system, and the suspected BEA hypertrophy and additional anomalies could be the result of secondary connections during the embryonal stage (18).

On follow-up echocardiography at 3 weeks and 12 weeks postoperatively, no residual flow and decreased LVIDDn, EDVI, E peak velocity, E/A ratio, and FS were observed. Decreased LVIDDn and EDVI were considered to result from the decreased left ventricular volume overload. Decreased left ventricular preload and filling pressure after surgical ligation could result in a decreased E peak and E/A ratio (32). Additionally, decreased FS might have resulted from decreased diastolic volume without a significant change in systolic volume and was considered a temporary postoperative status (32).

Although surgical ligation of suspected BEA hypertrophy and fistulas has been reported in two case reports (10, 15), there is a lack of studies describing changes in CT findings after surgical ligation of the shunts. Herein, follow-up CT scans at 3 weeks and 12 weeks after surgical ligation showed no residual flow of the large shunting vessel entering the RPA and no residual flow caudal to the ligation site of shunt 1, which was considered an anomalous origin of the right BEA connecting and supplying the peritracheal network. Shunt 3, which supplied the peritracheal network, was also ligated; the amount of the peritracheal network was markedly decreased, but a small amount of flow was observed. Shunt 2, considered an aberrant form of a hypertrophied left BEA, was not perfectly ligated, which was suspected to be the reason for the mild residual flow of the periesophageal network.

A previous report described cases that underwent echocardiography, angiography, and CT examinations before the surgical ligation of shunts (15). In three of the four dogs, only the large main shunts entering the pulmonary artery were surgically ligated, which resulted in immediate shrinkage of some or all tortuous vessels. One dog had at least two vessels in addition to the major vessel of aortic origin that underwent separate ligation, similar to the present case. However, the origins and characteristics of these additional vessels were not fully elucidated, and no postoperative CT was performed. Herein, a small amount of residual flow was observed in the tortuous network postoperatively; however, no residual flow was identified on echocardiography. As residual flow can only be identified on CT and not on echocardiography, and tortuous networks cannot be assessed on echocardiography, follow-up CT examination, in addition to echocardiography, is needed to thoroughly assess residual flow and the existence of remaining shunts.

This study has some limitations. First, on the follow-up CT, a mild residual flow in the periesophageal network was observed, which could have led to an aneurysm. However, no aneurysm was identified at the 3-month follow-up. In addition, it has been reported that the resolution of transient deterioration of left ventricular systolic function could be seen after 6 months of surgical or interventional ligation of L-to-R shunts (32). Second, no follow-up echocardiographic examination after 12 weeks was performed in this case. However, as in the present case, although postoperative echocardiographic parameters indicated resolution of the left ventricular volume overload, there was an insignificant amount of residual flow from the tortuous network. Even if a small amount of residual flow remains in the peritracheal–periesophageal network, the surgical ligation of

major shunt vessels can clinically help in the resolution of LV volume overload.

4 Conclusion

This report describes the preoperative and postoperative physical, echocardiographic, and CT features of BEA hypertrophy. BEA hypertrophy should be included as a differential diagnosis when a right-sided murmur is noted, a mosaic pattern at the distal RPA is observed on echocardiography, and a shunt of systemic arterial blood flow inserted into the pulmonary artery is seen on CT examination. Surgical ligation is a practical method for the occlusion of L-to-R shunts in BEA hypertrophy, which can decrease the volume overload of the heart and result in a remarkable decrease in the number of peritracheal and periesophageal networks.

Data availability statement

The raw data supporting the conclusions of this article will be made available by the authors, without undue reservation.

Ethics statement

Ethical approval was not required for the studies involving animals in accordance with the local legislation and institutional requirements because the manuscript is a case report of an imaging diagnosis and surgery of a client-owned companion animal, written informed agreement was obtained from the client instead. Written informed consent was obtained from the owners for the participation of their animals in this study.

Author contributions

YJ: Conceptualization, Data curation, Formal analysis, Funding acquisition, Investigation, Methodology, Project administration, Resources, Software, Supervision, Validation, Visualization, Writing – original draft, Writing – review & editing. JK: Conceptualization, Investigation, Methodology, Project administration, Validation, Writing – review & editing. SH: Writing – review & editing. KL: Conceptualization, Supervision, Validation, Writing – review & editing. HY: Conceptualization, Data curation, Formal analysis, Funding acquisition, Investigation, Methodology, Project administration, Resources, Software, Supervision, Validation, Visualization, Writing – original draft, Writing – review & editing.

Funding

The author(s) declare that no financial support was received for the research, authorship, and/or publication of this article.

Acknowledgments

The authors would like to thank clinicians in the Veterinary Medical Imaging and Surgery department of the Teaching Hospital of Jeonbuk National University for their assistance.

Conflict of interest

The authors declare that the research was conducted in the absence of any commercial or financial relationships that could be construed as a potential conflict of interest.

Publisher's note

All claims expressed in this article are solely those of the authors and do not necessarily represent those of their affiliated organizations, or those of the publisher, the editors and the reviewers. Any product that may be evaluated in this article, or claim that may be made by its manufacturer, is not guaranteed or endorsed by the publisher.

References

1. King T. *Elsevier's integrated pathology E-book*. Amsterdam: Elsevier Health Sciences (2006).

2. Buchanan JW. Patent ductus arteriousus morphology, pathogenesis, types and treatment. *J Vet Cardiol*. (2001) 3:7–6. doi: 10.1016/S1760-2734(06)70010-8

3. Slatter DH. *Textbook of small animal surgery*. Amsterdam: Elsevier Health Sciences (2003).

4. Jung S, Orvalho J, Griffiths LG. Aortopulmonary window characterized with two- and three-dimensional echocardiogram in a dog. *J Vet Cardiol*. (2012) 14:371–5. doi: 10.1016/j.jvc.2011.10.004

5. Nelson AW. Aorticopulmonary window in a dog. *J Am Vet Med Assoc*. (1986) 188:1055–8.

6. Pascon JPE, Ondani AC, Junior DP, Andrade JNM, Camacho AA. Aorticopulmonary septal defect in a dog: case report. *Arq Bras Med Vet Zootec*. (2010) 62:564–9. doi: 10.1590/S0102-09352010000300010

7. Guglielmini C, Pietra M, Cipone M. Aorticopulmonary septal defect in a German shepherd dog. *J Am Anim Hosp Assoc*. (2001) 37:433–7. doi: 10.5326/15473317-37-5-433

8. Claretti M, Pradelli D, Borgonovo S, Boz E, Bussadori CM. Clinical, echocardiographic and advanced imaging characteristics of 13 dogs with systemic-to-pulmonary arteriovenous fistulas. *J Vet Cardiol*. (2018) 20:415–24. doi: 10.1016/j.jvc.2018.10.001

9. Fujii Y, Aoki T, Takano H, Ishikawa R, Wakao Y. Arteriovenous shunts resembling patent ductus arteriosus in dogs: 3 cases. *J Vet Cardiol*. (2009) 11:147–51. doi: 10.1016/j.jvc.2009.04.005

10. Malik R, Bellenger C, Hunt G, Church D, Allan G. Aberrant branch of the bronchoesophageal artery mimicking patent ductus-arteriosus in a dog. *J Am Anim Hosp Assoc*. (1994) 30:162–4.

11. Yamane T, Awazu T, Fujii Y, Watanabe T, Muto M, Okutsu M, et al. Aberrant branch of the bronchoesophageal artery resembling patent ductus arteriosus in a dog. *J Vet Med Sci*. (2001) 63:819–22. doi: 10.1292/jvms.63.819

12. Scollan K, Salinardi B, Bulmer BJ, Sisson DD. Anomalous left-to-right shunting communication between the ascending aorta and right pulmonary artery in a dog. *J Vet Cardiol*. (2011) 13:147–52. doi: 10.1016/j.jvc.2011.01.003

13. Hsue W, Gunther-Harrington C, Visser L, Woodworth R. Anomalous left-to-right shunting vessel between the ascending aorta and right pulmonary artery and concurrent left peripheral pulmonary artery stenosis in a dog. *CASE (Phila)*. (2020) 4:534–9. doi: 10.1016/j.case.2020.08.006

14. Ledda G, Caldin M, Mezzalira G, Bertolini G. Multidetector-row computed tomography patterns of bronchoesphageal artery hypertrophy and systemic-to-pulmonary fistula in dogs. *Vet Radiol Ultrasound*. (2015) 56:347–58. doi: 10.1111/vru.12247

15. Culshaw GJ, Wagner T, Luis Fuentes V, Schwarz T, Yool DA, French AT, et al. Identification and surgical ligation of aortopulmonic vascular malformation causing left heart volume overload in 4 dogs. *J Vet Intern Med*. (2013) 27:583–7. doi: 10.1111/jvim.12081

16. Markovic LE, Kellihan HB, Roldán-Alzate A, Drees R, Bjorling DE, Francois CJ. Advanced multimodality imaging of an anomalous vessel between the ascending aorta and main pulmonary artery in a dog. *J Vet Cardiol*. (2014) 16:59–65. doi: 10.1016/j.jvc.2013.12.002

17. Newhard DK, Winter RL, Cline KA, Hathcock JT. Anomalous broncho-oesophageal arteries and peripheral systemic-to-pulmonary connections in an asymptomatic puppy. *Vet Rec Case Rep*. (2017) 5:e000392. doi: 10.1136/vetreccr-2016-000392

18. Bezuidenhout AJ. Unusual anomalies of the arteries at the base of the heart in a dog. *J S Afr Vet Assoc*. (1992) 63:32–5.

19. Yon JR, Ravenel JG. Congenital bronchial artery-pulmonary artery fistula in an adult. *J Comput Assist Tomogr*. (2010) 34:418–20. doi: 10.1097/RCT.0b013e3181d1e96e

20. Keene BW, Atkins CE, Bonagura JD, Fox PR, Haggstrom J, Fuentes VL, et al. ACVIM consensus guidelines for the diagnosis and treatment of myxomatous mitral valve disease in dogs. *J Vet Intern Med*. (2019) 33:1127–40. doi: 10.1111/jvim.15488

21. Cornell CC, Kittleson MD, Della Torre P, Häggström J, Lombard CW, Pedersen HD, et al. Allometric scaling of M-mode cardiac measurements in normal adult dogs. *J Vet Intern Med*. (2004) 18:311–21. doi: 10.1892/0891-6640(2004)18<311:asomcm>2.0.co;2

22. Lombard CW. Normal values of the canine M-mode echocardiogram. *Am J Vet Res*. (1984) 45:2015–8.

23. Chetboul V, Sampedrano CC, Concordet D, Tissier R, Lamour T, Ginesta J, et al. Use of quantitative two-dimensional color tissue Doppler imaging for assessment of left ventricular radial and longitudinal myocardial velocities in dogs. *Am J Vet Res*. (2005) 66:953–61. doi: 10.2460/ajvr.2005.66.953

24. Teshima K, Asano K, Sasaki Y, Kato Y, Kutara K, Edamura K, et al. Assessment of left ventricular function using pulsed tissue Doppler imaging in healthy dogs and dogs with spontaneous mitral regurgitation. *J Vet Med Sci*. (2005) 67:1207–15. doi: 10.1292/jvms.67.1207

25. Evans HE, De Lahunta A. *Miller's anatomy of the dog-E-book*. Amsterdam: Elsevier Health Sciences (2012).

26. Laitinen A, Laitinen LA, Moss R, Widdicombe JG. Organisation and structure of the tracheal and bronchial blood vessels in the dog. *J Anat*. (1989) 165:133–40.

27. Jacobs JP, Quintessenza JA, Gaynor JW, Burke RP, Mavroudis C. Congenital heart surgery nomenclature and database project: aortopulmonary window. *Ann Thorac Surg*. (2000) 69:S44–9. doi: 10.1016/s0003-4975(99)01236-9

28. Nielsen DG, Gotzsche O, Eika B. Objective structured assessment of technical competence in transthoracic echocardiography: a validity study in a standardised setting. *BMC Med Educ*. (2013) 13:47. doi: 10.1186/1472-6920-13-47

29. Park J-I, Choi R, Lee S-G, Hyun C. Retrospective study of patent ductus arteriosus in 37 dogs: clinical presentations and interventional therapy. *J Vet Clin*. (2013) 30:87–94.

30. Pugliese M, Biondi V, La Maestra R, Passantino A. Identification and clinical significance of heart murmurs in puppies involved in puppy trade. *Vet Sci*. (2021) 8:139. doi: 10.3390/vetsci8080139

31. Kim G, Ji Y, Jeong HG, Lee T, Lee K, Yoon H. Case report: imaging features of aorta-right atrial tunnel in a dog using two-dimensional echocardiography and computed tomography. *Front Vet Sci*. (2023) 10:1160390. doi: 10.3389/fvets.2023.1160390

32. Hamabe L, Kim S, Yoshiyuki R, Fukayama T, Nakata TM, Fukushima R, et al. Echocardiographic evaluation of myocardial changes observed after closure of patent ductus arteriosus in dogs. *J Vet Intern Med*. (2015) 29:126–31. doi: 10.1111/jvim.12517

frontiers | Frontiers in Veterinary Science

TYPE Case Report
PUBLISHED 12 September 2024
DOI 10.3389/fvets.2024.1472317

OPEN ACCESS

EDITED BY
Ozan Gündemir,
Istanbul University Cerrahpasa, Türkiye

REVIEWED BY
Sokol Duro,
Agricultural University of Tirana, Albania
Mihaela Spataru,
Ion Ionescu de la Brad University of Agricultural Sciences and Veterinary Medicine of Iași, Romania
Funda Yildirim,
Istanbul University-Cerrahpasa, Türkiye

*CORRESPONDENCE
Agata Godlewska
agata_godlewska@sggw.edu.pl

RECEIVED 29 July 2024
ACCEPTED 29 August 2024
PUBLISHED 12 September 2024

CITATION
Godlewska A, Dolka I, Borowczak I, Chomutowska E, Przeworski M, Różycka K and Barszcz K (2024) Case report: A nodular lesion in the ventral region of the neck in the rat as a starting point for considerations on differential diagnosis. *Front. Vet. Sci.* 11:1472317. doi: 10.3389/fvets.2024.1472317

Case report: A nodular lesion in the ventral region of the neck in the rat as a starting point for considerations on differential diagnosis

Agata Godlewska[1,2]*, Izabella Dolka[3], Ilona Borowczak[4], Ewa Chomutowska[4], Mirosław Przeworski[5], Katarzyna Różycka[1] and Karolina Barszcz[1]

[1]Department of Morphological Sciences, Institute of Veterinary Medicine, Warsaw University of Life Sciences (SGGW), Warszawa, Poland, [2]EDINA Veterinary Clinic PulsVet 24h, Warsaw, Poland, [3]Department of Pathology and Veterinary Diagnostics, Institute of Veterinary Medicine, Warsaw University of Life Sciences (SGGW), Warsaw, Poland, [4]Veterinary Clinic Forestvet, Warsaw, Poland, [5]Veterinary Clinic ANIMAL.MED, Gdańsk, Poland

The purpose of this case report is to present a poorly differentiated sarcoma in a pet rat. A veterinarian detected a small-sized nodular lesion in the ventral region of the neck during a follow-up visit related to another ailment. The anatomical structures found in the neck region in the rat and the differential diagnosis when deformities are palpated in this body part are discussed in detail. The patient underwent a total of four surgical procedures, as well as radiotherapy and chemotherapy. The rat survived in good condition for 144 days after finding the tumor.

KEYWORDS

pet rat, poorly differentiated sarcoma, tumor, ventral neck, differential diagnosis

Introduction

When a nodular lesion is found on palpation in the neck region in a rat, it is essential to consider all possible differential diagnoses. It is the authors' experience that it usually appears to be a tumor or an abscess, but it may be difficult to say with certainty where they originate from. Tumors of the mammary gland along with galactocele, salivary gland tumors and inflammation, enlarged lymph nodes in the course of lymphoid neoplasms, tumors of the thyroid and parathyroid glands, as well as tumors originating from the connective tissue, nerves, and vessels can be expected to appear in this region. When it comes to abscesses, these are usually subcutaneous deformities but may also arise in deeper tissues and organs of the neck (1, 2).

Case description

The patient was an 18-month-old male pet rat (*Rattus norvegicus* f. *domestica*) brought in for a follow-up visit associated with treatment for diabetes mellitus that was recognized 6 months earlier. To date, glucose levels had been controlled by subcutaneous insulin

administration. The owner measured the glucose twice daily and adjusted the dose according to the glucose level (1–3 IU 2x daily). On clinical examination, the rat was obese (BCS 5/5) (3), with a reduction of muscle mass in the pelvic limbs, typical of older males (4). A well-demarcated, nodular lesion of approximately 4 mm in diameter was palpable in the left ventral neck region. It doubled in size over the following 2 weeks. There were no symptoms directly related to its presence. A blood sample was taken under isoflurane anesthesia. The results showed slightly elevated GLDH, ALT levels, and monocyte count, which was not considered a contraindication to general anesthesia (Table 1). In the authors' opinion, the upper limit of urea is higher, and the lower limit of alpha-amylase is lower in rats than that given by Giknis and Clifford (5), so the results were deemed correct. Chest radiographs (Figure 1), echocardiography, and abdominal ultrasound were also performed. Chest radiographs showed a slight increase in lung opacity and a diffuse bilateral bronchial pattern with a slight loss of distinction of the heart contour, which was suggestive of pneumonia. There were no signs of metastases. Echocardiography showed left ventricular lumen dilatation with no impairment of systolic function, with a slight left atrial lumen dilatation and a slight aortic valve regurgitation. The abdominal ultrasound was unremarkable.

The lesion was removed along with a part of the left mandibular salivary gland and an adjacent lymph node. Histopathological examination revealed malignant myoepithelioma of the mandibular salivary gland. It was infiltrated by poorly circumscribed and nonencapsulated nodular neoplasm, composed of spindeloid neoplastic cells arranged in interwoven irregular bundles without distinct orientation. They infiltrated between acini and glandular structures. The neoplastic cells had indistinct cell borders, a moderate amount of eosinophilic cytoplasm, and one spindeloid to elongated hyperchromatic nucleus. Mild to moderate anisocytosis and anisokaryosis was seen. Neoplastic cells were present at the sample's margins. The lymph node was unremarkable.

The patient was referred for an oncology consultation. Therefore, a blood test was repeated. This time, hyperglycemia was noted along with monocytosis (Table 1), and the insulin dose was adjusted. It was decided to implement radiotherapy in a regimen of four fractions of 5Gy once a week.

Three weeks after the initiation of radiotherapy no recurrence was observed in both palpation and ultrasound examinations. However, another 4 weeks later (2.5 months after surgery), a considerable deformity could already be palpated, covering almost the entire ventral region of the neck. The lesion was solid, hypoechoic, multilobate, and moderately vascularized on ultrasound examination. It measured 25.2 × 12.8 mm. Its dorsal part was poorly demarcated from the surrounding tissues. In addition, multiple cysts of varying sizes, filled with echogenic fluid, were found. The tumor was located adjacent to the external jugular vein and the left common carotid artery. Due to the suspicion of tumor recurrence and poor prognosis, euthanasia was suggested, but the owner opted for another surgery, which was performed ahortly thereafter. Histopathological examination revealed a poorly differentiated sarcoma in the salivary gland's immediate vicinity (Figure 2).

Four days after surgery, an extensive deformity reappeared in the exact location. The overlying skin was thickened and ulcerated. Local recurrence was suspected, along with tumor infiltration of the skin. The owner decided to do a third and fourth (10 days apart) surgical removal of the tumor. During the third surgery, a hemostatic sponge with bleomycin was left in the wound, while the subsequent surgery included intratumoral administration of doxorubicin.

TABLE 1 Blood results and reference ranges.

Parameter	Blood results before the first surgery	Blood results before the oncology consult	Reference range according to Giknis and Clifford (5), to the authors*
RBC	9.42	8.94	7.62–9.99 T/L
Ht	47.2	47.4	38.5–52%
Hb	16.1	15.5	13.6–17.4 g/dL
MCV	50.1	53	46.3–56.2 fl
MCH	17.1	17.3	16.3–19.5 pg
MCHC	34.1	32.7	31.9–38.5 g/dL
WBC	5.29	5.2	1.98–11.06 G/L
Neutrophils	13.6	15.7	9–49.3%
Lymphocytes	76.6	72.7	44.7–87.1%
Monocytes	8.7	10.6	1–3.6%
Eosinophils	0.9	0.8	0.4–4%
Basophils	0.2	0.2	0–0.6%
PLT	841	1,137	574–1,253 G/L
ALT (GPT)	57.6	37.4	19–48 U/L
AST (GOT)	73.6	98.5	63–175 U/L
Alpha-amylase	577.1	435.7	1,223–2,109 U/L
TP	6.68	6.51	5.6–7.6 g/dL
CK	79	428	460–1,230
GLDH	39.6	15.2	0–17 U/L*
Creatinine	0.4	0.42	0.3–0.5 mg/dL
Urea	36.06	23.94	10.07–20 mg/dL
Glucose	135.5	457.2	106–184 mg/dL

* indicates, where the range level of GLDH is given.

Histopathological examination of the tumor and skin sections again revealed poorly differentiated sarcoma (Figure 2). An immunohistochemical (IHC) study of these lesions was performed. Monoclonal antibodies against cytokeratin (CK MNF116), vimentin (Vim), p63 protein (myoepithelial cell marker), and the EnVision™, Peroxidase/DAB system (Dako, Agilent Tech. Santa Clara, CA, United States) were used. The positive control was the canine mammary gland. CK and p63 expression were absent in the tumor cells, Vim expression was negative to weakly positive in some areas. Due to financial constraints, performing further IHC differential diagnostics was impossible, e.g., for cutaneous vascular tumors.

After the next 10 days, a considerable deformity measuring 25 × 12 mm was found again. The skin was covered with a wound from which bloody fluid was oozing out (Figure 3). Finally, euthanasia was performed as the rat was scratching intensely in this area, which led to bleeding. The patient also had reduced appetite and showed lower activity. The post-mortem examination revealed a nonencapsulated tumor, light pink in color, adjacent to the left external jugular vein, the left common carotid artery, and it penetrated deep into the soft tissues of the neck. No distant tumor metastases were found macroscopically.

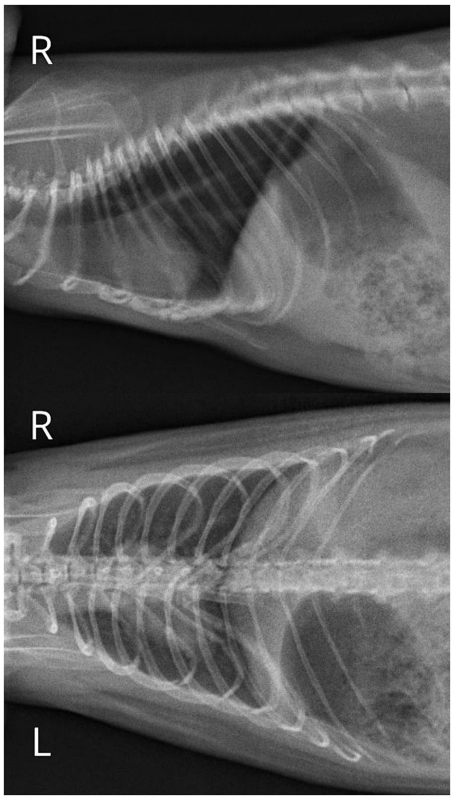

FIGURE 1
Chest radiographs showing a slight increase in lung opacity, diffuse and bilateral bronchial pattern with a slight loss of distinction of the heart contour, suggestive of pneumonia.

Discussion

The anatomy of the neck is complex mainly due to the multitude of soft tissues present in this region (1, 6). Several internal organs can be found here: salivary glands, lymph nodes, thyroid and parathyroid glands, esophagus, larynx, and trachea. In a rat, the first pair of mammary glands is also present (6). Besides the organs, the neck consists of muscles, ligaments, fasciae, vessels, nerves, and a vertebral column.

The salivary glands are represented by large and symmetrically lying clusters of glandular tissue: the paired sublingual, mandibular, and parotid glands. The mandibular salivary gland in a rat is located on the ventrolateral surface of the neck and extends from the angle of the mandible nearly to the thoracic inlet. It is oval in shape and reaches an average size of 10 × 15 × 5 mm. The four-lobed parotid gland borders it laterally and extends to the base of the external ear. The minor sublingual salivary gland is adjacent to its rostral part (6–8). Extraction of the lower incisors led to the enlargement of the mandibular and sublingual salivary glands due to hypertrophy and hyperplasia of its lobules. Rats show testosterone-dependent sexual dimorphism in the size of the mandibular salivary glands. Therefore, androgens, drugs that block their action and castration, may affect the size of this organ (7, 8). Salivary glands are relatively difficult to distinguish on palpation from the surrounding tissues.

The most common infectious agent capable of causing unilateral or bilateral inflammation of the mandibular and parotid glands, as well as the lacrimal glands and mandibular lymph nodes, is Sialodacryoadenitis virus (SDAV). The whole ventral neck region is usually swollen, which may also apply to the head. Rat coronavirus, polyomavirus, and cytomegalovirus infections usually progress without significant changes in the salivary glands (7, 8). In contrast, infection with *Klebsiella aerogenes* and *Staphylococcus aureus* can lead to abscess formation (8). As a consequence of trauma, the presence of salivary stones and foreign bodies blocking the outflow of saliva, mucocele and sublingual salivary cysts can form. However, these are rare in rats (7, 8).

The same refers to spontaneous and primary salivary gland tumors (8–11). According to Tsunenari et al., their incidence ranges from 0.02 to 0.8% (12). Cases of adenocarcinomas ranging from poorly to well differentiated (7, 9, 13), poorly differentiated carcinomas (9, 11–15), epithelial-myoepithelial carcinomas (9), myoepitheliomas (8, 9, 16, 17), or squamous cell carcinomas (7, 12) have been described in the literature. Tumors of mesenchymal origin - fibrosarcomas, undifferentiated sarcomas (7), and malignant peripheral nerve sheath tumors (7, 12) have all been found in rat salivary glands. In addition, the salivary glands can be involved in a neoplastic process in the course of leukemia (7). It is known from human medicine that salivary gland carcinomas can develop on top of existing benign tumors and progress from low-grade to high-grade malignancies (18).

In a rat, the mandibular salivary gland is adjacent to the cervical mammary gland, which is extensive in this species. The rat's mammary gland comprises four pairs of glands and six nipples. It is important to note that mammary tumors in older female rats are the second most common neoplasm (incidence – 32.92%) (19). They are also found in males, although much less frequently. Most of these are benign, such as fibroadenomas and adenomas, although carcinomas and sarcomas may also appear (7, 20). In addition to neoplasms, retention cysts (galactocele) containing milk, cellular debris, and sometimes inflammatory infiltration cells can be expected, mainly in older females (7).

Lymph nodes in the neck region in a rat are small, with a diameter of no more than 2–3 mm, making them undetectable on palpation in healthy animals. They may occur singly or in groups. Enlargement of lymph nodes in this area may be associated with inflammation and hyperplasia in the course of infections with pathogens, such as SDAV or *Mycoplasma* spp. (7). Lymph nodes can also be the site of tumor metastases, such as the cervical lymph nodes in case of thyroid tumor, the mandibular lymph nodes in case of schwannoma, or Zymbal's gland carcinoma (7).

Primary lymph node neoplasms such as lymphoma are rare in rats (7). They can infiltrate the skin and subcutaneous tissue. Lymphomas should be differentiated from large granular lymphocyte leukemia, the rat's most common type of lymphoid malignancy with an incidence of 3.75–5.42% of all neoplasms (19). It progresses with splenomegaly and hepatomegaly in the later course of the disease. Enlarged organs can easily be palpated. Massive enlargement of the mesenteric, mediastinal, and mandibular lymph nodes is also possible (7). Several round, large structures can then be palpated in both - the ventral region of the neck and the middle abdomen. The patient usually presents with dyspnea and marked leucocytosis, which may be accompanied by hemolytic anemia.

The thyroid gland in the rat is located directly behind the larynx and consists of two lobes connected by an isthmus. According to the literature, spontaneous non-neoplastic and neoplastic proliferation of

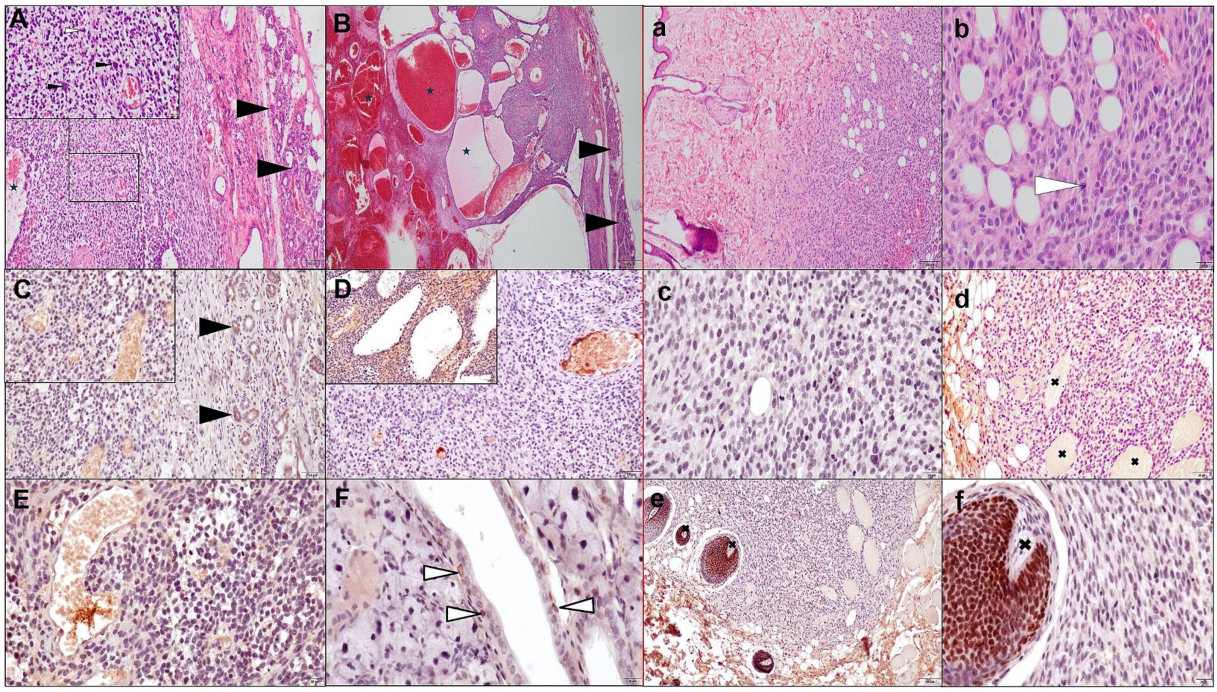

FIGURE 2
Histopathological image (hematoxylin-eosin-HE staining) and immunohistochemical (IHC) study of a poorly differentiated sarcoma located adjacent to the left mandibular salivary gland **(A,B,C–F)** and in the surrounding skin **(a,b,c–f)** being a recurrence. **(A,B)** Show a poorly demarcated, non-encapsulated tumor-rich cell neoplasm located near the salivary gland (black arrowhead) with loosely arranged neoplastic cells with indistinct cell borders, forming cystic vessel-like spaces filled to varying degrees with erythrocytes and eosinophilic fluid (asterisk). A pleomorphic tumor cells (oval, round, polygonal shape) with high anisokaryosis, a sparse cytoplasm, multinucleated cells present (inset: black thin arrowhead), and mitotic figures (white arrowhead) up to 4 in 10 HPF fields of view (2.37 mm^2),; sparse pale connective tissue with areas of hemorrhage. Immunohistochemical examination confirmed the mesenchymal origin of the neoplastic cells: negative cytoplasmic reaction for pan-cytokeratin (**C**, arrowheads indicate CK-positive salivary epithelial cells); weakly positive cytoplasmic reaction for vimentin, although it was negative in some areas **(D)**; no nuclear reaction for p63 protein in tumor cells **(E)**. Nuclear p63 reaction in salivary myoepithelial cells is indicated by white arrowheads **(F)**. **(a,b)** Show a poorly demarcated, non-encapsulated tumor-rich cell neoplasm arranged in short interlacing streams, located in the dermis and subcutaneous tissue, infiltrating muscle fibers and hair papillae (marked with a black shout in **d–f**). Pleomorphic tumor cells (oval, spindle, round, polygonal shape) with high anisokaryosis, visible 1–2 nucleoli, moderate slightly eosinophilic cytoplasm. Numerous mitotic figures (19/10HPF, [2.37 mm^2]) one of them indicated by a white arrowhead **(b)**. The stroma is scanty with areas of hemorrhage, but less extensive compared to the poorly differentiated sarcoma adjacent to the salivary gland. As in the sample of poorly differentiated sarcoma adjacent to the salivary gland, CK-negative **(c)**, Vim-positive to negative **(d)**, and p63-negative **(e,f)** neoplastic cells are shown. Hair matrix cells show nuclear positivity toward p63 **(e,f)**.

the thyroid gland - adenomas and carcinomas originating from follicular and thyroid C-cells, can be expected. Some carcinomas infiltrate surrounding tissues and may metastasize to regional lymph nodes and the lungs (7, 9, 19, 21). According to Nakazawa et al., thyroid neoplasms in rats are quite common, accounting for 2.5% of males and 8.33% of females (19), but can only be palpated when they reach a significant size. There are 1–2 mm parathyroid glands associated with the cranio-lateral surface of the thyroid, which can also undergo hyperplastic and neoplastic changes (7), the latter accounting for 1.25% in males (19). The authors rarely encounter thyroid and parathyroid tumors in rats in their practice

The Zymbal gland is a modified sebaceous gland found in rodents. It consists of 3–4 lobes, located rostro-ventrally to the external ear. Its duct opens adjacent to the tympanic membrane into the lumen of the external acoustic meatus. Hyperplasia of the Zymbal gland in the rat is not a response to primary degenerative or inflammatory changes involving the gland and is considered a pre-neoplastic lesion (7). Tumors from the Zymbal gland are adenomas, papillomas, but mainly carcinomas (7). Squamous cell carcinoma can infiltrate surrounding tissues and should be differentiated from squamous cell carcinoma of the skin. Zymbal gland neoplasms are palpable as bulky, slightly mobile lesions at the base of the external ear. Larger ones often ulcerate; the tumor may be visible in the lumen of the external acoustic meatus, may contain serous contents, and may be associated with swelling (7, 22).

Localization of lesions originating from the Zymbal gland is quite characteristic and is at the base of the external ear. However, the tumor may involve the lateral neck region if significant. It should also be borne in mind that malignant tumors of the Zymbal gland can give metastases to the salivary glands and the mandibular lymph nodes (7, 20).

In addition to the organs described, the neck contains cervical vertebrae, muscles, ligaments, joints, vessels, and nerves. All these structures are covered with skin and subcutaneous tissue. Thus, in the ventral region of the neck, one can also expect to find primary tumors of mesenchymal origin such as fibromas, fibrosarcomas, myxomas, myxosarcomas, histiocytic sarcomas, lipomas and liposarcomas, haemangiomas, haemangiosarcomas, perivascular wall tumors (formerly haemangiopericytomas), rhabdomyosarcomas, tumors arising from peripheral nerve sheaths and peripheral neuroblastic

FIGURE 3
Appearance of the tumor on the day of euthanasia.

tumors arising from neural crest (7). Piloleiomyoma and piloleiomyosarcoma have not been described in rats so far (7, 23).

Skin tumors of epithelial origin have also been reported in rats: papilloma and squamous cell carcinoma, basal cell tumor, adenoma and carcinoma of the sebaceous glands, trichoepithelioma, keratoacanthoma, myoepithelioma, as well as those originating from the lymphatic and hematopoietic system - cutaneous lymphoma, mast cell tumor, extramedullary plasmocytoma (7). Spontaneous osteosarcomas have been described in rats, including the vertebral column, and hence, this type of tumor might also be expected in the cervical vertebrae (24). Poorly differentiated sarcomas may have foci of bone metaplasia, which may contribute to misdiagnosis (7).

A small structure called the carotid body (carotid glomus) is found bilaterally near the internal and external carotid arteries. It comprises richly vascularized epithelial tissue and has a chemoreceptor function. The rat's carotid body weighs 60 µg (25). Tumors arising from the glomus are described in humans mainly as benign and painful deformities. There is no literature data regarding the occurrence of this type of lesion in rats.

In addition to neoplastic tumors, abscesses should also be considered in the differential diagnosis of nodular lesions in the neck region in a rat. Most commonly, these are subcutaneous abscesses that arise from skin damage, e.g., due to aggressive behavior between cagemates. Abscesses may be fluctuant and ulcerated. They can also be located in deeper tissues and originate from the organs of the neck. Infection can spread via the hematogenous and the lymphatic routes (1, 2).

In the presented case, a nodule in the ventral region of the neck was detected by a veterinarian during a standard check-up. The neck should be thoroughly palpated during the clinical examination of each patient, although relatively small and deeply located deformities may not be detected. Ultrasound may help determine the origin and extent of a nodular lesion and perform a biopsy.

Histopathological examination initially revealed a malignant myoepithelioma. Two further examinations were performed by a different histopathologist who diagnosed a poorly differentiated sarcoma. In addition, those latter two diagnoses were supported by immunohistochemistry, which ruled out the epithelial and myoepithelial origin of the tumor. However, it was not possible to confirm the vascular origin of the tumor, as indicated by multiple cavities filled with blood and proteinaceous fluid. Suspicion arose that the first diagnosis showing a malignant neoplasm was only a preliminary one, based on H-E examination alone, and it was still insufficient without immunohistochemistry.

Malignant myoepitheliomas are rare, diagnostically challenging biphasic tumors even for an experienced pathologist because of the spindle-shaped morphology of the cells in the malignant "sarcomatous" component, which can resemble sarcoma. On the other hand, it cannot be ruled out that the radiation therapy may have acted as an initiating factor in the development of the sarcoma. Radiation-induced soft tissue sarcomas (RISs) are a rare but potential late side effect of radiotherapy. According to the literature, rats developed mainly lymphomas and soft tissue sarcomas in the areas receiving radiation. Secondary sarcomas were observed at the edge of the irradiation field where the dose was higher. These areas are more prone to uncontrolled, disorganized repair tissue proliferation, leading to an increased risk of cell damage and mutagenesis and, therefore, the development of RIS (26, 27).

In this case, the epithelial-mesenchymal transition (EMT) should also be considered. ETM is essential in embryogenesis and wound healing but can also be involved in pathological processes such as cancer. It can be activated by chronic inflammation and immune disease as well as by repeated tissue trauma disrupting the healing of a wound (28). However, the authors believe it could have been sarcoma from the very beginning. After its surgical removal, the tumor could have recurred near the remaining mandibular salivary gland and the skin.

Low-grade sarcomas have been described in humans, dogs, cats, cattle, pigs, and horses. Clinically, they are rapidly growing, asymptomatic cutaneous or subcutaneous tumors, rarely giving metastases in dogs. However, they are considered to be locally invasive (29). Rapid growth is often accompanied by extensive necrosis (7).

Ideally, the diagnosis should be known before any treatment, including surgical intervention, is implemented. However, this is not easy to achieve in practice. A histological diagnosis can be problematic, especially for undifferentiated and poorly differentiated tumors, due to the tremendous histological heterogeneity of sarcomas and the recent change in nomenclature (23, 29). Cytopathological evaluation of a biopsy taken from the tumor may be helpful as a first step to exclude other possibilities, such as mast cell tumor (30). In human medicine, a fine-needle biopsy is not recommended for diagnosing sarcomas due to the insufficient material obtained with this procedure (31). A histopathological examination enriched by immunohistochemistry with a broad panel of antibodies is necessary to make a definitive diagnosis (23).

Treatment of soft tissue sarcomas is challenging in all animal species, including humans (29). There is a lack of information regarding the treatment of sarcomas in rats. Complete excision of the lesion with wide margins is the mainstay of treatment of metastasis-free lesions (29, 32). Incomplete excision of the tumor or leaving a narrow margin of healthy tissue, especially for poorly differentiated sarcomas, significantly increases the risk of local recurrence. In human and veterinary medicine, re-excision of surgical scar and radiotherapy is recommended (29, 30, 32). Postoperative radiotherapy can prolong the time to local recurrence (32). Perioperative chemotherapy with doxorubicin is effective in humans. It can also be considered an adjunctive treatment in veterinary medicine, though its efficacy in rats has not yet been known (30). Electrochemotherapy is a relatively new therapeutic technique that increases tumor cells' uptake of chemotherapeutic agents such as bleomycin (33).

Due to the tumor's location in the presented case, the possibility of maintaining safe tissue margins was slight from the beginning. Therefore, local recurrence had to be expected (29, 34). It took 2.5 months from the initial detection of the tumor to the emergence of the recurrence. When the recurrence was identified, the tumor was already approximately 2 cm in diameter. A further three surgeries, dictated by the owner's desire to continue the treatment, did not have a long-term effect, as the tumor grew back quite quickly each time.

It should be noted that the patient was in excellent condition most of the time, and his owner reported no distressing symptoms, including pain. Pathological lesions in the neck can induce pressure on the trachea and esophagus, leading to dyspnea, coughing, difficulty swallowing, and regurgitation. After each surgery, the rat awoke quickly and without complications. The recovery period was uneventful, and the patient did not require a protective collar. During treatment, the patient's other problems were adequately addressed an echocardiogram and abdominal ultrasound were performed, pneumonia was treated with antibiotics, and diabetic symptoms were controlled with insulin administration.

Conclusion

The presented case was a starting point for considerations on the differential diagnosis when a nodular lesion is found in the rat's ventral region of the neck. The authors' experience indicates that it usually appears to be a tumor or an abscesses. However, because the neck anatomy is complex, there are many possibilities when it comes to determining its origin. The neck region should be thoroughly palpated during clinical examination of any patient, especially its ventral part. This case also demonstrates how complicated the diagnostic and therapeutic process can be when a nodular lesion is found in the location mentioned above. The main conclusion from this case report is to increase the awareness of veterinary pathologists and oncologists that the final diagnosis should always be part of a broad-spectrum differential diagnosis combining histopathological and immunohistochemical data, including clinical and treatment history.

Diagnosing a malignant tumor in a rat does not necessarily mean a verdict, especially when in conjunction with a dedicated owner. With advances in human and veterinary medicine, new treatment options are emerging. However, their outcomes may have not yet been reported in rats and remain in the field of experimental medicine.

Data availability statement

The original contributions presented in the study are included in the article/supplementary material, further inquiries can be directed to the corresponding author.

Ethics statement

Ethical approval was not required for the studies involving animals in accordance with the local legislation and institutional requirements because this study used client-owned animal. Written informed consent was obtained from the owners for the participation of their animals in this study. Written informed consent was obtained from the owners of the animals for the publication of this case report.

Author contributions

AG: Conceptualization, Resources, Writing – original draft, Writing – review & editing. ID: Resources, Supervision, Writing – review & editing. IB: Resources, Writing – original draft, Writing – review & editing. EC: Resources, Writing – original draft, Writing – review & editing. MP: Resources, Writing – original draft. KR: Writing – review & editing. KB: Supervision, Writing – review & editing.

Funding

The author(s) declare that no financial support was received for the research, authorship, and/or publication of this article.

Acknowledgments

The authors would like to thank DVM Dominika Łyskawińska for her support while writing this article.

Conflict of interest

The authors declare that the research was conducted without any commercial or financial relationships that could be construed as a potential conflict of interest.

Publisher's note

References

1. McDowell RH, Hyser MJ. Neck abscess In: StatPearls. Treasure Island, FL: StatPearls Publishing (2024)

2. Paterson S. Skin diseases of exotic pets. UK: Blackwell Science (2006).

3. Hickman DL, Swan M. Use of a body condition score technique to assess health status in a rat model of polycystic kidney disease. *J Am Assoc Lab Anim Sci*. (2010) 49:155–9.

4. University of Missouri. Radiculoneuropathy. (2024). Available at: https://cvm.missouri.edu/diseases-of-research-animals-dora/rats/radiculoneuropathy/

5. Giknis MLA, Clifford CB. Data from: clinical laboratory parameters for Crl:WI (Han). Wilmington MA: Charles River Laboratories (2008).

6. Popesco P, Rajtova V, Horak J. Atlas Anatomii Małych Zwierząt Laboratoryjnych. Warszawa: PWRiL (2010).

7. Suttie AW. Boorman's pathology of the rat: reference and atlas. *2nd* ed. UK: Academic Press (2018).

8. Nolte T, Brander-Weber P, Dangler C, Deschl U, Elwell MR, Greaves P, et al. Nonproliferative and proliferative lesions of the gastrointestinal tract, pancreas and salivary glands of the rat and mouse. *J Toxicol Pathol*. (2016) 29:1S–125S. doi: 10.1293/tox.29.1S

9. Li Y, Kim HS, Kang MS, Shin SH, Koo KH, Kim CM, et al. A spontaneous epithelial-myoepithelial carcinoma of the submandibular gland in a Sprague-dawley rat. *J Toxicol Pathol*. (2013) 26:67–72. doi: 10.1293/tox.26.67

10. Nishikawa SN, Sano F, Akagi KT, Kada MO, Sugimoto J, Akagi ST. Spontaneous poorly differentiated carcinoma with cells positive for Vimentin in a salivary gland of a young rat. *Toxicol Pathol*. (2010) 38:315–8. doi: 10.1177/0192623309358905

11. Shimada Y, Yoshida T, Takahashi N, Akema S, Soma K, Ohnuma-Koyama A, et al. Poorly differentiated salivary gland carcinoma with prominent squamous metaplasia in a pregnant Wistar Hannover rat. *J Vet Med Sci*. (2016) 78:859–62. doi: 10.1292/jvms.15-0539

12. Tsunenari I, Amate JY, Sakuma S. Poorly differentiated carcinoma of the parotid gland in a six-week-old Sprague-Dawley rat. *Toxicol Pathol*. (1997) 25:225–8. doi: 10.1177/019262339702500213

13. Hosokawa S, Imai T, Hayakawa K, Fukuta T, Sagami F. Parotid gland papillary cystadenocarcinoma in a Fischer 344 rat. *Contemp Top Lab Anim Sci*. (2000) 39:31–3.

14. Ishikawa Y, Nishimori K, Tanaka K, Kadota K. Naturally occurring Mucoepidermoid carcinoma in the submandibular salivary gland of two mice. *J Comp Pathol*. (1998) 118:145–9. doi: 10.1016/s0021-9975(98)80006-6

15. Sumitomo S, Hashimura K, Mori M. Growth pattern of experimental squamous cell carcinoma in rat submandibular glands-an Immunohistochemical evaluation. *Eur J Cancer B Oral Oncol*. (1996) 32B:97–105. doi: 10.1016/0964-1955(95)00080-1

16. Schaudien D, Creutzenberg O, Wagner A, Dahlmann F, Rittinghausen S. Malignant Myoepithelioma of the parotid gland in a rat. *J Comp Pathol*. (2020) 176:162–4. doi: 10.1016/j.jcpa.2020.03.004

17. Sundberg JP, Hanson CA, Roor DR, Brown KS, Bedigian HB. Myoepitheliomas in inbred laboratory mice. *Vet Pathol*. (1991) 28:313–23. doi: 10.1177/030098589102800408

18. Cheuk W, Chan JKC. Advances in salivary gland pathology. *Histopathology*. (2007) 51:1–20. doi: 10.1111/j.1365-2559.2007.02719.x

19. Nakazawa M, Tawaratani T, Uchimoto H, Kawaminami A, Ueda M, Ueda A, et al. Spontaneous neoplastic lesions in aged Sprague-Dawley rats. *Exp Anim*. (2001) 50:99–103. doi: 10.1538/expanim.50.99

20. Hocker SE, Eshar D, Wouda RM. Rodent oncology. *Vet Clin North Am Exot Anim Pract*. (2017) 20:111–34. doi: 10.1016/j.cvex.2016.07.006

21. Bomhard E. Frequency of spontaneous tumors in Wistar rats in 30-months studies. *Exp Toxicol Pathol*. (1992) 44:381–92. doi: 10.1016/S0940-2993(11)80171-5

22. Pucheu-Haston M, Brandão J, Jones KL, Seals SL, Tully TN, Nevarez JG, et al. Zymbal Gland (auditory sebaceous gland) carcinoma presenting as otitis externa in a pet rat (*Rattus norvegicus*). *J Exot Pet Med*. (2016) 25:133–8. doi: 10.1053/j.jepm.2016.03.004

23. Ogawa T, Onozato T, Okuhara Y, Nagasawa T, Tamura T, Hayashi M. Spontaneous cutaneous soft tissue sarcoma with differentiation into fibroblasts in a Sprague-Dawley rat. *J Toxicol Pathol*. (2016) 29:119–24. doi: 10.1293/tox.2015-0069

24. Ruben Z, Rohrbacher E, Miller JE. Spontaneous osteogenic sarcoma in the rat. *J Comp Pathol*. (1986) 96:89–94. doi: 10.1016/0021-9975(86)90025-3

25. Gonzalez C, Almarez L, Obeso A, Rigual R. Carotid body chemoreceptors: from nature stimuli to sensory discharges. *Physiol Rev*. (1994) 74:829–98. doi: 10.1152/physrev.1994.74.4.829

26. Gomarteli K, Fleckenstein J, Kirschner S, Bobu V, Brockmann MA, Henzler T, et al. Radiation-induced malignancies after intensity-modulated versus conventional mediastinal radiotherapy in a small animal model. *Sci Rep*. (2019) 9:15489. doi: 10.1038/s41598-019-51735-3

27. Sheppard DG, Libshitz HI. Post-radiation sarcomas: a review of the clinical and imaging features in 63 cases. *Clin Radiol*. (2001) 56:22–9. doi: 10.1053/crad.2000.0599.

28. Sisto M, Lisi S, Ribatti D. The role of the epithelial-to-mesenchymal transition (EMT) in diseases of the salivary glands. *Histochem Cell Biol*. (2018) 150:133–47. doi: 10.1007/s00418-018-1680-y

29. Hollis AR. Undifferentiated sarcomas in humans and veterinary species. *Equine Vet Educ*. (2023) 35:509–11. doi: 10.1111/eve.13826

30. Cannon CP, Ballo MT, Zagars GK, Mirza AN, Lin PP, Lewis VO, et al. Complications of combined modality treatment of primary lower extremity soft-tissue sarcomas. *Cancer*. (2006) 107:2455–61. doi: 10.1002/cncr.22298

31. Robles-Tenorio A, Solis-Ledesma G. Undifferentiated pleomorphic sarcoma. [updated 2023 Apr 10] In: StatPearls. Treasure Island, FL: StatPearls Publishing (2024)

32. Liptak JM, Christensen NI. Soft tissue sarcomas In: DM Vail, DH Thamm and JM Liptak, editors. Withrow & MacEwen's small animal clinical oncology. *6th* ed. Louis, MO: Elsevier (2020). 404–31.

33. Rangela MMM, Luza JCS, Oliveiraa KD, Ojedab J, Freytag JO, Suzuki DO. Electrochemotherapy in the treatment of neoplasms in dogs and cats. *Austral J Vet Sci*. (2019) 51:45–51. doi: 10.4067/S0719-81322019000200045

34. Widemann BC, Italiano A. Biology and Management of Undifferentiated Pleomorphic Sarcoma, myxofibrosarcoma, and malignant peripheral nerve sheath tumors: state of the art and perspectives. *J Clin Oncol*. (2018) 36:160–7. doi: 10.1200/JCO.2017.75.3467

frontiers | Frontiers in Veterinary Science

TYPE Original Research
PUBLISHED 25 September 2024
DOI 10.3389/fvets.2024.1412552

OPEN ACCESS

EDITED BY
Sokol Duro,
Agricultural University of Tirana, Albania

REVIEWED BY
Maria Pilar Aparisi Gomez,
Auckland District Health Board, New Zealand
Namsoon Lee,
Chungbuk National University,
Republic of Korea

*CORRESPONDENCE
Sang-Kwon Lee
✉ sklee10@knu.ac.kr

RECEIVED 21 May 2024
ACCEPTED 12 September 2024
PUBLISHED 25 September 2024

CITATION
Lee H-W, Lee J-Y, Lee J-Y, Yu S-M, Lee K and Lee S-K (2024) Use of two-point and six-point Dixon MRI for fat fraction analysis in the lumbar vertebral bodies and paraspinal muscles in healthy dogs: comparison with magnetic resonance spectroscopy.
Front. Vet. Sci. 11:1412552.
doi: 10.3389/fvets.2024.1412552

Use of two-point and six-point Dixon MRI for fat fraction analysis in the lumbar vertebral bodies and paraspinal muscles in healthy dogs: comparison with magnetic resonance spectroscopy

Hye-Won Lee[1], Ji-Yun Lee[1], Joo-Young Lee[1], Seung-Man Yu[2], Kija Lee[1] and Sang-Kwon Lee[1]*

[1]Department of Veterinary Medical Imaging, College of Veterinary Medicine, Kyungpook National University, Daegu, Republic of Korea, [2]Department of Radiological Science, College of Medical Sciences, Jeonju University, Jeonju, Republic of Korea

Introduction: Fatty degeneration of the vertebral bodies and paravertebral muscles is associated with the presence, severity, and prognosis of spinal disease such as intervertebral disc degeneration. Therefore, the fat fraction (FF) of the vertebral bodies and paraspinal muscles has been considered a potential biomarker for assessing the pathophysiology, progression, and treatment response of spinal disease. Magnetic resonance spectroscopy (MRS) is considered the reference standard for fat quantification; however, it has limitations of a long acquisition time and is technically demanding. Chemical shift-encoding water-fat imaging, called the Dixon method, has recently been applied for rapid fat quantification with high spatial resolution. However, the Dixon method has not been validated in veterinary medicine, and we hypothesized that the Dixon method would provide a comparable assessment of the FF to MRS but would be faster and easier to implement in dogs.

Methods: In this prospective study, we assessed the FF of the lumbar vertebral bodies and paravertebral muscles from the first to sixth lumbar vertebrae using MRS, the two-point Dixon method (LAVA-FLEX), and the six-point Dixon method (IDEAL-IQ) and compared these techniques.

Results and discussion: The FFs of vertebral bodies and paravertebral muscles derived from LAVA-FLEX and IDEAL-IQ showed significant correlations and agreement with those obtained with MRS. In particular, the FFs obtained with IDEAL-IQ showed higher correlations and better agreement with those obtained with MRS than those derived by LAVA-FLEX. Both Dixon methods showed excellent intra- and interobserver reproducibility for FF analysis of the vertebral bodies and paraspinal muscles. However, the test–retest repeatability of vertebral body and paraspinal muscle FF analysis was low for all three sequences, especially for the paraspinal muscles. The results of this study showed that LAVA-FLEX and IDEAL-IQ have high reproducibility and that their findings were highly correlated with the FFs of the lumber vertebral bodies and paraspinal muscles determined by MRS in dogs. The FF analysis could be performed much more easily and quickly using LAVA-FLEX and IDEAL-IQ than using MRS. In conclusion, LAVA-FLEX and IDEAL-IQ can be used as routine procedures in spinal magnetic resonance imaging in dogs for FF analysis of the vertebral bodies and paraspinal muscles.

KEYWORDS

canine, chemical shift, intervertebral disc disease, magnetic resonance imaging, myosteatosis

1 Introduction

Intervertebral disc disease (IVDD) is a common spinal disease in dogs and probably the most common condition for performing spinal magnetic resonance imaging (MRI) in dogs (1). Although the mechanism of IVDD has not been elucidated, fatty infiltration of the vertebral bodies and paravertebral muscles May have a significant effect on the onset, progression, severity, and prognosis of IVDD (2–7). In humans, in addition to evaluating the disc and spinal cord, evaluation of fatty degeneration of the spine and paravertebral muscles using MRI has been widely performed for various spinal diseases including IVDD (8, 9). Those studies have revealed that fat quantification using MRI is correlated with histological examination findings and is associated with presence, severity, and prognosis of spinal disease.

In canine spinal MRI, assessment primarily focuses on disc degeneration, herniation, and spinal cord changes to diagnose IVDD. A few studies on fat assessment of the vertebral bodies and paraspinal muscles in dogs with IVDD have been conducted (4–7, 10, 11). Some studies have evaluated changes in the paravertebral muscles using cross-sectional areas of these muscles on computed tomography, but this method is time consuming and nonspecific for fatty degeneration (10, 11). Other studies have used MRI for assessing fatty degeneration of the paraspinal muscles. However, most studies conducted qualitative or quantitative evaluations based on cross-sectional areas of muscles or the signal changes on T1-weighted or short tau inversion recovery images, which is subjective and difficult when evaluating for diffuse changes (4–6).

There are two primary techniques for fat analysis using MRI in humans including magnetic resonance spectroscopy (MRS) and chemical shift imaging such as the Dixon method. Among them, MRS has been considered the gold standard for fat quantification (12, 13). However, the use of MRS is limited in clinics due to its long acquisition time, technically demanding nature, and associated sampling errors that lead to low spatial resolution (13–15). Chemical shift-encoding water-fat imaging, called the Dixon method, has recently been applied for rapid fat quantification with high spatial resolution (10, 12, 14). It acquires both in-phase (water + fat) and out-phase (water – fat) images and provides a series of four images including in-phase, out-phase, fat-only, and water-only images. The two-point Dixon method was traditionally used, but variants of the Dixon technique such as IDEAL-IQ have been developed to provide more consistent separation of fat and water signals (16, 17).

While several studies have demonstrated the accuracy of the Dixon method and its high clinical applicability for evaluating fat quantification in the spine and paravertebral muscles in humans, research in dogs remains limited (2, 3, 8, 9). To the best of author's knowledge, only one study has applied the two-point Dixon technique to assess paraspinal muscle myosteatosis in dogs with IVDD. This study revealed an association between myosteatosis in the multifidus muscle and outcomes (7). Because fat quantification MRI can be influenced by various factors such as the composition or size of the field of view, it is crucial to establish the accuracy, reproducibility, and repeatability before applying it in small dogs. The purpose of this study was to evaluate the feasibility of the traditional two-point Dixon method and a more recently developed six-point Dixon method compared with gold standard of MRS for fat fraction (FF) analysis of the vertebral bodies and paravertebral muscles in healthy dogs.

2 Materials and method

2.1 Animals

This study was a prospective experimental study. In this study, six purpose-bred beagles, including four intact female and two intact male dogs, were used. The median age of the dogs was 3 years (1–5 years), and the median weight was 13.4 kg (12.0–14.8 kg). All dogs were regarded as clinically healthy based on a physical examination, complete blood count, serum biochemistry, and thoracic and abdominal radiographs. The study protocol was authorized by the Institutional Animal Care and Use Committee at Kyungpook National University. The protocol for the care of the dogs adhered to the Guidelines for Animal Experiments of Kyungpook National University (No. KNU 2023–0590). Each laboratory beagle dog was housed in an individual pen and had no history of low back pain, spinal surgery, or metallic implant placement.

2.2 MRI acquisition

The dogs were fasted for 24 h prior to anesthesia induction for MRI. A 22-gauge catheter was placed into the cephalic vein, and 0.03 mg/kg of medetomidine (Medetin, 1 mg/mL, Dongbang, Gyeonggi-do, Korea) and 1 mg/kg of alfaxalone (Alfaxan®, 10 mg/mL, Careside, Gyeonggi-do, Korea) were administered to each dog. An endotracheal tube was placed, and anesthesia was maintained with isoflurane (Ifran®, 2–3%, Hana Pharm, Seoul, Republic of Korea) and oxygen (1–2 L/min). General anesthesia and breathing were controlled with a ventilator. Isotonic saline solution (0.9% NaCl, 3 mL/kg/h, JW Life Science, Seoul, Republic of Korea) was administered intravenously for the duration of the procedure.

All lumbar MRI images were obtained in dorsal recumbency with a 1.5-T MRI (Signa Explorer; GE Healthcare, Wisconsin, United States) using a 16-channel flex coil (GEM flix coil 16-M Array; GE Healthcare). After obtaining three-dimensional T1-weighted (T1W) sequences as a localizer, three-orthogonal T2-weighted (T2W) images covering the 11th thoracic vertebra to the sacrum including sagittal, transverse, and dorsal planes were obtained.

2.3 LAVA-FLEX, IDEAL-IQ, and MRS acquisition for FF of the vertebral bodies and paraspinal muscles

Based on the sagittal, transverse, and dorsal plane T2W images, fat quantification scanning was performed with three different sequences including the two-point Dixon method (LAVA-FLEX; GE Healthcare), the six-point Dixon method (IDEAL-IQ; GE Healthcare), and MRS. MRS was used as a reference standard for fat quantification in this study. Detailed parameters for each sequence are shown in Tables 1, 2. For LAVA-FLEX and IDEAL-IQ, both the sagittal plane in the centre of the lumbar spine and the transverse plane at the centre of the lumbar vertebral midbodies from L1–L6 were acquired for evaluating the vertebral bodies and paraspinal muscles, respectively. Both sequences automatically reconstructed fat signal-only, water signal-only, in-phase, and out-phase images. The IDEAL-IQ additionally provided an automatically calculated FF map (fat signal/fat signal + water signal) on the MRI machine workstation (Signa Explorer; GE Healthcare).

TABLE 1 Acquisition parameters of LAVA-FLEX and IDEAL-IQ for FF quantification of the lumbar vertebral bodies and paravertebral muscles.

Imaging parameters	LAVA-FLEX (two-point Dixon)		IDEAL-IQ (six-point Dixon)	
	Vertebra body	Muscle	Vertebra body	Muscle
Orientation	Sagittal	Transverse	Sagittal	Transverse
Repetition time (msec)	6	6	20	23
Echo time (msec)	2.1, 4.2	2.1, 4.2	3.5, 5.5, 7.4, 9.4, 11.4, 13.3	3.4, 5.4, 7.3, 9.3, 11.2, 13.2
Field of view (mm)	280 × 280	280 × 280	280 × 280	280 × 280
Matrix size	160 × 160	160 × 160	140 × 140	140 × 140
Section thickness (mm)	6.0	4.0	6.0	4.0
Intersection gap (mm)	0	0	0	0
No. of sections	40	40	40	40
Flip angle (degree)	12	12	5	5
No. of signals acquired	2	2	8	8
Bandwidth (kHz)	62.5	62.5	100	100
Imaging time (sec)	106	108	155	156

FF; fat fraction.

TABLE 2 Acquisition parameters of MRS for FF quantification of the lumbar vertebral bodies and paravertebral muscles.

Parameters	Vertebral bodies	Paravertebral muscles
Sequence type	Stimulated echo acquisition mode (STEAM)	
Repetition time (msec)	3,000	3,000
Echo time (msec)	35	35
Number of averages	32	32
Acquisition voxel (mm)	4.0 × 6.0 × 15.0	4.0 × 15.0 × 15.0
Number of signals acquisition	8	8
Imaging time (sec)	168	168

FF; fat fraction, MRS; magnetic resonance spectroscopy.

To acquire MRS as a standard of reference, single-voxel stimulated echo acquisition mode (STEAM) was used. Based on the three-orthogonal T2W images, multiple single spectroscopy voxels were positioned in the center of the lumbar vertebral bodies and paraspinal muscles from L1 to L6 (Figure 1). For the vertebral bodies, a voxel size of 4.0 × 6.0 × 15.0 mm was used. This voxel size was set to the largest size that does not include the cortical bone and surrounding muscles to prevent errors on MRS due to low signal-to-noise ratio. For the paraspinal muscles, a voxel was positioned in the left epaxial muscle at the level of each vertebral midbody using a voxel size of 4.0 × 15.0 × 15.0 mm. The voxels of the paravertebral muscles were set to the largest so that all sides of the voxels were surrounded by the muscles without including adjacent subcutaneous fat. Both the longissimus lumborum and iliocostal muscles were included because it was difficult to distinguish the fascial boundaries between these muscles in some cases.

2.4 FF analysis with LAVA-FLEX and IDEAL-IQ

The LAVA-FLEX and IDEAL-IQ images were analyzed on Picture Archiving and Communication System workstations (INFINITT; Infinitt Healthcare, Seoul, Korea). In LAVA-FLEX images, the FF was measured using fat signal-only images and in-phase images (fat + water signal) as follows: FF = fat signal / (fat + water signal). In IDEAL-IQ, the FF was measured using an automatically calculated FF map.

To evaluate the FF of the lumbar vertebral bodies, rectangular regions of interest (ROIs) (4.0 × 15.0 mm) were drawn on sagittal images centred on the lumbar vertebral bodies to exclude the cortical bone and paraspinal muscle (Figures 2A,C,E). To assess the FF of the paraspinal muscles, rectangular ROIs (15.0 × 15.0 mm) were drawn in the left epaxial muscles where it is surrounded by muscle at the level of each vertebral midbody (Figures 2B,D,F). We recorded the x, y, and z axis information of the MRS voxel range, then when drawing ROIs of the vertebral bodies and paraspinal muscles in LAVA-FLEX and IDEAL-IQ images, the evaluation area of ROIs was made to match the MRS voxels. In LAVA-FLEX, the ROIs drawn on the fat signal-only images were copied and pasted to the in-phase images to create the same ROI.

2.5 FF analysis in MRS

All spectroscopy images were processed using a commercial spectroscopy tool (LCModel version 6.3; LCModel Inc., Oakville, Canada), which involves post-processing and quantifications including noise filtering, apodization, baseline, phase correction, signal fitting of the peaks within the acquired spectra, and integration to determine the area under each spectral peak of interest. In the spectra, integrated signal intensity in the spectral regions of 0.5–2.0 ppm was assigned to fat, and 4.0–5.4 ppm was assigned to water. The FF was calculated as the ratio of fat peak areas to the sum of fat peak and water peak areas (14).

2.6 Reproducibility and test–retest repeatability test

To assess the test–retest repeatability of FF analysis using LAVA-FLEX, IDEAL-IQ, and MRS, the same experiment protocol was

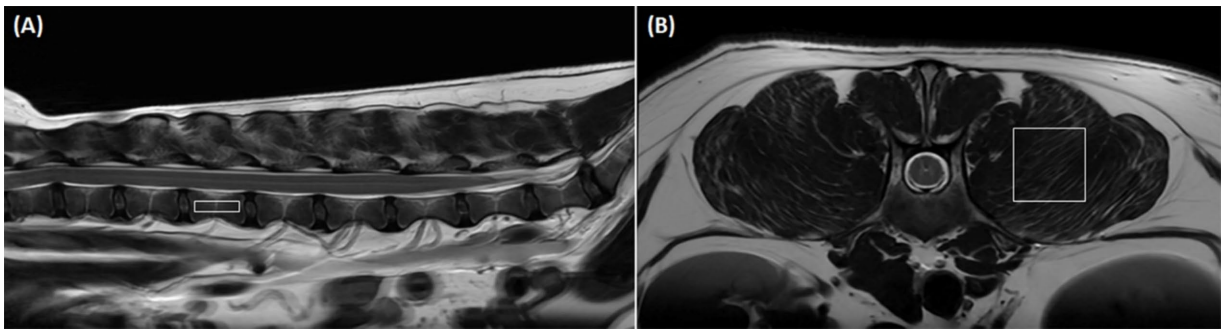

FIGURE 1
Positioning of the voxel in magnetic resonance spectroscopy (MRS) to analyze the fat fraction (FF) in the lumbar vertebral bodies and paraspinal muscles. **(A)** Shows a representative sagittal image of voxel positioning for vertebral body FF measurement with MRS. A voxel (4.0 × 6.0 × 15.0 mm) is positioned in the center of the lumbar vertebral body without including cortical bone and the paraspinal muscles based on transverse, sagittal, and dorsal images. **(B)** Shows a representative transverse image of voxel positioning for paraspinal muscle FF measurement with MRS. A voxel (4.0 × 15.0 × 15.0 mm) is positioned in the left epaxial muscles at the level of the vertebral midbody without including adjacent subcutaneous muscles based on transverse, sagittal, and dorsal images.

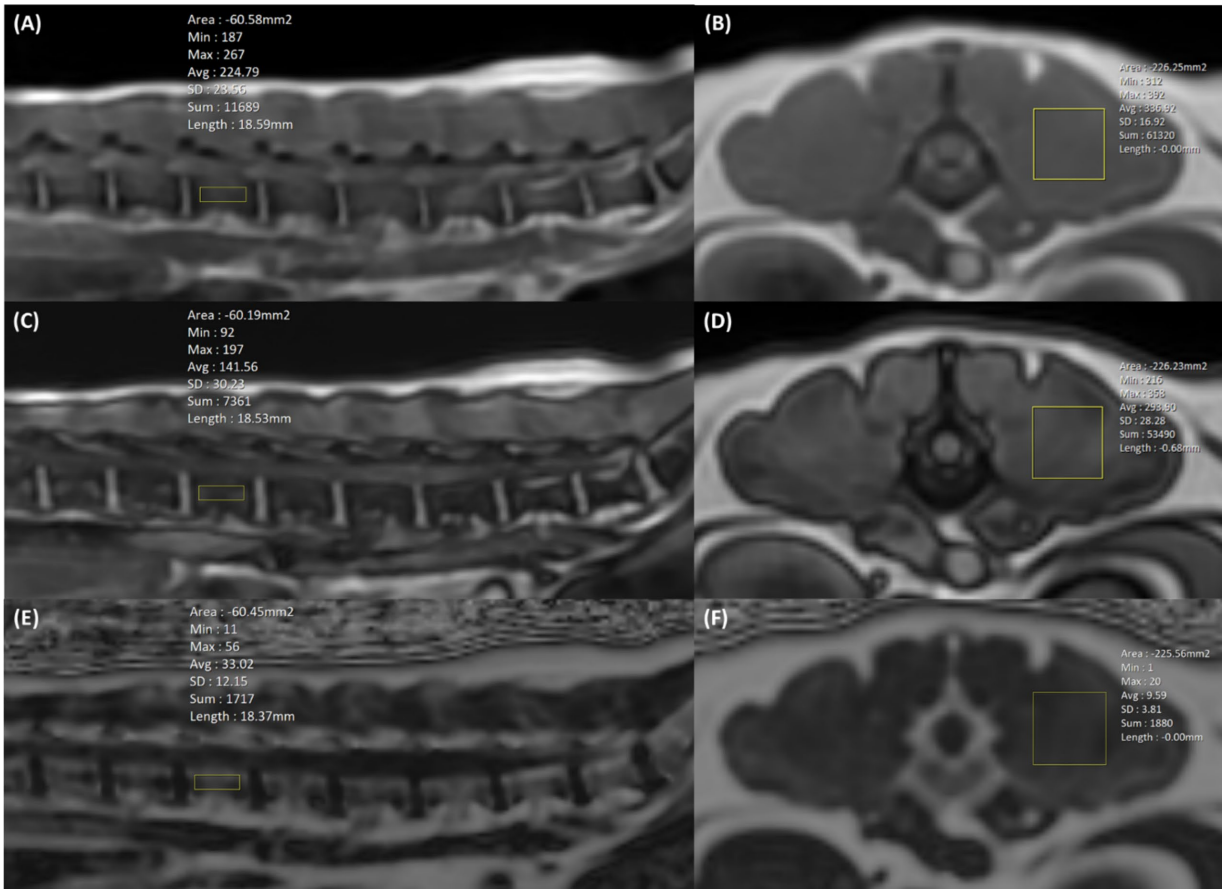

FIGURE 2
Positioning of the region of interest (ROI) in LAVA-FLEX **(A–D)** and IDEAL-IQ **(E,F)** to analyze the fat fraction (FF) in the lumbar vertebral bodies and paraspinal muscles. In LAVA-FLEX, the same two ROIs were used in in-phase **(A,B)** and out-phase images **(C,D)**, and in IDEAL-IQ, one ROI was used in the FF map **(E,F)**. In LAVA-FELX and IDEAL-IQ, a 4.0 × 15.0 mm ROI is positioned in the sagittal plane for vertebral body FF analysis, and a 15.0 × 15.0 mm ROI is positioned in the transverse plane for paraspinal muscle FF analysis. The ROIs of the vertebral bodies and paraspinal muscles were matched as closely as possible to the voxel from magnetic resonance spectroscopy (MRS).

performed again with a one-week interval and analyzed with the same methods as the first examination.

To evaluate the intra- and interobserver reproducibility of the LAVA-FLEX and IDEAL-IQ, one examiner (H-WL) analyzed the LAVA-FLEX and IDEAL-IQ images in the first exam three times, and three different examiners (H-WL, J-YL, J-YL) independently performed an analysis of the LAVA-FLEX and IDEAL-IQ without knowing the MRS results and each other's results. When measuring reproducibility, the ROI was drawn subjectively using the same ROI criteria without the location information of the MRS voxel; 4.0 × 15.0 mm ROIs were drawn on sagittal images centred on the lumbar vertebral bodies to exclude the cortical bone and paraspinal muscle for vertebral body analysis and 15.0 × 15.0 mm ROIs were drawn in the left epaxial muscles where it is surrounded by muscle at the level of each vertebral midbody. The reproducibility of MRS was not evaluated because MRS was analyzed using the program and did not depend on the examiner.

2.7 Statistical analysis

All continuous values are reported as means ± standard deviations (SDs). All statistical calculations were performed using IBM SPSS Statistics (SPSS 25.0, IBM SPSS statistics, New York, United States). Normality was assessed using the Kolmogorov–Smirnov test. In the analysis, the comparison between MRS and Dixon used Dixon data where ROIs were drawn consistent with MRS voxels based on MRS location information. To evaluate the difference in the FFs of the lumbar vertebral bodies and paraspinal muscles derived from MRS according to the sites and the differences among MRS, LAVA-FLEX, and IDEAL-IQ, the Friedman test and Wilcoxon signed-rank test were used. To assess the correlation and agreement between LAVA-FLEX and IDEAL-IQ and the reference standard of MRS, Spearman's correlation, linear regression, and the intraclass correlation coefficient (ICC) analyses were performed. It was considered statically significant if the p-value was less than 0.05 ($p < 0.05$). The following criteria were used to analyze the ICC: excellent (≥0.90), good (= 0.75 to 0.89), fair (0.50 to 0.74), and poor (<0.50) (1). The difference between each sequence was analyzed using Bland–Altman analysis.

The intra- and interobserver reproducibility of LAVA-FLEX and IDEAL-IQ were evaluated using the results of the first examination by calculating the ICC. The test–retest repeatability of fat quantification with MRS, LAVA-FLEX, and IDEAL-IQ was evaluated by assessing the difference in values between two separate scans and calculating the coefficient of variation (CV) and by Bland–Altman analysis. The CV was interpreted according to the following definitions: excellent (<10%), good (10 to 20%), acceptable (21 to 30%), and poor (>30%) (18).

3 Results

3.1 FFs of the lumbar vertebrae and paraspinal muscles according to each lumbar site

All MRI scans were performed without any complications in all dogs. Figure 3 shows the FF of the lumbar vertebral bodies and paraspinal muscles at each lumbar site derived from MRS. The FFs of the lumbar vertebral bodies were significantly different between the sites; the FFs of the caudal lumbar spine tended to be higher than those of the cranial lumbar spine (Table 3). There was no significant difference in the FFs of the paraspinal muscles according to the sites.

3.2 Comparison between MRS, LAVA-FLEX, and IDEAL-IQ

Figure 4 shows FFs of the lumbar vertebral bodies and paraspinal muscles at each lumbar site derived from MRS, LAVA-FLEX, and IDEAL-IQ. For the FFs of the vertebral bodies, there was no significant difference among the three sequences except for the FF of the 5th lumbar vertebral body (Table 4). The average FF of the vertebral bodies was significantly different between sequences, showing highest value with LAVA-FLEX and the lowest value with MRS. The paraspinal muscle FFs were significantly different between sequences at all sites; they were the lowest with LAVA-FLEX and the highest with MRS. The average FFs of the paraspinal muscles showed the same pattern.

Although the absolute FFs of the vertebral bodies and paraspinal muscles did not match between the sequences, there was a significant correlation between each sequence. The correlation and agreement between LAVA-FLEX and IDEAL-IQ compared with MRS are shown in Table 5. IDEAL-IQ showed higher correlation and agreement with MRS for the FFs of the lumbar vertebral bodies and paraspinal muscles than LAVA-FLEX. A linear regression results showed a significant linear relationship between the FFs derived with LAVA-FLEX and MRS and between IDEAL-IQ and MRS (Figure 5).

3.3 Reproducibility and test–retest repeatability

Table 6 shows the intra- and interobserver reproducibility of the FF analysis using LAVA-FLEX and IDEAL-IQ. All the FFs showed an excellent inter- and intraobserver reproducibility. Table 7 summarizes the differences, CVs, Bland–Altman analysis, and ICCs of the FFs derived with LAVA-FLEX, IDEAL-IQ and MRS between the first and second scans. The FFs of the vertebral bodies derived from IDEAL-IQ and the FFs of the vertebral bodies and paraspinal muscles derived from MRS showed significant differences between the first and second scans. The general test–retest repeatability was low for all sequences; in particular, the paraspinal muscle FFs showed poor test–retest repeatability.

4 Discussion

In this study, LAVA-FLEX and IDEAL-IQ showed excellent correlation and agreement with MRS for evaluating the FFs of the lumbar vertebral bodies and paraspinal muscles, which is consistent with the findings of previous human studies (12–15). However, the absolute FFs derived from LAVA-FLEX and IDEAL-IQ did not exactly match those derived from MRS, particularly in the paraspinal muscles. Our results showed that LAVA-FLEX and IDEAL-IQ slightly overestimated the FFs of the vertebral bodies, while they

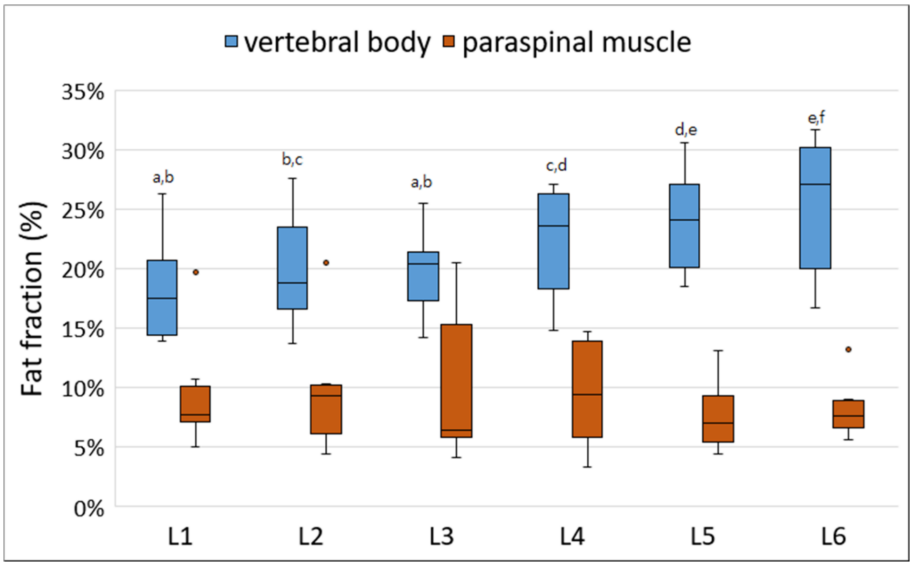

FIGURE 3
Box-and-whisker plots of fat fraction (FFs) for vertebral bodies and paraspinal muscles derived from magnetic resonance spectroscopy. The boxplot shows the range in data between the 25th and 75th quantiles within the box, line within box indicates median, and outliers are indicated by points. Different lower-case letters, which are at the top of the box plot, indicate significant differences between groups (a–f; $p < 0.05$). The FFs of the lumbar vertebral bodies were significantly different according to the lumbar levels; the FFs of the caudal lumbar spine tended to be higher than those of the cranial lumbar spine. There was no significant difference in the FFs of the paraspinal muscles according to the lumbar levels.

TABLE 3 Fat fracction of the lumbar vertebral bodies and paraspinal muscles derived from MRS according to each lumbar site.

Fat fraction (%)	Lumbar site						*P*-value
	L1	L2	L3	L4	L5	L6	
Vertebral body	18.41 ± 4.85^{a}	$20.01 \pm 5.26^{b,c}$	$19.77 \pm 3.99^{a,b}$	$22.15 \pm 5.17^{c,d}$	$24.03 \pm 4.84^{d,e}$	$25.25 \pm 6.42^{e,f}$	< 0.001
Paraspinal muscle	9.67 ± 5.24	9.84 ± 5.76	10.23 ± 7.11	9.49 ± 4.92	7.78 ± 3.26	8.29 ± 2.75	0.470

The data shown are reported as the mean ± standard deviation. $^{a-f}$ Within a column, values with different superscript letters differ significantly ($p < 0.05$). FF, fat fraction; MRS, magnetic resonance spectroscopy.

underestimated the FFs of the paravertebral muscles compared with the MRS. Although the exact cause of the difference between LAVA-FLEX or IDEAL-IQ and MRS is unknown, it May be explained by the multiple confounding factors for FF analysis in this study such as T2* effects, magnetic field inhomogeneity, T1 effects, the presence of multiple peaks in the fat spectrum, and eddy current effects (14, 19–23).

Among the aforementioned confounding factors, the T2* effect is an important factor in fat quantification of the vertebral bodies using MRS (14, 23). Vertebral bone marrow is comprised of trabecular bone, which is the principal source of magnetic field inhomogeneities in the vertebral bodies (24, 25). Magnetic field inhomogeneities shorten the T2* relaxation time of both water and fat components, which broadens the widths of water and fat peaks in MRS (14). As the widths of water and fat peaks become wider, they overlap, and the fat adjacent to water peak is obscured by the water, which leads to underestimation of the FF (14). Compared with MRS, the T2* effect from trabecular bone has a negligible contribution to the signal at gradient echo sequences such as LAVA-FLEX and IDEAL-IQ (14). Therefore, the T2* shortening effect of the trabecular bone May have affected the FFs derived from MRS, resulting in differences in the FFs of the lumbar vertebrae among LAVA-FLEX, IDEAL-IQ, and MRS in this study. Similar to our findings, previous human studies have shown that bone marrow FFs derived from MRS without considering T2* effects were lower than those measured by the Dixon technique (14). Unlike the vertebral bodies, it was thought that there was little T2* effect when evaluating the paraspinal muscle FFs using MRS because there no substance with a large T2* effect was present.

With the Dixon technique, such as LAVA-FLEX and IDEAL-IQ, T1 effects can affect FF measurement. Both LAVA-FLEX and IDEAL-IQ use a very short repetition time. The T1 relaxation time of water is significantly slower than that of fat; therefore, the signal of water May deteriorate as it is exposed to repetitive radiofrequency pulse before the signal is fully recovered due to the short repetition time (19, 20). Although efforts are made to compensate for this by using a low flip angle, the T1 relaxation effect May reduce water signal and contribute to overestimation of FFs with LAVA-FLEX or IDEAL-IQ compared with MRS (19, 20). This T1 effect could explain the overestimation of the vertebral body FF with LAVA-FLEX or IDEAL-IQ compared with MRS, but it is difficult to explain underestimation of paravertebral muscle FF in LAVA-FLEX and IDEAL-IQ. Additionally, when comparing LAVA-FLEX and IDEAL-IQ, LAVA-FLEX had a shorter repetition time and a higher flip angle, which would have resulted in a greater T1 effect and higher fat measurement. However, our results did

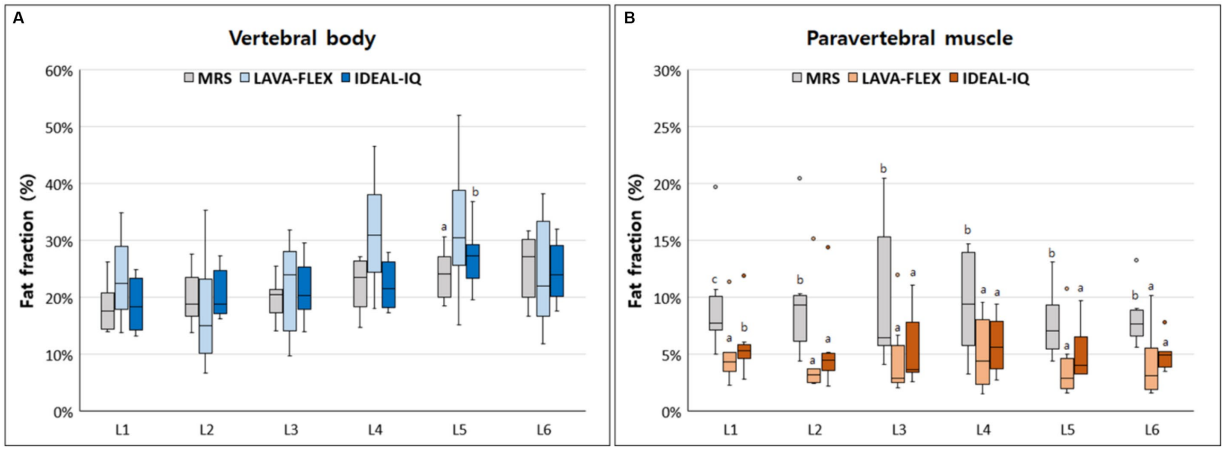

FIGURE 4
Box-and-whisker plots of fat fractions for **(A)** vertebral bodies and **(B)** paraspinal muscles derived from magnetic resonance spectroscopy (MRS), LAVA-FLEX and IDEAL-IQ. The boxplot shows the range in data between the 25th and 75th quantiles within the box, line within box indicates median, and outliers are indicated by points. Different lower-case letters, which are at the top of the box plot, indicate significant differences between groups (a, b, c; $p < 0.05$).

TABLE 4 Comparison among LAVA-FLEX, IDEAL-IQ, and MRS for FF quantification of the lumbar vertebral bodies and paraspinal muscles.

Fat fraction (%)	Site	MRS	LAVA-FLEX	IDEAL-IQ	*P*-value
Vertebral body	L1	18.41 ± 4.85	23.53 ± 8.11	18.80 ± 5.33	0.135
	L2	20.01 ± 5.26	17.75 ± 10.86	20.77 ± 4.90	0.846
	L3	19.77 ± 3.39	21.64 ± 9.13	21.41 ± 5.84	0.607
	L4	22.15 ± 5.17	31.52 ± 10.82	22.18 ± 4.68	0.223
	L5	24.03 ± 4.84^{a}	32.26 ± 12.90^{a}	27.18 ± 6.05^{b}	0.042
	L6	25.25 ± 6.42	24.37 ± 10.88	24.54 ± 5.86	0.846
	Average	21.60 ± 5.36^{a}	25.18 ± 11.10^{b}	22.48 ± 5.76^{b}	0.021
Paraspinal muscle	L1	9.67 ± 5.24^{c}	5.16 ± 3.22^{a}	5.97 ± 3.13^{b}	0.002
	L2	9.84 ± 5.76^{b}	5.04 ± 4.98^{a}	5.70 ± 4.39^{a}	0.009
	L3	10.23 ± 7.11^{b}	4.81 ± 3.90^{a}	5.57 ± 3.59^{a}	0.006
	L4	9.49 ± 4.92^{b}	5.13 ± 3.48^{a}	5.85 ± 2.72^{a}	0.009
	L5	7.78 ± 3.26^{b}	4.18 ± 3.47^{a}	5.24 ± 2.66^{a}	0.042
	L6	8.29 ± 2.75^{b}	4.34 ± 3.33 ^{a}	5.00 ± 1.58^{a}	0.009
	Average	9.22 ± 4.77^{c}	4.77 ± 3.52^{a}	5.55 ± 2.92^{b}	<0.001

The data shown are reported as the mean ± standard deviation. $^{a-c}$ Within a column, values with different superscript letters differ significantly ($p < 0.05$). FF; fat fraction, MRS; magnetic resonance spectroscopy.

not reflect this. Therefore, in this study, we believed that the T1 effect was not a major factor that contributed to the fat quantification.

In a previous human study, Dixon techniques tended to underestimate the FFs in organs with low FFs (13). In low fat content regions, image noise can have a significant impact on FFs due to a low signal to noise ratio. Therefore, the Dixon technique May have underestimated FFs due to errors from low signal values and image noise at the low FF sites (26). In our study, the FFs of the paraspinal muscles were low (< 10%) compared with those of the lumbar vertebral bodies (> 20%), and the image noise of the paraspinal muscles with LAVA-FLEX or IDEAL-IQ might be a cause of underestimation of the paraspinal muscle FFs compared with those derived from MRS. In this study, an analysis of image quality, such as signal-to-noise, was not conducted, and further studies are needed to evaluate the relationships among signal, noise, and FF value.

Although the absolute FFs derived from LAVA-FLEX or IDEAL-IQ did not completely match with those determined with MRS, LAVA-FLEX and IDEAL-IQ showed high correlation with MRS for both vertebral body and paraspinal muscle FF assessment. In particular, IDEAL-IQ showed a higher correlation and better agreement with MRS than LAVA-FLEX, which was consistent with the findings of human studies (11, 27). IDEAL-IQ, the 6-point Dixon technique, is thought to be more accurate for FF analysis than the 2-point Dixon-based LAVA-FLEX. There are several advantages of the multi-point Dixon technique compared with the traditional 2-point Dixon technique. The multi-point acquisition offers better chances to

TABLE 5 Correlation and agreement between LAVA-FLEX and IDEAL-IQ compared with MRS for FF quantification of the lumbar vertebral bodies and paraspinal muscles.

Parameter	Sequences	Correlation	Agreement			Bland–Altman analysis	
		r	*P*-value	ICC	*P*-value	Bias	95% LOA
Vertebral body	LAVA-FLEX vs. MRS	0.437	0.008	0.542	< 0.05	−3.6	−22.7 to 15.6
	IDEAL-IQ vs. MRS	0.859	< 0.001	0.915	< 0.01	−0.9	−6.9 to 5.2
Paraspinal muscle	LAVA-FLEX vs. MRS	0.750	< 0.001	0.885	<0.01	4.4	−0.8 to 9.7
	IDEAL-IQ vs. MRS	0.888	< 0.001	0.911	< 0.01	3.7	−0.8 to 8.1

FF, fat fraction; ICC, intraclass correlation coefficient; LOA, limits of agreement; MRS, magnetic resonance spectroscopy.

correct for the T2* effect, magnetic field inhomogeneity, and eddy currents effects. The multi-point acquisition requires a slightly longer repetition time, which increases signal-to-noise ratio and reduces T1 relaxation effects. However, a longer repetition time has the disadvantage of increasing the scan time. In this study, IDEAL-IQ took approximately 50 s longer than LAVA-FLEX. However, considering that both sequences could be acquired in less than 3 min and that IDEAL-IQ provides FF maps to reduce the analysis time, this small scan time difference is thought be negligible in clinical practice.

Both LAVA-FLEX and IDEAL-IQ had excellent intra- and interobserver reproducibility for vertebral body and paraspinal muscle FF evaluation. This means that when repetitive ROIs are drawn using the same criteria, even if the ROIs do not completely match, they have similar values and can be used clinically. IDEAL-IQ automatically provides an FF map; therefore, only one ROI is needed to measure the FF, but LAVA-FLEX requires that two of the same ROIs to be drawn separately on the fat-only and in-phase images. Therefore, we expected that LAVA-FLEX May show lower reproducibility than IDEAL-IQ, but the reproducibility of the two sequences was similar. This was thought to be because in this study, when drawing two ROIs on a fat-only image and an in-phase image with LAVA-FLEX, we copied one ROI and pasted it on the other image. Moreover, we expected that the reproducibility of paraspinal muscle FFs might be lower than that of the vertebral body FFs because the muscles are not square in shape and have unclear landmarks and margins compared with bone; however, the reproducibility of the FFs for the vertebral bodies and muscles were similar. This was thought to have reduced errors in ROI placement in this study. For accurate comparison with MRS, the ROI was set and analyzed based on the MRS voxel when setting the ROI location for the paraspinal muscles in LAVA-FLEX and IDEAL-IQ in this study.

Unlike their high reproducibility, MRS, LAVA-FLEX, and IDEAL-IQ all had low test–retest repeatability for both vertebral body and paraspinal muscle FF assessment. The test–retest repeatability was the lowest for LAVA-FLEX among the sequences. Although, in this study, the same criteria were used for the first and second examination when setting up voxels for MRS or drawing ROIs for LAVA-FLEX and IDEAL-IQ, but there May have been differences in the scan plane, dog's position, or setting of voxel or ROIs between first and second examination. However, these factors cannot be completely controlled in clinical practice. The paravertebral muscle FF assessment showed lower test–retest repeatability than that for the vertebral bodies, and there are several possible reasons for this finding. In this study, the voxel size of MRS and the analysis ROI in Dixon methods were larger in the paravertebral muscle than the vertebral body, which May have lowered repeatability. Unlike vertebral body, muscle is a flexible tissue that deforms easily between two scans, especially under anesthesia. Thus, repositioning the same voxel placement exactly as it was for the previous scan is more challenging for the paravertebral muscles than for the vertebral bodies. Moreover, the paravertebral muscle FF can shift depending on the shape and orientation of muscle (28). In addition, the anatomical muscle region used in the analysis May have affected the test–retest repeatability. In this study, when assessing the paraspinal muscle FF, voxels in MRS or ROIs in LAVA-FLEX and IDEAL-IQ May have contained two adjacent muscles rather than one specific muscle. This was because when setting up the voxel for MRS, it was difficult to evaluate a single muscle considering the square shape of the voxel and the size of voxel to obtain a sufficient signal. The inclusion of fascial boundaries and intermuscular fat May have contributed to the heterogeneity in analysis in this study. Since the scan plane and the dog's position cannot be entirely controlled during repeated scans, the optimal strategy to enhance repeatability May involve controlling the analysis of the ROI. In particular, LAVA-FLEX and IDEAL-IQ allow ROIs to be drawn freely regardless of their size and shape, making it easy to set an ROI for specific muscles. Further research focusing on repeatability using ROIs for specific muscles is needed.

When evaluating the FFs of the lumbar vertebrae and paraspinal muscles, it is important to know the physiological variance among healthy subjects. In humans, fatty infiltration can be affected by various factors such as the anatomical site, sex, age, obesity, and hormones; therefore, these factors should be considered when interpreting the FF (29–35). In this study, the FFs of the caudal lumbar vertebral bodies tended to be higher than those of the cranial lumbar spine in healthy dogs. Although there were no studies on fat content according to vertebral body location in dogs, the result of the present study was consistent with those obtained in human studies (29–31). A previous study showed increased FFs of the vertebral bodies from the first to the fifth lumbar vertebrae in healthy humans (29). In another study, a craniocaudal gradient of the vertebral FFs from T12 to L5 was observed in human patients without spinal bone disease (30). In human studies, centripetal bone marrow conversion has been suggested to be a cause of this lumbar vertebral FF gradient (29–32). In adult humans and dogs, the bone marrow converts from hematopoietic marrow to fatty marrow with a centripetal direction from the appendicular skeleton to the axial skeleton (31, 32). This centripetal conversion May contribute to the lumbar FF gradient. Another possible explanation is an indirect consequence of the increased mechanical stress on the caudal lumbar vertebrae (30). Since

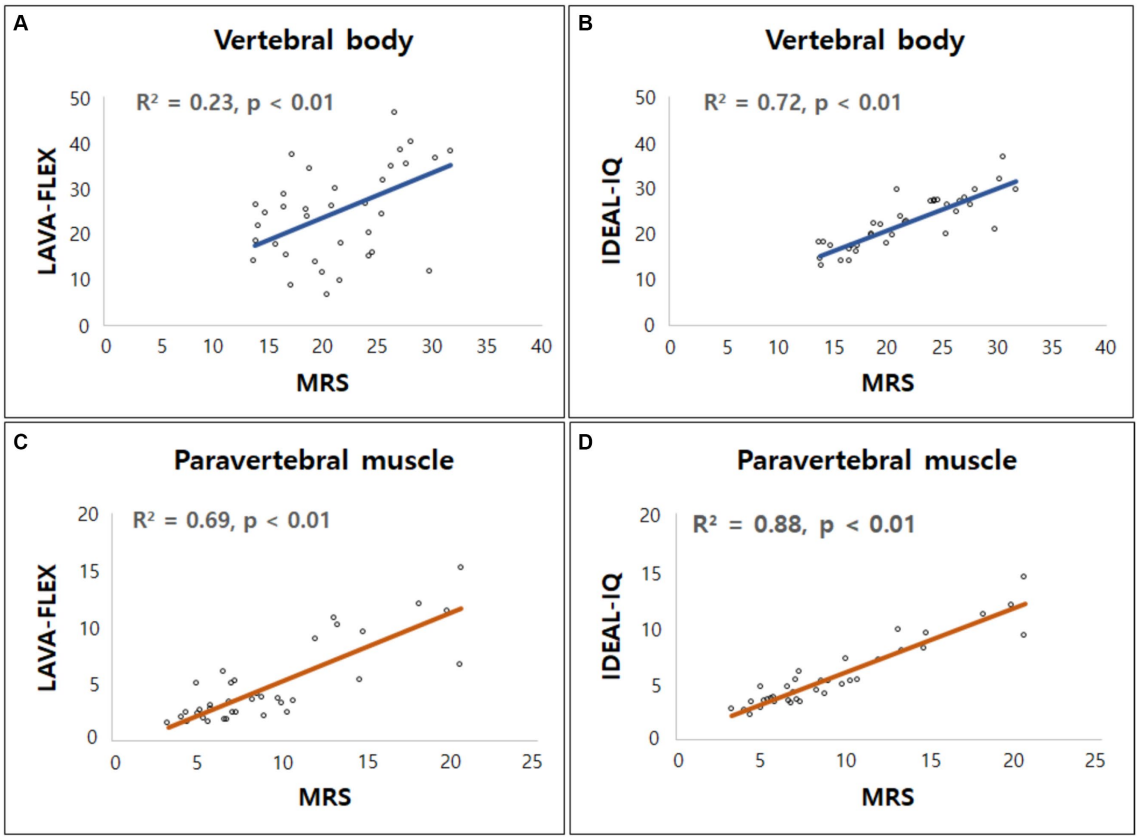

FIGURE 5
Linear regression model for fat fractions (FF) obtained from Dixon MRI (LAVA-FLEX and IDEAL-IQ) and magnetic resonance spectroscopy (MRS). Scatterplots correlate FFs derived from **(A)** LAVA-FLEX, **(B)** IDEAL-IQ for vertebral body, and **(C)** LAVA-FLEX, **(D)** IDEAL-IQ for paraspinal muscle along the y-axis with fat fraction measured with MRS along the x-axis. Correlation coefficient (R^2) was ranging from 0.23 to 0.69 for LAVA-FLEX and 0.72 to 0.88 for IDEAL-IQ.

TABLE 6 Intra- and interobserver reproducibility of FF analysis using LAVA-FLEX and IDEAL-IQ.

Sequence	Parameter	Interobserver reproducibility	Intraobserver reproducibility		
		ICC	95% CI	ICC	95% CI
LAVA-FLEX	Vertebral body	0.994	0.989–0.997	0.975	0.957–0.987
	Paraspinal muscle	0.998	0.996–0.999	0.998	0.997–0.999
IDEAL-IQ	Vertebral body	0.994	0.990–0.997	0.977	0.960–0.988
	Paraspinal muscle	0.999	0.997–0.999	0.999	0.998–0.999

CI, confidence interval; FF, fat fraction; ICC, intraclass correlation coefficient. An ICC < 0.50, between 0.50 and < 0.75, between 0.75 and < 0.90, and ≥ 0.90 was considered poor, fair, good, and excellent measurement reliability, respectively.

the sacropelvic complex is fixed, more force and stress are placed on the adjacent lower lumbar spine, which can cause higher fatty degeneration in the lower lumbar spine (30, 31).

Unlike the vertebral body FFs, there were no significant differences in the FFs of the paraspinal muscles according to the lumbar sites in this study. This result was not consistent with those from previous human studies, which showed that paravertebral muscle fatty infiltration generally increased from cranial to caudal, with the highest value at L5 (33–35). There are many possible causes for this discrepancy. First, relatively young dogs were included in this study. In humans, it was reported that lumbar paravertebral muscle fatty degeneration occurs relatively more slowly than vertebral body fatty degeneration with aging (33). Moreover, the younger the age of the individual, the less pronounced the difference in fatty degeneration of the paraspinal muscles according to the anatomical level (35). Therefore, we suggest that the age of dogs May have contributed to the lack of a FF gradient in the paraspinal muscles; however, due to the small number of subjects, differences by age could not be analyzed in this study. Second, the location of the muscles analyzed May have affected the results. In previous studies, fatty degeneration was most evident in the multifidus muscle in human patients with IVDD (33, 34). However, we did not include the multifidus muscle in this study because the cross-sectional area of this muscle was too small to place the voxel in it for MRS. Therefore, degenerative changes in the muscles

TABLE 7 Difference, coefficient of variance, Bland–Altman agreement, and ICC of the vertebral body and paraspinal muscle fat fractions between the first and second scans.

Sequence	Site	Mean ± SD (%)		*p*-value	CV (%)	Bland–Altman Bias (95% LOA)	ICC (95% CI)
		1st scan	2nd scan				
LAVA-FLEX	Vertebral body	25.18 ± 11.10	26.47 ± 8.89	0.293	38.7	−1.29 (−16.31–13.72)	0.830 (0.667–0.913)
	Paraspinal muscle	4.77 ± 3.52	4.19 ± 2.64	0.134	69.2	0.58 (−5.34–6.51)	0.691 (0.394–0.842)
IDEAL-IQ	Vertebral body	22.48 ± 5.76	23.84 ± 5.82	0.000	25.0	−1.36 (−5.03–2.30)	0.973 (0.946–0.986)
	Paraspinal muscle	5.55 ± 2.92	5.37 ± 2.64	0.777	50.7	0.18 (−1.94–2.30)	0.961 (0.923–0.980)
MRS	Vertebral body	21.60 ± 5.36	24.11 ± 4.55	0.000	22.3	−2.51 (−6.73–1.72)	0.951 (0.903–0.975)
	Paraspinal muscle	9.22 ± 4.77	7.97 ± 4.10	0.001	51.9	1.25 (−2.62–5.12)	0.948 (0.898–0.974)

CI, confidence interval; CV, coefficient of variance; ICC, intraclass correlation coefficient; LOA, limits of agreement; MRS, magnetic resonance spectroscopy, SD, standard deviation.

May have been underestimated in this study. Unlike humans, dogs walk on all four limbs, so there May not be a difference in loading on the paravertebral muscles in the rear compared to the front like in humans. However, as far as author's knowledge, there was no previous study to prove this.

In humans, many studies have been conducted to apply the FF of the vertebral bodies and paraspinal muscles in healthy subjects and patients with spinal diseases such as IVDD (2, 3, 8, 9, 12–16). These studies showed an association between the FF and histological IVDD grade, neurological symptom, and prognosis (2, 3, 8, 15). A recent study in dogs suggested that there is a correlation between fat degeneration and neurologic grade in dogs with IVDD and the potential use of fat degeneration as a biomarker in dogs with IVDD (7). In that study, paravertebral muscle fat fraction was not associated with the outcome of dogs with IVDD. However, due to the lack of studies in dogs, more data are needed in patients with IVDD. The results of this study suggest that LAVA-FLEX or IDEAL-IQ can be used as a routine sequence in dogs when obtaining spinal MRI in future studies to identify the association of fat infiltration in the vertebral bodies and paraspinal muscles with IVDD in dogs.

Although not included in the analysis in this study, LAVA-FLEX and IDEAL-IQ have several advantages for clinical use compared with MRS. First, these Dixon techniques are much faster for FF analysis, particularly when analyzing multiple sites. In this study, it took approximately 17 min for MRS to obtain the FFs of the vertebral bodies at each of six levels from L1–L6, whereas with LAVA-FLEX and IDEAL-IQ, it took less than 3 min. Second, LAVA-FLEX and IDEAL-IQ do not require post-processing compared with MRS, making them easy for clinicians to use. Third, MRS can only analyze the voxel set at the time of acquisition, while LAVA-FLEX and IDEAL-IQ allow setting and modification of the ROI in the obtained image. In addition, MRS requires the use of voxels of a certain size or a certain cuboid shape, but LAVA-FLEX and IDEAL-IQ can specify small ROIs with free shapes, allowing flexibility for evaluating specific anatomical muscles. Finally, LAVA-FLEX and IDEAL-IQ provide fat suppression images. When evaluating spinal disease, fat suppression images are necessary to distinguish the lesion from the epidural fat or paraspinal fat. Dixon techniques provide homogeneous and reliable fat separation and thus can be used as alternative sequences to other fat suppression images (16).

There were several limitations in this study. First, this study included only a small number of individuals. To overcome this limitation, analysis was performed at six different vertebral sites, but comparisons of more samples are needed through prospective studies in patients. Second, subjects included in this study were of the same breed and were similar in age and weight; thus, we could not consider various factors that can affect the FF. In humans, several factors including age, sex, and body weight can affect the FF; therefore, the FF in dogs could similarly be affected by various factors (29–35). However, these limitations did not pose a problem for the main purpose of this study, which was to evaluate the feasibility of LAVA-FLEX and IDEAL-IQ for assessing the FF compared with MRS. Further studies with larger numbers of subjects and wider range of variation in subject characteristics such as age, gender, body condition score, and breed are needed. Third, in this study, the FFs of the vertebral bodies and paraspinal muscles were not compared with histopathological findings. Previous human studies have showed a high correlation between Dixon-based or MRS-based FFs and histological results, but they have not been validated in dogs (35, 36). Although this study did not compare FFs to histological findings, we believe that the feasibility of LAVA-FLEX and IDEAL-IQ for evaluating the FFs of the lumbar vertebral bodies and paraspinal muscles in dogs was verified because it was compared with FFs derived from MRS, which is well-known as the gold standard method for FF evaluation.

5 Conclusion

In conclusion, the results of this study showed that LAVA-FLEX and IDEAL-IQ have high reproducibility and are highly correlated with MRS, the gold standard method, for measuring the FFs of the lumbar vertebral bodies and paraspinal muscles in dogs. In addition, the FFs can be obtained and analyzed much more easily and quickly with these methods compared with MRS. Therefore, we believe that LAVA-FLEX and IDEAL-IQ can be used as routine methods in spinal MRI in dogs.

Data availability statement

The datasets presented in this study can be found in online repositories. The names of the repository/repositories and accession number(s) can be found in the article/supplementary material.

Ethics statement

The animal study was approved by Institutional Animal Care and Use Committee at Kyungpook National University. The study was

conducted in accordance with the local legislation and institutional requirements.

Author contributions

H-WL: Conceptualization, Data curation, Formal analysis, Investigation, Software, Writing – original draft. J-YuL: Formal analysis, Investigation, Validation, Writing – review & editing. J-YoL: Formal analysis, Investigation, Validation, Writing – review & editing. S-MY: Formal analysis, Software, Writing – review & editing. KL: Project administration, Supervision, Writing – review & editing. S-KL: Conceptualization, Funding acquisition, Project administration, Supervision, Writing – original draft, Writing – review & editing.

Funding

The author(s) declare that financial support was received for the research, authorship, and/or publication of this article. This research was supported by the National Research Foundation of Korea (NRF) grant funded by the Korean Ministry of Science and ICT (2022R1G1A1006476).

Conflict of interest

The authors declare that the research was conducted in the absence of any commercial or financial relationships that could be construed as a potential conflict of interest.

Publisher's note

References

1. Thompson K, Moore S, Tang S, Wiet M, Purmessur D. The chondrodystrophic dog: a clinically relevant intermediate-sized animal model for the study of intervertebral disc-associated spinal pain. *JOR Spine*. (2018) 1:e1011. doi: 10.1002/jsp2.1011

2. Wang Z, Zhao Z, Han S, Hu X, Ye L, Li Y, et al. Advances in research on fat infiltration and lumbar intervertebral disc degeneration. *Front Endocrinol*. (2022) 13:1067373. doi: 10.3389/fendo.2022.1067373

3. Engelke K, Chaudry O, Gast L, Eldib MA, Wang L, Laredo JD, et al. Magnetic resonance imaging techniques for the quantitative analysis of skeletal muscle: state of the art. *J Orthop Translat*. (2023) 42:57–72. doi: 10.1016/j.jot.2023.07.005

4. Boström AF, Hielm-Björkman AK, Chang YM, Weller R, Davies ES. Comparison of cross sectional area and fat infiltration of the epaxial muscles in dogs with and without spinal cord compression. *Res Vet Sci*. (2014) 97:646–51. doi: 10.1016/j.rvsc.2014.09.006

5. Lerer A, Nykamp SG, Harriss AB, Gibson TW, Koch TG, Brown SH. MRI-based relationships between spine pathology, intervertebral disc degeneration, and muscle fatty infiltration in chondrodystrophic and non-chondrodystrophic dogs. *Spine J*. (2015) 15:2433–9. doi: 10.1016/j.spinee.2015.08.014

6. Morrison EJ, Baron-Chapman ML, Chalkley M. MRI T2/STIR epaxial muscle hyperintensity in some dogs with intervertebral disc extrusion corresponds to histologic patterns of muscle degeneration and inflammation. *Vet Radiol Ultrasound*. (2021) 62:150–60. doi: 10.1111/vru.12932

7. Beale CC, Secrest SA. MRI assessment of epaxial myosteatosis in dogs with intervertebral disc extrusions and associations with patient factors and outcome. *Vet Radiol Ultrasound*. (2021) 62:687–96. doi: 10.1111/vru.13019

8. Ji Y, Hong W, Liu M, Liang Y, Deng Y, Ma L. Intervertebral disc degeneration associated with vertebral marrow fat, assessed using quantitative magnetic resonance imaging. *Skeletal Radiol*. (2020) 49:1753–63. doi: 10.1007/s00256-020-03419-7

9. Gassert FG, Kranz J, Gassert FT, Schwaiger BJ, Bogner C, Makowski MR, et al. Longitudinal MR-based proton-density fat fraction (PDFF) and T2* for the assessment of associations between bone marrow changes and myelotoxic chemotherapy. *Eur Radiol*. (2023) 34:2437–44. doi: 10.1007/s00330-023-10189-y

10. Müller A, Forterre F, Vidondo B, Stoffel MH, Hernández-Guerra Á, Plessas IN, et al. Evaluation of paraspinal musculature in small breed dogs with and without atlantoaxial instability using computed tomography. *Vet Comp Orthop Traumatol*. (2022) 35:305–13. doi: 10.1055/s-0042-1748860

11. Lee JY, Hwang TS, Lee HC. CT evaluation of age-related changes in Epaxial muscle attenuation and cross-sectional area for sarcopenia and Myosteatosis in small breed dogs. *J Vet Clin*. (2023) 40:182–8. doi: 10.17555/jvc.2023.40.3.182

12. Lee SH, Yoo HJ, Yu SM, Hong SH, Choi JY, Chae HD. Fat quantification in the vertebral body: comparison of modified Dixon technique with single-voxel magnetic resonance spectroscopy. *Korean J Radiol*. (2019) 20:126–33. doi: 10.3348/kjr.2018.0174

13. Fischer MA, Nanz D, Shimakawa A, Schirmer T, Guggenberger R, Chhabra A, et al. Quantification of muscle fat in patients with low back pain: comparison of multi-echo MR imaging with single-voxel MR spectroscopy. *Radiology*. (2013) 266:555–63. doi: 10.1148/radiol.12120399

14. Karampinos DC, Melkus G, Baum T, Bauer JS, Rummeny EJ, Krug R. Bone marrow fat quantification in the presence of trabecular bone: initial comparison between water-fat imaging and single-voxel MRS. *Magn Reson Med*. (2014) 71:1158–65. doi: 10.1002/mrm.24775

15. Jung M, Rospleszcz S, Löffler MT, Walter SS, Maurer E, Jungmann PM, et al. Association of lumbar vertebral bone marrow and paraspinal muscle fat composition with intervertebral disc degeneration: 3T quantitative MRI findings from the population-based KORA study. *Eur Radiol*. (2023) 33:1501–12. doi: 10.1007/s00330-022-09140-4

16. Lins CF, Salmon CEG, Nogueira-Barbosa MH. Applications of the Dixon technique in the evaluation of the musculoskeletal system. *Radiol Bras*. (2020) 54:33–42. doi: 10.1590/0100-3984.2019.0086

17. Bainbridge A, Bray TJ, Sengupta R, Hall-Craggs MA. Practical approaches to bone marrow fat fraction quantification across magnetic resonance imaging platforms. *J Magn Reson Imaging*. (2020) 52:298–306. doi: 10.1002/jmri.27039

18. Gomes FP. Curso de estatística experimental. Piracicaba: Nobel Press (1985).

19. Bydder M, Yokoo T, Hamilton G, Middleton MS, Chavez AD, Schwimmer JB, et al. Relaxation effects in the quantification of fat using gradient echo imaging. *J Magn Reson Imaging*. (2008) 26:347–59. doi: 10.1016/j.mri.2007.08.012

20. Karampinos DC, Yu H, Shimakawa A, Link TM, Majumdar S. T1-corrected fat quantification using chemical shift-based water/fat separation: application to skeletal muscle. *Magn Reson Med*. (2011) 66:1312–26. doi: 10.1002/mrm.22925

21. Hernando D, Haldar JP, Sutton BP, Ma J, Kellman P, Liang ZP. Joint estimation of water/fat images and field inhomogeneity map. *Magn Reson Med*. (2008) 59:571–80. doi: 10.1002/mrm.21522

22. Hernando D, Hines CD, Yu H, Reeder SB. Addressing phase errors in fat-water imaging using a mixed magnitude/complex fitting method. *Magn Reson Med*. (2012) 67:638–44. doi: 10.1002/mrm.23044

23. Karampinos DC, Ruschke S, Dieckmeyer M, Eggers H, Kooijman H, Rummeny EJ, et al. Modeling of T2* decay in vertebral bone marrow fat quantification. *NMR Biomed*. (2015) 28:1535–42. doi: 10.1002/nbm.3420

24. Wehrli FW, Song HK, Saha PK, Wright AC. Quantitative MRI for the assessment of bone structure and function. *NMR Biomed*. (2006) 19:731–64. doi: 10.1002/nbm.1066

25. Karampinos DC, Ruschke S, Dieckmeyer M, Diefenbach M, Franz D, Gersing AS, et al. Quantitative MRI and spectroscopy of bone marrow. *J Magn Reson Imaging*. (2018) 47:332–53. doi: 10.1002/jmri.25769

26. Liu CY, McKenzie CA, Yu H, Brittain JH, Reeder SB. Fat quantification with IDEAL gradient echo imaging: correction of bias from T1 and noise. *Magn Reson Med*. (2007) 58:354–64. doi: 10.1002/mrm.21301

27. Elfaal M, Supersad A, Ferguson C, Locas S, Manolea F, Wilson MP, et al. Two-point Dixon and six-point Dixon magnetic resonance techniques in the detection, quantification and grading of hepatic steatosis. *World J Radiol*. (2023) 15:293–303. doi: 10.4329/wjr.v15.i10.293

28. Krššák M, Lindeboom L, Schrauwen-Hinderling V, Szczepaniak LS, Derave W, Lundbom J, et al. Proton magnetic resonance spectroscopy in skeletal muscle: experts' consensus recommendations. *NMR Biomed*. (2021) 34:e4266. doi: 10.1002/nbm.4266

29. Liney GP, Bernard CP, Manton DJ, Turnbull LW, Langton CM. Age, gender, and skeletal variation in bone marrow composition: a preliminary study at 3.0 tesla. *J Magn Reson Imaging*. (2007) 26:787–93. doi: 10.1002/jmri.21072

30. Ognard J, Demany N, Mesrar J, Aho-Glélé LS, Saraux A, Salem DB. Mapping the medullar adiposity of lumbar spine in MRI: a feasibility study. *Heliyon*. (2021) 7:e05992. doi: 10.1016/j.heliyon.2021.e05992

31. Cristy M. Active bone marrow distribution as a function of age in humans. *Phys Med Biol*. (1981) 26:389–400. doi: 10.1088/0031-9155/26/3/003

32. Gurevitch O, Slavin S, Feldman AG. Conversion of red bone marrow into yellow–cause and mechanisms. *Med Hypo*. (2007) 69:531–6. doi: 10.1016/j.mehy.2007.01.052

33. Crawford RJ, Volken T, Valentin S, Melloh M, Elliott JM. Rate of lumbar paravertebral muscle fat infiltration versus spinal degeneration in asymptomatic populations: an age-aggregated cross-sectional simulation study. *Scoliosis Spinal Disord*. (2016) 11:21–9. doi: 10.1186/s13013-016-0080-0

34. Crawford RJ, Filli L, Elliott JM, Nanz D, Fischer MA, Marcon M, et al. Age- and level- dependence of fatty infiltration in lumbar paravertebral muscles of healthy volunteers. *AJNR Am J Neuroradiol*. (2016) 37:742–8. doi: 10.3174/ajnr.A4596

35. Lee SH, Park SW, Kim YB, Nam TK, Lee YS. The fatty degeneration of lumbar paraspinal muscles on computed tomography scan according to age and disc level. *Spine J*. (2017) 17:81–7. doi: 10.1016/j.spinee.2016.08.001

36. Samet JD, Deng J, Schafernak K, Arva NC, Lin X, Peevey J, et al. Quantitative magnetic resonance imaging for determining bone marrow fat fraction at 1.5 T and 3.0 T: a technique to noninvasively assess cellularity and potential malignancy of the bone marrow. *Pediatr Radiol*. (2021) 51:94–102. doi: 10.1007/s00247-020-04809-8

frontiers | Frontiers in Veterinary Science

TYPE Original Research
PUBLISHED 11 November 2024
DOI 10.3389/fvets.2024.1431777

OPEN ACCESS

EDITED BY
Tomasz Szara,
Warsaw University of Life Sciences, Poland

REVIEWED BY
Takehiko Kakizaki,
Kitasato University, Japan
Ottmar Distl,
University of Veterinary Medicine Hannover, Germany

*CORRESPONDENCE
M. Hagenbach
✉ Marie.Hagenbach@vetmed.uni-giessen.de

†These authors have contributed equally to this work and share senior authorship

RECEIVED 12 May 2024
ACCEPTED 01 October 2024
PUBLISHED 11 November 2024

CITATION
Hagenbach M, Bierau J, Cruz AM, Koch C, Manso-Díaz G, Büttner K, Staszyk C and Röcken M (2024) Visualization of anatomical structures in the carpal region of the horse using cone beam computed tomography in comparison with conventional multidetector computed tomography.
Front. Vet. Sci. 11:1431777.
doi: 10.3389/fvets.2024.1431777

Visualization of anatomical structures in the carpal region of the horse using cone beam computed tomography in comparison with conventional multidetector computed tomography

M. Hagenbach[1]*, J. Bierau[1], A. M. Cruz[1], C. Koch[2], G. Manso-Díaz[3], K. Büttner[4], C. Staszyk[5†] and M. Röcken[1†]

[1]Equine Clinic (Surgery, Orthopedics), Justus-Liebig-University Giessen, Giessen, Germany, [2]Department of Clinical Veterinary Medicine, Vetsuisse Faculty, Swiss Institute of Equine Medicine (ISME), University of Bern, Bern, Switzerland, [3]Department of Animal Medicine and Surgery, Faculty of Veterinary Medicine, Universidad Complutense de Madrid, Madrid, Spain, [4]Unit for Biomathematics and Data Processing, Justus-Liebig-University Giessen, Giessen, Germany, [5]Institute of Veterinary-Anatomy, -Histology and -Embryology, Faculty of Veterinary Medicine, Justus-Liebig-University Giessen, Giessen, Germany

Introduction: In the diagnostics of orthopedic diseases in the horse, diagnostic imaging often plays a decisive role. Cone beam computed tomography (CBCT) imaging is used in both human and small animal medicine and becoming increasingly popular. To see whether CBCT imaging can be useful in the diagnosis of orthopedic diseases of the carpal region of the horse and to explore possible limitations we compared CBCT images with multidetector computed tomography (MDCT) images of the carpal region of equine cadaveric specimens.

Materials and methods: Twenty-eight forelimbs from fifteen horses, slaughtered for reasons unrelated to this study, were examined. Native and contrast enhanced CBCT and MDCT scans were performed. Anatomical structures were blindly evaluated by three independent experienced observers using a visual scoring system previously reported and adapted to the equine carpal region. A descriptive evaluation was carried out as well as Spearman's rank correlation and interobserver agreement was shown by percent agreement (PA).

Results: Visualization of osseous structures was excellent in both MDCT and CBCT. Articular cartilage could only be assessed in contrast enhanced scans whereby MDCT showed a slightly better visualization than CBCT. Soft tissue structures were generally difficult to assess. An exception were the medial and lateral palmar intercarpal ligament, which could not be visualized in native but were well visualized in contrast enhanced scans in both MDCT and CBCT images.

Discussion/conclusion: For the evaluation of osseous structures and some intraarticular ligaments after contrast enhancement, CBCT serves as a reliable diagnostic imaging modality for the equine carpal region. However, soft tissue structures and cartilage are imaged more reliably using MDCT.

KEYWORDS

horse, carpal joint, cone beam computed tomography, multidetector computed tomography, anatomy, diagnostic

1 Introduction

Diseases of the carpal region are a common source of lameness and loss of performance, especially in racehorses (1–4). In a cohort of 114 Standardbred racehorses in training, lameness was localized to the carpal region in 28% of the horses, overall, and in 56% of the horses with forelimb lameness, making carpal lameness most common in this study population (5). The most commonly described reasons for carpal lameness are developmental (e.g., incomplete ossification), degenerative, inflammatory, infectious, or traumatic (e.g., carpal fractures) insults (1, 6). The carpal joint represents a complex anatomic region with numerous osseous and non-calcified structures, i.e., cartilaginous elements, intra- and extraarticular ligaments as well as tendons and tendon sheaths (7). Different diagnostic imaging modalities are employed in the diagnostic workup of the carpal region in horses. In practice, radiographic projections of the extended as well as of the flexed carpus are taken, but diagnostic yield is limited due to superimposition of relevant anatomical structures. To avoid this, cross-sectional imaging modalities are gaining practical relevance in the diagnosis of carpal problems. In a previous study (8) of imaging of articular cartilage lesions, computed tomography (CT) arthrography showed the highest sensitivity (69,9%), followed by magnetic resonance (MR) arthrography (53,5%). The intraarticular injection of contrast medium in the antebrachiocarpal and middle carpal joints significantly improved the visibility of these lesions. The majority of comparative imaging studies in horses focuses on comparing magnetic resonance imaging (MRI), multidetector computed tomography (MDCT), and digital radiography (9). Taking a closer look at the different CT technologies currently in use for examinations of the equine carpal region, the conventional MDCT and cone beam computed tomography (CBCT) are to be considered. In MDCT imaging, a fan-shaped x-ray beam is rotated in a helical progression around the area of interest. For this the patient is moved at consistent speed in relation to and through the CT-gantry, producing image planes slice by slice. These slices are subsequently assembled into a 3D-reconstruction (10). In CBCT imaging, on the other hand, a fixed cone-shaped x-ray beam is projected onto a flat panel detector, while rotated around the region of interest within a gantry that remains in a fixed position in relation to the patient. The thereby acquired volumetric data is sampled with multiple projections of the complete field of view (FOV) from just a single rotation (11–13).

CBCT has its origins in various fields of human medicine such as angiography and intra-operative imaging procedures (14), radiotheraphy guidance (15), and mammography (16). Today, it finds widespread application in advanced dentistry and maxillofacial surgery (17) as well as image guided spine surgery (18). Additionally, CBCT imaging is used in diagnostic imaging of human extremities, allowing for rapid true to size visualization of osseous structures and to a lesser extend also of soft-tissue structures (19).

The progressive development of CBCT imaging in human medicine has brought forward numerous CBCT imaging units that are useful for application in veterinary medicine (9). Thus, for example, dental abnormalities in cats and dogs were examined with CBCT imaging (20, 21). Moreover, CBCT technology was described for the assessment of osseous maxillofacial structures and dentition in rabbits (22, 23).

Although the general diagnostic potential of standing CBCT for the equine carpal region has been mentioned (24), no systemic evaluation of the CBCT data quality exists. Thus, the aim of this study was to assess and evaluate clinically relevant structures of the equine carpal region in a comparative study using CBCT and MDCT scans.

2 Materials and methods

2.1 Cadaveric specimens

Twenty-eight forelimbs from fifteen horses, slaughtered for reasons unrelated to this study, were examined (Table 1). Before separating the limbs at mid-antebrachium level, a cable tie was fastened approximately 100 mm proximal of the antebrachiocarpal joint to avoid entrapment of air. After separation, the limbs were clipped and cleaned before radiographs were projected in four different planes (dorso-palmar, latero-medial, dorsolateral-palmaromedial oblique and dorsomedial-palmarolateral oblique) using a high-frequency generator (Siemens Optitop 150/40/80, 70 kV and 2.5 mAs) and a DR flat panel detector (Fujifilm, FDR D-EVO II C24). The specimens were then stored for a maximum of 24 h at 4°C before CBCT and MDCT scans were carried out.

2.2 CBCT and MDCT scans

The FDA-approved CBCT scanner (O-arm®, Medtronic Inc.) for application in surgical environments was used in high definition (HD) mode with 120 kV, 120 mAs and a FOV of 200 mm. The FOV was large enough for all forelimbs examined. The MDCT scans were carried out with a helical 16-slice MDCT scanner (Somatom® Definition AS Siemens, Erlangen, Germany). The device settings of 130 kV, 173 mAs, and 0,6 mm slices were applied for all image acquisitions with a FOV of 256 mm, running both soft tissue and bone algorithms.

First, a native CBCT scan and then a native MDCT scan were carried out with the limbs laying on the dorsal side. Subsequently, a 1:1 mixture of contrast medium (Xenetix® 300, Guerbet, Sulzbach, Germany) and isotonic saline solution 0,9% (Braun Ecofl®, B. Braun Melsungen AG, Germany) was injected by dorsal approach in both the antebrachiocarpal (ACJ) and middle carpal joints (MCJ) with a 20 G cannula (Stercan®, B. Braun Melsungen AG, Germany) until the joints were ballooned (average volume 20 mL). Immediately afterwards the carpal joints were flexed and extended thirty times to get an even distribution of the injected solution. Subsequently, the limbs were scanned again with both MDCT and CBCT applying the same device settings as used for the native scans.

10.3389/fvets.2024.1431777

TABLE 1 Patient data.

Horse number	Carpus number	Age (years)	Breed	Sex	Leg
1	1	12	Warmblood	Gelding	Right forelimb
1	2	12	Warmblood	Gelding	Left forelimb
2	3	14	Tinker horse	Mare	Left forelimb
3	4	16	Thoroughbred	Mare	Right forelimb
3	5	16	Thoroughbred	Mare	Left forelimb
4	6	19	Warmblood	Gelding	Right forelimb
4	7	19	Warmblood	Gelding	Left forelimb
5	8	19	Warmblood	Mare	Right forelimb
5	9	19	Warmblood	Mare	Left forelimb
6	10	20	Pony	Mare	Right forelimb
6	11	20	Pony	Mare	Left forelimb
7	12	23	Warmblood	Mare	Right forelimb
7	13	23	Warmblood	Mare	Left forelimb
8	14	24	Haflinger	Mare	Right forelimb
8	15	24	Haflinger	Mare	Left forelimb
9	16	25	Warmblood	Mare	Right forelimb
9	17	25	Warmblood	Mare	Left forelimb
10	18	25	Noriker	Gelding	Right forelimb
10	19	25	Noriker	Gelding	Left forelimb
11	20	26	Icelandic horse	Mare	Right forelimb
11	21	26	Icelandic horse	Mare	Left forelimb
12	22	26	Icelandic horse	Mare	Right forelimb
12	23	26	Icelandic horse	Mare	Left forelimb
13	24	27	Warmblood	Gelding	Right forelimb
13	25	27	Warmblood	Gelding	Left forelimb
14	26	28	Haflinger	Mare	Right forelimb
14	27	28	Haflinger	Mare	Left forelimb
15	28	29	Quarter horse	Gelding	Left forelimb

2.3 Image evaluation

A DICOM viewing software (DICOM Horos® viewer) was used in a quiet and darkened examination room with the help of a MacBook Pro®, 2,3 GHz Dual-Core Intel Core i5, MacOs Ventura 13.4 to display the MDCT and CBCT scans while a multiplanar reconstruction tool was utilized for the different slice planes. Numbers were randomly given for each forelimb and the observers could allocate the two different modalities to the respective limb. All observers [two board-certified equine surgeons (CK, AC) and one board-certified large animal radiologist (GMD)] were experienced in interpreting MDCT and CBCT images. The observers were instructed to evaluate the visibility of the following clinically relevant structures using a scoring system adapted from Bierau et al. (25):

Osseous structures (Figure 1):

- Distal aspect of the radius (DR)
- Proximal (antebrachial) row of the carpal bones (incl. Accessory carpal bone) (AR)
- Distal (metacarpal) row of the carpal bones (MR)
- Proximal aspects of the metacarpal bones (PMC)

Articular structures (Figure 1):

- Cartilage of DR
- Cartilage of AR
- Cartilage of MR
- Cartilage of PMC

Soft tissue structures (Figure 2):

- Digital extensor tendons (DET)
- Deep digital flexor tendon (DDFT)
- Superficial digital flexor tendon (SDFT)
- Carpal flexor tendon sheath (CFTS)
- Collateral ligaments of the carpus (CL)
- Medial palmar intercarpal ligament (MPIL)
- Lateral palmar intercarpal ligament (LPIL)
- Origin of the suspensory ligament (OSL)

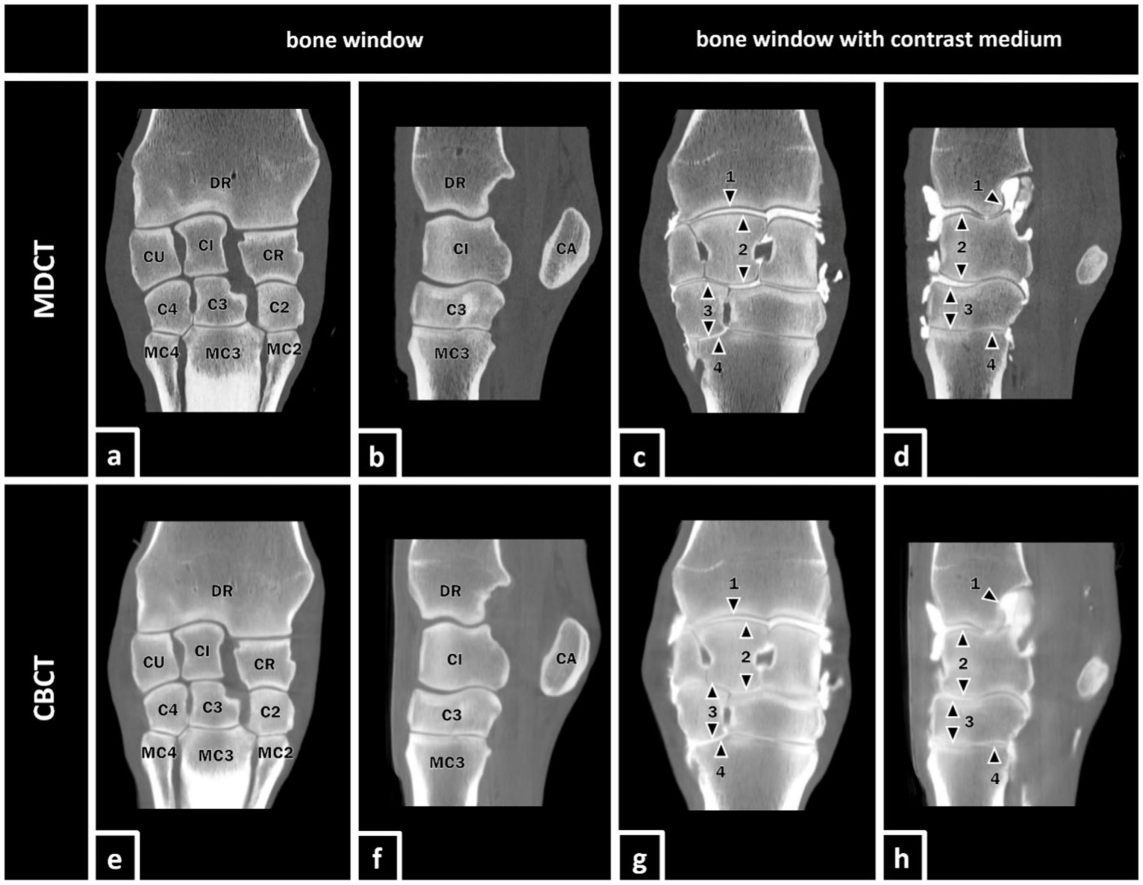

FIGURE 1
MDCT and CBCT images of the right forelimb of a 19-year-old gelding. The visibility of the listed osseous and articular structures was evaluated in MDCT and CBCT images with and without contrast enhancement. Osseous structures **(a,b,e,f)** (DR) distal radius, (CU) ulnar carpal bone, (CI) intermediate carpal bone, (CR) radial carpal bone, (CA) accessory carpal bone, (C4) fourth carpal bone, (C3) third carpal bone, (C2) second carpal bone, (MC4) fourth metacarpal bone, (MC3) third metacarpal bone, and (MC2) second metacarpal bone. Articular structures (**c,d,g,h**; marked with black arrows): (1) cartilage of DR, (2) cartilage of the antebrachial (proximal) row, (3) cartilage of the metacarpal (distal) row, and (4) cartilage of proximal MC3.

For the evaluation of the images, a modified visual scoring system according to Vallance et al. (26) and Bierau et al. (25) was used. The scoring system consists of visual assessment scores from zero to three using subjective criteria for visibility for each structure. A score value of zero indicates that the evaluated structure was not visible. If a structure was poorly visualized, only identified by its location and signal intensity but not by margins, shape, or size, the observers scored the structure with a score value of one. A score value of two indicated that the structure could be clearly identified by its location, shape, and signal intensity but the margins were not clearly delineated. The highest score value of three represented a structure that was well visualized and clearly delineated by its location, shape, signal intensity, size, and margins (Figure 3).

2.4 Statistics

For the statistical analysis a statistical software (SAS® 9.4) was used. A descriptive evaluation and comparison of the different recordings from the two devices before and after injection of contrast medium (MDCT native, CBCT native, MDCT contrast, and CBCT contrast) was performed belonging the visualization of the aforementioned anatomical structures (Table 2). The agreement of CBCT with MDCT was determined with the help of Spearman's rank correlation coefficient (r_s) and percent agreement (PA) represents the interobserver agreement. A correlation coefficient of $r_s > 0.4$ represents acceptable agreement and $r_s > 0.7$ represents good agreement. For the parameter percent agreement also a value close to 1 defines a good agreement between the different observers.

3 Results

3.1 Comparison of native MDCT and CBCT images

All osseous structures examined in this study (DR, AR, MR, PMC; in total $n = 112$) were well visualized in native CBCT as well as in native MDCT (MDCT and CBCT mean score 3.0, PA = 1). The cartilage of these structures was not be seen in any of the native scans (MDCT and CBCT mean score 0.0, PA = 1). In general, soft tissue structures were better visualized in MDCT than in CBCT scans. In detail, tendons/tendon sheaths (MDCT mean score 1.42, PA = 0.42 vs. CBCT mean score 0.49, PA = 0.56)

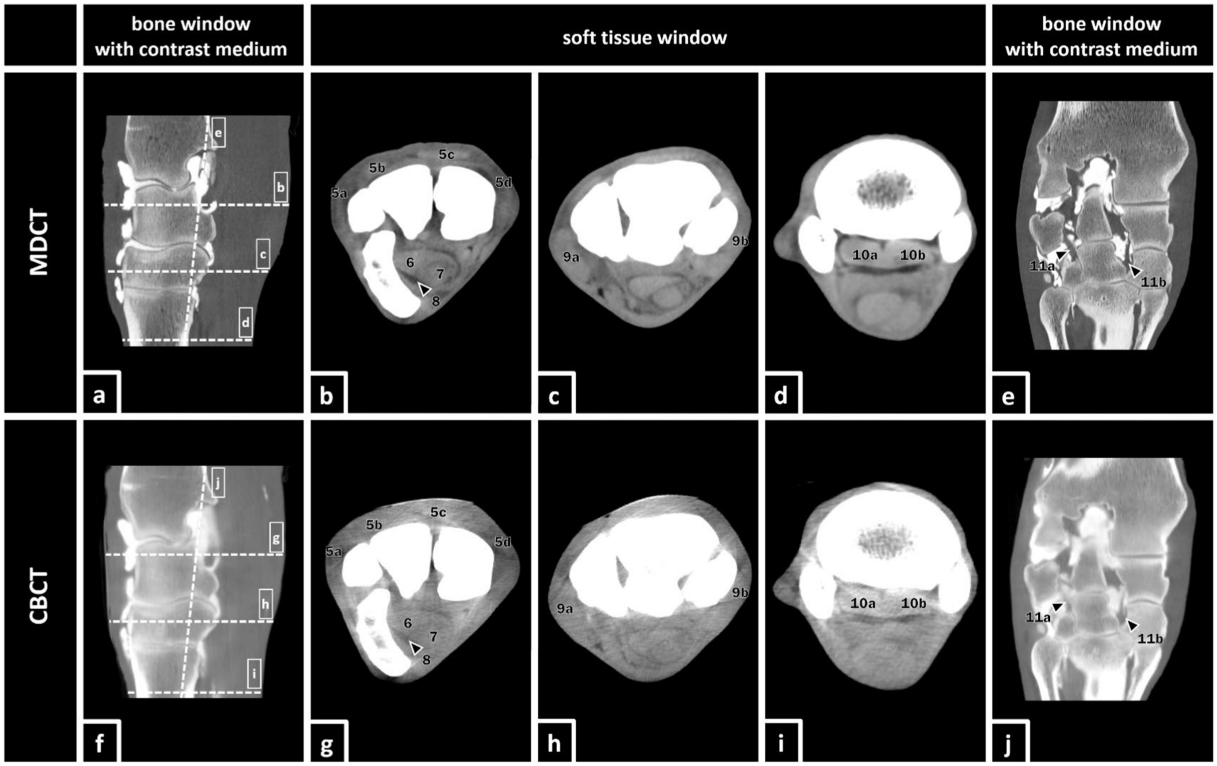

FIGURE 2
MDCT and CBCT images of the right forelimb of a 19-year-old gelding. The visibility of the listed soft tissue structures was evaluated in MDCT and CBCT images with and without contrast enhancement. Soft tissue structures: (5a) lateral digital extensor tendon, (5b) dorsal (common) digital extensor tendon, (5c) extensor carpi radialis tendon, (5d) abductor pollicis longus tendon, (6) deep digital flexor tendon (DDFT), (7) superficial digital flexor tendon (SDFT), (8) carpal flexor tendon sheath (CFTS), (9a) lateral collateral ligament of the carpus, (9b) medial collateral ligament of the carpus, (10a+b) origin of the suspensory ligament (OSL), (10a) lateral lobe, (10b) medial lobe, (11a) lateral palmar intercarpal ligament (LPIL), and (11b) medial palmar intercarpal ligament (MPIL).

were better visualized than ligaments (MDCT mean score 0.78, PA = 0.38 with r_s from 0.80 to 0.99 vs. CBCT mean score 0.24, PA = 0.93 with r_s from 0.84 to 0.93). Intracarpal ligaments (MPIL and LPIL) were not well visualized, neither in native CBCT (score 0.0, PA = 1) nor in native MDCT scans (mean score 0.33, PA = 0.33).

3.2 Comparison of native MDCT with contrast enhanced MDCT and native CBCT with contrast enhanced CBCT

The intraarticular injection of contrast medium did not change the visibility of osseous structures neither in MDCT (mean score 3.0, PA = 1) nor in CBCT (mean score 3.0, PA = 0.99). A significant improvement of the visualization of cartilage was shown after contrast enhancement in both MDCT (mean score 2.30, PA = 0.67 with r_s from 0.73 to 0.83) and CBCT (mean score = 1.69, PA = 0.32 with r_s from 0,45 to 0.61), whereby the visualization was better in MDCT than in CBCT. When focusing on the articular structures, the cartilage of DR was rated the highest (MDCT mean score 3.0, PA = 1 vs. CBCT mean score 2.38, PA = 0.30) while the cartilage of the PMC showed the lowest score (MDCT mean score 1.2, PA = 0.24 vs. CBCT mean score 0.86, PA = 0.42). Tendons and tendon sheaths had low scores in both MDCT and CBCT, where MDCT showed better visibility (mean score 1.45, PA = 0.54) than CBCT (mean score 0.28, PA = 0.55). The MPIL and LPIL, as intraarticular ligaments, were significantly better visualized after contrast enhancement (r_s = 0.94) in both MDCT (mean score 2.67, PA = 0.33) and CBCT (mean score 2.5, PA = 0.32), while CL could almost not be visualized (MDCT mean score 0.33, PA = 0.33 vs. CBCT mean score 0.01, PA = 0.98). The OSL was better visualized in MDCT (mean score 1.99, PA = 0.89) than in CBCT (mean score 1.18, PA = 0.70) but this did not improve significantly with contrast enhancement.

4 Discussion

In the present study, reconstructed CBCT and MDCT images of clinically relevant anatomical structures of the equine carpal region were acquired in fresh cadaveric specimens and compared with the help of a scoring system. While osseous structures were well visualized in both modalities before and after contrast enhancement, cartilage could only be seen after the injection of contrast medium. The visibility of cartilage after contrast enhancement was better in MDCT than in CBCT. For soft tissue structures such as ligaments, tendons and tendon sheaths, the MDCT images showed superior quality in general.

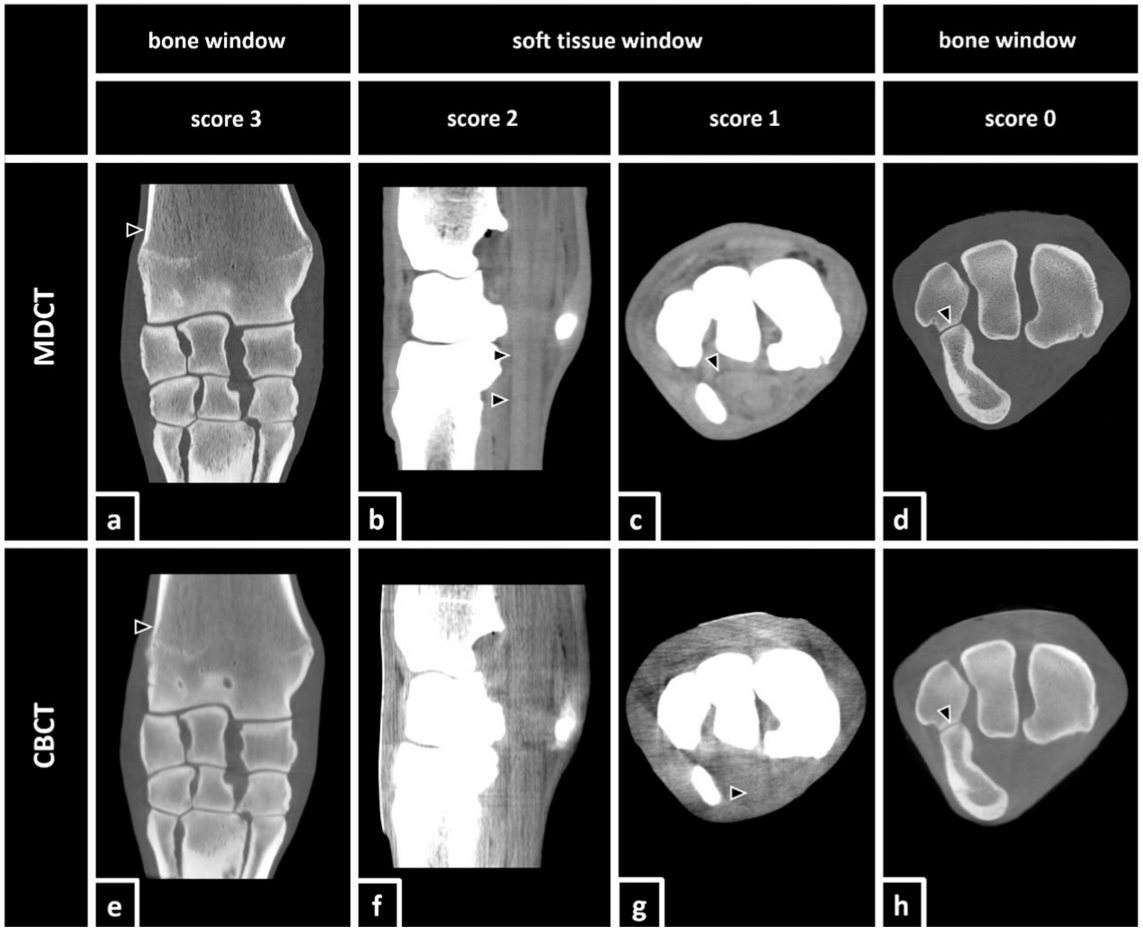

FIGURE 3
Definition of the utilized scoring system according to Vallance et al. (26) and Bierau et al. (25) including examples of differently scored anatomical structures. Score 3: **(a,e)** The distal aspect of the radius (black arrows) was clearly visualized and delineated by its location, shape, attenuation, size, and margin in both, MDCT and CBCT. Score 2: **(b)** In MDCT, the deep digital flexor tendon (black arrows) was clearly identified by location, shape, and attenuation, but the margins were not clearly delineated. In the accompanying CBCT image **(f)**, none of the structures was scored 2. Score 1: **(c)** In MDCT, the carpal flexor tendon sheath (black arrow) was poorly visualized, but detectable, and was identified by its location and attenuation but not by margins, shape, or size. In the accompanying CBCT image **(g)**, the superficial digital flexor tendon (black arrow) was scored 1. Score 0: **(d,h)** Although the lining of the cortical bone (black arrows) of the ulnar carpal bone and the accessory carpal bone was clearly visible, the belonging cartilage remained invisible.

4.1 Conditions of CBCT

In this study, CBCT showed a similar capacity in the visualization of osseous structures compared to images produced by MDCT. After contrast enhancement, indirect visualization of cartilage improved for both modalities, but more so in MDCT. When focusing on the periarticular soft tissue structures, neither of the two modalities performed well, regardless of the use of contrast enhancement. However, following contrast enhancement, the MPIL and LPIL became well visualized in both modalities. This is explained by their intraarticular position and the corresponding possibility of an indirect representation when visualizing the synovial space, similar to the principle of indirect articular cartilage visualization by adding contrast medium to the synovia.

One of the disadvantages of CBCT imaging is the cone beam effect, which occurs because of the divergence of the cone-shaped x-ray beam. That's why more information is recorded for centered structures than for peripheral objects and leads to more peripheral noise and other artefacts such as more scatter radiation, reduced contrast resolution and with that poorer soft tissue visualization (13, 27, 28). Motion artefacts are often described as a major factor for disruption and repetitions of examinations. Unlike in MDCT imaging, where motion artefacts are restricted to the segment that is being scanned at the time of patient movement, in CBCT all images reconstructed from the acquired volume will show motion artefacts, because the x-ray beam only rotates once around the subject of interest. Obviously, because this study was performed on cadaveric specimens, this limiting effect could not be assessed. However, based on clinical experience, motion artefacts are less frequently a limiting factor when scanning extremities compared to heads in standing CBCT imaging of horses and other equids (13, 24). Furthermore, post-processing motion correction software is under development (27). For the used CBCT scanner in this study (O-arm® (Medtronic), O-arm caliber 699 mm), the FOV is limited for 397 × 160 mm with a resolution of 512 × 512 × 192 voxel. For some regions of interest, such as the equine head or the stifle joint, it can necessitate more than one

TABLE 2 Visualization score and technique comparison of cone beam computed tomography (CBCT) and conventional multidetector computed tomography (MDCT).

Technique	Statistics	Joint				Tendons/ Tendon sheaths				Ligaments			
		Cartilage DR	Cartilage AR	Cartilage MR	Cartilage PMC	DET	DDFT	SDFT	CFTS	CL	MPIL	LPIL	OSL
MDCT native, $n = 84$	Median (range)	0.00 (0–0)	0.00 (0–0)	0.00 (0–0)	0.00 (0–0)	2.00 (1–2)	2.00 (1–2)	2.00 (1–2)	1.00 (0–2)	1.00 (0–2)	0.00 (0–1)	0.00 (0–1)	2.00 (1–3)
	Mean	0.00	0.00	0.00	0.00	1.74	1.72	1.66	0.57	0.68	0.33	0.33	1.80
	Percent agreement	1.00	1.00	1.00	1.00	0.48	0.45	0.45	0.31	0.32	0.33	0.33	0.55
MDCT contrast, $n = 84$	Median (range)	3.00 (3–3)	3.00 (2–3)	2.00 (1–3)	1.00 (0–3)	1.00 (0–2)	2.00 (1–2)	2.00 (1–2)	1.00 (0–2)	0.00 (0–1)	3.00 (2–3)	3.00 (2–3)	2.00 (1–3)
	Mean	3.00	2.98	2.06	1.16	1.19	1.93	1.91	0.78	0.33	2.67	2.67	1.99
	Percent agreement	1.00	0.98	0.46	0.24	0.14	0.86	0.81	0.35	0.33	0.33	0.33	0.89
CBCT native, $n = 84$	Median (range)	0.00 (0–0)	0.00 (0–0)	0.00 (0–0)	0.00 (0–0)	0.00 (0–1)	1.00 (0–2)	1.00 (0–1)	0.00 (0–1)	0.00 (0–0)	0.00 (0–0)	0.00 (0–0)	1.00 (0–2)
	Mean	0.00	0.00	0.00	0.00	0.46	0.72	0.69	0.06	0.00	0.00	0.00	0.97
	Percent agreement	1.00	1.00	1.00	1.00	0.36	0.49	0.50	0.90	1.00	1.00	1.00	0.70
CBCT contrast, $n = 84$	Median (range)	2.00 (1–3)	2.00 (1–3)	1.00 (0–3)	1.00 (0–2)	0.00 (0–1)	0.00 (0–1)	0.00 (0–1)	0.00 (0–1)	0.00 (0–1)	3.00 (0–3)	3.00 (0–3)	1.00 (0–3)
	Mean	2.36	2.19	1.40	0.81	0.17	0.44	0.44	0.07	0.01	2.50	2.50	1.18
	Percent agreement	0.30	0.29	0.26	0.42	0.67	0.33	0.33	0.88	0.98	0.32	0.32	0.70
Comparisons:													
MDCT native vs. CBCT native	Spearman's rank correlation	r_s =*	r_s =*	r_s =*	r_s =*	$r_s = 0.23$	$r_s = 0.58$	$r_s = 0.57$	$r_s = 0.23$	r_s =*	r_s =*	r_s =*	$r_s = -0.02$
	p-value	*p* =*	*p* =*	*p* =*	*p* =*	$p = 0.04$	$p \leq 0.01$	$p \leq 0.01$	$p = 0.03$	*p* =*	*p* =*	*p* =*	$p = 0.89$
MDCT contrast vs. CBCT contrast	Spearman's rank correlation	r_s =*	$r_s = -0.12$	$r_s = 0.54$	$r_s = 0.47$	$r_s = 0.15$	$r_s = -0.25$	$r_s = -0.36$	$r_s = 0.32$	$r_s = 0.16$	$r_s = 0.94$	$r_s = 0.94$	$r_s = 0.24$
	p-value	*p* =*	$p = 0.29$	$p \leq 0.01$	$p \leq 0.01$	$p = 0.18$	$p = 0.02$	$p \leq 0.01$	$p \leq 0.01$	$p = 0.16$	$p \leq 0.01$	$p \leq 0.01$	$p = 0.03$

*The correlation coefficient could not be calculated, because there was not enough variance in the present data (see percent agreement). DR, distal aspect of the radius; AR, antebrachial (proximal) row of the carpal bones (incl. Accessory carpal bone); MR, metacarpal (distal) row of the carpal bones; PMC, proximal aspects of the metacarpal bones (MCII, III, IV); DET, digital extensor tendons; DDFT, deep digital flexor tendon; SDFT, superficial digital flexor tendon; CFTS, carpal flexor tendon sheath; CL, collateral ligaments; MPIL, medial palmar intercarpal ligament; LPIL, lateral palmar intercarpal ligament; OSL, origin of the suspensory ligament.

10.3389/fvets.2024.1431777

scan to complete the whole examination (27). The scans of the carpal region in this study were even performed with the smaller cylindrical volume of 212 × 160 mm and we were able to confirm that this was sufficient for all examinations carried out.

4.2 CBCT vs. MDCT

The overall portrayal of the anatomic structures appears to be of higher quality when produced with MDCT scanners than when produced with CBCT scanners. However, particularly in regards to the visualization of osseous tissues, there appeared to be only minor differences between CBCT and MDCT imaging of the carpal joint of horses. Further investigations with known or provoked pathologies would have to be conducted to determine the effect on diagnostic yield and reliability when comparing the two modalities.

For computed tomographic arthrography of articular structures, MDCT showed better visualization than CBCT and the different soft tissue structures, except MPIL and LPIL, were difficult to assess with and without contrast enhancement and with both MDCT and CBCT (Table 2). Because two-dimensional imaging reaches its limits in such complex anatomical areas as the equine carpal joints, three-dimensional diagnostic imaging such as MRI, MDCT, and CBCT are the modalities of choice for comprehensive diagnostics. For the portrayal of cartilage lesions in equine carpal joints, computed tomographic arthrography showed a higher sensitivity than contrast-enhanced MRI scans (8), while the current study suggests that CBCT could not really join this category. Although CBCT deals with different disadvantages as mentioned before, the modality also has its merits that should be considered. Particular in regards to its practical advantages, CBCT imaging represents a valuable adjunctive and alternative modality to MDCT and other three-dimensional imaging modalities in horses. CBCT scans are mostly well tolerated even in standing sedated horses, probably because of low noise and the fast acquisition time, because neither the gantry nor the patient is moving during the examination (13). Furthermore, it can be applied both as a preoperative planning tool and due to its ability to be mobile as an intraoperative three-dimensional imaging modality in horses and lower radiation dose and acquisition costs compared to MDCT scanners are described as well as a slightly higher spatial resolution (27, 29). When it comes to the decision what kind of imaging modality should be used for different clinical cases, the diagnostic value of the chosen modality is of highest importance. However, the practicability, technical features, and purchase conditions should not be neglected either.

4.3 Visibility of MPIL and LPIL

Because the MPIL and LPIL are reported as significant sources of carpal lameness and instability in horses (30–33), they were also part of this investigation. In a study of 1992, the number of horses with MPIL injuries was suspected to be much higher than previously thought (34) but one of the biggest challenges is the significant imaging representation. Although radiography and ultrasonography can be used to assess the MPIL and LPIL, these modalities are limited. Likewise, arthroscopy as a minimally-invasive diagnostic modality has its limitations in assessing the intercarpal ligaments because of the restricted window of visualization (30, 35). In contrast, MRI and CT arthrography are valuable diagnostic imaging modalities to assess the intercarpal ligaments (30, 36). The portrayal of MPIL and LPIL after contrast enhancement in CT corresponds well with that in MRI. However, MRI requires more scan time than CT imaging, making CT arthrography a valid alternative (30). This was confirmed in the present study, where the intercarpal ligaments became reliably visible after contrast enhancement in both MDCT and CBCT imaging (Figure 4). A possible reason for the relatively low interobserver agreement (PA = 0.33) for these two intraarticular ligaments could be that one observer scored these two ligaments with an MDCT mean score of 2.00 and CBCT mean score of 1.61 while the other two observers scored them with an MDCT mean score of 3.00 and CBCT mean score of 2.95. Nevertheless, even in MDCT as well as in CBCT, they showed a significant improvement of visualization after contrast enhancement ($r_s = 0.94$) overall. To our knowledge, there are no previous studies about the portrayal of MPIL and LPIL in CBCT imaging.

4.4 Communication between carpometacarpal joint and OSL

In this study, an enrichment of contrast medium in the OSL was observed in several forelimbs after intraarticular injection in the ACJ and MCJ (Figure 5). Even if the MDCT image and the CBCT image in this figure are at the same level, the contrast medium is already more widely distributed in CBCT than in MDCT. CBCT scans were performed immediately after MDCT scans, which may have resulted in a slightly different distribution of contrast medium. In previous studies, a connection of the OSL with the CMCJ could already be shown (30, 38). Communication between areas of the carpal joint and the OSL were also registered in this study, whereupon the clinical relevance needs to be examined in more detail in further studies. The accumulation of contrast medium in the OSL could be seen in both, MDCT and CBCT. It must be noted that contrast solutions used for diagnostic anesthesia or for intraarticular medication may have different properties and therefore behave differently in life animals with weight bearing extremities and compared with the mixture of contrast agents used in this study on cadaveric specimens.

4.5 Visibility of cartilage after contrast enhancement

Cartilage was only visualized indirectly after injection of contrast enhancement. Overall, the visibility of the cartilage in contrast-enhanced scans was slightly better in MDCT than in CBCT scans, but decreased from proximal to distal in both modalities. The joint capsule of the ACJ therefore has a wide dorsal recessus and has the greatest range of motion and thus cartilaginous surface area. Further distally is the MCJ, which contributes less to the range of motion of the carpus and is less voluminous. The articulating osseous structures of the CMCJ, the bones of the distal/metacarpal row of the carpal joint, and the metacarpal bones, offer flatter joint surfaces. These are tight joints with a narrow joint capsule and therefore almost no room for joint movement (39). These morphological particularities together with the fact of thinner cartilage in the distal joint compartments (40) explain the poorer visibility of articular cartilage in distal carpal aspects.

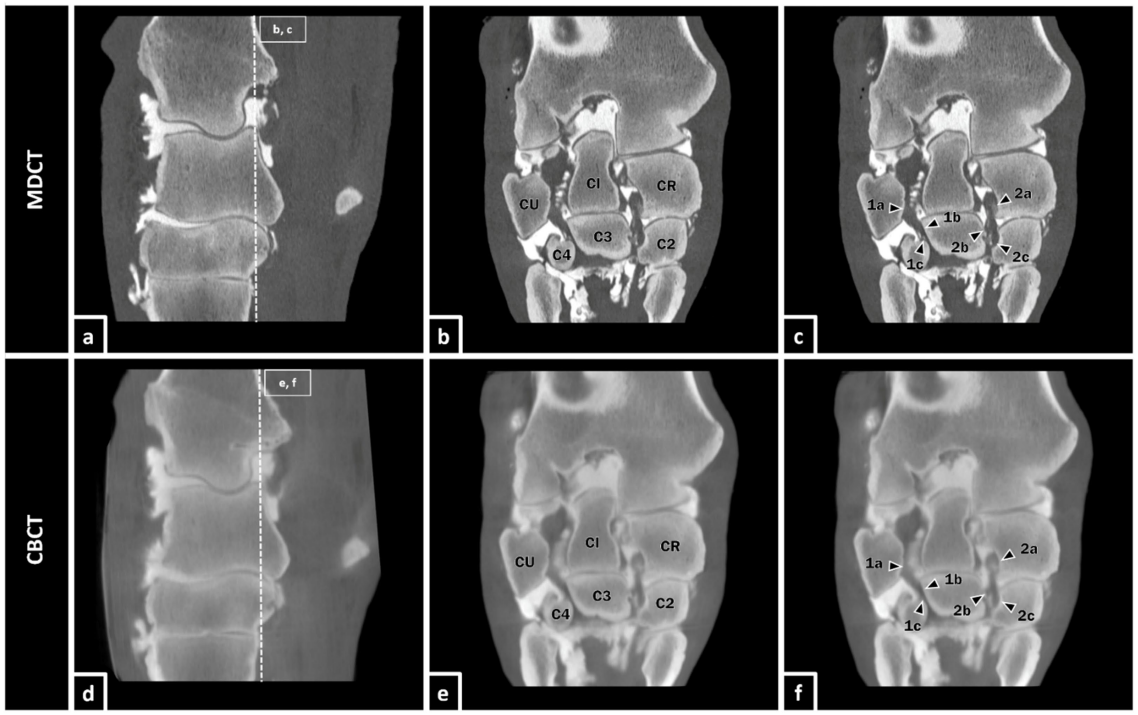

FIGURE 4
Equine carpal region in sagittal section **(a,d)**. Depiction of the MPIL and LPIL in coronal section as representants of the equine intracarpal ligaments in bone window after contrast enhancement in MDCT **(b,c)** and CBCT **(e,f)** of a 25-year-old gelding. The LPIL (1a-c) reaches from the distal part of the palmaromedial surface of the ulnar carpal bone (CU) to the proximal palmarolateral surface of the third carpal bone (C3) and also, with a few fibers, to the palmaromedial surface of the fourth carpal bone (C4). The MPIL (2a-c) ranges from the distolateral surface of the radial carpal bone (CR) to the proximal palmaromedial surface of the third carpal bone (C3) and the proximal palmarolateral aspect of the second carpal bone (C2) (37).

However, in terms of clinical relevance, this observation can probably be neglected, since the pathological changes in the articular structures tend to occur in the more proximal areas with more mobility and movement-induced stress (5–7).

4.6 Impact of evaluation

In this study, an adapted scoring system was used to compare CBCT and MDCT images with each other and among the different observers. It is about a subjective assessment as there is no objective data for comparison. In evaluation of MDCT images, Hounsfield units (HU) are used to identify structural changes and even only slight differences. A comparable parameter in CBCT is shown by gray scale (voxel value), but even if there is a strong correlation between HU in MDCT and gray levels in CBCT, it is not possible to directly convert HU in gray levels of CBCT due to the high influence of artefacts in CBCT (41). In addition, different reconstruction algorithms make a direct objective comparison impossible. This is due to technical differences between the two modalities.

For the anatomical structures in which a percent agreement of one and therefore no variance in the scores could be achieved, no r_s could be calculated, which does not mean that the r_s is equal to zero or one, but that the agreement is 100% and the r_s could not be calculated due to a lack of variance of the scores [all zero (for example category joint native CBCT as well as MDCT) or all three (for example category osseous structures native and contrast, CBCT as well as MDCT)]. This has to be taken into account when interpreting the results.

4.7 Selection of statistical parameters

In order to compare the results as best as possible, both between CBCT and MDCT as well as in native and contrast enhanced scan, we decided to perform a descriptive evaluation of the exact scores from the different recordings and also to calculate Spearman's rank correlation coefficient (r_s) and percent agreement (PA) (Table 2).

PA refers to the proportion of times that two sets of data agree, so in this case how often two observers give the same score for an anatomical structure in one setting and is therefore calculated based on the raw data values for a direct comparison. For the PA a value close to 1 defines a good agreement between the different observers. The advantages of the PA are that it shows an exact match and can be calculated for all structures, even if there is no variance in the data due to a complete match. One disadvantage that cannot be ignored, however, is that the possibility that some agreements could occur purely by chance cannot be taken into account. For this reason we also calculated the r_s, which portrays the strength and direction of association between two variables from the different devices. A correlation coefficient of $r_s > 0.4$ represents acceptable agreement and $r_s > 0.7$ represents good agreement. In this case for example it indicates if the direction of scoring is the same, even if two observers scored an anatomical structure with different scores. This parameter is calculated based on the ranks of the data rather than the raw data values. Advantages are that r_s is robust to outliers and non-linear relationships, but one important disadvantage is that r_s cannot be calculated if there is not enough variance in the present data. This is an important fact in our study, as for some structures we were unable to

calculate r_s due to complete agreement and therefore lack of variance of the data. However, a complete agreement is still a valuable statement for us, as it allows us to say that certain anatomical structures can be represented equally well or poorly in both modalities. That's why we chose these two parameters, as they each have their advantages and compensate for or take into account the disadvantages of the other parameter in the best possible way.

4.8 Limitations

Image acquisition was carried out on fresh cadaveric specimens within 24 h of death, which is why the examinations are comparable to those conducted in recumbent horses under general anesthesia rather than in standing sedated horses. Some disadvantages such as motion artefacts, which are named as major sources for repetition of examinations (13, 24), are therefore excluded from critical assessment. Furthermore, the effect of weight bearing and tension in the tissues on different anatomical structures such as outpouchings and the contribution of contrast medium could not be considered in this study. When comparing these results to findings under clinical conditions, the different properties of injection media must be considered as well. Local anesthetics for example are described to have a lower molecular weight than the here-used contrast medium, which may have influence on the distribution pattern in the tissue (37).

5 Conclusion

CBCT imaging represents a valid alternative to conventional MDCT imaging for the three-dimensional assessment of osseous structures of the equine carpal region. Regarding the evaluation of osseous tissues, both modalities yield practically equivalent diagnostic information, while avoiding limitations caused by superimposition. Therefore, and particularly when taking potential advantages regarding the practicability and technical features of CBCT imaging into account, it represents a cost-effective and practical option for diagnostic imaging for issues relating to osseous structures of the equine carpal joint. In cases that require visualization of cartilage, contrast enhancement is unavoidable, and the visualization of these structures is better in MDCT than in CBCT imaging. Soft tissue structure visualization is rather poor, regardless of modality tested here, except for the

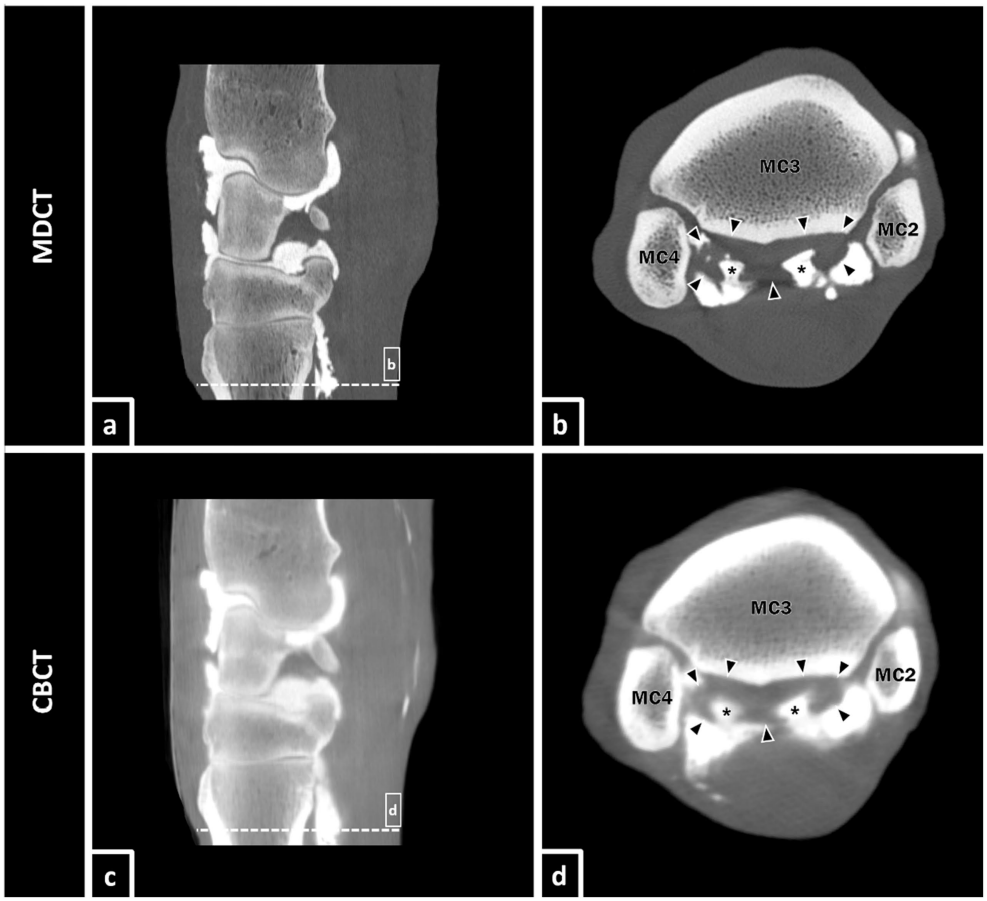

FIGURE 5
Equine carpal region in sagittal section **(a,c)**. Presence of positive contrast medium (asterisks) in the lateral and medial lobe of the proximal suspensory ligament (borders of the OSL are defined by black arrows) in transversal section **(b,d)** after injection of a mixture of contrast medium in the ACJ and MCJ. The lateral and medial palmarodistal outpouchings of the CMCJ are apparently filled with contrast medium too and it appears to exist a connection to the lobes of the OSL.

intraarticular ligaments, which are well visualized after contrast enhancement. As there is too much uncertainty, CBCT can not be recommended for visualization of cartilage and soft tissues in the equine carpal region. On the basis of the present study, further investigations are intended regarding the visualization of pathologies of the carpal region using standing CBCT in patients.

Data availability statement

The original contributions presented in the study are included in the article/supplementary material, further inquiries can be directed to the corresponding author.

Ethics statement

The animal study was approved by Animal Welfare Officer of the Justus-Liebig-University Giessen, Giessen, Germany. The study was conducted in accordance with the local legislation and institutional requirements.

Author contributions

MH: Writing – original draft. JB: Writing – review & editing. AC: Investigation, Writing – review & editing. CK: Investigation, Writing – review & editing. GM-D: Investigation, Writing – review & editing. KB: Data curation, Writing – review & editing. CS: Supervision, Writing – review & editing. MR: Supervision, Writing – review & editing.

Funding

The author(s) declare that no financial support was received for the research, authorship, and/or publication of this article.

Conflict of interest

The authors declare that the research was conducted in the absence of any commercial or financial relationships that could be construed as a potential conflict of interest.

Publisher's note

All claims expressed in this article are solely those of the authors and do not necessarily represent those of their affiliated organizations, or those of the publisher, the editors and the reviewers. Any product that may be evaluated in this article, or claim that may be made by its manufacturer, is not guaranteed or endorsed by the publisher.

References

1. Engiles JB, Stewart H, Janes J, Kennedy LA. A diagnostic pathologist's guide to carpal disease in racehorses. *J Vet Diagn Invest*. (2017) 29:414–30. doi: 10.1177/1040638717710238

2. Ross MWDS ed. Diagnosis and management of lameness in the horse. St. Louis, Mo: Elsevier/Saunders (2011).

3. Jeffcott LB, Rossdale PD, Freestone J, Frank CJ, Towers-Clark PF. An assessment of wastage in thoroughbred racing from conception to 4 years of age. *Equine Vet J*. (1982) 14:185–98. doi: 10.1111/j.2042-3306.1982.tb02389.x

4. Ramzan PHLPL. Musculoskeletal injuries in thoroughbred racehorses: a study of three large training yards in Newmarket, UK (2005-2007). *Vet J*. (2011) 187:325–9. doi: 10.1016/j.tvjl.2009.12.019

5. Steel CM, Hopper BJ, Richardson JL, Alexander GR, Robertson ID. Clinical findings, diagnosis, prevalence and predisposing factors for lameness localised to the middle carpal joint in young Standardbred racehorses. *Equine Vet J*. (2006) 38:152–7. doi: 10.2746/042516406776563332

6. Auer J. Diseases of the carpus. *Vet Clin North Am Large Anim Pract*. (1980) 2:81–100. doi: 10.1016/s0196-9846(17)30176-3

7. Baxter GM. Adams and Stashak's lameness in horses. Hoboken, NJ: John Wiley & Sons, Inc. (2020).

8. Suarez Sanchez-Andrade J, Richter H, Kuhn K, Bischofberger AS, Kircher PR, Hoey S. Comparison between magnetic resonance imaging, computed tomography, and arthrography to identify artificially induced cartilage defects of the equine carpal joints. *Vet Radiol Ultrasound*. (2018) 59:312–25. doi: 10.1111/vru.12598

9. Stewart HL, Siewerdsen JH, Nelson BB, Kawcak CE. Use of cone-beam computed tomography for advanced imaging of the equine patient. *Equine Vet J*. (2021) 53:872–85. doi: 10.1111/evj.13473

10. Hu H. Multi-slice helical CT: scan and reconstruction. *Med Phys*. (1999) 26:5–18. doi: 10.1118/1.598470

11. Kyriakou Y, Struffert T, Dörfler A, Kalender WA. Grundlagen der Flachdetektor-CT (FD-CT). *Radiologe*. (2009) 49:811–9. doi: 10.1007/s00117-009-1860-9

12. Scarfe WC, Farman AG. What is cone-beam CT and how does it work? *Dent Clin N Am*. (2008) 52:707–30. doi: 10.1016/j.cden.2008.05.005

13. Koch C, Pauwels F, Schweizer-Gorgas D. Technical set-up and case illustrations of orthopaedic cone beam computed tomography in the standing horse. *Equine Vet Educ*. (2021) 33:255–62. doi: 10.1111/eve.13290

14. Robb RA. The dynamic spatial Reconstructor: an X-ray video-fluoroscopic CT scanner for dynamic volume imaging of moving organs. *IEEE Trans Med Imaging*. (1982) 1:22–33. doi: 10.1109/TMI.1982.4307545

15. Cho PS, Johnson RH, Griffin TW. Cone-beam CT for radiotherapy applications. *Phys Med Biol*. (1995) 40:1863–83. doi: 10.1088/0031-9155/40/11/007

16. Chen BNR. Cone-beam volume CT mammographic imaging: feasibility study. *Proc SPIE*. (2001) 4320:655–664. doi: 10.1117/12.430894

17. Scarfe WC, Farman AG, Sukovic P. Clinical applications of cone-beam computed tomography in dental practice. *J Can Dent Assoc*. (2006) 72:75–80.

18. Karhade AV, Vasudeva VS, Pompeu YA, Lu Y. Image guided spine surgery: available technology and future potential. *Austin Neurosurg*. (2016) 3:1–5.

19. Carrino JA, Al Muhit A, Zbijewski W, Thawait GK, Stayman JW, Packard N, et al. Dedicated cone-beam CT system for extremity imaging. *Radiology*. (2014) 270:816–24. doi: 10.1148/radiol.13130225

20. Roza MR, Silva LAF, Barriviera M, Januario AL, Bezerra ACB, Fioravanti MCS. Cone beam computed tomography and intraoral radiography for diagnosis of dental abnormalities in dogs and cats. *J Vet Sci*. (2011) 12:387–92. doi: 10.4142/jvs.2011.12.4.387

21. Van Thielen B, Siguenza F, Hassan B. Cone beam computed tomography in veterinary dentistry. *J Vet Dent*. (2012) 29:27–34. doi: 10.1177/089875641202900105

22. Riggs GG, Arzi B, Cissell DD, Hatcher DC, Kass PH, Zhen A, et al. Clinical application of cone-beam computed tomography of the rabbit head: part 1—Normal dentition. *Front Vet Sci*. (2016) 3:93. doi: 10.3389/fvets.2016.00093

23. Riggs GG, Cissell DD, Arzi B, Hatcher DC, Kass PH, Zhen A, et al. Clinical application of cone beam computed tomography of the rabbit head: part 2-dental disease. *Front Vet Sci*. (2017) 4:5. doi: 10.3389/fvets.2017.00005

24. Pauwels FE, van der Vekens E, Christan Y, Koch C, Schweizer D. Feasibility, indications, and radiographically confirmed diagnoses of standing extremity cone beam computed tomography in the horse. *Vet Surg*. (2021) 50:365–74. doi: 10.1111/vsu.13560

25. Bierau J, Cruz AM, Koch C, Manso-Diaz G, Büttner K, Staszyk C, et al. Visualization of anatomical structures in the fetlock region of the horse using cone beam computed tomography in comparison with conventional multidetector computed tomography. *Front Vet Sci*. (2023) 10:1278148. doi: 10.3389/fvets.2023.1278148

26. Vallance SA, Bell RJW, Spriet M, Kass PH, Puchalski SM. Comparisons of computed tomography, contrast enhanced computed tomography and standing low-field magnetic resonance imaging in horses with lameness localised to the foot. Part 1: anatomic visualisation scores. *Equine Vet J*. (2012) 44:51–6. doi: 10.1111/j.2042-3306.2011.00372.x

27. Klopfenstein Bregger MD, Koch C, Zimmermann R, Sangiorgio D, Schweizer-Gorgas D. Cone-beam computed tomography of the head in standing equids. *BMC Vet Res*. (2019) 15:289. doi: 10.1186/s12917-019-2045-z

28. Jaju PP, Jain M, Singh A, Gupta A. Artefacts in cone beam CT. *OJST*. (2013) 3:292–7. doi: 10.4236/ojst.2013.35049

29. Colombo P, Moscato A, Pierelli A, Cradinale F, Torresin A. Medtronic O-arm: image quality and radiation dose assessment in 3D imaging (2012). 670 p.

30. Gray SN, Puchalski SM, Galuppo LD. Computed tomographic arthrography of the intercarpal ligaments of the equine carpus. *Vet Radiol Ultrasound*. (2013) 54:245–52. doi: 10.1111/vru.12033

31. Bramlage LR, Schneider RK, Gabel AA. A clinical perspective on lameness originating in the carpus. *Equine Vet J Suppl*. (1988) 20:12–8. doi: 10.1111/j.2042-3306.1988.tb04642.x

32. Whitton RCRR. The intercarpal ligaments of the equine midcarpal joint, part 2: the role of the palmar intercarpal ligaments in the restraint of dorsal displacement of the proximal row of carpal bones. *Vet Surg*. (1997) 26:367–73. doi: 10.1111/j.1532-950x.1997.tb01695.x

33. Kannegieter NJCS. The incidence and severity of intercarpal ligament damage in the equine carpus. *Aust Vet J*. (1993) 70:89–91. doi: 10.1111/j.1751-0813.1993.tb03283.x

34. McIlwraith CW. Tearing of the medial palmar intercarpal ligament in the equine midcarpal joint. *Equine Vet J*. (1992) 24:367–71. doi: 10.1111/j.2042-3306.1992.tb02857.x

35. Whitton RC, Kannegieter NJ, Rose RJ. Postoperative performance of racing horses with tearing of the medial palmar intercarpal ligament. *Aust Vet J*. (1999) 77:713–7. doi: 10.1111/j.1751-0813.1999.tb12905.x

36. Nagy ADS. Magnetic resonance anatomy of the carpus of the horse described from images acquired from low-field and high-field magnets. *Vet Radiol Ultrasound*. (2011) 52:273–83. doi: 10.1111/j.1740-8261.2010.01773.x

37. Whitton RC, McCarthy PH, Rose RJ. The intercarpal ligaments of the equine midcarpal joint, part 1: the anatomy of the palmar and dorsomedial intercarpal ligaments of the midcarpal joint. *Vet Surg*. (1997) 26:359–66. doi: 10.1111/j.1532-950x.1997.tb01694.x

38. Gerdes C, Morgan R, Terry R, Foote A, Smith R. Computed tomographic arthrography, gross anatomy and histology demonstrate a communication between synovial invaginations in the proximal aspect of the third interosseous muscle and the carpometacarpal joint in horses. *Front Vet Sci*. (2022) 9:958598. doi: 10.3389/fvets.2022.958598

39. Nickel R, Schummer A, Seiferle E. Lehrbuch der Anatomie der Haustiere. Berlin, Hamburg: Parey (2004). 625 p.

40. Andersen C, Griffin JF, Jacobsen S, Østergaard S, Walters M, Mori Y, et al. Validation of ultrasonography for measurement of cartilage thickness in the equine carpus. *Vet Radiol Ultrasound*. (2022) 63:478–89. doi: 10.1111/vru.13085

41. Molteni R. Prospects and challenges of rendering tissue density in Hounsfield units for cone beam computed tomography. *Oral Surg Oral Med Oral Pathol Oral Radiol*. (2013) 116:105–19. doi: 10.1016/j.oooo.2013.04.013

frontiers | Frontiers in Veterinary Science

TYPE Original Research
PUBLISHED 09 December 2024
DOI 10.3389/fvets.2024.1506670

OPEN ACCESS

EDITED BY
Ozan Gündemir,
Istanbul University Cerrahpasa, Türkiye

REVIEWED BY
Rui Alvites,
University of Oporto, Portugal
Howard Dobson,
Invicro, United States
Didar Aydin Kaya,
Istanbul University-Cerrahpasa, Türkiye

*CORRESPONDENCE
Elizabeth Boudreau
✉ bboudreau@cvm.tamu.edu

RECEIVED 05 October 2024
ACCEPTED 11 November 2024
PUBLISHED 09 December 2024

CITATION
DuPont EB and Boudreau E (2024) Canine medial retropharyngeal lymph node measurements on T2 spin-echo sequences at 3T.
Front. Vet. Sci. 11:1506670.
doi: 10.3389/fvets.2024.1506670

Canine medial retropharyngeal lymph node measurements on T2 spin-echo sequences at 3T

Emily B. DuPont and Elizabeth Boudreau*

School of Veterinary Medicine and Biomedical Sciences, Department of Small Animal Clinical Sciences, Texas A&M University, College Station, TX, United States

Introduction: The objective of this study is to estimate reference values for medial retropharyngeal lymph nodes (MRLNs) measured in high-field (3T) MRI studies of the canine head/brain using transverse T2 spin-echo images and to determine if dogs with structural brain disease exhibit medial retropharyngeal lymph nodes that are larger than expected from estimated reference values.

Methods: The study population comprises 142 MRLNs from 71 dogs with no evidence of structural brain disease and normal CSF evaluation and 116 MRLNs from 58 dogs with structural brain disease confirmed by histopathology as of infectious or neoplastic origin, or to represent meningoencephalitis of unknown etiology.

Results: Based on this sample, MRLNs are expected to measure 2.9–12.4 mm in maximum short-axis transverse diameter. Interobserver measurement differences are ~1 mm in 95% of the sampled subjects. Lymph node size is correlated with body weight (R = 0.47–0.52) and age (R = −0.39 – −0.47).

Discussion: No difference was found between the lymph node size of dogs with structural brain disease of any type, or overall, compared to that of dogs without structural brain disease.

KEYWORDS

cervical, MUO, glymphatic, magnetic resonance imaging, dog

1 Introduction

The idea of lymphatic vessels contributing to the drainage of cerebrospinal fluid (CSF) from the central nervous system has been a topic of ongoing investigation over the past few decades. It has been demonstrated that across numerous mammalian species, CSF exits the central nervous system to enter the lymphatics present in the nasal submucosa (Figure 1) (1, 2). This pattern remained constant among the species studied, suggesting it could be a feature in all mammals. In the dog, the tissues of the head, including the nasal cavity, drain in part via lymphatic vessels to the retropharyngeal lymph center (3). It has been shown experimentally that fluid injection into the subarachnoid space of a dog results in increased cervical lymphatic drainage (4).

The retropharyngeal lymph center in the dog is most consistently represented by the medial retropharyngeal lymph node (MRLN), which also serves as the collective terminal for drainage from midline structures of the head, including the nasal cavity.

Given the evidence of drainage of the CSF from the central nervous system to the nasal lymphatics and the known pathway from the nasal lymphatics to the retropharyngeal lymph center, it can be suspected that there may be a connection between the CSF and the retropharyngeal lymph center. There has been speculation that disease of the central nervous system may impact the size or appearance of the MRLNs due to this supposed connection. Although previous studies have investigated the size of MRLNs in dogs using the modalities

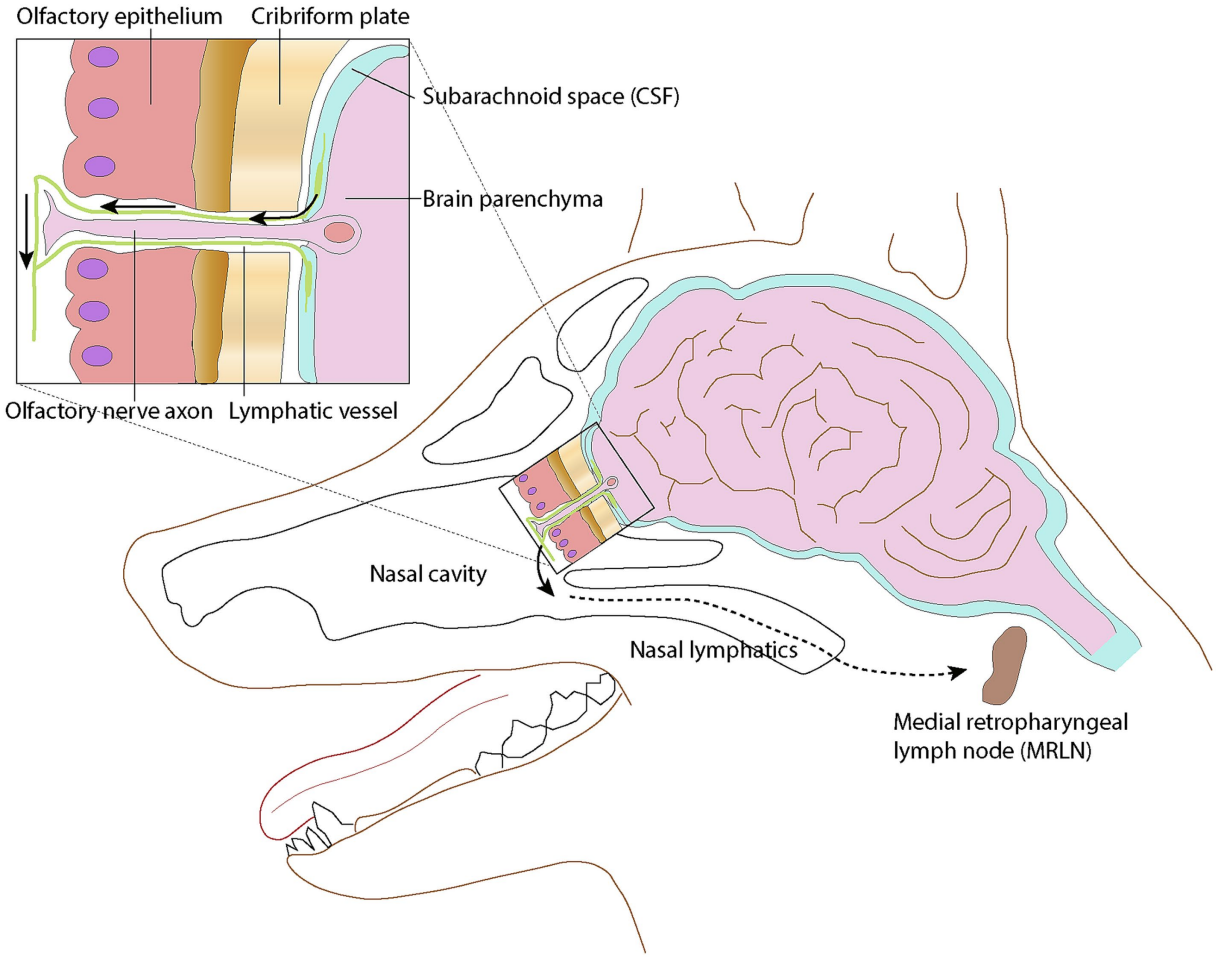

FIGURE 1
Schematic representation of the lymphatic drainage pathway via the cribriform plate into the nasal lymphatics. Lymphatic vessels surround olfactory nerve cell axons as they penetrate the cribriform plate, then merge with lymphatic vessels in the submucosa of the caudal nasal cavity. Modified from (1); licensed under CC BY 4.0.

of ultrasound, CT, and MRI, as well as their characteristics in various head and neck diseases, their appearance and size in the context of central nervous system diseases have not been extensively studied.

The medial retropharyngeal lymph node can be imaged during MRI studies of the brain and cranial cervical spine; however, they are not routinely or intentionally included, and there have been few studies investigating the appearance or size of the medial retropharyngeal lymph node using MRI in dogs. To the authors' knowledge, there have been no studies directly comparing the MRI appearance of medial retropharyngeal lymph nodes of neurologically normal dogs to dogs with structural brain disease. In a study looking at the appearance of inflammatory vs. neoplastic medial retropharyngeal lymph nodes in dogs and cats, neoplastic lymph nodes were found to often be bigger in size than those with inflammatory disease (5). The possibility of using the size of the medial retropharyngeal lymph nodes as an aid in suspecting potential etiologies for structural brain disease remains a topic in need of further investigation.

This study aimed to first summarize the size of the medial retropharyngeal lymph nodes in normal dogs without evidence of structural brain disease and second to determine if their size was increased in dogs with structural brain disease. The hypothesis was that there could be enlargement of the medial retropharyngeal lymph nodes with neoplastic, infectious, or immune-mediated diseases of the central nervous system, likely due to reactivity from drainage of the CSF.

2 Materials and methods

2.1 Case selection

This was a single-institution retrospective study evaluating canine brain MRIs performed on a single 3T MRI[1] over 12 years (2011–2023). Identified subjects were required to have transverse T2-weighted spin-echo images without fat suppression (TR: 3500–8,000 ms; TE: 85–96 ms; slice thickness 2.5–3.0 mm) that included both left and right MRLNs at their maximal transverse diameter.

Control subjects were defined as dogs with finalized MRI interpretations that did not identify any structural abnormalities of the imaged region and a normal cerebrospinal fluid analysis, defined

1 MAGNETOM Verio, Siemens Medical Solutions USA, Inc., Malvern, PA.

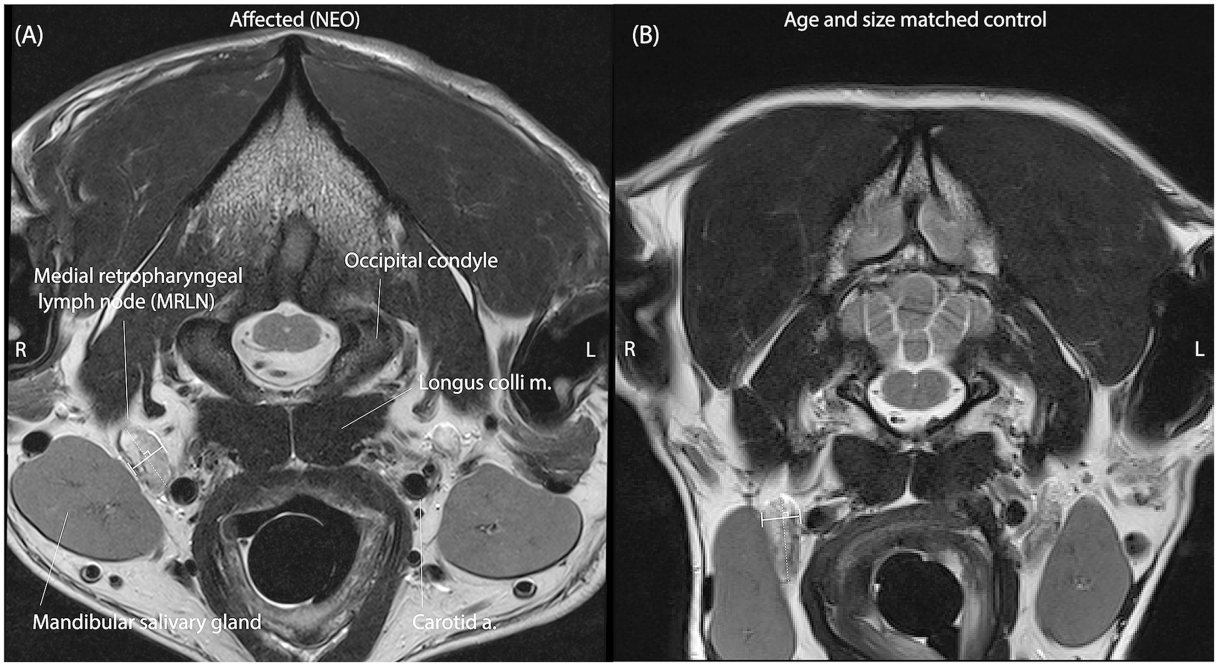

FIGURE 2
Representative T2 spin-echo slices are selected by both observers independently to represent the M_SATD of the right medial retropharyngeal lymph node in two different dogs. **(A)** A dog with intracranial neoplasia (affected subgroup NEO). **(B)** A dog of similar size and age from the control group. Anatomical landmarks for identification of the MRLN are labeled in panel A. In each panel, the solid white line between perpendicular shorter white lines illustrates the selected short-axis transverse diameter of the lymph node for the represented slice.

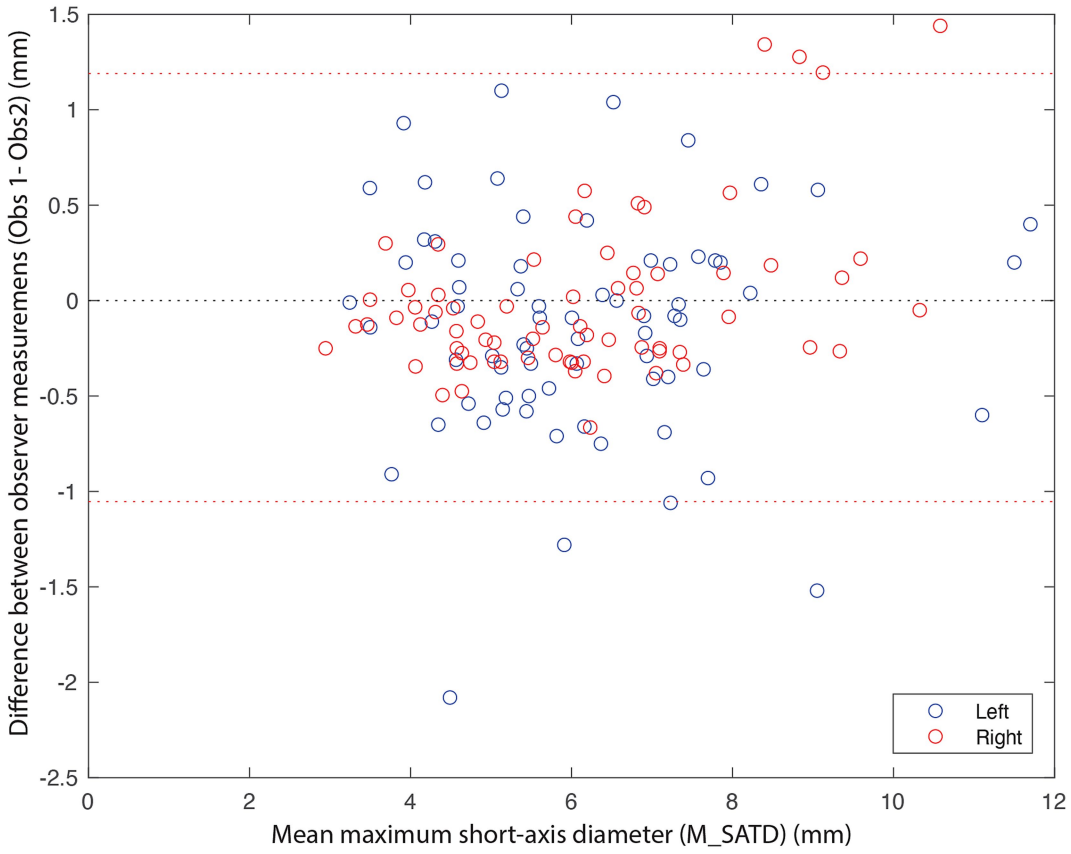

FIGURE 3
Bland–Altman plot of M_SATD measurements by two observers for the left (blue circles) and right (red circles) medial retropharyngeal lymph nodes of all control cases (n = 142). The red dotted lines indicate the 2.5 and 97.5% quantiles of differences between the measurements of the two observers. The black dotted line indicates 0.

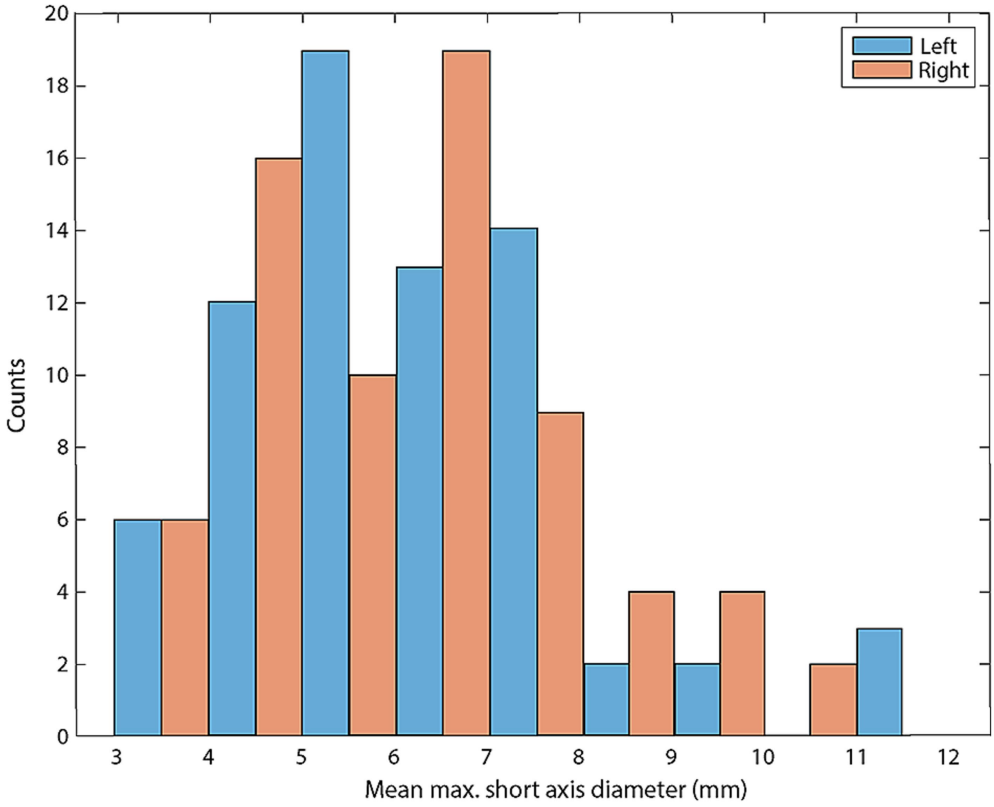

FIGURE 4
Histogram of mean M_SATD for each control lymph node (in mm; n = 142). Blue bars indicate left medial retropharyngeal lymph nodes and red bars indicate right medial retropharyngeal lymph nodes.

as ≤5 nucleated cells/μL, ≤30μg/dL protein, and hemodilution ≤ 500 RBC/μL.

Affected subjects were required to have necropsy or biopsy-confirmed diagnoses and were categorized into one of the three etiological groups: infectious (INF), meningoencephalitis of unknown etiology (MUO), or primary CNS neoplasia (NEO).

2.2 Lymph node measurement

MRLNs were identified by their location medial to the mandibular salivary gland and lateral to the common carotid artery near the level of the atlanto-occipital joint (Figure 2) (6). Two observers blinded to all clinical information viewed only the T2 transverse spin-echo series and identified slices representing the maximum short-axis transverse diameter (M_SATD) of the left and right MRLNs independently. In cases where more than one MRLN was identified on a side, only the larger one was recorded. For both the left and right sides, each observer used a caliper to estimate the M_SATD in millimeters (7).

2.3 Statistical analysis

Descriptive statistics, histograms, correlation coefficients, and Bland–Altman plots were generated using MATLAB.[2] A Shapiro–Wilk test was used to evaluate normality. A 95% confidence interval for the difference in observer measurements is reported as quantiles. Intra-class correlation coefficients and 95% confidence intervals were calculated using MedCalc.[3] For the estimation of reference intervals, the Clinical & Laboratory Standards Institute (CLSI) guidelines (8) were followed as instantiated in MedCalc (see text footnote 3). The averages of the two observers' measurements were Box–Cox transformed with lambda estimated from each data set. A Shapiro–Wilk test was used again to evaluate normality, and Tukey's test was used to identify outliers. The robust method with 10,000 Boostrap iterations was used to calculate the 90% CI for the upper and lower limits of the reference intervals. General mixed-effects linear regression was performed on log-transformed control measurements in MATLAB (see text footnote 2) using the Statistics and Machine Learning Toolbox function fitglme, with age and weight as fixed effects variables and side (left or right), observer, and subject as random effects variables. The residuals were visually inspected for outliers, and the model was refit after their removal.

A Kruskal–Wallis test, as instantiated in MATLAB (see text footnote 2), was used to evaluate for differences in age and weight between affected subgroups. Repeated-measures ANOVA, as instantiated in MATLAB (see text footnote 2), on rank-transformed data, was used to evaluate the effect of the etiological group (INF, MUO, or NEO) on the difference between measured lymph node size

2 MATLAB R2022a Update 2, maci64, MathWorks, Natick, MA.

3 MedCalc Statistical Software version 22.023, MedCalc Software, Ltd., Ostend, Belgium.

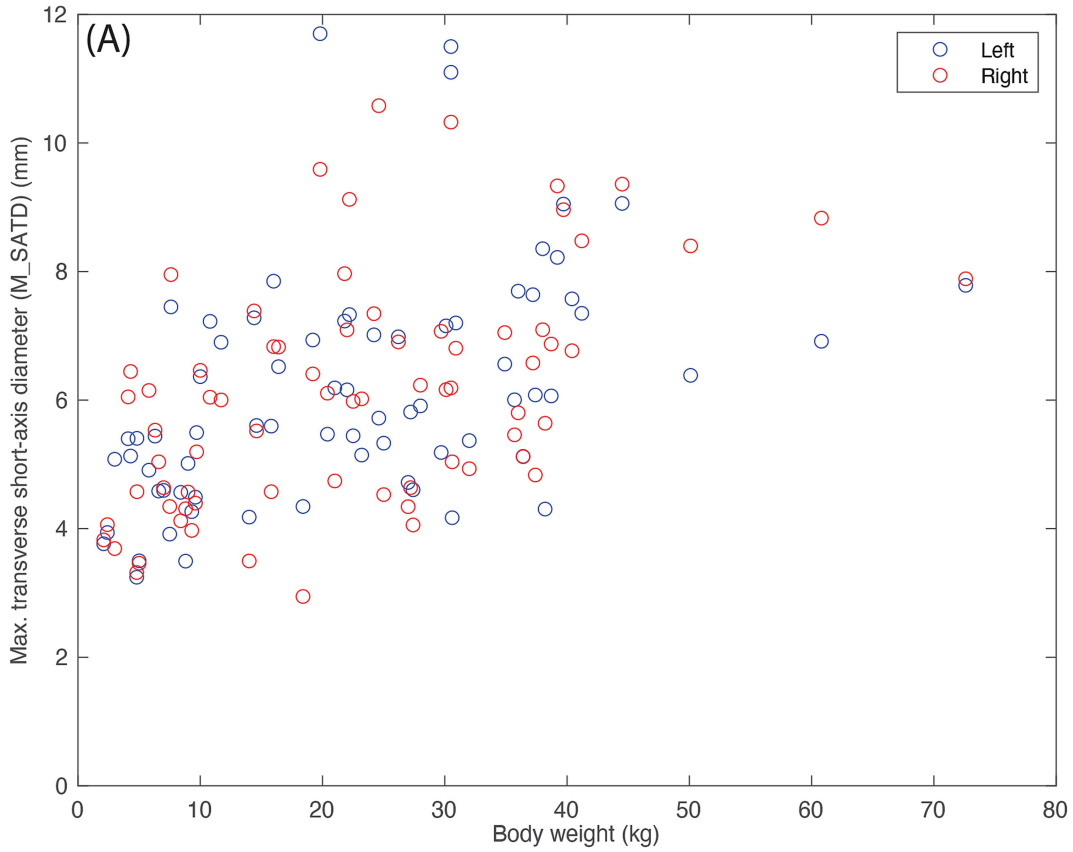

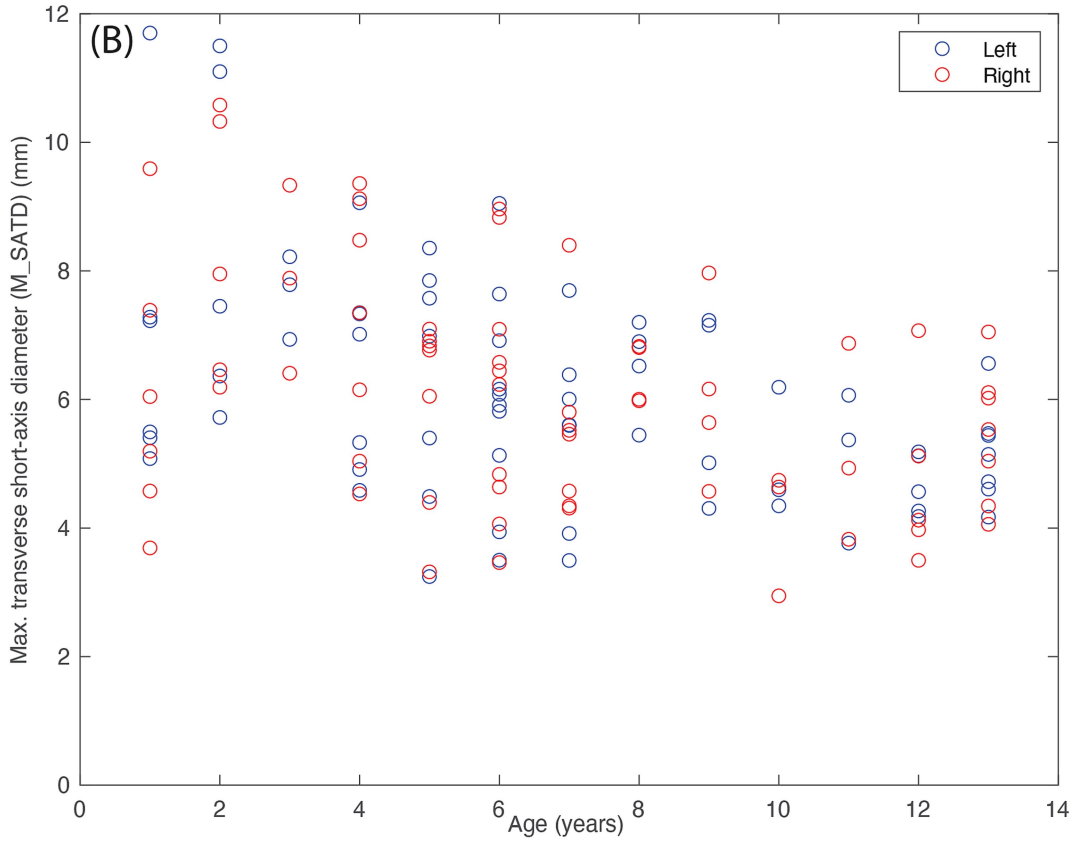

FIGURE 5
Lymph node size (average of the measurements of the two observers). **(A)** As a function of body weight (in kg), and **(B)** as a function of age (in years) for control subjects (n = 142). Blue circles indicate left medial retropharyngeal lymph nodes, and red circles indicate right medial retropharyngeal lymph nodes.

TABLE 1 Reference ranges with 90% CI of the lower and upper bound for left and right MRLN in control subjects (n = 71 for left and n = 71 for right).

Reference ranges for left and right medial retropharyngeal lymph node M_SATD in control subjects (mm)				
	Lower bound	90% CI	Upper bound	90% CI
Left	3.5	3.2–3.8	11	9.9–12.4
Right	3.2	2.9–3.6	10.1	9.3–10.9

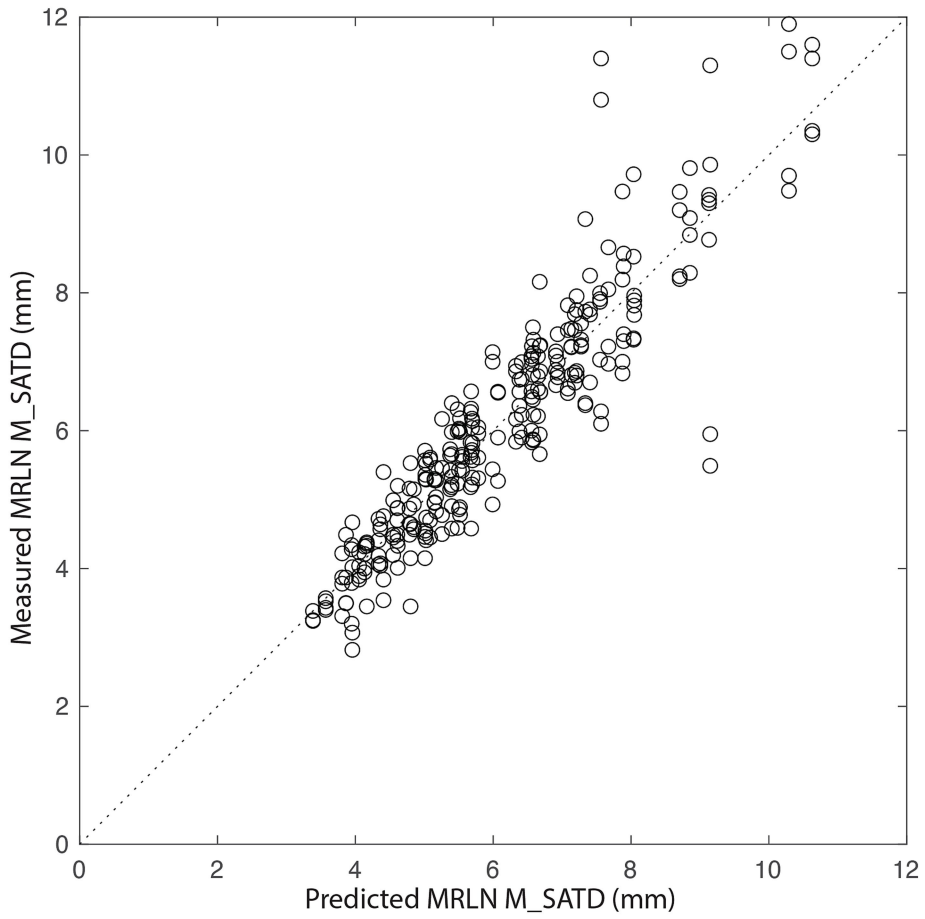

FIGURE 6
Measured MRLN size vs. that predicted by the generalized linear mixed-effects model. The dotted line represents y = x. Each circle is a single measurement for a single MRLN (left or right) for a single observer (n = 284).

AND the size predicted by the linear regression model established from the control data. A p-value of <0.05 was used to reject null hypotheses (Figures 1, 2).

3 Results

3.1 Control subjects

In total, 71 control subjects were identified. The median age of the control subjects was 6 years (1–13), and the median weight was 22 kg (2.1–72.6). A Bland–Altman plot was used to qualitatively assess inter-observer agreement for the measurement of M_SATD (Figure 3). The 95% CI for the difference in measurements between the two observers was [−1.0–1.2 mm]. The intraclass coefficient for the two observers was 0.92 (95% CI: 0.89–0.94). The distribution of the average of the two observers' measurements for the control sample is shown in Figure 4.

The average of the two observers' measurements was modestly correlated with weight (Figure 5A; R_{left} = 0.47 and R_{right} = 0.52) and anti-correlated with age (Figure 5B; R_{left} = −0.47 and R_{right} = −0.39). Based on these average measurements, reference intervals were created for left and right MRLN as described above (Table 1). Transformed data were normally distributed, and no outliers were identified.

To further evaluate the relationship of body weight and age to lymph node size, we created a general linear mixed-effects regression model for lymph node size based on subject age and weight using control data, as described above. The initial model was refit after the removal of outliers (9/284 values). In the final model, residuals were normally distributed, and R^2 = 0.90. Figure 6 shows the relationship

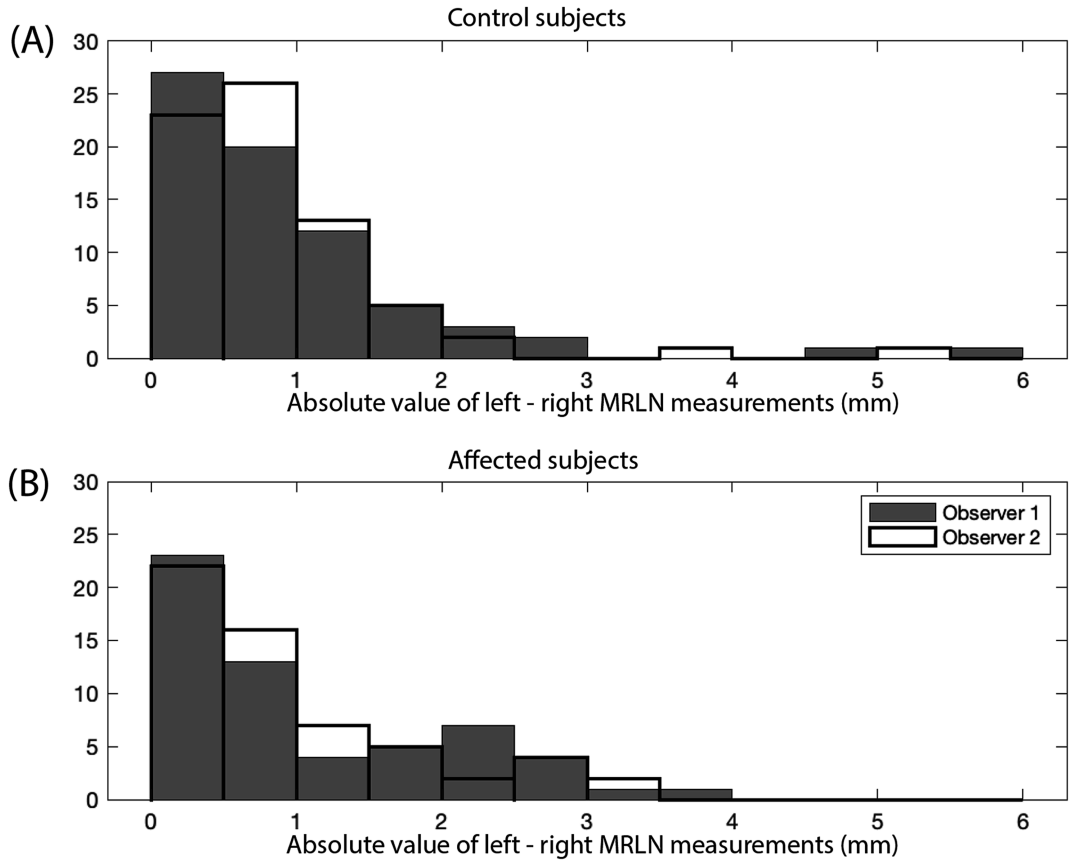

FIGURE 7
Absolute value of the difference between left and right MRLN measurements (mm). Measurements for observer 1 are shown as gray bars, and measurements for observer 2 are shown as black outlined bars. **(A)** Control subjects (n = 142), and **(B)** affected subjects (n = 116).

TABLE 2 Diagnoses for affected subjects in each subcategory (MUO, INF, and NEO), total n = 58.

Specific diagnoses for affected subjects		
	Diagnosis	Counts
MUO (n = 21)	Necrotizing meningoencephalitis	5
	Granulomatous meningoencephalitis	7
	Undefined meningoencephalitis	9
INF (n = 10)	Fungal	6
	Protozoal	2
	Viral	1
	Bacterial (abscess)	1
NEO (n = 27)	Meningioma	11
	Glioma	13
	Choroid plexus papilloma	2
	Malignant peripheral nerve sheath tumor	1

between measured lymph node size and that predicted by the final model. The largest lymph node sizes are not well-predicted by the model, with a bias toward underestimation.

Left–right asymmetry for the MRLNs was generally small (Figure 7A). The median difference between left and right MRLNs was 0.68 mm (range 0.05–4.9) based on average measurements for the control subjects.

3.2 Affect subjects

In total, 58 affected subjects were identified. These comprised 10 subjects with infectious disease (INF), 21 subjects with meningoencephalitis of unknown origin (MUO), and 27 subjects with primary nervous system neoplasia (NEO) (Table 2). The median age of the affected subjects was 6 years (1–13), and the

TABLE 3 Median and range for lymph node size (average measurements of the two observers) for affected subgroups (MUO, INF, and NEO) and predictions of same based on a linear regression model created from control subject data.

Measured and predicted M_SATD in affected subjects (mm)							
		Median		Min		Max	
		Measured	Predicted	Measured	Predicted	Measured	Predicted
MUO ($n = 21$)	Left	6	5.5	4.6	4.1	9.1	8.9
	Right	6.1	5.7	4.5	4.1	9.1	8.6
INF ($n = 10$)	Left	8	7.5	4.9	5.5	10.8	8.9
	Right	8	7.7	5.2	4.7	10.8	8.6
NEO ($n = 27$)	Left	6.1	6.1	3.2	4.1	10.4	8.9
	Right	6	5.9	3.3	4.1	9.6	8.6

median weight was 22 kg (2.1–54.5). For the subgroups, the median age of INF was 3.5 years (1–11), and the median weight was 26.8 kg (9.2–39.5). The median age of MUO was 5 years (1–12), and the median weight was 9.2 kg (2.1–33.6). The median age of NEO was 8 years (3–13), and the median weight was 29.1 kg (4.2–54.5). Dogs with infectious brain disease or MUO, were younger than those with primary CNS neoplasia ($p = 0.02$). Dogs with MUO were smaller than those with infectious brain disease or CNS neoplasia ($p < 10^{-3}$).

Lymph node measurements are again reported as the average of the measurements of two observers. The median and range of lymph node size for each affected subgroup are shown in Table 3. Asymmetry between left and right MRLN was similar between affected subjects and control subjects (Figure 7B, as compared to Figure 7A). The median difference between left and right MRLNs was 0.23 mm (range 0–1.26) based on average measurements for the affected subjects.

3.3 Comparison of affected subjects to expected lymph node size based on control subjects

For each affected subject, the average M_SATD of the left and right MRLNs, as measured by the two observers, was compared to the reference ranges established for the control data set. No lymph nodes were larger than the upper 90% CI of the estimated reference range.

We then predicted the expected size of the left and right MRLNs in affected subjects, using the age and weight of the affected subjects as input to the linear regression model created using control subject data. The median predicted measurement and range are shown alongside the measured values for each affected subgroup in Table 3. Figure 8 shows the relationship between measured and predicted lymph node size, separated by affected subgroup. The median value of the difference between measured and predicted lymph node size was not different from zero for any subgroup.

4 Discussion

The measured maximum short-axis diameter of the MRLNs in dogs using T2 spin-echo transverse images acquired on 3T MRI had similar minimum values but higher maximum values than those previously reported for CT (7). In contrast, the range of measured values was slightly narrower than those reported sonographically (9). These measurements were similar between the two independent observers.

For dogs with structurally normal brains, body weight and age had a modest relationship to MRLN size, consistent with previous reports using ultrasound (9). The relationship between age, weight, and lymph node size was generally well-represented by a generalized mixed-effects linear regression model for all but the largest lymph nodes, which were associated with the largest and youngest dogs. This discrepancy may be due to the small number of control subjects within this demographic in our sample or could indicate a more complex interplay between body weight and the maturation of MRLNs.

Compared to a reference range based on dogs with normal head/brain MRI and normal CSF tap, dogs with a diagnosis of infectious brain disease, MUO, or primary CNS neoplasia had similar MRLN size. This is likely due to the wide reference range of lymph node sizes for control subjects. There were age- and weight-related differences among the subjects in the affected subgroups, consistent with previously reported demographic characteristics associated with disease risk. When a linear model designed to account for age- and weight-related variability in lymph node size was used to predict MRLN size in dogs with structural brain disease, small systematic differences were seen between predicted and measured sizes, though these did not reach significance. Specifically, the model tended to underestimate lymph node size for dogs with infectious brain disease. However, these dogs were also significantly younger (and slightly larger) than the control subject sample, and the model is demonstrated to underestimate lymph node size in such cases, regardless of disease state. Therefore, we conclude that MRLN size is not consistently larger in dogs with structural infectious brain disease than in control subjects.

Limitations of this study include its retrospective nature and small sample size. Due to variations in dog head size and shape, medial retropharyngeal lymph nodes are not routinely included in the evaluation of the canine brain, so few available studies met our inclusion criteria. Given the correlation, though modest, between lymph node size and subject body weight and age, more accurate reference ranges for normal canine medial retropharyngeal lymph node size could be generated from data stratified by these variables. However, our control sample is too small to allow for useful estimation of normal population parameters in subgroups; furthermore, the between-subject variability in lymph node size is relatively large compared to the

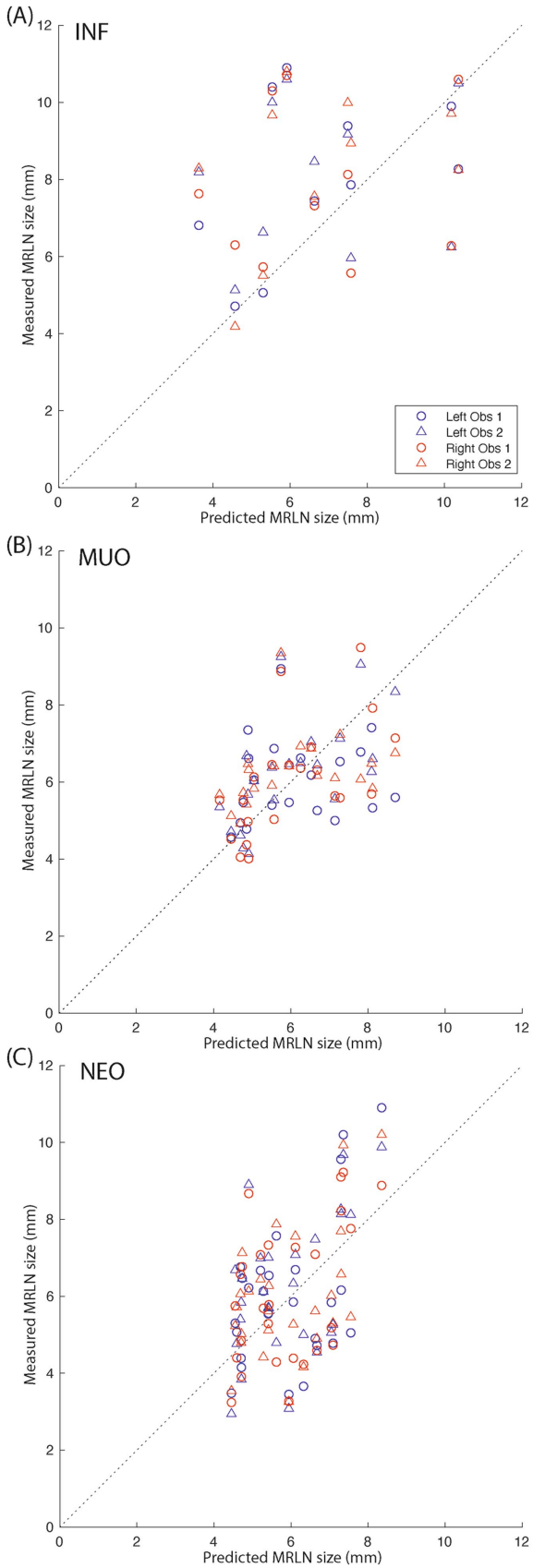

FIGURE 8
Measured vs. predicted lymph node size for affected subjects. **(A)** Infectious subjects; **(B)** subjects with MUO; and **(C)** subjects with intracranial neoplasia. The dotted black lines indicate y = x. Blue markers indicate left medial retropharyngeal lymph nodes, and red markers indicate right medial retropharyngeal lymph nodes. Circles indicate observer 1 measurements, and triangles indicate observer 2 measurements.

effects attributable to age and body weight, so reference ranges are expected to remain relatively broad even if these factors can be accounted for. An additional concern is that the control sample may not accurately reflect a truly normal population of dogs, given that these dogs underwent brain MRI due to clinical findings consistent with neurological disease.

Within the limits of this study, MRLN size in dogs, measured as M_SATD on transverse T2 spin-echo 3T MRI, is similarly estimated by independent observers, depends mildly on body weight and age, and cannot be used to prioritize differentials for structural brain disease. Despite the failure of this study to reject the null hypothesis, we believe there are several avenues available for future investigation of the relationship between intracranial disease lymphatics of the head and neck. Size is just one parameter that may indicate lymphadenopathy; evaluation of additional imaging parameters (such as the pattern of contrast enhancement post-gadolinium), though potentially more difficult to standardize between observers, may be more sensitive markers of lymph node disease. Given high inter-individual variability, a within-subject comparison design, such as the evaluation of lymph node size in the same individuals in diseased (pre-treatment) vs. healthy (post-treatment) states, may also be better suited to detect small changes in lymph node size. Finally, direct sampling of the medial retropharyngeal lymph nodes, either premortem (such as under ultrasound guidance) or on postmortem histology, may provide a complementary method to detect changes in the cellular makeup of these tissues in association with different intracranial disease states.

Data availability statement

The raw data supporting the conclusions of this article will be made available by the authors, without undue reservation.

Author contributions

ED: Writing – original draft, Writing – review & editing. EB: Writing – original draft, Writing – review & editing.

Funding

The author(s) declare that no financial support was received for the research, authorship, and/or publication of this article.

Conflict of interest

The authors declare that the research was conducted in the absence of any commercial or financial relationships that could be construed as a potential conflict of interest.

Generative AI statement

The authors declare that no Generative AI was used in the creation of this manuscript.

Publisher's note

References

1. Chae J, Choi M, Choi J, Yoo SJ. The nasal lymphatic route of CSF outflow: implications for neurodegenerative disease diagnosis and monitoring. *Anim. Cells Syst.* (2024) 28:45–54. doi: 10.1080/19768354.2024.2307559

2. Johnston M, Zakharov A, Papaiconomou C, Salmasi G, Armstrong D. Evidence of connections between cerebrospinal fluid and nasal lymphatic vessels in humans, non-human primates and other mammalian species. *Cerebrospinal Fluid Res.* (2004) 1:2. doi: 10.1186/1743-8454-1-2

3. Belz GT, Heath TJ. Lymph pathways of the medial retropharyngeal lymph node in dogs. *J Anat.* (1995) 187:517–26.

4. Leeds SE, Kong AK, Wise BL. Alternative pathways for drainage of cerebrospinal fluid in the canine brain. *Lymphology.* (1989) 22:144–6.

5. Johnson PJ, Elders R, Pey P, Dennis R. Clinical and magnetic resonance imaging features of inflammatory versus neoplastic medial retropharyngeal lymph node mass lesions in dogs and cats. *Vet Radiol Ultrasound.* (2016) 57:24–32. doi: 10.1111/vru.12288

6. Kneissl S, Probst A. Magnetic resonance imaging features of presumed normal head and neck lymph nodes in dogs. *Vet Radiol Ultrasound.* (2006) 47:538–41. doi: 10.1111/j.1740-8261.2006.00182.x

7. Belotta AF, Sukut S, Lowe C, Waldner C, Randall EK, MacDonald VS, et al. Computed tomography features of presumed normal mandibular and medial retropharyngeal lymph nodes in dogs. *Can J Vet Res.* (2022) 86:27–34.

8. CLSI. Defining, establishing, and verifying reference intervals in the clinical laboratory. Pennsylvania: Clinical and laboratory standards institute (2016).

9. Ruppel MJ, Pollard RE, Willcox JL. Ultrasonographic characterization of cervical lymph nodes in healthy dogs. *Vet Radiol Ultrasound.* (2019) 60:560–6. doi: 10.1111/vru.12784

frontiers | Frontiers in Veterinary Science

TYPE Original Research
PUBLISHED 23 December 2024
DOI 10.3389/fvets.2024.1496944

OPEN ACCESS

EDITED BY
Ozan Gündemir,
Istanbul University Cerrahpasa, Türkiye

REVIEWED BY
Lora Koenhemsi,
Istanbul University Cerrahpasa, Türkiye
Yusuf Altundag,
Istanbul University-Cerrahpasa, Türkiye

*CORRESPONDENCE
Min Su Kim
✉ minsukim@snu.ac.kr

RECEIVED 15 September 2024
ACCEPTED 27 November 2024
PUBLISHED 23 December 2024

CITATION
Umh H, Youp K-a, Lee J, Seo D, Lim S, Namgoong B, Choe A, Hong H, Lee N, Kim I, Yoon J, Choi J, Lee K, Yoon H and Kim MS (2024) Morphologic study of patent ductus arteriosus based on computed tomography data in 25 dogs.
Front. Vet. Sci. 11:1496944.
doi: 10.3389/fvets.2024.1496944

Morphologic study of patent ductus arteriosus based on computed tomography data in 25 dogs

Heesung Umh[1], Kyoung-a Youp[2], Jeongmin Lee[2], Daeyun Seo[1], Seongsoo Lim[1], Beomkwan Namgoong[1], Ahreum Choe[1], Hyeajeong Hong[1], Nanju Lee[1], Isong Kim[1], Junghee Yoon[1], Jihye Choi[1], Kichang Lee[3], Hakyoung Yoon[3] and Min Su Kim[1]*

[1]Department of Veterinary Clinical Science, College of Veterinary Medicine and Research Institute for Veterinary Science, Seoul National University, Seoul, Republic of Korea, [2]Korea Animal Medical Center, Cheongju-si, Chungcheongbuk-do, Republic of Korea, [3]College of Veterinary Medicine, Jeonbuk National University, Jeonju, Republic of Korea

Introduction: The objective of this study is to analyze the morphology and measurement dimensions of patent ductus arteriosus (PDA) based on computed tomography images.

Methods: The present study retrospectively evaluated computed tomography angiography data from 25 client-owned dogs diagnosed with PDA. PDA was reconstructed based on the central axis and the minimum diameter, ampulla diameter, angle, ampulla cross-section area, and length values were measured at specific measurement sites. Additionally, the minimum diameter ratio, ampulla diameter ratio, ampulla cross-section diameter, and ampulla cross-section diameter/ampulla diameter ratio values were calculated based on direct measurement values.

Results and discussion: The morphology of PDA was distributed as follows: 48% Type IIA, 20% Type IIB, and 32% Type III. A significant correlation was observed between the minimal diameter sagittal and transverse and the ampulla diameter sagittal and transverse, body weight, and angle (descending aorta to PDA). A significant association was observed between ampulla diameter (in both the sagittal and transverse planes) and body weight. The minimal diameter ratio did not demonstrate a significant correlation with the ampulla diameter, body weight, angle and length. However, the ampulla diameter ratio exhibited a significant correlation with the length of the PDA and the angle (descending aorta to PDA). The minimal diameter ratio displayed results that were more closely approximated by a circle, whereas the ampulla diameter ratio showed results that were relatively oval. The ampulla cross-section diameter values differed by an average of 14% from the previously used reference length, ampulla diameter sagittal.

Conclusion: The computed tomography image demonstrated the distinctive cross-sectional configuration of the PDA, which could potentially facilitate advanced pre-procedural planning or the creation of novel occluding devices in the future.

KEYWORDS

patent ductus arteriosus, intervention, computed tomography, morphology, dimension

1 Introduction

Patent ductus arteriosus (PDA) is common cause of canine congenital heart disease (1). The mortality rate of PDA is reported to be 64% within one year without proper closure and is 16.9 times higher than in patients who undergo closure. Therefore, PDA ductal closure is recommended as soon as possible when left-to-right PDA is diagnosed (2–4). In veterinary medicine, mechanical closure, such as open surgical ligation or minimally invasive techniques, is the mainstay of treatment to close PDAs (4, 5). Recent studies have demonstrated that minimally invasive techniques can be a good alternative for patients with PDA when surgical ligation is not suitable, showing good results with fewer complications and comparable survival rates to surgical ligation (6, 7). However, the placement of inappropriately sized occlusion devices can lead to several sizing complications (8), including device embolization, mild to severe residual flow, and deformation or protrusion of the device (8–16). Although not all of these sizing complications are fatal, severe ischemia, hemolysis and death secondary to embolization has been reported in human (17). Furthermore, embolization-related death has been reported in a dog (18). Therefore, accurate measurement of PDA dimensions and morphology classification (such as minimal duct diameter, ampulla duct diameter, and morphology type) are essential for selecting optimal size of occlusion device (19–22).

Recently in veterinary medicine, trans-arterial angiography with fluoroscopy, transthoracic echocardiography (TTE), transesophageal echocardiography (TEE), and computed tomography (CT) have been used for measuring PDA dimensions (22–28). Angiography with fluoroscopy is commonly used tool and serves as a standard for new measurement methods (20, 25, 28). Fluoroscopy can be used pre-, during, and post-the procedure and can be used to measure dimensions, morphology, and is useful after the procedure to assess proper closure. However, it has limitations of underestimation due to assessing only the sagittal mono plane (22). TTE has the advantages of non-invasive nature, assessment of hemodynamic status, and pre-, intra-, and post-procedural evaluation. However, limitations have been reported, including a tendency for overestimation and limited visualization because of lung interference (20). Transesophageal echocardiography offers advantages over fluoroscopy and TTE, including lung independence, usability throughout the procedure, and minimal measurement deviation. However, it has limitations such as high probe costs, the need for skilled operators, and risks of displacing structures or obstructing PDA and aortic flow (26, 28). The idea of using CT for measurement was proposed to overcome the above limitations. (1) Less prone to overestimation and underestimation that can occur with angiography with fluoroscopy and TTE, (2) visualization of extra cardiac structures is clear because imaging is not limited by lungs (27). In addition, (3) the CT does not cause displacement of structures, which is limitation of TEE, and in human medicine, (4) CT provide more accurate measurements of PDA compared to transthoracic echocardiography. However, CT also has limitations such as radiation hazard, contrast hypersensitivity and repeated anesthesia (29). However, only a few case reports or studies with small numbers of patients have been reported on the measurement of PDA by CT in veterinary medicine. The aim of this study is to present the dimensional features of PDA identified on CT in dogs.

2 Materials and methods

2.1 Computed tomography data

A retrospective analysis was conducted based on data from client-owned dogs diagnosed with PDA at three different animal hospitals (Seoul National University, Jeonbuk National University, and Chengju Korea Animal Medical Center) from 2016 to 2024. All included dogs underwent thoracic CT scans and angiography as part of the treatment planning process. 25 dogs with well-defined PDA structures were included in this study, whereas 4 dogs with indistinct boundaries with surrounding structures were excluded. The patients underwent CT (Aquillion 64 ™, Toshiba Medical Systems, Tochigi, Japan /ALEXION 16 ™, Toshiba Medical Systems, Tochigi, Japan/Somatom Scope 16 ™, Siemens AG Medical Solutions, Forchheim, Germany) imaging in a head first prone position under endotracheal intubation and general anesthesia. Iodinated contrast agent (Omnipaque ™ 300, GE Healthcare, Oslo, Norway) was administered for angiography. CT data were collected to visualize the PDA, with respiration controlled during the imaging process to minimize movement of the thoracic cavity and internal organs. Measurements of the PDA were taken using the multiplanar reconstruction mode within Radiant DICOM Viewer (64-bit, version 2024.1; Medixant, Poznan, Poland). The measurements were obtained using the length, angle, and closed polygon measuring tools available within the multiplanar reconstruction mode.

2.2 PDA reconstruction

For PDA measurement in CT images, the central axis (30) was defined as follows: The axis along which the centroid of the pulmonary ostium, the distal point of the PDA on the dorsal plane of the CT image, and the centroid of the descending aorta ventral, the proximal point of the PDA, are connected. To measure the vertical cross-section along the central axis, a reconstruction was performed in which the anatomical longitudinal and central axis of the PDA were aligned. After reconstruction, the adequacy of the reconstruction was determined by checking whether the centroids coincided on ventral to dorsal scroll without movement of the crossing cursor on the CT dorsal plane (Figure 1).

2.3 PDA morphology classification and dimension measurement

The specific measurement site was set as the location where the reference position of fluoroscopy angiography (23) corresponded to the sagittal plane of the reconstructed PDA CT (Figure 2). First, we measured length of PDA from the pulmonary ostium to the junction of the descending aorta and PDA along the cranial border. The minimal duct diameter measurement site was defined as the area with the smallest diameter in the vertical cross-section along the central axis if a clear constriction was identified at the level of the pulmonary ostium, or the area with the smallest diameter in the vertical cross-section along the central axis if no clear constriction was identified at the level of the pulmonary ostium. The ampulla duct diameter measurement site was defined as the midpoint of the length range (Figure 2) and the maximal ampulla diameter measurement site

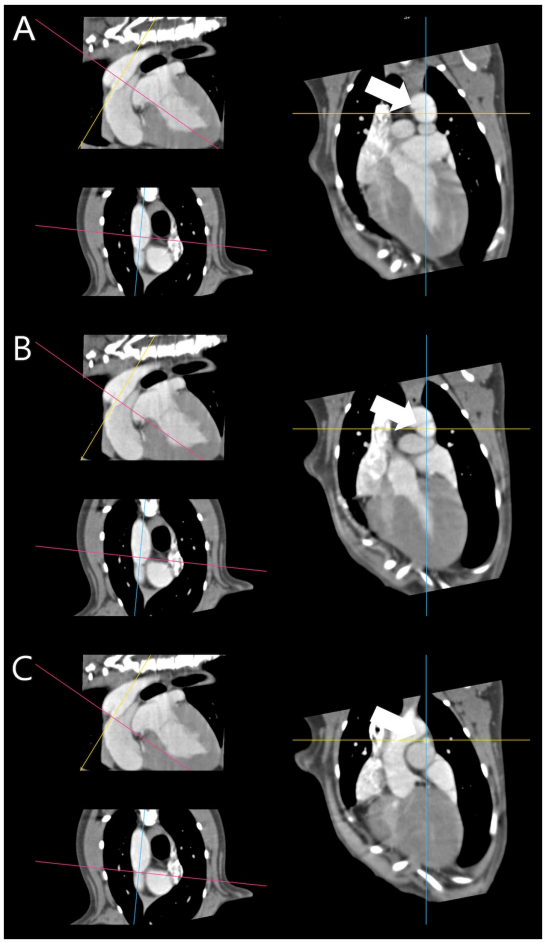

FIGURE 1
Reconstructed patent ductus arteriosus based on central axis. **(A)** Proximal point centroid (white arrow). **(B)** Mid point centroid (white arrow). **(C)** Distal point centroid (white arrow). The centroids [**(A–C)** – white arrow] coincided on ventral to dorsal scroll without movement of the crossing cursor.

was defined as the proximal connection point between PDA and descending aorta. Diameter measurements were defined as the length of the transverse and sagittal cursors crossing the contrasting structures in cross-section identified in the dorsal plane at specific measurement sites (minimal duct site, ampulla duct site) of the PDA structures as transverse diameter and sagittal diameter, respectively (Figure 3). To measure the angle, we defined the axis connecting the point where the central axis of the PDA intersects the dorsal wall of the descending aorta and the centroid of the segment 10 mm posterior to that point as the aorta axis, and evaluated the degree between the central axis of PDA and the aorta axis as the angle. The morphology classification of PDA was established using angiographic morphology type classification criteria (degree of ductal tapering, and the presence, absence, or location of abrupt ductal narrowing) in dogs (24) and updated morphology type refined through TEE (28), matching the mid-sagittal plane morphology on CT scans. The degree of ductal tapering was based on the calculation of the ratio between the minimum diameter and the ampulla diameter or the maximum ampulla diameter if either the sagittal or transverse diameter met the criteria.

2.4 Calculation value

A recent study evaluating the PDA based on TEE (28) reported that the vertical cross-section of the PDA is not perfectly circular. In addition, a human study confirmed that the PDA is a flexible structure that can be deformed by the deployed device, rather than a fixed structure (31). Considering these studies, we quantified the degree of non-circularity in cross-sections at different measurement sites and evaluated calculation values to establish the size relationship between the non-circular PDA cross-sections and the circular occluder device. Based on the directly measured values, Minimal duct diameter ratio (MDR) and Ampulla diameter ratio (ADR) were calculated by calculating the ratio between sagittal diameter and transverse diameter to quantify the degree of non-circularity of the structure. Ampulla cross section diameter (ACD), which calculates the diameter value when the value of ampulla cross section area (Aarea), which is a non-circular structure, is converted to a circle with the same width, was calculated as follow ($ACD = 2^* \sqrt{\frac{Aarea}{\pi}}$). To compare the ACD value to the Ampulla diameter sagittal (ADS) value that we had previously used to define the Ampulla diameter on the monoplane, we calculated the ACD/ADS ratio which is the ratio of the difference value ADS to the ACD value.

2.5 Statistical analysis

Statistical evaluation was performed using SPSS for windows 29.0.1.0 (IBM) and GraphPad Prism 8 (Dotmatics). Normality was assessed using Shapiro–Wilk test. For comparability with subsequent studies, regardless of normality, we report mean ± SD, median, and range values in Table 1. Pearson correlation coefficient was used to evaluate the correlation between ampulla diameter sagittal (ADS) and ampulla diameter ratio (ADR) and other data that follow normality, and Spearman correlation coefficient was used to evaluate the correlation between minimal diameter sagittal (MDS), minimal diameter transverse (MDT), minimal diameter ratio (MDR), ampulla diameter transverse (ADT), length of PDA, angle (descending aorta to PDA), body weight (BW) and age that do not follow normality. Angle of PDA, length and ADR displayed as linear regression. A p value <0.05 was considered to be statistically significant.

3 Results

A total 25 dogs were included in study. The breed distribution of the dogs was as follows: Maltese 32% (8/25), Pomeranian 20% (5/25), mixed breed 12% (3/25), Poodle 8% (2/25), Bichon 8% (2/25), Bedlington terrier 4% (1/25), Cocker spaniel 4% (1/25), Miniature pincher 4% (1/25), Spitz 4% (1/25), Welsh corgis 4% (1/25). The gender distribution consists of females 67% (15, Intact 7, neutered 8) and males 33% (10, Intact 5, neutered 5). The median Age of dogs at the time of CT scan was 12 months (range 2 to 113 months) in 25 dogs. The median Body weight was 3.22 kg (range 0.93 to 9.5 kg) in 22 of the 25 dogs, excluding 3 dogs for which data was lost. In all patients, the course of the PDA is such that the proximal part starts from the ventral part of the aorta and the distal part travels in a cranio-lateral direction before reaching the dorsal part near the

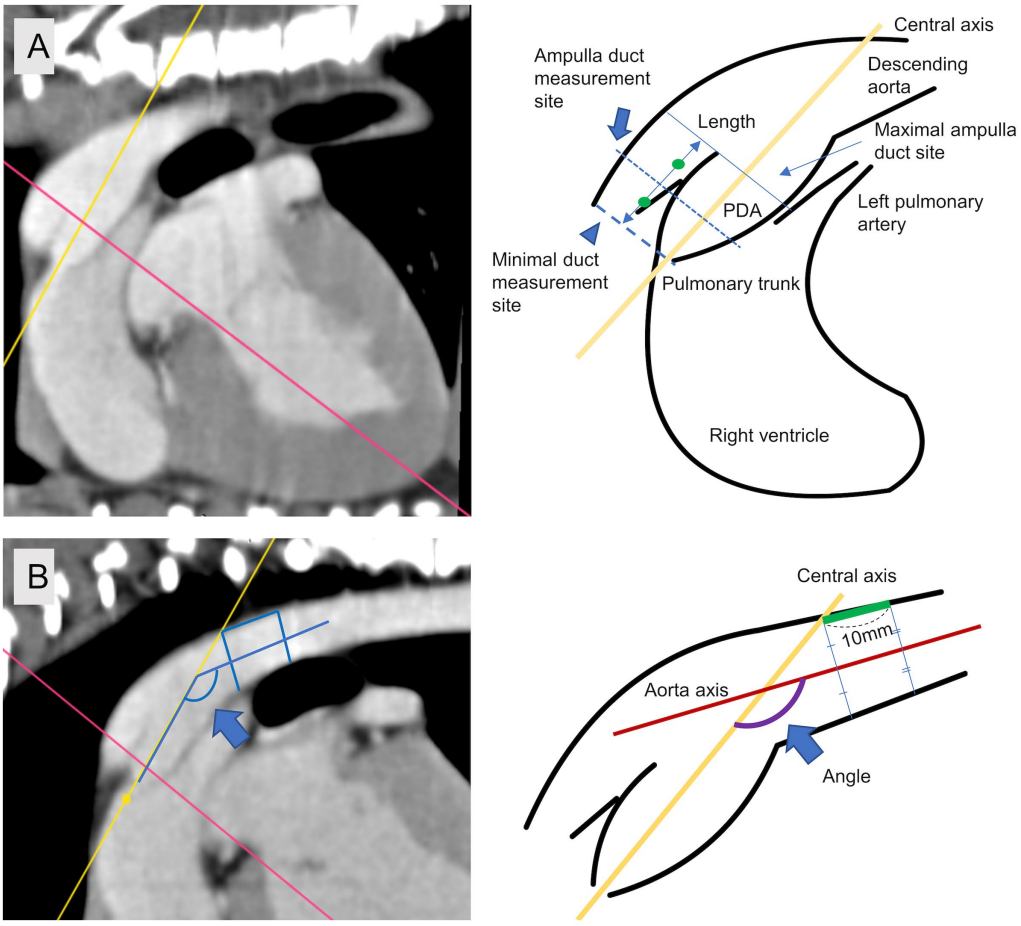

FIGURE 2
Specific measurement site. **(A)** Minimal duct site (arrow head), ampulla duct site (arrow), length. **(B)** Measuring site of angle between central axis and aorta axis (blue arrow).

bifurcation of the main pulmonary artery. Based on morphology evaluation, the distribution of PDA types was as follows: Type IIA ($n = 12$, 48%), Type IIB ($n = 5$, 20%), and Type III ($n = 8$, 32%), while Type I, Type IV and Type V were not identified in this study. The ductal measurements of PDA and calculation values are presented in Table 1. Minimal diameter sagittal (MDS) was significantly correlated with ADS (Pearson, $r = 0.839$, $p < 0.001$), ADT (Spearman, $r = 0.542$, $p = 0.005$), BW (Spearman, $r = 0.546$, $p = 0.009$), angle (Spearman, $r = -0.552$, $p = 0.004$), and MDT was significantly correlated with ADS (Pearson, $r = 0.808$, $p < 0.001$), ADT (Spearman, $r = 0.542$, $p = 0.005$), BW (Spearman, $r = 0.546$, $p = 0.009$), and angle (Spearman, $r = -0.482$, $p = 0.015$). MDS and MDT were not significantly correlated with other variables such as length of PDA and age.

Ampulla diameter sagittal (ADS) was significantly correlated with MDS, MDT, and BW (Pearson, $r = 0.636$, $p = 0.001$), but not with other such as length of PDA, angle, or age. Similarly, Ampulla diameter transverse (ADT) was significantly correlated with MDS, MDT, and BW (Spearman, $r = 0.522$, $p = 0.013$), but not with other length of PDA, angle, or age. Length of PDA was significantly associated with length (Spearman, $r = 0.551$, $p = 0.004$). Angle was significantly associated with MDS, MDT and length of PDA.

MDR did not show a significant correlation with other variables. On the other hands ADR showed significantly correlated with length (Pearson, $r = -0.467$, $p = 0.019$) and angle (Pearson, $r = -0.677$, $p < 0.001$) (Figure 4). The ACD/ADS ratio was significantly correlated with the length (Pearson, $r = 0.507$, $p = 0.01$) and angle (Pearson, $r = 0.684$, $p < 0.001$). No correlations were found with any other variables.

4 Discussion

The accurate measurement for device selection during a PDA intervention is of great importance in order to minimize the occurrence of side effects and to ensure the successful closure of the PDA. In order to achieve accurate measurement, this study presented the measurement criteria using CT scan and characterized the measurement dimension. The fact that PDA structure may not be a perfect circle (4), where differences in sagittal and transverse values may exist for minimal diameters, was identified in previous studies (28) and also confirmed in this study. In this regard, the distribution of the shape at the minimum diameter in the population identified in the previous study (28) was found to be oval (17/24, 70.8%) and circular (7/24, 29.2%). However, in this study, the distribution of the

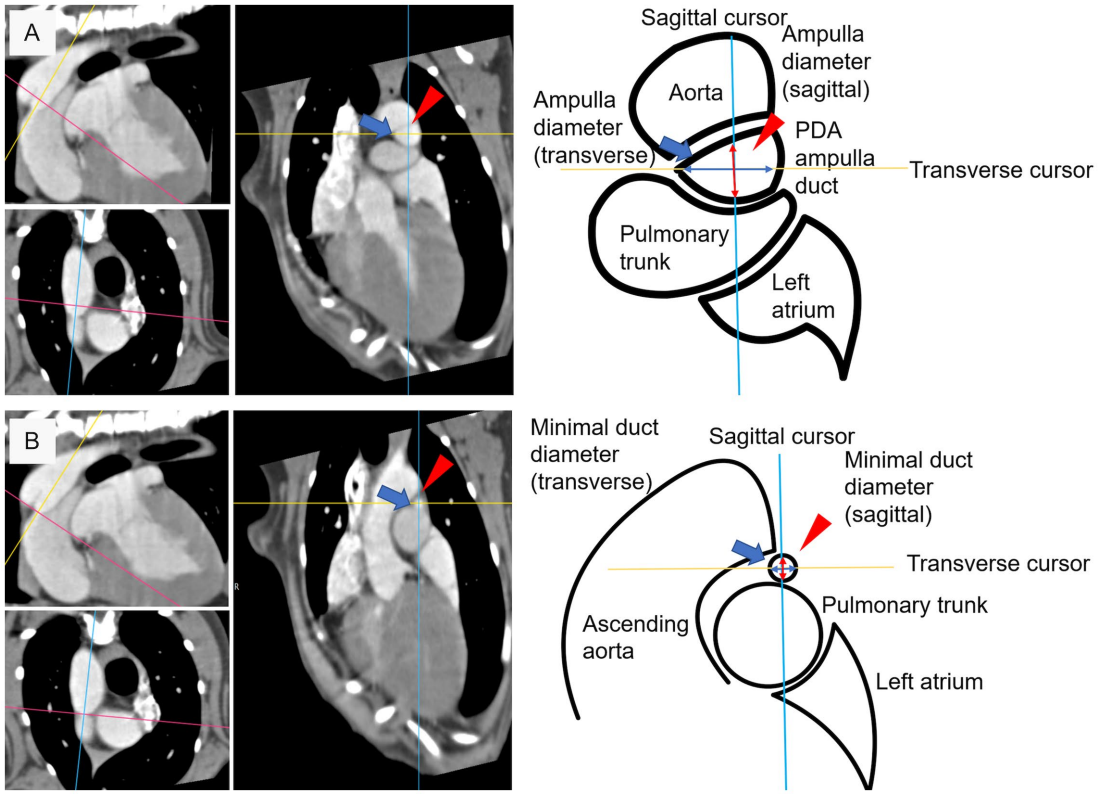

FIGURE 3
Diameter measuring criteria at specific measurement site. **(A)** Sagittal diameter (red arrow head) and transverse diameter (blue arrow) at ampulla duct site. **(B)** Sagittal diameter (red arrow head) and transverse diameter (blue arrow) at minimal duct site.

shape at the same shape criterion was found to be somewhat different: oval (5/25, 25%) and circular (20/25, 75%). A possible reason for this difference is the difference in the criteria axis used. In this study, the pulmonary ostium or minimal duct was measured at the smallest diameter part of the central axis or the area where the axis connects to the pulmonary artery in previous studies based on dimensional measurements, whereas in studies based on 3D-TEE, a cross section across the pulmonary ostium was first established and then axis perpendicular to it (28). This difference in the slope of the representative axis is considered to be a factor that may have caused the difference in proportions.

Ampulla diameter ratio is similar to the previous study (28) in that the cross section of the ampulla has an oval shape rather than a circular shape, and in this study, it was found to be close to an oval shape with a length difference between ADS and ADT. The difference in the proportion was identified in a previous study (28) as oval shape (19/24, 79%) and circular shape (5/21, 21%), and this study showed a similar distribution of proportions as oval shape (19/25, 82%) and circular shape (6/25, 18%) when evaluated using the same criteria (28) as the previous study. Furthermore, similar to previous study (28), we found that the ratio of MDR to ADR is not always a consistent structure with the same circular and oval shapes. In addition, the significant negative correlation between ADR and length of PDA and angle suggests that PDA with angle and length larger than the representative values are likely to have a more oval shaped cross-sectional area. We consider that this may reduce the possibility of error in device size selection due to overlooking the transverse diameter due to interpretation based on mono-plane evaluation in the conventional sagittal plane diameter. Based on the results of this study and previous studies (28), it can be seen that the measurement plane should be considered when measuring structures that are considered to be non-perfectly circular (Figure 4), as the difference in the measurement value may be due to the characteristics of the structure rather than the difference in the tool. It is therefore necessary to further refine the measurement diameter in order to align it with the measurable dimension structure of the tools, which can be classified into the following categories: Sagittal diameter tool (Trans-arterial angiography, TEE-2D), Transverse diameter tool (TTE-R and TTE-L), Sagittal + transverse diameter tool (TEE-3D, CT) plane.

Compared to the mean angle of PDA 148.8 ± 7.6 degrees (range 117 to 164, median 150) in a previous trans-arterial angiography study (27) that presented the angle between the descending aorta and PDA, we showed that the mean angle of PDA 134.2 ± 13.63 degrees (range 103 to 156, median 137.7) was smaller in this study. In three dimensions, the PDA is mostly traveling in the cranio-ventral direction, and in this regard, we confirmed that there may be some differences in the angle between the data evaluated in the mono-plane and the multiplane (Figure 5). In the future, it is considered that the newly considered angle may be helpful for the development of catheters aimed at trans-arterial access.

The ACD/ADS ratio, one of the calculations values, was investigated to determine the correlation between the circularly designed occlusion device and the PDA ampulla, which is identified as oval. Currently, most size criteria for occlusion devices are based on

TABLE 1 Patient and patent ductus arteriosus measurement data.

	Mean	Median	SD	Range	Normality
BW (kg)	3.09	3.23	2.18	0.93–9.5	No
Age (month)	16.61	12.00	32.66	2–113	No
MDS (mm)	3.26	3.16	1.87	1.54–8.45	No
MDT (mm)	3.51	3.16	2.14	1.49–9.18	No
MDR	0.93	0.97	0.10	0.69–1.06	No
ADS (mm)	4.78	4.89	1.65	2.24–9.47	Yes
ADT (mm)	6.08	5.62	2.44	3.06–13.40	No
ADR	0.79	0.74	0.16	0.57–1.16	Yes
Aarea (cm^2)	0.23	0.22	0.22	0.06–1.00	No
ACD (cm)	0.54	0.53	0.20	0.27–1.13	No
ACD/ADS ratio	1.14	1.19	0.13	0.88–1.42	Yes
Length (mm)	6.81	7.16	2.80	3.42–15.8	No
Angle (degree)	134.21	137.70	13.36	103.00–156.00	No

Aarea, ampulla cross section area; ACD, ampulla cross section dimeter; ADR, ampulla diameter ratio; ADS, ampulla diameter sagittal; ADT, ampulla diameter transverse; BW, body weight; MDR, minimal diameter ratio; MDS, minimal diameter sagittal; MDT, minimal diameter transverse; PDA, patent ductus arteriosus.

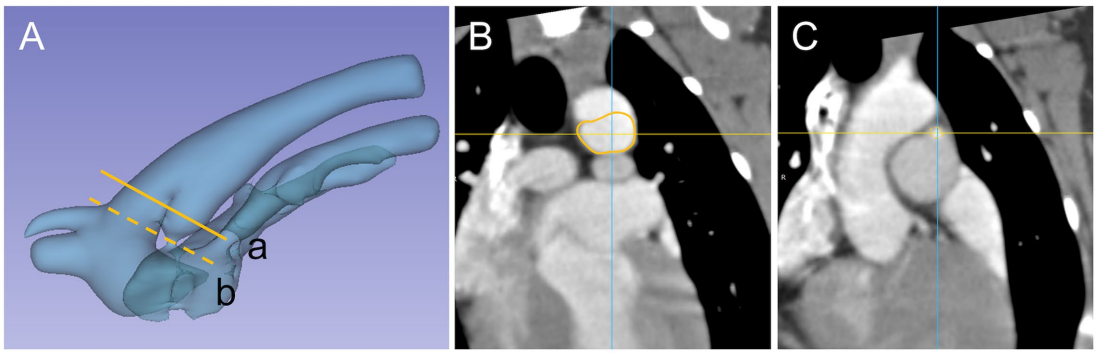

FIGURE 4
PDA 3D model and cross section appearance at specific measurement site, Patent ductus arteriosus (PDA) and surrounding vasculature displayed as **(A)** a three-dimensional model and specific measurement site (a) ampulla diameter (line), (b) minimal diameter (dash line). Cross section appearance of **(B)** ampulla duct (line) and **(C)** minimal duct (dash line).

a single diameter measured on a mono-plane, and there is no literature that considers the property of non-circular structures that can have multiple diameters depending on the criteria. In addition, as it has been reported in the literature that PDA structures can be flexibly stretched rather than fixed (31). We checked the ratio of the difference between the diameter of the non-circular cross section (ACD) and the ADS, a mono-plane measurement that has been used as the basis for setting the size of the occlusion device. The ACD/ADS ratio was found to be mean 1.14 ± 0.13 (range 0.88 to 1.42, median 1.19) indicating that the ADS value was measured as much as 14% smaller than the ACD value. Considering these differences, we propose to consider replacing the traditional device selection criteria, ADS, with an ACD that is tailored to the cross-sectional width of each patient. As opposed to the previous, it has been confirmed in both human and veterinary studies that deformation of the device may occur due to excessively oversized devices or the structure of the PDA (17, 32). In this regard, it is considered that future research: (1) the shape of PDA that flexibly deforms due to device expansion and (2) the maximum expansion level relative to the new reference diameter that does not cause device deformation may be a good idea to solve the current sizing complication.

This study has several limitations. First, it is unclear whether the minimal duct diameter site set relative to the central axis is the same site as the conventional measurement, which is a direct measurement of the structure across the pulmonary ostium. This is due to the fact that the minimal duct site is a smaller structure and more tortuous structure compared to other measurement dimensions. Second, the statistical reliability is reduced due to the small number of patients. Third, the comparison with fluoroscopy (angle between PDA and descending aorta) was based on statistical data of previous studies, not within the same individual, making it difficult to confirm statistical significance. Fourth, it is a retrospective study and the interpretation is based on CT scans taken under different conditions, which makes the data inconsistent across conditions. Nevertheless, it is valuable to present a measure of PDA based on CT, which can serve as a comparison and measurement standard for future studies. As a further study, it is considered necessary to present a representative value of PDA patients based on CT data from a larger study, and to establish

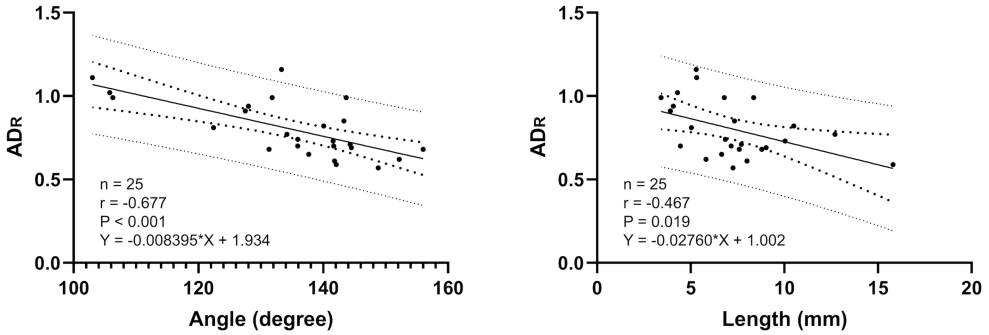

FIGURE 5
Linear association of PDA length (mm), angle (degree) and ADR. The solid line represents the line of best fit, the inner larger dotted lines represents the 95% confidence intervals for the best fit and the outer dotted lines represents the 95% prediction interval for the observation.

the substitutability and role of tools based on the comparison of multiple tools in the same patient for future intervention procedures.

In conclusion, computed tomography (CT) images are capable of assessing morphology and dimensions in a conventional tool. The distinctive cross-sectional shape, which can only be observed in three-dimensional structures, represents the primary distinction between this approach and conventional measuring tools. It is anticipated that CT will contribute to a reduction in sizing complications in future interventional procedures through the implementation of sophisticated pre-planning techniques or the development of new devices.

Data availability statement

The datasets presented in this study can be found in online repositories. The names of the repository/repositories and accession number(s) can be found in the article/supplementary material.

Ethics statement

Ethical approval was not required for the studies involving animals in accordance with the local legislation and institutional requirements because this study was conducted based on data from CT scans, a diagnostic method for PDA patients, conducted with the consent of owners, so approval from the Laboratory Animal Ethics Committee was not required. Written informed consent was obtained from the owners for the participation of their animals in this study.

Author contributions

HU: Methodology, Writing – review & editing, Data curation, Formal analysis. K-aY: Data curation, Writing – review & editing. JL: Data curation, Writing – review & editing. DS: Data curation, Writing – review & editing. SL: Data curation, Writing – review & editing. BN: Data curation, Writing – review & editing. AC: Data curation, Writing – review & editing. HH: Data curation, Writing – review & editing. NL: Data curation, Writing – review & editing. IK: Data curation, Writing – review & editing. JY: Data curation, Writing – review & editing. JC: Data curation, Writing – review & editing. KL: Data curation, Writing – review & editing. HY: Data curation, Writing – review & editing. MK: Conceptualization, Methodology, Project administration, Supervision, Writing – original draft, Writing – review & editing.

Funding

The author(s) declare that financial support was received for the research, authorship, and/or publication of this article. This study was supported by the National Research Foundation of Korea (NRF) grants funded by the Korean Government (MSIT) (No. 2022R1F1A1065215).

Conflict of interest

The authors declare that the research was conducted in the absence of any commercial or financial relationships that could be construed as a potential conflict of interest.

Publisher's note

All claims expressed in this article are solely those of the authors and do not necessarily represent those of their affiliated organizations, or those of the publisher, the editors and the reviewers. Any product that may be evaluated in this article, or claim that may be made by its manufacturer, is not guaranteed or endorsed by the publisher.

References

1. Brambilla PG, Polli M, Pradelli D, Papa M, Rizzi R, Bagardi M, et al. Epidemiological study of congenital heart diseases in dogs: prevalence, popularity, and volatility throughout twenty years of clinical practice. *PLoS One*. (2020) 15:1–17. doi: 10.1371/journal.pone.0230160

2. Eyster GE, Eyster JT, Cords GB, Johnston J. Patent ductus arteriosus in the dog: characteristics of occurrence and results of surgery in one hundred consecutive cases. *J Am Vet Med Assoc*. (1976) 168:435–8.

3. Saunders AB, Gordon SG, Boggess MM, Miller MW. Long-term outcome in dogs with patent ductus arteriosus: 520 cases (1994-2009). *J Vet Intern Med*. (2014) 28:401–10. doi: 10.1111/jvim.12267

4. Buchanan JW. Patent ductus arteriosus morphology, pathogenesis, Types and Treatment. *J Vet Cardiol*. (2001) 3:7–16. doi: 10.1016/S1760-2734(06)70010-8

5. Broaddus K, Tillson M. Patent ductus arteriosus in dogs. *Compend Contin Educ Vet*. (2010) 32:E3.

6. Ranganathan B, Leblanc NL, Scollan KF, Townsend KL, Agarwal D, Milovancev M. Comparison of major complication and survival rates between surgical ligation and use of a canine ductal occluder device for treatment of dogs with left-to-right shunting patent ductus arteriosus. *J Am Vet Med Assoc*. (2018) 253:1046–52. doi: 10.2460/javma.253.8.1046

7. Karn M, Potter BM, Pierce KV, Scansen BA. Medial insertion of the patent ductus arteriosus characterized by computed tomography angiography in a cat and dog. *J Vet Cardiol*. (2022) 41:145–53. doi: 10.1016/j.jvc.2022.02.003

8. Wesselowski S, Saunders AB, Gordon SG. Relationship between device size and body weight in dogs with patent ductus arteriosus undergoing Amplatz canine duct Occluder deployment. *J Vet Intern Med*. (2017) 31:1388–91. doi: 10.1111/jvim.14797

9. Singh MK, Kittleson MD, Kass PH, Griffiths LG. Occlusion devices and approaches in canine patent ductus arteriosus: comparison of outcomes. *J Vet Intern Med*. (2012) 26:85–92. doi: 10.1111/j.1939-1676.2011.00859.x

10. Gordon SG, Saunders AB, Achen SE, Roland RM, Drourr LT, Hariu C. Transarterial ductal occlusion using the Amplatz® canine duct Occluder in 40 dogs. *J Vet Cardiol*. (2010) 12:85–92. doi: 10.1016/j.jvc.2010.04.004

11. Achen SE, Miller MW, Gordon SG, Saunders AB, Roland RM, Drourr LT. Transarterial ductal occlusion with the amplatzer vascular plug in 31 dogs. *J Vet Intern Med*. (2008) 22:1348–52. doi: 10.1111/j.1939-1676.2008.0185.x

12. Campbell FE, Thomas WP, Miller SJ, Berger D, Kittleson MD. Immediate and late outcomes of transarterial coil occlusion of patent ductus arteriosus in dogs. *J Vet Intern Med*. (2006) 20:83–96. doi: 10.1111/j.1939-1676.2006.tb02827.x

13. Craciun I, Silva J, Dutton LC, Loureiro J, Novo MJ. Two-and three-dimensional transesophageal echocardiographic assessment and successful occlusion of a window-like patent ductus arteriosus in two dogs. *J Vet Cardiol*. (2024) 51:214–9. doi: 10.1016/j.jvc.2023.12.004

14. Belachsen O, Sargent J, Koffas H, Schneider M, Wagner T. The use of Amplatzer vascular plug II in 32 consecutive dogs for transvenous occlusion of patent ductus arteriosus. *J Vet Cardiol*. (2022) 41:88–98. doi: 10.1016/j.jvc.2021.05.005

15. Silva J, Domenech O, Mavropoulou A, Oliveira P, Locatelli C, Bussadori C. Transesophageal echocardiography guided patent ductus arteriosus occlusion with a duct occluder. *J Vet Intern Med*. (2013) 27:1463–70. doi: 10.1111/jvim.12201

16. Wesselowski S, Saunders AB, Gordon SG. Anatomy, baseline characteristics, and procedural outcome of patent ductus arteriosus in German shepherd dogs. *J Vet Intern Med*. (2019) 33:471–7. doi: 10.1111/jvim.15401

17. Faella HJ, Hijazi ZM. Closure of the patent ductus arteriosus with the Amplatzer PDA device: immediate results of the international clinical trial. *Catheter Cardiovasc Interv*. (2000) 51:50–4. doi: 10.1002/1522-726X(200009)51:1<50::AID-CCD11>3.0.CO;2-6

18. Carlson JA, Achen SA, Saunders AB, Gordon SG, Miller MW. Delayed embolization of an Amplatz® canine duct occluder in a dog. *J Vet Cardiol*. (2013) 15:271–6. doi: 10.1016/j.jvc.2013.10.001

19. Nguyenba TP, Tobias AH. The Amplatz® canine duct occluder: a novel device for patent ductus arteriosus occlusion. *J Vet Cardiol*. (2007) 9:109–17. doi: 10.1016/j.jvc.2007.09.002

20. Schneider M, Hildebrandt N, Schweigl T, Wehner M. Transthoracic echocardiographic measurement of patent ductus arteriosus in dogs. *J Vet Intern Med*. (2007) 21:251–7. doi: 10.1111/j.1939-1676.2007.tb02957.x

21. Nguyenba TP, Tobias AH. Minimally invasive per-catheter patent ductus arteriosus occlusion in dogs using a prototype duct Occluder. *J Vet Intern Med*. (2008) 22:129–34. doi: 10.1111/j.1939-1676.2007.0009.x

22. Stokhof AA, Sreeram N, Wolvekamp WTC. Transcatheter closure of patent ductus arteriosus using occluding spring coils. *J Vet Intern Med*. (2000) 14:452–5. doi: 10.1111/j.1939-1676.2000.tb02255.x

23. Matthias S. Percutaneous angiography of patent ductus arteriosus in dogs: techniques, results and implications for intravascular occlusion. *JVC*. (2003) 5:21–7. doi: 10.1016/S1760-2734(06)70048-0

24. Miller MW, Gordon SG, Saunders AB, Arsenault WG, Meurs KM, Lehmkuhl LB, et al. Angiographic classification of patent ductus arteriosus morphology in the dog. *J Vet Cardiol*. (2006) 8:109–14. doi: 10.1016/j.jvc.2006.07.001

25. Saunders AB, Miller MW, Gordon SG, Bahr A. Echocardiographic and angiographic comparison of ductal dimensions in dogs with patent ductus arteriosus. *J Vet Intern Med*. (2007) 21:68–75. doi: 10.1111/j.1939-1676.2007.tb02930.x

26. Saunders AB, Achen SE, Gordon SG, Miller MW. Utility of transesophageal echocardiography for transcatheter occlusion of patent ductus arteriosus in dogs: influence on the decision-making process. *J Vet Intern Med*. (2010) 24:1407–13. doi: 10.1111/j.1939-1676.2010.0587.x

27. Henjes CR, Nolte I, Wefstaedt P. Multidetector-row computed tomography of thoracic aortic anomalies in dogs and cats: patent ductus arteriosus and vascular rings. *BMC Vet Res*. (2011) 7:7. doi: 10.1186/1746-6148-7-57

28. Doocy KR, Saunders AB, Gordon SG, Jeffery N. Comparative, multidimensional imaging of patent ductus arteriosus and a proposed update to the morphology classification system for dogs. *J Vet Intern Med*. (2018) 32:648–57. doi: 10.1111/jvim.15068

29. Lee SJ, Yoo SM, Son MJ, White CS. The patent ductus arteriosus in adults with special focus on role of ct. *Diagnostics*. (2021) 11:1–10. doi: 10.3390/diagnostics11122394

30. Barratt DC, Ariff BB, Humphries KN, SAMCG T, Hughes AD. Reconstruction and quantification of the carotid artery bifurcation from 3-D ultrasound images. *IEEE Trans Med Imaging*. (2004) 23:567–83. doi: 10.1109/TMI.2004.825601

31. Tomita H, Fuse S, Hatakeyama K, Chiba S. Stretching of the ductus an important factor in determining the outcome of coil occlusion. *Jpn Circ J*. (1999) 63:593–6. doi: 10.1253/jcj.63.593

32. Fatehi A, Maadani M, Abdi S, Norouzi J. Frequent oversizing during Amplatzer device deployment for percutaneous PDA closures. *Iranian Heart J*. (2009)

frontiers | Frontiers in Veterinary Science

TYPE Original Research
PUBLISHED 31 December 2024
DOI 10.3389/fvets.2024.1484189

OPEN ACCESS

EDITED BY
Caner Bakici,
Ankara University, Türkiye

REVIEWED BY
Mihaela Spataru,
Ion Ionescu de la Brad University of Agricultural Sciences and Veterinary Medicine of Iași, Romania
Nedzad Hadziomerovic,
University of Sarajevo, Bosnia and Herzegovina

*CORRESPONDENCE
Sokol Duro
durosokol@ubt.edu.al

RECEIVED 21 August 2024
ACCEPTED 11 December 2024
PUBLISHED 31 December 2024

CITATION
Uçmak ZG, Kurban İ, Uçmak M, Özbezek MF, Kılıçarslan MR, Duro S, Szara T and Gündemir O (2024) Assessment of uterine caruncles, uterine cervix, and vulva during the postpartum period in Kivircik ewes with shear-wave elastography.
Front. Vet. Sci. 11:1484189.
doi: 10.3389/fvets.2024.1484189

Assessment of uterine caruncles, uterine cervix, and vulva during the postpartum period in Kivircik ewes with shear-wave elastography

Zeynep Günay Uçmak[1], İbrahim Kurban[2], Melih Uçmak[1], Mehmet Fatih Özbezek[3], Mehmet Ragıp Kılıçarslan[1], Sokol Duro[4]*, Tomasz Szara[5] and Ozan Gündemir[6]

[1]Obstetrics and Gynaecology Department, Faculty of Veterinary Medicine, Istanbul University-Cerrahpaşa, Istanbul, Türkiye, [2]Equine and Training Program, Vocational School of Veterinary Medicine, Istanbul University-Cerrahpaşa, Istanbul, Türkiye, [3]Institute of Graduate Studies, Istanbul University-Cerrahpaşa, Istanbul, Türkiye, [4]Department of Anatomy, Faculty of Veterinary Medicine, Agricultural University of Tirana, Tirana, Albania, [5]Department of Morphological Sciences, Institute of Veterinary Medicine, Warsaw University of Life Sciences-SGGW, Warsaw, Poland, [6]Department of Anatomy, Faculty of Veterinary Medicine, Istanbul University-Cerrahpasa, Istanbul, Türkiye

Introduction: This study aims to quantify the shear wave speed (SWS) and stiffness of the uterine cervix (close to the internal cervical ostium (IOC) which is the cranial portion of cervix and close to the external cervical ostium (EOC) which is the caudal portion of cervix), caruncular areas, and vulvar labia during the postpartum period in healthy Kivircik ewes by using shear-wave elastography. Power Doppler ultrasonography was performed to evaluate the color pixel percentage (CPP) of the caruncles.

Methods: The study included 13 healthy pregnant Kivircik ewes, which were randomly selected. A total of 12 measurements were taken from the uterine cervix and vulva from the postpartum first day to PP42 (daily for the first week and weekly from PP14 to PP42). However, only eight measurements were obtained from the caruncles because they could not be visible after day 14.

Results: The time-dependent differences in the widest cross-sectional diameter of the caruncles were statistically significant ($p < 0.001$) both in ewes giving birth to singletons and twins. As a result of power Doppler ultrasonography examination, the time-dependent differences in the CPP of the caruncles were statistically significant ($p < 0.01$) in ewes giving birth to both singletons and twins. The diameter of the cervix at PP3 was significantly higher than the ones at PP14, PP21, PP28 ($p < 0.05$). The SWS and stiffness in the IOC for all ewes at PP35 were significantly higher than the ones at PP1, PP4, PP7, and PP14 ($p < 0.05$ and $p < 0.01$; respectively). However, the time-dependent differences in SWS and stiffness in the EOC were not statistically significant ($p > 0.05$). The time-dependent differences in the SWS and stiffness in the vulva were statistically significant ($p < 0.001$) in ewes giving birth to both singletons and twins.

Discussion: In conclusion, it is possible to describe the changes throughout the postpartum period and evaluate the involution of the uterine cervix, caruncles, and vulvar labia and tissue stiffness with significant results by B mode ultrasonography, power Doppler and shear wave elastography. We provided valuable information to elucidate the differences in the involution process of the uterine cervix, caruncles, and vulva concerning the number of offspring during the postpartum period in Kivircik ewes.

KEYWORDS
caruncula, cervix, elastography, postpartum period, vulva

Introduction

The puerperal and postpartum periods are characterized by many physiological changes in the genital organs after delivery in ewes (1). Uterine involution is defined as the return of the uterus to its non-pregnant status and physiological function after parturition (2). Involution of the uterus is remarkably high in the first week of the postpartum period but is influenced by breed, management, season, dystocia, and suckling (3, 4). The completion period of uterine involution was shorter for ewes that lambed at the end of winter than for those lambing at the onset of summer (5). Also, the parity affected uterine involution, completed earlier in primiparous than in pluriparous ewes (6). The rate of uterine involution in ewes with singleton parturition was higher than that with triplet parturition. Thus, different litter sizes significantly affected postpartum uterine horn recovery more than the caruncles (2). Complete uterine involution occurs between 17–40 days of postpartum (7), and is determined by the size of the uterus and the restoration of the endometrium (8). Uterine involution in ewes involves the remodeling of both caruncular and intercaruncular areas of the uterine wall and the termination of differentiated uterine gland functions characteristic of pregnancy (9). After the expulsion of the placenta, the caruncles assume a concave shape, and their morphological appearance changes from concave to convex in the regression phase (7). Complete involution of caruncles takes 28 days, while complete regeneration takes more than 4 weeks after parturition (10, 11). It involves necrosis and separation of septa from underlying stroma and regrowth of epithelium from the caruncular edges (10). Due to the similar echotexture of the caruncles and the endometrium, it can be challenging to differentiate caruncles from endometrium foldings using ultrasonography around days 5–8 (7). The contour of the caruncle may be visible as round or oval from days 3 to 10 postpartum, and its diameter is undetectable after day 10 (2).

Diagnostic ultrasound has become an essential tool in veterinary medicine and provides an inexpensive, non-invasive method for further examination of the reproductive tract in male and female farm sheep (12, 13). Doppler ultrasonography provides information about blood flow and vascular perfusion. There are various reports on changes in uterine blood flow during the postpartum period in Kivircik sheep (14, 15). Ultrasonographic elastography enables the assessment of tissue elasticity and stiffness, and qualitative and quantitative applications of elastography are widely used in various reproductive organs in ewes (1, 16, 17). Maternal and fetal tissue elasticity in pregnant ewes was quantified by elastographic analysis, and the shear wave velocity of placentoma remained constant throughout gestation (17). Peralta et al. (16) quantify cervical stiffness using shear wave elastography in preterm birth and induced labor in pregnant sheep. Mariano et al. (1) evaluated the stiffness of the uterine wall (endometrium/myometrium) during the involution in healthy Santa Inês ewes by using Acoustic Radiation Force Impulse (ARFI) elastography.

This study aims to quantify the shear wave speed (SWS) and stiffness of the uterine cervix (close to the internal cervical ostium (IOC) which is the cranial portion of cervix and close to the external cervical ostium (EOC) which is the caudal portion of cervix), caruncular areas, and vulvar labia during the postpartum period in healthy Kivircik ewes by using shear-wave elastography. Also, power Doppler ultrasonography was performed to evaluate the color pixel percentage (CPP) of the caruncles.

Materials and methods

This study was approved by the Unit Ethics Committee of İstanbul University-Cerrahpaşa, Faculty of Veterinary Medicine, İstanbul, Türkiye (Approval No. 2023/22).

Animals and study design

The study was conducted at the Istanbul University-Cerrahpaşa Faculty of Veterinary Medicine Sheep Farm located at 40°59′19.3″N, 28°43′36.1″E during the parturition season (March to May). Thirteen healthy pregnant Kivircik ewes were randomly selected [body weight: 55–60 kg, body condition score (BCS): 3.5/5]. A semi-intensive feeding program was implemented on ewes between the ages of 2–4 years. The ultrasonography measurements began to be obtained 24 h after the delivery. The first measurement taken 24 h after birth was called postpartum 1 (PP1). Ultrasound measurements were taken daily for a week (PP1 to PP7) and weekly from the first week until the 42nd postpartum day (PP14, PP21, PP28, PP35, PP42). All measurements were performed by the same operator and at the same period of the day (9:00–11:00 a.m.).

Ultrasound examinations

All ultrasound measurements (B-mod, power Doppler ultrasound, shear-wave elastography) were performed transabdominally by using Resona i9 (Mindray, China) with linear transducer (L20-5 s). All ewes were laid on their right side (Figure 1A). The uterine caruncles were evaluated transabdominally. Also, the uterine cervix was visualized in the proximal lateral side of the mammary lobes in a longitudinal view (Figure 1B). For evaluation of the vulva, the transducer was positioned vertically on both vulvar labia (Figure 1C).

B-mod ultrasonography

The widest cross-sectional diameters of uterine caruncles and uterine cervix were measured by B-mode ultrasonography. Additionally, the mean thickness of both vulvar labia was recorded. The settings of the B-mod ultrasound examinations in the caruncles, cervix, and vulva were as follows: the frequency (harmonic) (FH) was 18, gain (G) was 55, iBeam was +2, iclear was +3, dynamic rate (DR) was 130, SSI was 1,540.

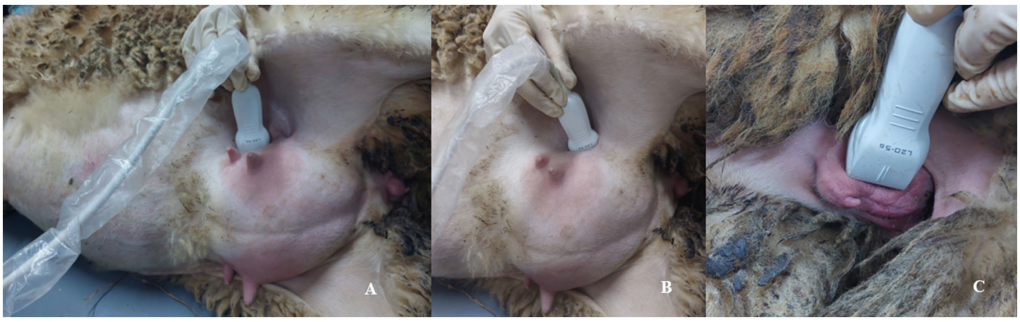

FIGURE 1
Posture of the sheep and positioning of the transducer during an ultrasound examination. **(A)** Evaluation of the uterine caruncles, transabdominally. **(B)** Visualisation of the cervix in the proximal lateral side of the mammary lobes. **(C)** Evaluation of the vulva with vertically positioned transducer.

Power Doppler ultrasonography

Power Doppler images were quantified by measuring the color pixel percentage (CPP). The calculations were performed automatically by the ultrasound device. The vascularization in caruncles was evaluated in this study. The settings of the power Doppler ultrasonography were frequency (F) 11, G 60, pulse repetition frequency (PRF) 1.5 k, and Wall filter (WF) 215 Hz. Before elastography examinations, power Doppler was performed to visualize the blood vessels in the caruncles and cervix.

Shear wave elastography

All measurements were performed in avascular areas of the relevant tissues (uterine caruncles, cervix, and vulva). The settings during elastography examination were HQE off, quality penetration Estory frequency (Q Pen), Map E2, and opacity (OP) was 4, iLay was off, and filter was 1 for all evaluated tissues. Stiffness (EkPa) and SWS (Cs, m/sn) were measured in the caruncle, cervix, and vulva. Qualitative and quantitative image analyses were activated. During elastography measurements, the motion stability index (M-STB index) was defined as green with ≥4 stars, and the reliability index (RI) was ≥85%. For quantification of the elasticity, the region of interest (ROI) was circular and kept constant at 2 mm in diameter for each tissue. The mean value of 4 ROI measurements was taken to determine the elasticity of the caruncles and vulva.

A total of 4 ROI areas which 2 ROIs close to the internal cervical ostium (IOC) where is the cranial portion of cervix and 2 ROIs close to the external cervical ostium (EOC) where is the caudal portion of cervix, were taken to evaluate the elasticity of the uterine cervix in a longitudinal view.

Statistical analysis

Statistical analysis was performed by using the SPSS 23.0 program. The normal distribution of the data was checked with the Shapiro–Wilk test. The homogenicity of variance was analyzed using Levene's test. The differences between ewes that gave birth to single offspring and those that gave birth to twins were evaluated using the t-test. The time-dependent differences in caruncles, cervix, and vulva were assessed using the General Linear Model and Repeated Measures of Anova. Tukey test was performed to evaluate the differences in the parameters between the examination days. Associations of the evaluated parameters (thickness/diameter, CPP%, SWS-m/sn, stiffness-EkPA) in related tissues were assessed with Pearson's correlation test. Results were expressed as the means and standard errors. Significance was accepted as $p < 0.05$.

Results

All ewes expulsed their placenta within 9 h after the delivery. Four of the 13 ewes had twin offsprings, while the rest of the nine ewes had singleton offsprings. A total of 12 measurements were taken on day PP1 to PP7-PP14-PP21-PP28-PP35-PP42 from the uterine cervix and vulva. Only eight measurements were obtained from uterine caruncles because they could not be visible after the day PP14.

Uterine caruncles

The time-dependent differences in the broadest cross-sectional diameter of the caruncles were statistically significant in ewes giving birth to both singletons ($p < 0.001$) and twins ($p < 0.01$) (Table 1). A decrease in the diameter of the caruncles was determined from PP1 to PP14. While the caruncular diameter of all ewes at PP1 was not different from at PP2, it was significantly higher than the rest of the examination days ($p < 0.05$). Additionally, at PP1 and PP2, the widest cross-sectional diameter of caruncles in ewes giving birth to twins was significantly higher than in ewes giving birth to singletons ($p < 0.05$). However, at PP3 and PP4, the widest cross-sectional diameter of caruncles in ewes giving birth to twins tended to be higher than in ewes giving birth to singletons ($p = 0.05$). In B-mod ultrasonography, the caruncles had an exact shape at PP1 but blurred and dispersed at PP7 and PP14 (Figure 2).

As a result of the power Doppler examination, CPP% were measured in uterine caruncles (Figure 3). The time-dependent differences in the CPP% were statistically significant ($p < 0.01$, respectively) in ewes giving birth to both singletons and twins (Table 1). Values of CPP at PP1 were significantly higher than at PP7 and PP14 ($p < 0.05$).

10.3389/fvets.2024.1484189

TABLE 1 The time-dependent differences in the evaluated parameters of the caruncles in ewes giving birth to both singletons and twins.

	PP1	PP2	PP3	PP4	PP5	PP6	PP7	PP14	*P*
Diameter									
Singleton ($n = 9$)	1.67 ± 0.09	1.50 ± 0.08	1.43 ± 0.07	1.34 ± 0.05	1.42 ± 0.07	1.36 ± 0.07	1.28 ± 0.10	1.05 ± 0.11	<0.001
Twin ($n = 4$)	2.09 ± 1.66	1.95 ± 0.16	1.81 ± 0.22	1.65 ± 0.19	1.51 ± 0.14	1.44 ± 0.14	1.25 ± 0.09	0.95 ± 0.14	<0.01
P	<0.05	<0.05	=0.05	=0.05	ns	ns	ns	ns	ns
CPP%									
Singleton ($n = 9$)	2.78 ± 1.05	2.67 ± 1.05	1.36 ± 0.51	1.20 ± 0.73	2.12 ± 1.30	2.01 ± 0.82	0.48 ± 0.23	0.35 ± 0.20	<0.01
Twin ($n = 4$)	7.43 ± 4.83	1.92 ± 1.00	2.73 ± 1.98	1.15 ± 0.49	4.26 ± 1.82	1.96 ± 1.45	0.45 ± 0.29	0.33 ± 0.23	<0.01
P	ns	ns	ns	ns	ns	ns	ns	ns	ns
Cs (m/sn)									
Singleton ($n = 9$)	2.29 ± 0.10	2.26 ± 0.11	2.55 ± 0.18	2.33 ± 0.18	2.06 ± 0.10	1.97 ± 0.15	2.04 ± 0.19	1.41 ± 0.12	<0.05
Twin ($n = 4$)	2.28 ± 0.14	2.52 ± 0.12	2.27 ± 0.15	2.61 ± 0.31	2.31 ± 0.13	2.58 ± 0.04	2.49 ± 0.21	1.89 ± 0.10	<0.05
P	ns	ns	ns	ns	ns	ns	ns	ns	ns
EkPA									
Singleton ($n = 9$)	16.71 ± 1.62	17.79 ± 2.23	19.74 ± 2.73	18.87 ± 3.77	14.37 ± 0.95	14.09 ± 2.86	13.82 ± 2.54	9.29 ± 1.38	<0.05
Twin ($n = 4$)	15.81 ± 2.29	19.32 ± 2.07	18.01 ± 1.91	21.19 ± 5.46	14.91 ± 2.62	20.76 ± 0.88	20.58 ± 3.18	13.24 ± 0.35	<0.05
P	ns	ns	ns	ns	ns	ns	ns	ns	ns

P: Significance, ns: $P < 0.05$.

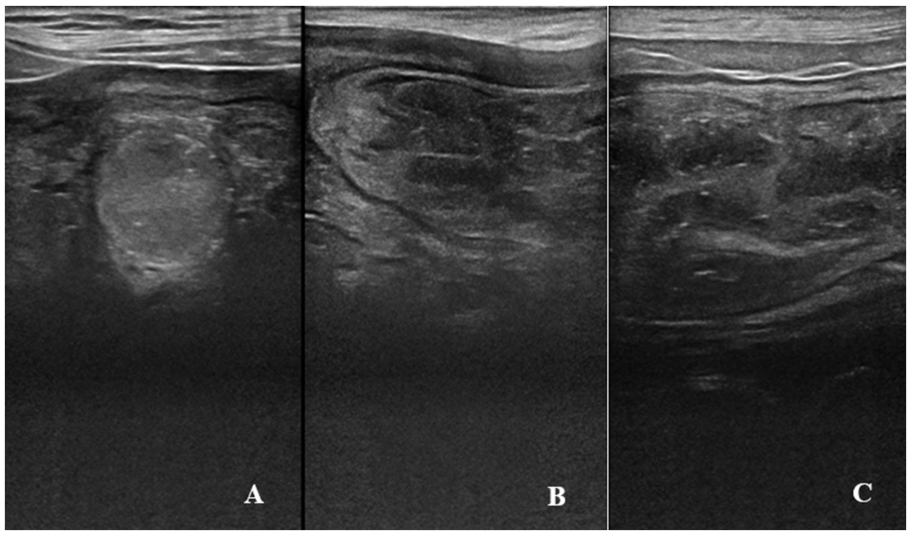

FIGURE 2
B-mod ultrasonographic evaluation of uterine caruncles. **(A)** Spherical shape of a caruncle at PP1. **(B)** Caruncular area with an inconsistent and blurred appearance at PP7. **(C)** Dispersed caruncular area at PP14.

The time-dependent differences in SWS (m/sn) and stiffness (EkPA) in the caruncles were statistically significant ($p < 0.05$) in ewes giving birth to both singletons and twins (Table 1). The caruncular SWS (m/sn) and stiffness (EkPa) of all ewes at PP14 were significantly lower than at PP1 and PP2 ($p < 0.05$) (Figure 4).

The association between the widest cross-sectional diameter, CPP%, SWS, and the stiffness of uterine caruncles was evaluated. The widest cross-sectional diameter of caruncles was not significantly associated with the SWS and stiffness of the caruncles ($p > 0.05$). At PP2 and PP5, the stiffness of the caruncles was inversely correlated with CPP% ($p < 0.01$, $p < 0.05$, respectively). The median, percentiles, maximal and minimal values of diameter, stiffness and CPP% belong to the caruncles of all ewes on the examination days are given in Figure 5.

10.3389/fvets.2024.1484189

Cervix uteri

The examination of the uterine cervix included the widest diameter, SWS (Cs, m/sn), and stiffness (EkPA). The SWS and stiffness values of IOC and EOC were taken in a longitudinal view of cervix (Figures 6, 7). The time-dependent differences in the diameter of the cervix were statistically significant ($p < 0.01$) in ewes giving birth to both singletons and twins (Table 2). At PP3, the widest cross-sectional diameter of the cervix in ewes giving birth to twins was significantly higher than in ewes giving birth to singletons ($p < 0.05$). However, at PP35, the widest cross-sectional diameter of the cervix in ewes giving birth to twins tended to be higher than in ewes giving birth to singletons ($p = 0.07$). The diameter of the cervix uteri of all ewes at PP3 was significantly higher than PP14, PP21, and PP28 ($p < 0.05$). The time-dependent differences in the SWS (m/sn) and stiffness (EkPA) at the IOC were statistically significant ($p < 0.01$ and $p = 0.001$) in ewes giving birth to both singletons and twins (Table 2). The SWS at the IOC for all ewes at PP35 was significantly higher than at PP1, PP4, PP7, and PP14 ($p < 0.05$). Also, at PP35, SWS and stiffness at the IOC were significantly higher in ewes giving birth to twins compared to the ewes giving birth to singletons ($p < 0.001$). The stiffness at the IOC at PP35 for all ewes was significantly high from at PP1, PP4, PP7, and PP14 ($p < 0.01$), while it tended to be high from at PP2, PP5, and PP6 ($p = 0.07$). However, the time-dependent differences in the SWS and stiffness at the EOC were not statistically significant ($p > 0.05$). At PP3, SWS and stiffness at the EOC in ewes giving birth to singletons were significantly higher compared to the ewes giving birth to twins ($p < 0.01$). At PP21, the mean stiffness at the EOC in ewes giving birth to singletons was significantly higher compared to the ewes giving birth to twins ($p < 0.05$), however, SWS at the EOC in ewes giving birth to singletons tended to be higher than in ewes giving birth to twins ($p = 0.08$). At PP35, the stiffness at the EOC in ewes giving birth to singletons tended to be higher compared to the ewes giving birth to twins ($p = 0.07$).

The association between the widest diameter, SWS, and stiffness of the uterine cervix was evaluated. At PP6 and PP21, SWS at the IOC was inversely associated with the diameter of the cervix ($p < 0.01$ and $p < 0.05$, respectively). However, at PP2 and PP4, SWS at the IOC tended to be inversely associated with the diameter of the cervix ($p = 0.05$ and $p = 0.06$, respectively). At

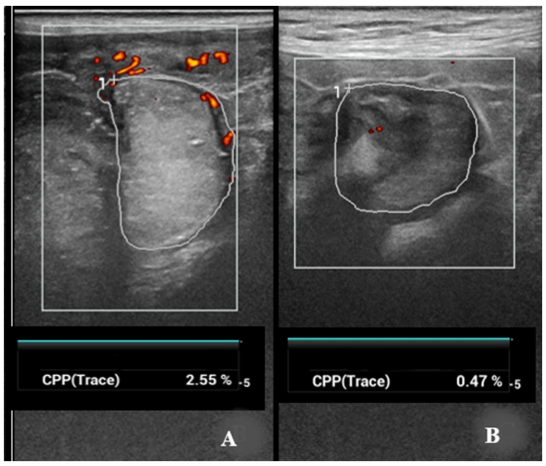

FIGURE 3
Power Doppler ultrasonographic evaluation and quantification of the vascularization on the uterine caruncles. **(A)** Quantification of colored pixels and moderate vascularization on a caruncle at PP6. **(B)** Low vascularization on a caruncle and decrease in CPP at PP14.

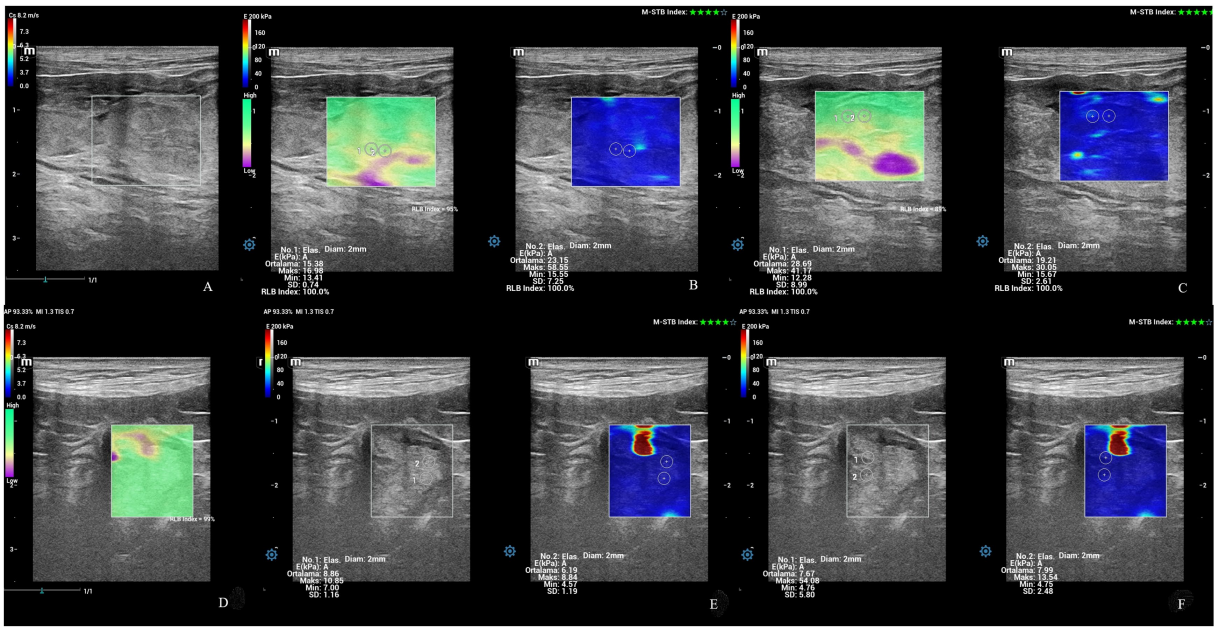

FIGURE 4
Shear wave elastography of caruncles. **(A)** Caruncule in a square ROI with a concave shape at PP1. **(B,C)** Qualitative map of shear wave elastography and quantitative evaluation of a caruncle with total 4 ROI at PP1. **(D)** An image of shear waves with 99% RLB index. **(E,F)** Qualitative map of shear wave elastography and quantitative evaluation of a caruncle with inconsistent and blurred appearance and total 4 ROI at PP14.

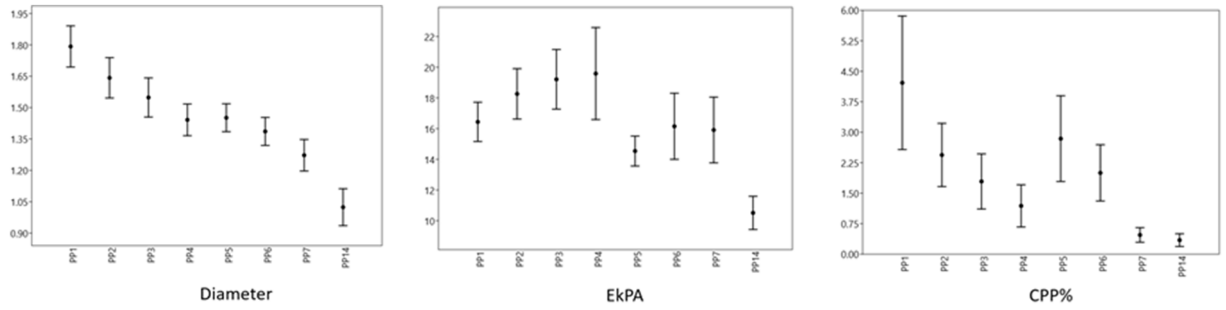

FIGURE 5
Uterine caruncle values. The point represents the median, the margins represent the percentiles (25 and 75), and the extensions of the bars represent the maximal and minimal values.

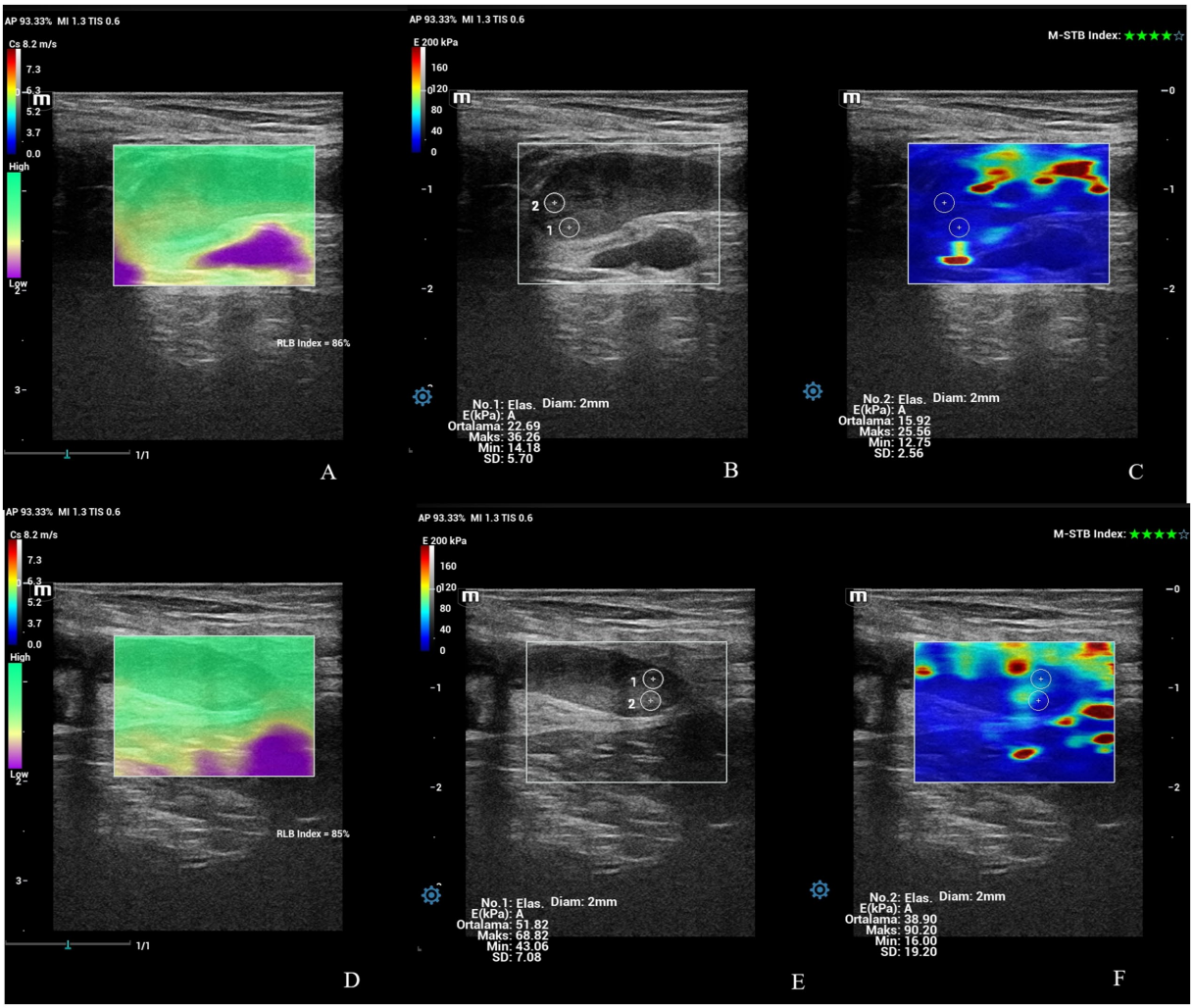

FIGURE 6
Shear wave elastography at the IOC and EOC at PP1 belonging to an ewe giving birth to twin offspring. **(A)** Shear wave image at the IOC with 86% RLB index. **(B)** Quantitative evaluation of the IOC with 2 ROI. M-STB index: 4 stars. **(C)** Qualitative map of shear wave elastography at the IOC. **(D)** Shear wave image at the EOC with 85% RLB index. **(E)** Quantitative evaluation at the EOC with 2 ROI. M-STB index: 4 stars. **(F)** Qualitative map of shear wave elastography at EOC.

PP4 and PP6, the stiffness at the IOC was inversely associated with the diameter of the cervix ($p < 0.01$ and $p = 0.01$, respectively). The widest diameter of the cervix was not significantly associated with both SWS and stiffness at the EOC in all examination times ($p > 0.05$). The median, percentiles, maximal and minimal values of diameter and elastography

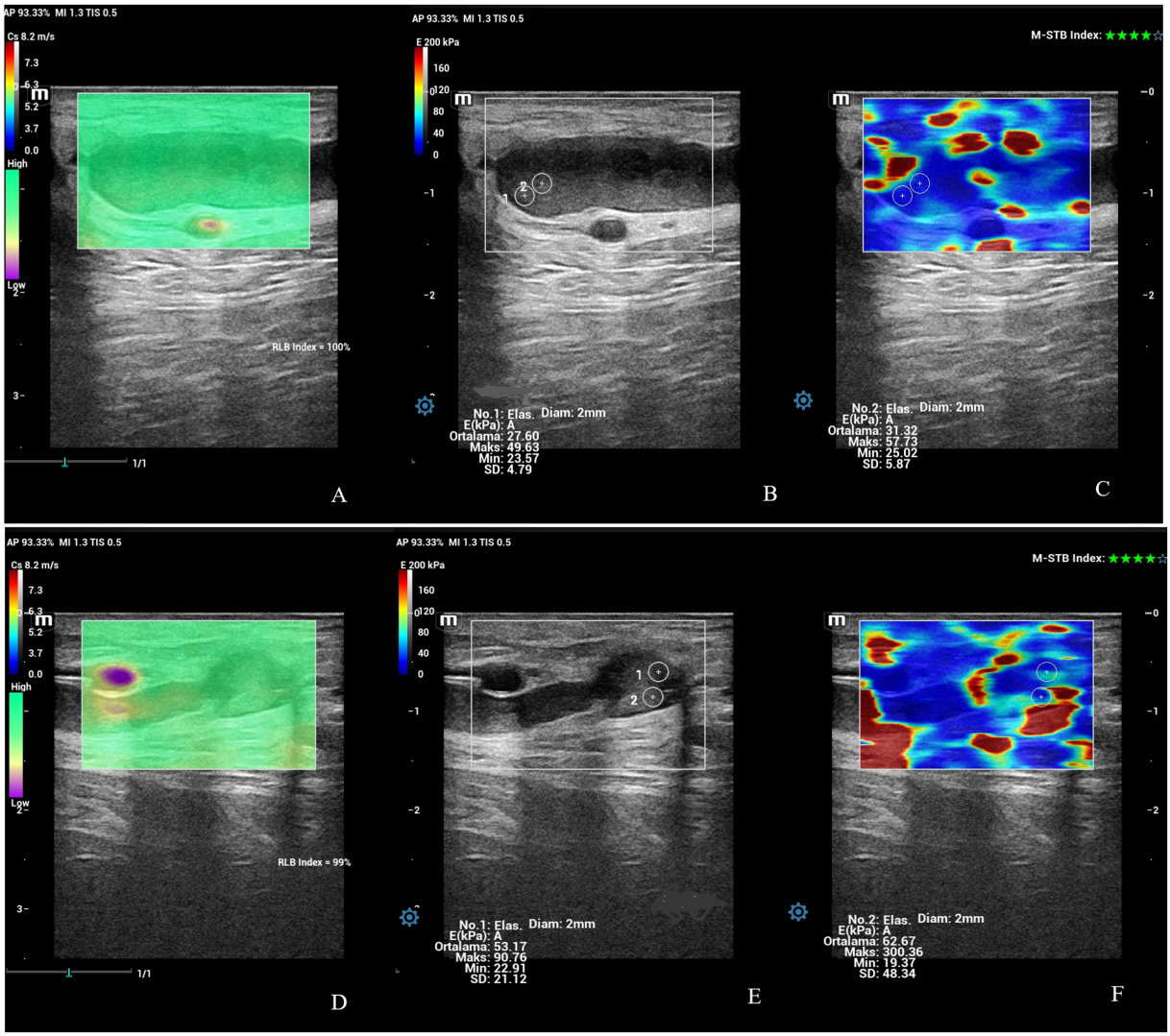

FIGURE 7
Shear wave elastography at the IOC and EOC at PP42 belonging to an ewe giving birth to singleton offspring. **(A)** Shear wave image at the IOC with 100% RLB index. **(B)** Quantitative evaluation at IOC with 2 ROI. M-STB index: 4 stars. **(C)** Qualitative map of shear wave elastography at the IOC. **(D)** Shear wave image at the EOC with 99% RLB index. **(E)** Quantitative evaluation at the EOC with 2 ROI. M-STB index: 4 stars. **(F)** Qualitative map of shear wave elastography at the EOC.

measurements of the cervix (IOC, EOC) of all ewes on the examination days are given in Figure 8.

Vulva

Examining the vulva, the mean thickness of both vulvar lips, SWS (Cs, m/sn), and stiffness (EkPA) (Figure 9) were evaluated. The time-dependent differences in the mean thickness of both vulvar lips were statistically significant ($p < 0.001$) in ewes giving birth to both singletons and twins (Table 3). At PP42, the mean thickness of both vulvar lips in ewes giving birth to twins was significantly higher than in ewes giving birth to singletons ($p < 0.05$). The thickness of the vulva for all ewes at PP1 was significantly high from at PP2, PP3 ($p < 0.01$) and from the other examination days ($p < 0.001$).

The time-dependent differences in the SWS (m/sn) and stiffness (EkPA) in the vulva were statistically significant ($p < 0.001$) in ewes giving birth to both singletons and twins (Table 3). At PP6, the SWS in ewes giving birth to singletons was significantly higher than in ewes giving birth to twins ($p < 0.05$). While the vulvar SWS of all ewes at PP1 tended to be low from at PP2, PP3, PP5, and PP7 ($p = 0.07$), it was significantly low from the rest of the examination days ($p < 0.01$). The vulvar stiffness of all ewes at PP1 was significantly low from at PP4, PP5 and PP14 ($p < 0.05$) and at PP21, PP28, PP35, PP42 ($p < 0.01$).

The association between the thickness, SWS, and stiffness of the vulva were evaluated. At PP35, the thickness of the vulva was significantly associated with the SWS ($p < 0.05$), while the thickness of the vulva tended to be related to the SWS at PP5 ($p = 0.06$). The stiffness of the vulva was not significantly correlated with the thickness of the vulva for all examination times ($p > 0.05$). The median, percentiles, maximal and minimal values of thickness and elastography

TABLE 2 The time-dependent differences in the evaluated parameters of the cervix uteri in ewes giving birth to both singletons and twins.

	PP1	PP2	PP3	PP4	PP5	PP6	PP7	PP14	PP21	PP28	PP35	PP42	*P*
Diameter													
Singleton (*n* = 9)	0.65 ± 0.03	0.64 ± 0.03	0.60 ± 0.02	0.58 ± 0.03	0.64 ± 0.04	0.55 ± 0.04	0.56 ± 0.03	0.51 ± 0.03	0.52 ± 0.04	0.52 ± 0.04	0.50 ± 0.03	0.50 ± 0.03	<0.01
Twin (*n* = 4)	0.62 ± 0.09	0.71 ± 0.10	0.79 ± 0.09	0.66 ± 0.05	0.64 ± 0.06	0.67 ± 0.06	0.65 ± 0.03	0.55 ± 0.07	0.55 ± 0.07	0.55 ± 0.08	0.67 ± 0.11	0.59 ± 0.08	<0.01
P	ns	ns	<0.05	ns	ns	ns	ns	ns	ns	ns	0.07	ns	ns
Internal Cs (m/sn)													
Singleton (*n* = 9)	2.96 ± 0.31	2.78 ± 0.26	3.62 ± 0.5	2.7 ± 0.12	3.05 ± 0.36	3.51 ± 0.46	3.44 ± 0.32	2.93 ± 0.24	3.87 ± 0.62	3.67 ± 0.41	3.51 ± 0.24	4.00 ± 0.38	<0.01
Twin (*n* = 4)	3.44 ± 0.68	3.47 ± 0.73	3.51 ± 0.3	2.71 ± 0.61	3.48 ± 0.2	2.89 ± 0.48	3.05 ± 0.05	3.59 ± 0.23	3.53 ± 0.83	3.10 ± 0.27	6.27 ± 0.50	3.98 ± 0.51	<0.01
P	ns	ns	ns	ns	ns	ns	ns	ns	ns	ns	<0.001	ns	<0.05
Internal EkPA													
Singleton (*n* = 9)	30.46 ± 6.75	26.11 ± 5.16	51.92 ± 15.75	23.27 ± 2.19	32.57 ± 8.89	47.20 ± 11.83	41.20 ± 8.58	28.28 ± 4.56	59.45 ± 23.21	47.49 ± 10.30	39.86 ± 5.62	58.65 ± 9.75	=0.001
Twin (*n* = 4)	40.41 ± 17.21	42.07 ± 18.12	39.94 ± 6.6	29.74 ± 15.66	38.20 ± 4.42	29.75 ± 9.06	29.21 ± 0.67	39.98 ± 5.06	45.91 ± 21.47	30.91 ± 5.46	138.41 ± 28.79	54.04 ± 13.7	=0.001
P	ns	ns	ns	ns	ns	ns	ns	ns	ns	ns	<0.001	ns	<0.01
External Cs (m/sn)													
Singleton (*n* = 9)	3.49 ± 0.51	3.71 ± 0.27	4.57 ± 0.44	3.53 ± 0.32	5.35 ± 1.01	4.29 ± 0.63	4.93 ± 0.63	6.13 ± 0.96	4.23 ± 0.35	4.56 ± 0.34	5.22 ± 0.65	5.35 ± 0.80	ns
Twin (*n* = 4)	3.83 ± 0.36	2.99 ± 0.25	3.18 ± 0.10	4.79 ± 2.10	2.99 ± 0.44	3.40 ± 0.56	6.04 ± 3.01	4.13 ± 0.41	3.17 ± 0.22	3.52 ± 0.45	3.47 ± 0.26	3.62 ± 0.52	ns
P	ns	ns	<0.01	ns	ns	ns	ns	ns	=0.08	ns	ns	ns	<0.05
External EkPA													
Singleton (*n* = 9)	49.47 ± 18.47	45.77 ± 6.60	75.21 ± 16.59	41.76 ± 8.02	118.40 ± 44.51	71.15 ± 24.46	88.67 ± 23.41	146.20 ± 44.32	61.75 ± 12.20	69.13 ± 8.82	103.93 ± 29.40	119.07 ± 34.23	ns
Twin (*n* = 4)	47.52 ± 11.14	29.64 ± 3.28	31.55 ± 2.38	118.64 ± 101.59	29.77 ± 8.56	39.94 ± 13.57	198.50 ± 163.54	55.64 ± 11.49	31.83 ± 4.02	40.75 ± 9.97	38.20 ± 5.23	45.08 ± 12.15	ns
P	ns	ns	<0.01	ns	ns	ns	ns	ns	<0.05	ns	=0.07	ns	ns

P: Significance, ns: $P < 0.05$.

10.3389/fvets.2024.1484189

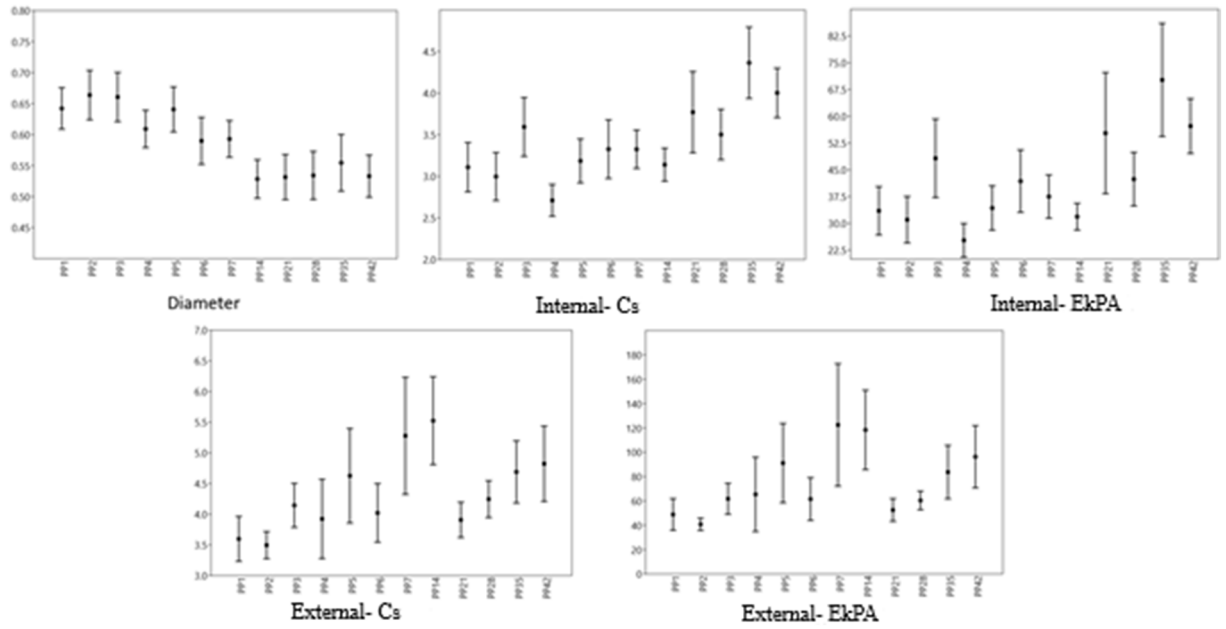

FIGURE 8
Cervix values. The point represents the median, the margins represent the percentiles (25 and 75), and the extensions of the bars represent the maximal and minimal values.

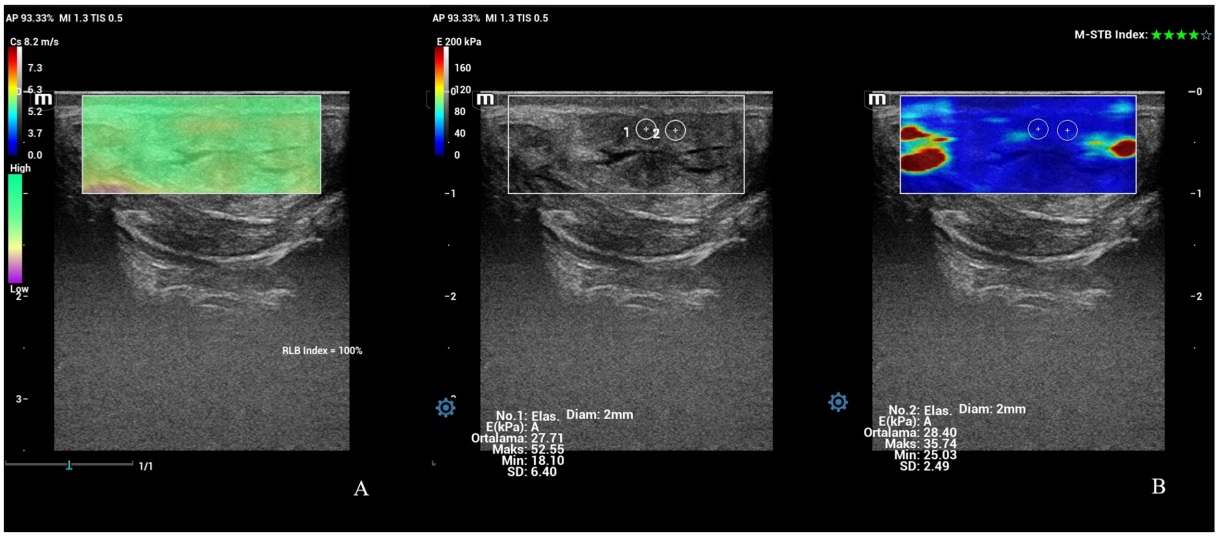

FIGURE 9
Shear wave elastography of vulva at PP6. **(A)** An image of shear waves with 100% RLB index. **(B)** Qualitative map of shear wave elastography and quantitative evaluation of a vulvar labium. M-STB index: 4 stars.

measurements of the vulva of all ewes on the examination days are given in Figure 10.

Discussion

The genital tract returns to the pregravid state after many progressive changes in the postpartum period. Non-invasive imaging techniques such as B-mode ultrasonography, Doppler ultrasonography, and elastography were preferred to evaluate the genital system during the postpartum period in ewes (1, 15, 18). Although there are many studies on the evaluation of uterine involution by using B-mod (6) and Doppler ultrasonography (14, 15), there are limited elastography studies on the postpartum term in ewes (1). In this study, the changes in caruncles, cervix uteri, and vulva were investigated by using non-invasive imaging techniques (B-mod ultrasonography, power Doppler ultrasonography, and shear wave elastography). To our knowledge, this is the first study to evaluate the elasticity of the

TABLE 3 The time-dependent differences in the evaluated parameters of the vulva in ewes giving birth to both singletons and twins.

	PP1	PP2	PP3	PP4	PP5	PP6	PP7	PP14	PP21	PP28	PP35	PP42	*P*
Thickness													
Singleton ($n = 9$)	0.51 ± 0.01	0.41 ± 0.01	0.46 ± 0.01	0.44 ± 0.01	0.433 ± 0.01	0.422 ± 0.01	0.388 ± 0.01	0.382 ± 0.01	0.383 ± 0.01	0.373 ± 0.01	0.377 ± 0.01	0.344 ± 0.01	<0.001
Twin ($n = 4$)	0.52 ± 0.02	0.47 ± 0.01	0.43 ± 0.02	0.41 ± 0.02	0.438 ± 0.01	0.436 ± 0.02	0.429 ± 0.02	0.421 ± 0.02	0.409 ± 0.02	0.405 ± 0.02	0.386 ± 0.006	0.410 ± 0.01	<0.001
P	ns	ns	ns	ns	ns	ns	ns	ns	ns	ns	ns	<0.05	ns
Cs (m/sn)													
Singleton ($n = 9$)	2.91 ± 0.14	3.10 ± 0.14	3.24 ± 0.17	3.14 ± 0.13	3.09 ± 0.14	3.06 ± 0.07	3 ± 0.09	3.07 ± 0.08	3.32 ± 0.11	3.28 ± 0.09	3.35 ± 0.13	3.56 ± 0.15	<0.001
Twin ($n = 4$)	2.39 ± 0.20	2.64 ± 0.10	2.89 ± 0.01	3.29 ± 0.16	2.87 ± 0.05	2.79 ± 0.04	2.90 ± 0.11	2.86 ± 0.14	3.05 ± 0.07	3.15 ± 0.15	3.28 ± 0.16	3.54 ± 0.09	<0.001
P	ns	ns	ns	ns	ns	<0.05	ns	ns	ns	ns	ns	ns	ns
EkPA													
Singleton ($n = 9$)	27.22 ± 2.88	29.84 ± 2.93	31.06 ± 2.78	30.15 ± 1.85	27.76 ± 1.38	30.52 ± 2.09	29.7 ± 2.15	29.3 ± 1.87	32.84 ± 1.74	35.2 ± 3	34.82 ± 2.66	44.14 ± 3.56	<0.001
Twin ($n = 4$)	18.53 ± 3.12	21.7 ± 1.67	27.03 ± 2.11	33.82 ± 3.52	29.73 ± 2.95	24.74 ± 0.51	25.87 ± 2.06	25.25 ± 2.47	28.2 ± 2.07	30.11 ± 4.21	32.39 ± 3.63	38.23 ± 4.95	<0.001
P	ns	ns	ns	ns	ns	ns	ns	ns	ns	ns	ns	ns	ns

P: Significance, ns: $P < 0.05$.

10.3389/fvets.2024.1484189

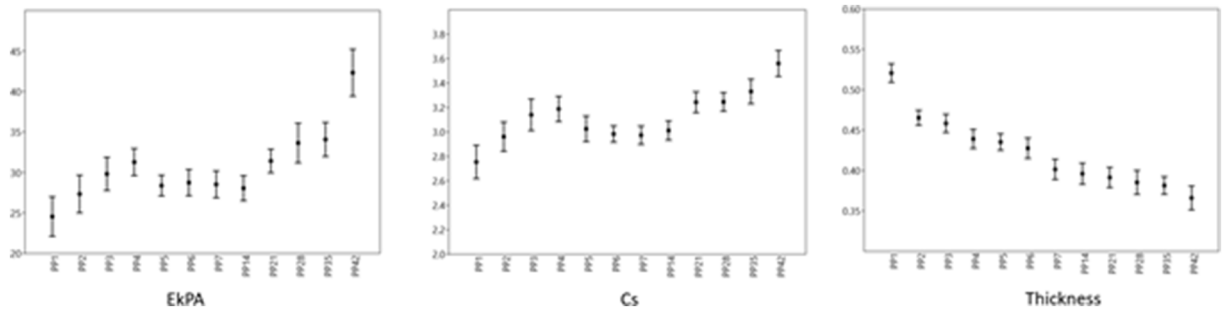

FIGURE 10
Vulva values. The point represents the median, the margins represent the percentiles (25 and 75), and the extensions of the bars represent the maximal and minimal values.

caruncles, cervix uteri, and vulva during the postpartum period in ewes.

The size of the caruncles had a progressive, significant reduction afterward in the degeneration and necrosis on their surface, especially during the first week after lambing (7, 18). During the regression process, caruncles change their appearance from concave to convex imaged the caruncles with inconsistent and blurred structures at the longitudinal section taken on the fourth day postpartum during a transcutaneous examination at the inguinal area (18). In line with Ioannidi et al. (18), caruncles were concave until the fourth day of the postpartum period. Most authors have reported that imaging of caruncles by using B-mod ultrasonography after the 10th day postpartum was not possible and rare (7, 19). Differentiating the caruncles from uterine endometrial folds is usually tricky (7). Kähn (20, 21) mentioned that caruncles were visible during the second week after lambing despite their decreased size. Ababneh and Degefa (19) imaged the caruncles subsequently to the 13th day postpartum. Similar to the previous reports (19–21), there was a reduction in the size of the caruncles during the first 14 days of postpartum in both ewes giving birth to singleton offspring and twin offspring in the present study. Also, the shape of the caruncles was inconsistent, and their appearance was blurred on days PP7 and PP14 in this study. In line with the researchers (7, 19), caruncles were not visible after the evaluation point at PP14. Fernandes et al. (22) reported that the sex of newborns and single or twin partitions did not affect the placental expulsion time and cotyledons diameter ($p > 0.05$). Similarly, placental expulsion was completed within 9 h after delivery in all ewes in this study. Enginler et al. (23) indicated that Saanen's gestation type (single and twin) and parity (primiparous and pluriparous) had no significant effect on caruncular diameter in the involution period except on day 13. However in this study, caruncular diameters of the ewes with twin parturition were significantly higher in the first 2 days of postpartum compared to the singleton parturitions.

O'Shea and Wright (11) evaluated the involution and regeneration of the endometrium following parturition in the ewes by light-and electron microscopy. Eight days after parturition, degeneration of the tissues of the placentomas was more marked, and caruncles appeared weakly vascularized. Fifteen days after parturition, the dead placental tissue had separated from the caruncles (11). Fernandes et al. (22) reported that necrotic plaques are released in caruncular involution in the second week of the postpartum period in ewes, and re-epithelialization of the caruncular region occurs during the third or fourth postpartum week. Henao-Gonzalez et al. (24) investigated the ultrasonographic screening of dairy cows with normal uterine involution, and they stated that caruncular vascular supply decreases throughout the involution process. In harmony with the previous reports, the caruncular diameter and vascularization (CPP%) of the caruncles were reduced from PP1 to PP14, regardless of the number of offspring in this study ($p < 0.001$ and $p < 0.01$, respectively). During the involution, CPP was not different between the single or twin parturition ($p > 0.05$). It was thought that the reduction of the caruncular vascularization on the postpartum period occurred due to the degeneration of the caruncular tissues in ewes.

Elastography is a non-invasive imaging technique used to evaluate tissue stiffness. Alan et al. (25) assessed the placental stiffness in pregnant women with fetal anomalies using ARFI elastography. They indicated that placental stiffness was significantly higher in pregnancies with fetal anomalies compared to healthy individuals. In addition, Alan et al. (25) did not observe a correlation between placental thickness and elasticity parameters. Da Silva et al. (17) assessed the maternal and fetal structures in pregnant ewes by using ARFI elastography. They indicated that the shear wave velocity of the placentomes remained constant through gestation in ewes. Although in this study the evaluation term was different from the previous reports, the caruncular SWS (m/sn) and stiffness (EkPa) of all ewes at PP14 were significantly lower than from at PP1 and PP2 ($p < 0.05$). The higher SWS and stiffness values of the caruncles obtained on day PP1 and PP2 could be related to the caruncular necrosis while the lower values obtained on day PP14 could be related with the release of the necrotic tissues and the onset of the re-epithelialization process (necrotic tissue; stiffer, re-epithelialization tissue; softer). In line with Alan et al. (25), the broadest cross-sectional diameter of the caruncles was not related to the elastography parameters ($p > 0.05$). To the authors' knowledge, this is the first study that evaluates the caruncular stiffness in the postpartum involution process in ewes.

The cervix is composed of layers of collagen and smooth muscles. The structure of the cervix is associated with collagen hyaluronan, matricellular proteins, and proteoglycans, and they cause the cervix to mature. Following birth, the cervix rapidly recovers (26). The process of involution in cows was assessed by

the reduced diameter of the cervix at postpartum (27). Harkness and Harkness (28) stated that the circumference of the cervix in rats falls in 8 h to about one-third of that at parturition. Subsequently, there is a slower fall until the eighth day, when the value is about an eighth of that at parturition (28). The diameter of the cervix in cows is accepted as a valuable indicator of the involution process (29). They reported that involution of the cervix in cows was affected by parity and type of postpartum discharge. The diameter of the cervix during 2 to 6 weeks postpartum regressed both in multiparous and primiparous cows with normal or abnormal discharge (29). Usmani et al. (30) observed slower involution of the cervix and uterus in buffaloes with subclinical bacterial uterus infection. Although the cervix's involution rate is affected by the disease, it has been reported that the diameter of the cervix decreases by half when involution is completed in both healthy buffalos and those with uterine infections (30). Miettinen (31) indicated that the time duration for the involution of the cervix (approximately 30 days) was quite similar in primiparous and multiparous (3. parity) cows, and the cervix diameter looked alike at 3 weeks after parturition in primiparous and multiparous (3. parity) cows. Unlike the researchers (29, 30) in the present study, uterine infection was absent during the postpartum period in ewes, which were all multiparous. In this study, the diameter of the cervix uteri of all ewes at PP3 was significantly higher than PP14, PP21, and PP28 ($p < 0.05$). Only at PP3, the diameter of cervix in twin parturitions was higher than the ewes giving birth to singleton offspring.

The usefulness of elastography is not only valuable in obstetrics but may also play a significant role in gynecological conditions. In humans, SWS at the cervix was evaluated in healthy pregnant women (32), hysterectomy specimens of premenopausal women (33), pregnant women with pathological cervix (34) and differentiation of the benign from the malignant cervical lesions (35). In rats, the elastic and viscous behavior of the cervix was evaluated by a hydroxyproline assay, which measures collagen content (36). Mariano et al. (1) assessed the stiffness of the uterine wall parenchyma in healthy ewes during postpartum 30 days. They found that the mean shear velocity values of the uterine wall in quantitative elastography did not differ. Peralta et al. (16) investigated cervical stiffness by using shear wave elastography in pregnant ewes, which are induced with dexamethasone for cervical ripening. They observed a significant decrease in SWS in the first 4–8 h after dexamethasone compared to controls, which was thought to be associated with cervical ripening induced by dexamethasone. Studies have described elastography with significant results in veterinary research, but this is the first study to evaluate cervical stiffness during postpartum 42 days in Kivircik ewes. This study evaluated SWS and stiffness in a longitudinal view of the cervical canal on the IOC and EOC during the postpartum period. Regardless of the offspring number, the SWS and stiffness at the IOC were significantly higher at PP35 compared to the evaluation points at PP1-PP4-PP7-PP14. Liu et al. (2) reported that uterine involution was completed by day 30 postpartum in ewes with singleton parturitions, by day 35 postpartum with twin parturitions, and by day 40 postpartum with triplet parturitions. Tanaka et al. (37) measured the shear wave velocity before, immediately after, and 1 and 2 h after placental delivery to determine the cervical stiffness in women with vaginal delivery. They did not observe a significant alteration in the stiffness of the cervix over time. This may be due to the fact that the study (37) was conducted in a limited time that did not fully cover the involution period of the uterus. Although the evaluation time scale in the present study differs from the report by Tanaka et al. (37), time-dependent differences in the elasticity parameters belonging to the EOC were nonsignificant while they were significant at the IOC. The lower SWS and stiffness values at the IOC obtained on PP1, PP4, PP7 and PP14 compared to PP35 could be related to the involution process of the cervix and the change in the composition of it (ripened; soft, involuted; stiff). Although the broadest cross-sectional diameter of the cervix was significantly related to the SWS value of the IOC at PP6 and PP21, there was no relation between the diameter of the cervix and elasticity parameters of the EOC for all evaluated times. In this study, the lack of time-dependent change in SWS and stiffness values in EOC may be due to the fact that the changes in the compositions and involutions of EOC and IOC are different and these changes are more dramatic in IOC. We believe this study provides important and novel information about the objective quantification of cervical stiffness (IOC and EOC) during the postpartum period.

The vulva is the external genital organ in females, ranging from 10 cm to 12 cm in cows, while for does and ewes, it is a quarter of the length (38). During parturition, the cervix, vagina, and vulva are the physical and anatomic barriers (39). At the parturition, some externally visible changes occur in animals. The most important external changes of approaching parturition are seen in the udder, vulva, and pelvic ligaments and, to some extent, in the behavior (40). The vulva becomes progressively edematous, flaccid, and enlarged (2 to 5 times the average size) as parturition approaches in most domestic animals (41). Saut et al. (42) investigated vulvar edema in dairy cows for 43 postpartum days. The severity of vulvar edema disappeared after the 3rd postpartum day, and a significant decrease in vulvar edema was observed until the 43rd postpartum day (42). The thickness of the vulva for all ewes at PP1 was significantly high from at PP2, PP3 ($p < 0.01$) and from the other examination days ($p < 0.001$). The decrease in the thickness of the vulva is due to the reduction of vulvar edema in the postpartum period. The SWS and stiffness values of the vulvar lips at PP1 were significantly lower compared to at PP14, PP21, PP28, PP35, and PP42. This may be due to the softness of the vulvar lips as a result of the edema at PP1. To the best of our knowledge, this is the first study in ewes to evaluate the elasticity of the vulva in the postpartum period.

Conclusion

Recent studies have reported ultrasonography (B-mode and Doppler) as a valuable tool for evaluating the involution process in ewes. In our research, it was possible to describe the changes throughout the postpartum period and assess the involution of uterine cervix, caruncles, and vulvar labia and tissue stiffness during postpartum involution by B mode ultrasonography, power Doppler ultrasonography, and shear wave elastography with significant results. We provided valuable information to elucidate the differences in the involution process concerning the offspring number during the postpartum period in Kivircik ewes. Shear wave elastography may be a

valuable method for objectively quantifying the stiffness of the gynecological tissue and organs.

Data availability statement

The original contributions presented in the study are included in the article/supplementary material, further inquiries can be directed to the corresponding author.

Ethics statement

The animal study was approved by Unit Ethics Committee of İstanbul University-Cerrahpaşa, Faculty of Veterinary Medicine, İstanbul, Türkiye (Approval No. 2023/22). The study was conducted in accordance with the local legislation and institutional requirements.

Author contributions

ZU: Conceptualization, Methodology, Resources, Writing – original draft, Writing – review & editing. İK: Resources, Writing – original draft, Writing – review & editing. MU: Resources, Writing – original draft, Writing – review & editing. MÖ: Methodology, Resources, Writing – original draft, Writing – review & editing. MK: Supervision, Writing – original draft, Writing – review & editing. SD: Writing – original draft, Writing – review & editing. TS: Investigation, Writing – original draft, Writing – review & editing. OG: Supervision, Writing – original draft, Writing – review & editing.

Funding

The author(s) declare that no financial support was received for the research, authorship, and/or publication of this article.

Conflict of interest

The authors declare that the research was conducted in the absence of any commercial or financial relationships that could be construed as a potential conflict of interest.

The reviewer NH declared a past co-authorship with the authors SD, TS, OG to the handling editor.

Publisher's note

References

1. Mariano RSG, Santos VJC, Taira AR, Silva PDA, Rodriguez MGK, Padilha-Nakaghi LC, et al. Characterization of uterine involution using B-mode ultrasonography, color Doppler, and elastography (acoustic radiation force impulse) for assessing postpartum in Santa Inês ewes. *Anim Reprod*. (2023) 20:e20220110. doi: 10.1590/1984-3143-AR2022-0110

2. Liu Z, Zhang W, Zhu C, Chen X, Zhao Y, Wang Y, et al. Effect of different litter size on the rate of postpartum uterine involution in Hu sheep. *Kafkas Univ Vet Fak Derg*. (2022) 28:275–80. doi: 10.9775/kvfd.2021.26965

3. Rubianes E, Ungerfeld R. Uterine involution and ovarian changes during early post-partum in autumn lambing Corriedale ewes. *Theriogenology*. (1993) 40:365–72. doi: 10.1016/0093-691X(93)90274-9

4. Naznin F, Hasan M, Bhuiyan MMU, Bari FY, Juyena NS. Monitoring of uterine involution in indigenous ewes using ultrasonography. *Bangl Vet J*. (2019) 53:29–34. doi: 10.32856/BVJ-53-2019.04

5. Hayder M, Ali A. Factors affecting the postpartum uterine involution and luteal function of sheep in the subtropics. *Small Rumin Res*. (2008) 79:174–8. doi: 10.1016/j.smallrumres.2008.07.023

6. Zdunczyk S, Stanislaw M, Baranski W, Janowski T, Szczepanski W, Jurczak A, et al. Postpartum uterine involution in primiparous and pluriparous Polish longwool sheep monitored by ultrasonography. *Bull Vet Inst Pulawy*. (2004) 48:255–8.

7. Hauser B, Bostedt H. Ultrasonographic observations of the uterine regression in the ewe under different obstetrical conditions. *J Vet Intern Med*. (2002) 49:511–6. doi: 10.1046/j.1439-0442.2002.00496.x

8. Van Wyk LC, Van Niekerk CH, Hunter GL. Influence of exogenous hormones and season of lambing on uterine involution in the sheep. *Agroanimalia*. (1972) 4:77–82.

9. Gray CA, Stewart MD, Johnson GA, Spencer TE. Postpartum uterine involution in sheep: histoarchitecture and changes in endometrial gene expression. *Reproduction-Cambridge*. (2003) 125:185–98. doi: 10.1530/rep.0.1250185

10. Van Wyk LC, Van Niekerk CH, Belonje PC. Involution of the postpartum uterus of the ewe. *J S Afr Vet Assoc*. (1972) 43:19–26.

11. O'Shea JD, Wright PJ. Involution and regeneration of the endometrium following parturition in the ewe. *Cell Tissue Res*. (1984) 236:477–85. doi: 10.1007/BF00214253

12. Scott PR. Applications of diagnostic ultrasonography in small ruminant reproductive management. *Anim Reprod Sci*. (2012) 130:184–6. doi: 10.1016/j.anireprosci.2012.01.013

13. Meinecke-Tillmann S. Basics of ultrasonographic examination in sheep. *Small Rumin Res*. (2017) 152:10–21. doi: 10.1016/j.smallrumres.2016.12.023

14. Dal GE, Enginler SO, Cetin AC, Baykal K, Sabuncu A. B-mode and Doppler ultrasonographic assessment of uterine involution in ewes treated with two different doses of prostaglandinf 2α. *Acta Sci Vet*. (2020) 48:1765. doi: 10.22456/1679-9216.105041

15. Enginler SÖ, Evkuran Dal G, Çetin AC, Sabuncu A, Baykal K. Determination of the effects of oxytocin and carazolol on uterine involution by pulsed-wave Doppler ultrasonography in Kivircik ewes. *Ankara Univ Vet Fak Derg*. (2024) 71:63–71. doi: 10.33988/auvfd.1025621

16. Peralta L, Mourier E, Richard C, Charpigny G, Larcher T, Aït-Belkacem D, et al. In vivo evaluation of cervical stiffness evolution during ınduced ripening using shear wave elastography, histology, and 2 photon excitation microscopy: Insight from an animal model. *PLoS One*. (2015) 10:e0133377. doi: 10.1371/journal.pone.0133377

17. da Silva PD, Uscategui RAR, Santos VJ, Taira AR, Mariano RS, Rodrigues MG, et al. Acoustic radiation force impulse (ARFI) elastography to assess maternal and fetal structures in pregnant ewes. *Reprod Domest Anim*. (2019) 54:498–505. doi: 10.1111/rda.13384

18. Ioannidi KS, Mavrogianni VS, Valasi I, Barbagianni MS, Vasileiou NGC, Amiridis GS, et al. Ultrasonographic examination of the uterus of ewes during the post-partum period. *Small Rumin Res*. (2017) 152:74–85. doi: 10.1016/j.smallrumres.2016.12.014

19. Ababneh MM, Degefa T. Ultrasonic assessment of puerperal uterine involution in Balaby goats. *J Vet Med*. (2005) 52:244–8. doi: 10.1111/j.1439-0442.2005.00718.x

20. Kähn W. Ultrasonography as a diagnostic tool in female animal reproduction. *Anim Reprod Sci*. (1992) 28:1–10. doi: 10.1016/0378-4320(92)90085-R

21. Kähn W, Volkmann D eds. Veterinary reproductive ultrasonography. Hannover: Schlutersche (2004). 256 p.

22. Fernandes CE, Cigerza CF, Pinto GS, Miazi C, Barbosa-Ferreira M, Martins CF. Parturition characteristics and uterine involution in native sheep from Brazilian Pantanal. *Cienc Anim Bras*. (2013) 14:245–52. doi: 10.5216/cab.v14i2.17926

23. Enginler SÖ, Sandal Aİ, Erzengin ÖM, Yüksel H, Ertürk E, Doğan N, et al. Effects of gestation type and parity on uterus ınvolution in Saanen does. *Animal Health Prod Hyg*. (2014) 3:288–93.

24. Henao-Gonzalez M, Ferrer MS, Jiménez-Escobar C, Palacio-Baena LG, Maldonado-Estrada JG. Ultrasonographic screening of dairy cows with normal uterine involution or developing postpartum uterine disease using B-mode, color, and spectral Doppler. *Vet Med Int*. (2023) 2023:2597332. doi: 10.1155/2023/2597332

25. Alan B, Göya C, Tunc S, Teke M, Hattapoğlu S. Assessment of placental stiffness using acoustic radiation force impulse elastography in pregnant women with fetal anomalies. *Korean J Radiol*. (2016) 17:218–23. doi: 10.3348/kjr.2016.17.2.218

26. Yoshida K, Jayyosi C, Lee N, Mahendroo M, Myers KM. Mechanics of cervical remodeling: insights from rodent models of pregnancy. *Interface Focus*. (2019) 9:20190026. doi: 10.1098/rsfs.2019.0026

27. Kaidi R, Brown PJ, David JS, Etherington DJ, Robins SP. Uterine collagen during involution in cattle. *Matrix*. (1991) 11:101–7. doi: 10.1016/S0934-8832(11)80213-1

28. Harkness ML, Harkness RD. The mechanical properties of the uterine cervix of the rat during involution after parturition. *J Physiol*. (1965) 156:112–20. doi: 10.1113/jphysiol.1961.sp006661

29. Oltenacu PA, Britt JH, Braun RK, Mellenberger RW. Relationships among the type of parturition, type of discharge from the genital tract, involution of the cervix, and subsequent reproductive performance in Holstein cows. *J Dairy Sci*. (1983) 66:612–9. doi: 10.3168/jds.S0022-0302(83)81832-3

30. Usmani RH, Ahmad N, Shafiq P, Mirza MA. Effect of subclinical uterine infection on cervical and uterine involution, estrous activity and fertility in postpartum buffaloes. *Theriogenology*. (2011) 55:563–71. doi: 10.1016/S0093-691X(01)00426-5

31. Miettinen PVA. Uterine involution in Finnish dairy cows. *Acta Vet Scand*. (1990) 31:181–5. doi: 10.1186/BF03547560

32. Hernandez-Andrade E, Aurioles-Garibay A, Garcia M, Korzeniewski SJ, Schwartz AG, Ahn H, et al. The effect of depth on shear-wave elastography was estimated in the internal and external cervical os during pregnancy. *J Perinat Med*. (2014) 42:549–57. doi: 10.1515/jpm-2014-0073

33. Carlson LC, Feltovich H, Palmeri ML, Dahl JJ, Munoz del Rio A, Hall TJ. Estimation of shear wave speed in the human uterine cervix. *Ultrasound Obstet Gynecol*. (2014) 43:452–8. doi: 10.1002/uog.12555

34. Gennisson JL, Muller M, Ami O, Kohl V, Gabor P, Musset D, et al. Shear wave elastography in obstetrics: Quantification of cervix elasticity and uterine contraction. Proceedings of the 2011 IEEE International Ultrasonics Symposium (IUS), 18–21 October. Orlando, FL, USA (2011) (pp. 2094–2097). doi: 10.1109/ULTSYM.2011.0519

35. Lu R, Xiao Y, Liu M, Shi D. Ultrasound elastography in the differential diagnosis of benign and malignant cervical lesions. *J Ultrasound Med*. (2014) 33:667–71. doi: 10.7863/ultra.33.4.667

36. Barone WR, Feola AJ, Moalli PA, Abramowitch SD. The effect of pregnancy and postpartum recovery on the viscoelastic behavior of the rat cervix. *J Mech Med Biol*. (2012) 12:1250009–125000917. doi: 10.1142/S0219519412004399

37. Tanaka T, Makino S, Saito T, Yorifuji T, Koshiishi T, Tanaka S, et al. Attempt to quantify uterine involution using acoustic radiation force impulse before and after placental delivery. *J Med Ultrasound*. (2011) 38:21–5. doi: 10.1007/s10396-010-0292-5

38. Williard ST, Joe Bearden H, Fuquay JW eds. Applied animal reproduction. Upper Saddle River, NJ: Pearson Prentice Hall (2004). 456 p.

39. Zaleha P, Vargová M, Kadasi M, Smitka P, Smarzik M, Kovac G. Effect of postpartum uterine involution on folliculogenesis, oestrus, and conception in cows. *Rocz Nauk Pol Tow Zootech*. (2013) 9:57–65.

40. Safdar AHA, Kor NM. Parturition mechanisms in ruminants: A complete overview. *Eur J Exp Biol*. (2014) 4:211–8.

41. Purohit G. Parturition in domestic animals: A review. *Webmed Central Reprod*. (2010) 1:10.

42. Saut JPE, Oliveira RSBR, Martins CFG, Moura ARF, Tsuruta AS, Nasciutti NR, et al. Clinical observations of postpartum uterine involution in crossbred dairy cows. *Vet Not*. (2011) 17:16–25.

frontiers | Frontiers in Veterinary Science

TYPE Original Research
PUBLISHED 15 January 2025
DOI 10.3389/fvets.2024.1510253

OPEN ACCESS

EDITED BY
Ozan Gündemir,
Istanbul University Cerrahpasa, Türkiye

REVIEWED BY
Nedzad Hadziomerovic,
University of Sarajevo,
Bosnia and Herzegovina
Burcu Onuk,
Ondokuz Mayıs University, Türkiye

*CORRESPONDENCE
Lukas Kleiner
✉ Lukas.kleiner@marigin.ch

RECEIVED 12 October 2024
ACCEPTED 31 December 2024
PUBLISHED 15 January 2025

CITATION
Kleiner L, Wolf N, Precht C, Haenssgen K, Forterre F and Düver P (2025) Feline sacroiliac luxation: comparison of fluoroscopy-controlled freehand vs. computer-navigated drilling in the sacrum—a cadaveric study.
Front. Vet. Sci. 11:1510253.
doi: 10.3389/fvets.2024.1510253

Feline sacroiliac luxation: comparison of fluoroscopy-controlled freehand vs. computer-navigated drilling in the sacrum—a cadaveric study

Lukas Kleiner[1]*, Nicole Wolf[2], Christina Precht[3], Kati Haenssgen[4], Franck Forterre[2] and Pia Düver[2]

[1]Divison of Small Animal Surgery, Department of Clinical Veterinary Medicine, Tierklinik Marigin, Feusisberg, Switzerland, [2]Divison of Small Animal Surgery, Department of Clinical Veterinary Medicine, Vetsuisse-Faculty, University of Bern, Bern, Switzerland, [3]Divison of Clinical Radiology, Department of Clinical Veterinary Medicine, Vetsuisse-Faculty, University of Bern, Bern, Switzerland, [4]Divison of Veterinary Anatomy, Department of Clinical Research and Veterinary Public Health, Vetsuisse-Faculty, University of Bern, Bern, Switzerland

Introduction: Sacroiliac luxation is a common traumatic feline injury, with the small size of the sacral body being a challenge for surgical stabilization. This study compared an innovative computer-guided drilling method with the conventional fluoroscopy-controlled freehand technique. Neuronavigation, using CT-based planning and real-time tracking, was evaluated against the freehand method for accuracy and time efficiency.

Materials and methods: Bilateral sacroiliac luxation was induced in 20 feline cadavers. One side of the sacral body was drilled using fluoroscopy, and the other with neuronavigation (Stealth Station S8). A reference frame was affixed to the sacral spinous process for tracking. Ten cats were operated on by an ECVS diplomate and 10 by a resident. Postoperative cone beam CT images were used to assess both techniques, comparing the accuracy of the planned corridor vs. the actual drill hole in the sacrum. A learning curve for both methods was estimated by measuring procedure time.

Results: CT scan assessments showed all 40 drill holes achieved "surgically satisfactory" results. The computer-navigated technique demonstrated an average deviation of 1.9 mm (SD 1.0 mm) at the entry point and 1.6 mm (SD 0.8 mm) at the exit point. The pins of 3/20 reference frames penetrated the vertebral canal, creating a risk for potential clinical complications. The neuronavigation-guided procedures took an average of 23 min and 37 s (SD 8 min 34 s), significantly longer than the freehand technique, which averaged 9 min and 47 s (SD 3 min 26 s). A steep learning curve was observed with neuronavigation.

Discussion: The neuronavigation-guided technique achieved accuracy is comparable to the fluoroscopy-controlled method, is offering real-time feedback and has potential for highly precise surgeries near critical anatomical structures. However, significant attention must be given to the placement of the reference frame, as it is placed blindly and presents a potential risk for errors and complications. Despite its longer duration, the neuronavigation method shows promise for improving precision in complex surgical scenarios.

KEYWORDS

neuronavigation, stealth station S8, computer-navigated surgery, sacroiliac luxation, cat, cadaveric study

1 Introduction

One of the most common fracture sites after trauma in cats is the pelvic region (1). Up to 60% of cases of pelvic fractures involve the sacroiliac joint. Sacroiliac fracture luxations are injuries most commonly observed following falls from height or after motor vehicle trauma and usually occur in combination with other pelvic fractures or soft tissue injuries. In cats, sacroiliac dislocations are bilateral in approximately 15% of cases (1).

Based on the radiologically assessed grade of displacement and the clinical symptoms, either conservative management or surgical treatment may be considered. Surgical stabilization is indicated in cases of severe pain, neurologic deficits, pelvic canal stenosis, and/or when rapid return to weight-bearing activity is desired (2–4). The most common surgical method is the placement of a lag screw through the iliac wing into the sacrum, either through an open or minimally invasive approach. Both methods are usually performed under fluoroscopic control, but can also be performed without fluoroscopy (5–7). There are also reports of successful stabilization using single transiliosacral pin (8), transiliosacral toggle suture (9), transileal pin/bolt/screw (10), ventral screw placement (11) and tension band technique (12). Placement of the lag screw within the sacral body is the most critical part of the procedure, as the safe corridor is small and there are several important structures which should not be damaged during the surgery (termination of the spinal cord and nerve roots dorsally, intervertebral disc cranially and important nerves and vascular structures ventrally). The optimal entry point and angle of the screw were analyzed in several studies (13–15). For sufficient bone purchase, the screw should penetrate 60% of the sacral diameter (16).

Previous studies evaluated open and minimally invasive placement of lag screws under fluoroscopic control. Malpositioning of the screw was seen in 7.5–12.5% of cases, which directly led to revision surgery or had an increased risk of postoperative implant loosening (5, 7, 10, 16).

In human medicine, computer technology has been used in the operating room for years to improve the accuracy and safety of various procedures. Especially for brain and spine surgery, neuronavigation enables accurate implant placement by visualizing the corridor being drilled and any deviations of the planned corridor in real-time (17–19). The technique is considered safe and effective in humans for sacroiliac joint surgery (20–22).

In veterinary medicine the use of neuronavigation is described for placing toggle constructs across the coxofemoral joint and fracture treatment in horses (23–25), minimally invasive spinal stabilization in dogs (26), vertebral pin placement in dogs (27), craniectomies in dogs with osteochondrosarcoma (28) and brain biopsies in dogs and cats (29). In horses this technique is used in clinical cases to place implants in the proximal phalanx, the third metatarsal bone, the ulna or the medial femoral condyle (24).

To date, the author is not aware of any studies on the application of neuronavigation for the surgical treatment of feline sacroiliac luxation. The purpose of this study was to evaluate the accuracy and safety of this technology for treatment of feline sacroiliac luxation. We hypothesized that drilling a hole in the sacrum using computer-navigated drilling through neuronavigation would be at least as accurate as conventional freehand drilling under fluoroscopic control. Additionally, we expect a steep learning curve, particularly for computer-navigated drilling, due to improvement in workflow execution and the application of the new technique. This is expected to affect the overall surgery duration.

2 Materials and methods

Bilateral sacroiliac luxations were created in 20 feline cadavers and a drill hole was placed into the sacral body on each side. One side was operated on using conventional fluoroscopy-controlled freehand technique and one side was operated on using the new neuronavigation technique.

2.1 Cadavers

Twenty cadavers of skeletally mature cats were included in the study. All cats died or were euthanized due to medical conditions unrelated to this study at the clinics of the authors. Cats had to be free of pelvic and sacral pathologies, which was confirmed by an initial cone beam computed tomography (CBCT; O-arm, Medtronic, Louisville, Colorado) scan. Thus, exclusion criteria were pelvic fractures, sacroiliac luxation, lumbosacral (sub)luxation, sacral fractures and neoplasia.

All cadavers were prepared in an identical manner. A ventral approach to the pelvic symphysis (30) was performed in dorsal recumbency. The pelvic symphysis was then separated using an oscillating saw (Colibri II; DePuy Synthes, West Chester, PA) to simulate the instability occurring in clinical cases due to additional pelvic fractures. Finally, a standard dorsolateral open approach to the wing of the ilium and dorsal aspect of the sacrum (30) was performed in lateral recumbency to manually separate the sacrum from the ilium with a raspatorium. This was done bilaterally resulting in a total of 40 sacroiliac luxations.

2.2 Order of procedures

All procedures were performed by either an ECVS Diplomate or a second year ECVS resident. The planning for the computer-navigated technique was performed by another ECVS resident, and had no prior experience with the navigation software before. The decision as to which of the two surgeons would begin with the first cadaver was randomly assigned. The two surgeons then took turns to conduct the surgery to ensure that the learning curve of the person doing the planning was distributed as evenly as possible. Both techniques [computer-navigated (CN group) vs. fluoroscopy-controlled freehand (FC group)] were performed on each cadaver.

The decision as to which side of each cadaver was used for fluoroscopy-controlled and which was used for computer-navigated surgery, as well as which side was started with, was randomized.

As a result, each surgeon performed 10 procedures of each technique.

2.3 Technical equipment

For intraoperative imaging a mobile CBCT unit (O-arm) was used, which was connected to the surgical navigation system StealthStation S8 (Medtronic) and provided two-dimensional and 3D images. The StealthStation S8 (SS) allows tracking of the surgical instruments relative to the patient's anatomy on a screen.

The unit was used either for fluoroscopy (FC group) or to perform a CBCT and neuronavigation (CN group).

2.4 Surgical procedure

All animals were placed in lateral recumbency for both procedures, controlled by fluoroscopy with the O-arm. Correct positioning (was achieved with towels) was evaluated by superimposition of the transverse processes of the seventh lumbar vertebra. The approach to the wing of the ilium and the dorsal aspect of the sacrum was already performed during cadaver preparation.

The goal of both techniques was to position the drill hole centrally within the first sacral body, with its end at 50% of the mid-transversal width.

After completion of each procedure, a control CBCT was performed to evaluate the drill hole within the sacrum.

2.4.1 Computer-navigated drilling

The neuronavigation system from Medtronic consists of two parts: the O-arm for performing fluoroscopy and CBCT scans and the SS, a surgical navigation system that allows the surgeon to follow the position of instruments live on the screen during surgery. The position of the patient and the instruments is determined by optical tracking via an infrared camera. For this purpose, a reference frame with 4 reflecting spheres needs to be attached to the bone, into which the navigated hole will be drilled, while the drill used must be equipped with a tracker (sure track 2, Medtronic).

With this system, the surgeon can plan a corridor on the 3D reconstruction on the screen and track the instruments in different planes in real time during surgery.

The placement of the reference frame in the spinous process of the feline sacrum is performed without direct visualization. An anatomical study assessed the optimal position of the pin from the reference frame to minimize the risk of compromising critical anatomical structures.

2.4.1.1 Anatomical landmarks for reference frame placement

The skin and dorsal musculature over the sacrum, medially to the bilateral dorsolateral approach, were dissected and reflected caudally. The fascial layer and fatty tissue were subsequently removed. The dorsal sacrococcygeal muscle was then detached from the sacrum to expose the dorsal sacral foramina. With the dorsal sacral foramina exposed, the dorsal rami were carefully dissected and visualized (Figure 1A).

To achieve adequate stabilization of a smooth pin in the small feline sacrum, two fixation points are required: one at the spinous process of the first or second sacral vertebra and another at the sacral roof (Figure 1B). Ensuring a secure hold in the spinous process necessitates precise placement of the pin. Inserting the pin too dorsally in the spinous process may not provide sufficient stability, while inserting it too ventrally risks penetrating the vertebral canal. Therefore, the optimal insertion point is at the transition from the middle to the dorsal third of the spinous process. This strategic placement minimizes the risk of vertebral canal penetration while maximizing the anchoring strength necessary for effective stabilization. The pin should be placed at an angle of 30–45 degree angle (Figure 1C) to avoid entering the vertebral canal medially and the dorsal sacral foramina laterally. Especially when targeting the second spinous process, a steep enough angle needs to be chosen to avoid the dorsal sacral foramen where the dorsal branch of the second sacral nerve emerges. The dorsal branches of the sacral nerves are interconnected and innervate the lateral and medial dorsal sacrococcygeal muscles, as well as the overlying skin areas. In the event of nerve irritation or injury, the likelihood of significant

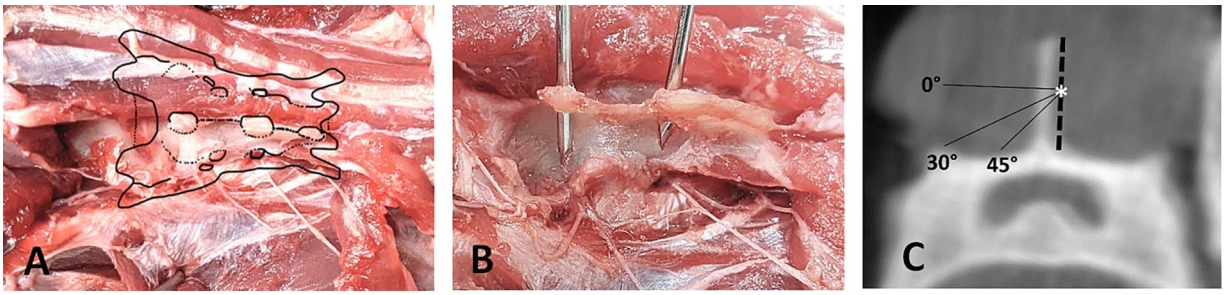

FIGURE 1
Landmarks for reference frame placement. **(A)** Dorsal view on dissected feline sacrum with visualization of the dorsal sacral foramina. **(B)** Position of accurately placed pins in the spinous processes of S1 and S2, making contact to the sacral roof medial to the dorsal sacral foramina. **(C)** Transverse CBCT-Image of S1 showing the safe angle for placing the reference frame pin, starting at the mid-height of the spinous process (*).

complications remains low due to the limited functional significance of the affected structures (31).

2.4.1.2 Reference frame placement

The cadavers were placed in the lateral position on the table and a blunt dissection was performed down to the spinous process of the first or second sacral vertebra through the existing incision from the former approach.

A 3D-printed reference frame (Figure 2A) was used. The material (Tough 1,500 Resind, Formlabs Inc., Somerville, United States) is light weighted and was printed with six central holes. A smooth 1.4 mm pin was drilled through one of these holes using press fit fixation. The pin with the pre-positioned reference frame was then placed using a surgical drill (Colibri II), according to the anatomical study, starting in the middle third to dorsal third of the height of the spinous process and at a 30 to 45-degree angle from ipsilateral through the spinous process of the first or second sacral vertebra in contralateral direction to anchor in the roof of the sacrum. The choice which of the two spinous processes to use was made individually, and in cases of malpositioning or fracture, the alternate spinous process was utilized.

The pin was then bent dorsally toward the table to prevent the reference frame from interfering with the drilling device and to ensure that the spheres on the reference frame could be detected by the infrared camera at all times.

The position of the reference frame pin was evaluated on the postoperative CBCT images.

2.4.1.3 Computer-navigated drilling

The camera of the SS was positioned so that it was able to detect both the reference frame with at least three of the four reflecting spheres and the reflecting reference points on the O-arm simultaneously (Figure 2C).

The CBCT images are uploaded directly to the SS. The corridor is planned by defining the entry and target points on the 3D reconstruction.

Before the planned corridor could be drilled, the required instruments (sure track 2 (Figure 2B) and passive planar sharp, Medtronic) had to be registered and calibrated with the tracking device of the SS. Verification of correct registration is essential during computer-navigated surgery to ensure that the position of the instrument on the patient reflects the position of the instrument on the same anatomical structure on the screen. To confirm correct calibration, the tip of the drill bit was positioned adjacent to the entry point of the pin of the reference frame on the spinous process and it was accepted only if the position could be verified in all three planes on the screen. If the images on the screen showed an identical position as the drill bit on the patient, drilling into the sacral body along the planned corridor could be started. The drill hole is then drilled using the guidance on the screen (Figure 3). In the initial two cases, a 1.8 mm drill was utilized. Due to the presence of a slightly inclined joint surface, which increased the risk of drill slipping, the initial drill size was changed in the following cases to 1.1 mm. The 1.1 mm drill hole was over drilled with a 1.8 mm drill bit.

2.4.2 Fluoroscopy-controlled drilling

The iliac wing is retracted by an assistant, to allow visualization of the sacral wing. The surgeon placed a 0.8 mm Kirschner wire in the sacral wing using a surgical drill and aimed for the described position for a drill hole in the sacral body of cats (14, 16). The position of the wire was controlled under fluoroscopy and corrected if necessary. Targeting was focused on the center of the first sacral body. Depending on the surgeon's preference a 0.8 mm Kirschner wire was used for all attempts or the size was changed to a 1.25 mm Kirschner wire. Fluoroscopic control was performed after each repositioning. Afterwards the hole within the sacral wing and body was drilled with

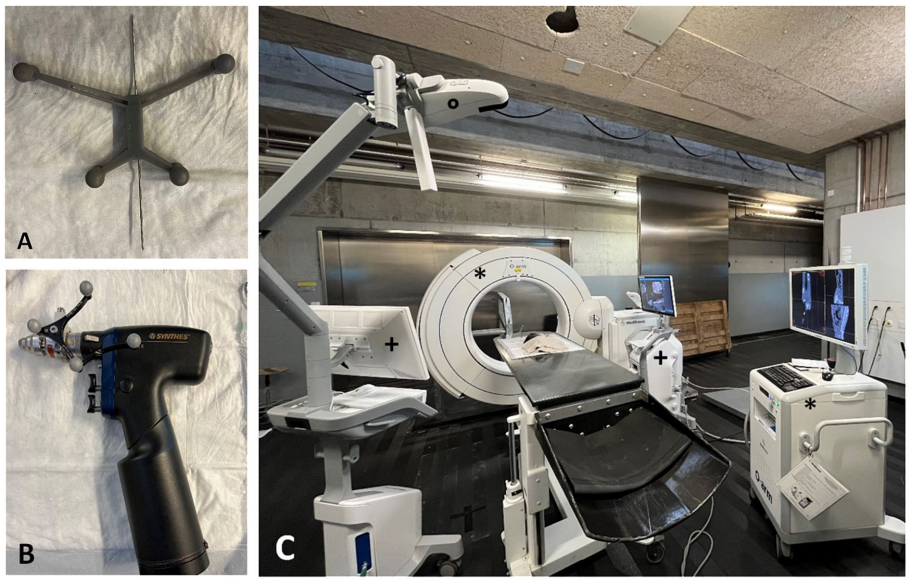

FIGURE 2
(A) 3D-printed reference frame with pre-positioned 1.4 mm smooth pin. **(B)** Surgical drill (Colibri II) with sure track 2 allows the surgeon to follow the position of the drill tip live on the screen. **(C)** Set-up for the computer-navigated drilling: O-arm with screen (*), Stealth Station S8 with two screens (+) and the infrared camera for optical tracking (o).

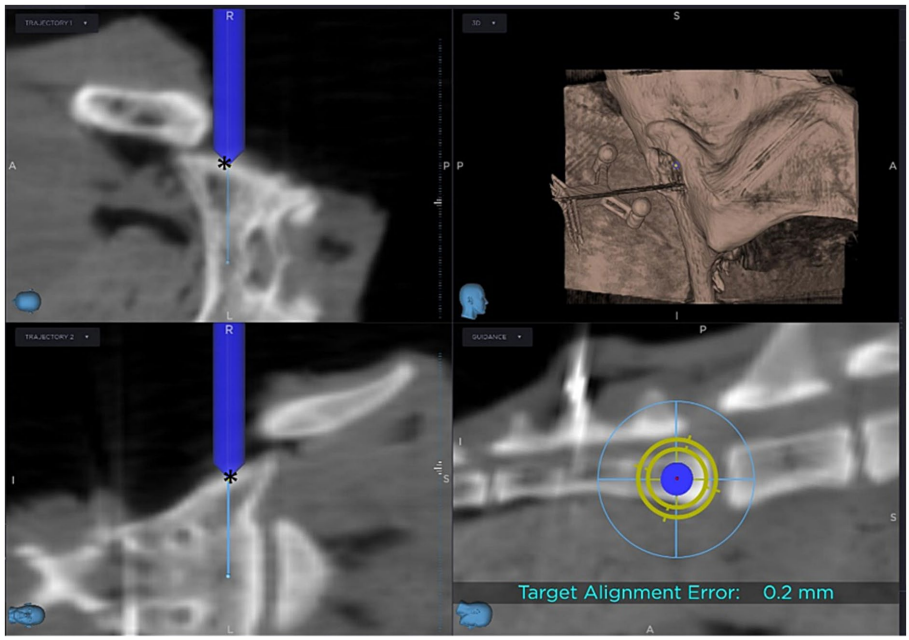

FIGURE 3
Screen view during computer-navigated drilling: The blue cylinder represents the drill bit, with its tip positioned at the entry point (*) of the planned corridor.

a surgical drill bit. Depending on surgeons' preference the determined position was first drilled with a smaller drill bit (1.1 mm, 1.5 mm) and then finalized with a 1.8 mm drill bit or no predrilling was performed.

2.5 Evaluation of the accuracy of the computer-navigated procedure

To assess the accuracy of the computer-navigated technique, entry and target points for the drilled holes were defined on postoperative CT images using SS software (Medtronic), analogous to the initial plan. Pre- and postoperative CT images were manually superimposed using the SS software. This allowed a direct comparison between the initial planned corridor and the actual drill hole. To objectify the assessment, the coordinates of the respective entry and target points were described by the following distance formula (26):

$$Deviation\,[mm] = \sqrt{(X2 - X1)^2 + (Y2 - Y1)^2 + (Z2 - Z1)^2}$$

2.6 Radiologic evaluation and comparison of the two techniques

The postoperative CBCT images were evaluated by a Diplomate of the European College of Veterinary Diagnostic Imaging (DipECVDI). The assessment focused on the positioning of the drill holes in all 40 cases and the positioning of the reference frame pins in the 20 cases of the SN group.

Drill holes were classified using a grading scale (Table 1) into Grades 1 to 3. Grade 1 indicated optimal placement within the vertebral body, Grade 2 denoted drill holes in contact with or eroding the cortex, and Grade 3 signified cortex violation. Grade 1 and 2 can be considered satisfactory operation results. Grade 3 is regarded as unsatisfactory surgical result because violation of surrounding structures may occur. For Grades 2 and 3, the direction of the deviation was further described using letters a-d, describing the direction of deviation (a = deviation in dorsal direction; b = deviation in ventral direction; c = deviation in cranial direction; d = deviation in caudal direction).

Grades 1 and 2 were categorized as "surgically satisfactory" results since adequate stability is ensured despite cortical erosion. Additionally, this classification is supported by the fact that no significant anatomical structures are compromised or injured.

The position of the reference frame pins was evaluated using a modified grading scale (Table 2). Grade 1 indicated optimal placement through the spinous process into the sacral wing, while Grade 3a represented penetration into the spinal canal, and Grade 3b indicated penetration of the ventral cortex.

2.7 Evaluation of surgical time

Time was recorded for all procedures. As the approach to luxate the sacroiliac joint, was already performed in all cases "Time total" started with manipulation of the luxated sacroiliac joint by the surgeon/assistant to place the first Kirschner wire in the FC-group and with placing the reference frame in the CN-group. It ended in both groups with finishing the 1.8 mm drill hole within the sacral body. The "time total" was divided into "time on patient" and "time off patient." "Time on patient" was defined as time needed for the surgical procedures itself (manipulation to visualize the sacral body, placement of reference frame or Kirschner wires

10.3389/fvets.2024.1510253

TABLE 1 Safety drilling coridors.

Safety grade	Safety name	Description
1	Well IN	Trajectory within the vertebra, intact cortex of the vertebral canal floor and the ventral aspect of the sacrum
2a	Just, IN	Trajectory within the vertebra, in contact or eroding the cortex of the vertebral canal floor
3a	Too Far, IN	Trajectory violating the cortex of the vertebral canal floor or within the vertebra canal
2b	Just, Out	Trajectory within the vertebra, in contact or eroding the ventral aspect of the sacrum
3b	Too Far, Out	Trajectory violating the ventral cortex of the sacrum or ventrally outside of the sacrum
2c	Just, CRAN	Trajectory within the vertebra, in contact or eroding the cranial endplate of S1
3c	Too Far, CRAN	Trajectory violating the cranial endplate of SI or within the IVDS L7/S1
2d	Just, CAUD	Trajectory within the vertebra, in contact or eroding the caudal endplate of S1
3d	Too Far, CAUD	Trajectory violating the caudal endplate of SI or within S2

Classification scheme to assess safety. The drilling corridor is assessed in the 60% ipsilateral part of the vertebral body and wings of S1.

TABLE 2 Safety patient tracker.

Safety grade	Safety name	Description
1	IN	Trajectory within the dorsal spinous process of S1 or S2 and unilaterally in the sacral wing of S1 or S2
3a	Too Far, IN	Trajectory within vertebral canal
3b	Too Far, OUT	Trajectory in soft tissues ventrally to the sacrum

Modified classification scheme to assess safety of the patient tracker.

and the drilling process itself). "Time off patient" was defined as the time required for all the imaging procedures (both groups) and planning of the drill hole (CN-group).

2.8 Statistical analysis

To assess the effect of the surgery technique on the total surgery time and the two partial times "time off patient" and "time on patient," a Wilcoxon signed-rank test was used after demonstrating the violation of the normality distribution using the Shapiro–Wilk test of normality. Additionally, visual inspection showed a right-skewed distribution of the data and a nonlinear distribution of the residues in the quantile-quantile plot. As the two surgeries were performed on each side of the same cadaver, the surgeries were considered as paired samples to account for an eventual effect of the cadaver on the outcome. To compare the effect of the two surgeons an unpaired sample Wilcoxon was used instead. A post-hoc power calculation was performed and confirmed that the sample size n = 20 for each technique was sufficient to reach a power of 96%.

To understand the learning effect, the first 10 surgeries (first five of each surgeon) were grouped and compared to the last 10 using the unpaired sample Wilcoxon signed-rank test. The data splitting in two groups reduced the previously described skewness of the data distribution. However, as the sample size for each group was also reduced to $n = 10$ we decided to use a non-parametric test, as a normal distribution is difficult to prove with a small sample size.

To compare the frequencies of the gradings assigned to the drill holes for the radiologic evaluation, the Fisher's exact test was chosen as for some of the grades there were less than five observations.

The accuracy of the guided procedure deviation to the target at the "entry" and "target" position was compared between the two surgeons using the t-test, as the data points suggested normal distribution in the Q-Q plot visualization, and this impression was confirmed with a Shapiro–Wilk normality test ($n = 10$ in each group).

The statistical analysis was performed using the statistical software R (version 4.3.1) in RStudio (Posit Software, version 2023.09.1.494).

3 Results

3.1 Study population

The cadavers of 20 skeletally mature cats (16 domestic shorthair, one domestic longhair, one Birman, one Persian, one Siamese) were included, of which 13 were males and seven were females with weights ranging from 1.78 to 5.49 kg (mean 3.45 kg).

3.2 Evaluation of the accuracy of the computer-navigated procedure

3.2.1 Neuronavigation

Across all 20 cases, the average deviation was 1.9 mm at the entry point (standard deviation (SD) 1.0 mm), and 1.6 mm at the target point (SD 0.8 mm). The experienced surgeon demonstrated a mean deviation of 1.9 mm at the entry point (SD 0.5 mm) and 1.8 mm at the target point (SD 0.9 mm). In contrast, the inexperienced surgeon demonstrated a mean deviation of 2.0 mm at the entry point (SD 1.4 mm) and 1.5 mm at the target point (SD 0.6 mm).

There was no statistically significant difference in drill hole accuracy between the two surgeons. When comparing the first four cases to the last four cases no statistically significant difference was observed.

3.3 CT scan evaluation of the drill holes

3.3.1 Neuronavigation

In the CN group, 11/20 cases were judged as Grade 1 (Figure 4A), with 2 /20 cases classified as Grade 2a and 7/20 cases as Grade 2b (Figure 4B). The experienced surgeon achieved Grade 1 in 5/10 cases, Grade 2a in 1/10 cases, and Grade 2b in 4/10 cases. The inexperienced surgeon achieved Grade 1 in 6/10 cases, Grade 2a in 1/10 cases, and Grade 2b in 3/10 cases.

All 20 cases achieved "surgically satisfactory" results.

No statistically significant difference concerning the grading was found between the surgeons.

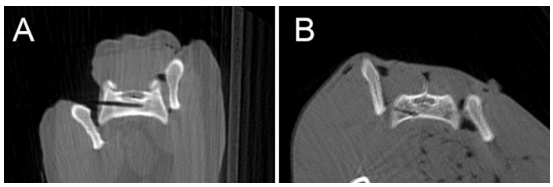

FIGURE 4
Postoperative CBCT-images showing a drill hole judged as grade 1 "Well IN" **(A)** and another one as grade 2b "Just OUT" **(B)**.

3.3.2 Fluoroscopy

In the FC group, 15/20 cases were classified as Grade 1, and 5/20 were Grade 2b. With the experienced surgeon achieving 8/10 Grade 1 and 2/10 Grade 2b, while the inexperienced surgeon reached 7/10 Grade 1 and 3/10 Grade 2b.

All 20 cases achieved "surgically satisfactory" results.

3.3.3 Comparison of the two techniques

All drill holes from both groups were either centrally located within the vertebral body (Grade 1) or in contact with the vertebral cortex (Grade 2). None of the drill holes breached the cortex (Grade 3), indicating satisfactory surgical outcomes for all cases.

Furthermore, neither in the FC-group nor in the CN-group, did any of the drill holes extended into the proximity of the cranial vertebral endplate or caudal vertebral border. No statistically significant difference was found between the two techniques concerning the radiological evaluation of safe drill corridors in the sacral body.

3.4 CT scan evaluation of the reference frame

3.4.1 Neuronavigation

In 16 out of 20 cases, the pin was satisfactorily anchored in the 1st or 2nd spinous process and sacral wing. In one case (case 1) from the experienced surgeon, the pin extended through the sacral wing into the soft tissue ventrolateral to the sacral wing. In 3 cases (cases 2, 3, 10), one from the experienced surgeon and two from the inexperienced surgeon, the pin extended into the spinal canal.

In 6 out of 20 cases, the reference frame had to be placed twice: in three cases (cases 2, 13, 14) due to spinous process fracture, in one case (case 3) due to a blunt pin, in one case (case 18) due to poor recognition by the camera, and in one case (case 17) due to insufficient pin anchoring resulting in unstable fixation.

3.5 Surgery time

3.5.1 Neuronavigation

For all 20 cases, the average duration was 23 min 37 s (SD 8 min 34 s). The average "time off patient" was 12 min 17 s (SD 5 min 11 s), while the average "time on patient" was 11 min 19 s (SD 6 min 17 s). 60% of the time reduction was achieved during the 'time off patient' phase, while the remaining 40% was saved during the 'time on patient' phase.

The surgery time was significantly reduced after a few cases ($p < 0.001$). While the first 10 cases took an average of 28 min 55 s (SD 8 min 29 s), the time was reduced to 18 min 19 s (SD 4 min 33 s) for the second 10 cases (Figure 5).

The experienced surgeon took an average of 5 min less than the inexperienced surgeon for both the first and second 10 cases; however, no statistically significant difference between the surgeons was found.

3.5.2 Fluoroscopy

For all 20 cases a mean duration of 9 min 47 s (SD 3 min 26 s) was noted. The "time off patient" took 3 min 54 s in average (SD 1 min 42 s), while the "time on patient" lasted 5 min 52 s (SD 2 min 26 s).

An improvement in time was also observed in the fluoroscopically controlled cases. While the first 10 cases took an average 11 min 54 s (SD 3 min 16 s), this time was reduced to 7 min 39 s (SD 2 min 3 s) for the second 10 cases (Figure 5).

A non-statistically significant difference of approximately 1 min was noted in the mean "time total" between the experienced and the inexperienced surgeon.

3.5.3 Comparison of the two techniques

The CN group exhibited a markedly longer procedural duration compared to the FC group, with this difference being statistically significant ($p < 0.001$).

4 Discussion

Our initial hypothesis regarding the safety of neuronavigation is partially supported, given that there was no statistically significant difference observed between the computer-navigated and fluoroscopy-controlled freehand surgical techniques in terms of sacral drilling. However, the placement of the reference pin in the spinous process posed an increased risk of penetrating critical structures. Furthermore, we can accept our second hypothesis as surgery time decreases significantly with experience.

All drilled holes in both techniques resulted in surgically satisfactory outcomes. Both methods demonstrated a good performance compared to a previous study on lag screw stabilization of cadaveric feline sacroiliac luxation, with an error rate of 8% and clinical studies including dogs and cats with complication rates up to 12.5% (5, 7, 16).

The high accuracy of neuronavigation is reflected in the small deviation between the planned and drilled entry and target points, with 1.9 mm (SD 1.0 mm) and 1.6 mm (SD 0.8 mm). A comparable study evaluated the accuracy of minimally invasive drilling screw corridors in the thoracolumbar spine and found slightly larger discrepancies between the planned and actual drill hole positions, with a significant difference between an experienced (mean deviation for the entry point of 2.2 mm and for the target point of 3.0 mm) and a novice surgeon (mean deviation for the entry point of 3.7 mm and for the target point of 5.0 mm) (26). It should be noted that this involved a different anatomical location, was conducted using a minimally invasive approach and drilling was performed by a 2.5 mm drill bit, which limits the direct comparability of the results.

During the present study it was noticed that accurate drilling with neuronavigation was simplified by predrilling with a smaller drill bit (1.1 mm). It reduces the risk of slippage on the slightly oblique surface

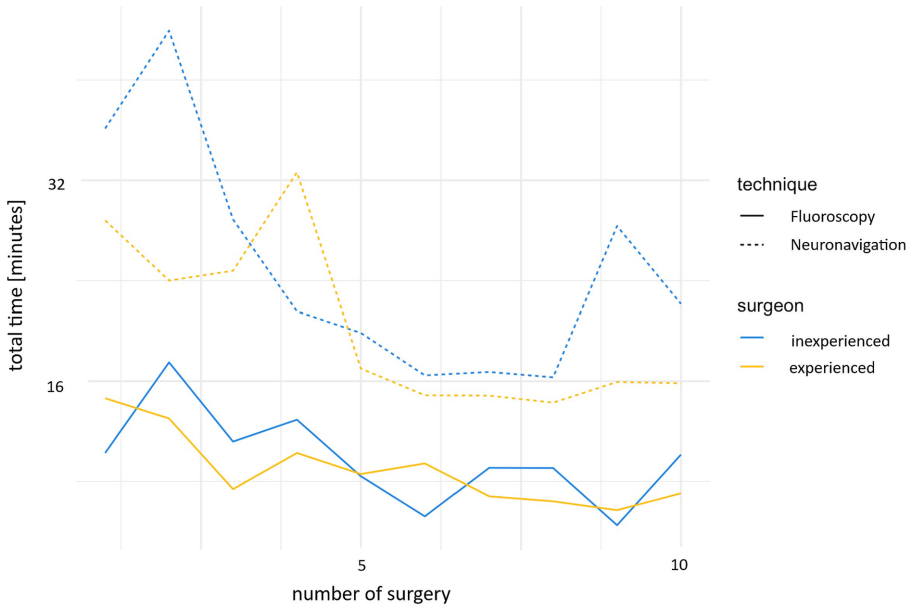

FIGURE 5
Development of the time required for neuronavigation and fluoroscopy during the study, comparing the experienced and inexperienced surgeons.

of the sacral wing during the initial rotation of the drill bit. As well the drill bit is shorter and therefore less prone to bending, what was found to introduce discrepancies between the actual position of the drill tip and the calculated position based on the sensor within the handpiece. In human medicine, longer drill bits are associated with increased inaccuracies, particularly when used with small diameter drill bits. To address this issue, specialized alignment devices have been developed to enhance accuracy and mitigate potential errors during drilling procedures (32). The weight of the Colibri handpiece was another factor found to make accurate drilling more difficult in the present study. A pencil-shaped drill device could potentially simplify the drilling process at this anatomical location.

Regarding safety, it is noteworthy that the challenges encountered in positioning the reference frame, particularly at the beginning of the study, somewhat diminish the perceived safety of neuronavigation. Placing the reference frame emerges as the most critical step of the computer-navigated drilling. Ensuring the correct and stable placement of the reference frame is crucial for the successful execution of a computer-navigated procedure. Any displacement of the reference frame could lead to navigation inaccuracies and compromise the surgical outcome. Therefore, meticulous attention to the positioning and stability of the reference frame is essential to ensure accurate navigation during the procedure. In two cases in this study, movement of the reference frame resulted in a discrepancy between CBCT images and patient positioning. This was noticed during preoperative checks, and the reference frame was repositioned, allowing the surgery to proceed without complications. This highlights the importance of preoperative verification of the correlation between the position of the instruments displayed on the screen and their actual position in the surgical field.

Spinous process fracture occurred in four cases, attributed to excessively dorsal pin placement, as the tip of the process lacks adequate stability due to very thin bone. Even no clinical relevance is expected from minor fracture at the tip of the spinous process, correct positioning is essential to reduce possible complications.

In four cases the positioning of the reference frame pin was incorrect. One pin traversed from the sacral wing slightly into the ventrolateral soft tissue, which is not expected to cause any clinical complications. Three pins penetrated the cortex of the vertebral canal. The termination point of the spinal cord in cats remains controversial in the literature, with reports varying between the caudal end of L7 and S3. This variability may be influenced by factors such as age and breed-specific differences, though these remain under discussion (4, 31, 33). The clinical significance of penetrating the vertebral canal at this level remains uncertain, therefore it should be avoided to prevent potential complications. With practice, the risk of penetrating the spinal canal might be reduced, as can be seen from the fact that the experienced surgeon no longer had any complications with the pin after the third case.

To reduce the risk of penetrating vital structures while positioning the pin of the reference frame, various techniques could be further evaluated. An alternative to smooth pins would be the utilization of threaded pins, which are proven to result in more stable constructs (34) and therefore could be anchored into the spinous process only, avoiding the risk of penetrating the spinal canal. In several studies from human and veterinary medicine fixation of the reference frame on the spinous process with a clamp is described (19, 26). In the authors opinion this technique is not feasible in the cat due to the small size of the sacral spinous processes. In a different study from human medicine with unilateral affected sacroiliac joint, anchoring the reference frame into the ilium on the non-affected site is described (20). Another described technique connects the reference frame to the operating table or a device fixated to the patient, respectively, the bone of interest (19, 24). However, the bone must be rigidly fixed, as even the slightest movement may jeopardize the success of the procedure. In the

authors opinion stable fixation of the small and light weighted feline sacrum is difficult but could be investigated in further studies.

Safety extends beyond the drilling process itself and heavily relies on the experience of the surgical team, especially in procedures involving neuronavigation. Proper operation of equipment and the effective use of software require coordinated efforts and familiarity among team members. Ensuring that each member is well-versed in their specific role can significantly enhance the efficiency and accuracy of the procedure. Thus, training and practice are essential to optimize outcomes and reduce time when using advanced navigation techniques.

Time is a crucial factor in surgery, as prolonged anesthesia not only places additional stress on the patient but also increases the risk of complications (35). Despite a significant time-reduction noted over 20 cases in the CN-group, the average duration for procedures using neuronavigation remained longer compared to the fluoroscopy-controlled freehand procedures. Especially, the "time off patient," was found to be longer for the CN-group. These findings suggest that although neuronavigation enables accurate surgical planning and procedures, its implementation requires additional time for preoperative planning compared to fluoroscopy. To minimize the duration as effectively as possible, it is crucial that the staff are well-versed in the software to enable highly efficient planning. The alignment of the reference frame, the marking of the Colibri, and the SS8 camera setup should be planned and tested before the surgery to prevent any interference during tracking and to avoid timeloss during surgery. Additional time can be saved by practicing the placement of the reference frame to avoid unstable placement, as this may necessitate restarting the process from the beginning. In general, neuronavigation should be repeatedly tested and practiced on cadavers before being applied to clinical cases.

The time for preoperative positioning was not measured; however, it was noted that the FC group required more complex positioning, as correct lateral positioning is crucial for the success of the procedure. Computer-navigated drilling can be performed with an oblique positioning as well, but lateral positioning facilitates planning of the drill corridor in the authors opinion.

The main limitation of this study is certainly its cadaveric nature with induced sacroiliac luxation and without the typically concurrent soft tissue injuries. The normally concomitant pelvic fractures were simulated by osteotomy of the pubic symphysis. Additionally, both sacroiliac joints were luxated prior to the study, necessitating bilateral surgical approaches, to standardize conditions for all procedures. This resulted in a highly unstable environment conducive to easy mobilization but not representative of the clinical scenario in live animals, where manipulation of the sacral wing can be quite different, especially in cases where the trauma happened several days before surgery and muscular contraction is evident. Furthermore, the study focused solely on the isolated step of drilling into the sacral body, while the subsequent procedural steps were initially disregarded. Although we have attempted to mimic concurrent injuries, the complexity of surrounding soft tissue changes and additional fractures cannot be fully replicated in a live patient. Live animal studies are required to evaluate neuronavigation in clinical conditions. Ideally, a clinical study on cats with unilateral sacroiliac luxation would assess the safety of this technique *in vivo*. In cases of unilateral sacroiliac luxation, additional options for securing the reference frame are available, such as fixation on the non-luxated iliac wing, and the risk of penetrating the spinal canal could be eliminated.

In addition, preoperative and postoperative CBCT images were manually superimposed for accuracy assessment using SS software to compare the final drilling hole to the planned hole. Even as this method allows for direct comparison, it is important to note that manual superimposition can introduce sources of error. The automatic superimposition tool in the SS software proved unreliable due to discrepancies in the bony structures between preoperative and postoperative CT images. These variations were caused by manipulation of the iliac wing during surgery.

A significant drawback for clinical application of neuronavigation is the substantial financial investment required to implement this technology. In addition to the Stealth Station, a compatible CBCT unit (O-arm) is necessary. The more clinical indications are evaluated and described for the use of neuronavigation, the more economically viable such an investment becomes.

5 Conclusion

Neuronavigation can be effectively implemented after several practice cases, allowing surgical fixation of sacroiliac luxation in cats. Placement of the reference frame pin must be practiced beforehand to ensure proper positioning. With proper training, it provides real-time feedback and allows performing complex procedures with high accuracy. The new technique shows great potential, and its successful application in clinical cases is conceivable, but must be evaluated in further studies. The required equipment represents a significant financial investment and necessitates a well-coordinated team for successful implementation.

Data availability statement

The raw data supporting the conclusions of this article will be made available by the authors, without undue reservation.

Ethics statement

Ethical approval was not required for the studies involving animals in accordance with the local legislation and institutional requirements because the animal cadavers used in this study were ethically sourced from animals that were euthanized for medical reasons unrelated to the research. No animals were sacrificed specifically for this study. Written informed consent was not obtained from the owners for the participation of their animals in this study because the animal cadavers utilized in this study were donated by owners for scientific research purposes prior to the determination of this specific study.

Author contributions

LK: Conceptualization, Formal analysis, Investigation, Methodology, Project administration, Resources, Visualization, Writing – original draft, Writing – review & editing. NW: Conceptualization, Investigation, Methodology, Project administration, Resources, Writing – review & editing. CP:

Methodology, Resources, Supervision, Validation, Visualization, Writing – review & editing. KH: Investigation, Methodology, Resources, Validation, Visualization, Writing – review & editing. FF: Conceptualization, Methodology, Project administration, Resources, Supervision, Writing – review & editing. PD: Conceptualization, Investigation, Methodology, Project administration, Resources, Supervision, Validation, Writing – review & editing.

Funding

The author(s) declare that no financial support was received for the research, authorship, and/or publication of this article.

Acknowledgments

The authors would like to thank Julien Guevar for the 3D printing and provision of the reference frames, as well as Mathieu de Preux for the technical support in the application of neuronavigation.

Conflict of interest

The authors declare that the research was conducted in the absence of any commercial or financial relationships that could be construed as a potential conflict of interest.

Generative AI statement

The authors declare that no Gen AI was used in the creation of this manuscript.

Publisher's note

References

1. Bookbinder PF, Flanders JA. Characteristics of pelvic fracture in the cat. *Vet Comp Orthop Traumatol*. (1992) 5:122–7. doi: 10.1055/s-0038-1633081

2. Bird FG, De VF. Conservative management of sacroiliac luxation fracture in cats: medium- to long-term functional outcome. *J Feline Med Surg*. (2020) 22:575–81. doi: 10.1177/1098612X19867516

3. Meeson RL, Geddes AT. Management and long-term outcome of pelvic fractures: a retrospective study of 43 cats. *J Feline Med Surg*. (2017) 19:36–41. doi: 10.1177/1098612X15606958

4. Tobias KM, Johnston SA, (eds). Veterinary surgery: small animal. 2nd ed. St. Louis (MO): Elsevier (2018).

5. Fischer A, Binder E, Reif U, Biel M, Bokemeyer J, Kramer M. Closed reduction and percutaneous fixation of sacroiliac luxations in cats using 2.4 mm cannulated screws - a cadaveric study. *Vet Comp Orthop Traumatol*. (2012) 25:22–7. doi: 10.3415/VCOT-11-05-0074

6. Déjardin LM, Marturello DM, Guiot LP, Guillou RP, DeCamp CE. Comparison of open reduction versus minimally invasive surgical approaches on screw position in canine sacroiliac lag-screw fixation. *Vet Comp Orthop Traumatol*. (2016) 29:290–7. doi: 10.3415/VCOT-16-02-0030

7. Rollins A, Balfour R, Szabo D, Chesvick CM. Evaluation of fluoroscopic-guided closed reduction versus open reduction of sacroiliac fracture-Luxations stabilized with a lag screw. *Vet Comp Orthop Traumatol*. (2019) 32:467–74. doi: 10.1055/s-0039-1693471

8. Parslow A, Simpson DJ. Bilateral sacroiliac luxation fixation using a single transiliosacral pin: surgical technique and clinical outcomes in eight cats. *J Small Anim Pract*. (2017) 58:330–6. doi: 10.1111/jsap.12659

9. Froidefond B, Moinard M, Caron A. Outcomes for 15 cats with bilateral sacroiliac luxation treated with transiliosacral toggle suture repair. *Vet Surg*. (2023) 52:983–93. doi: 10.1111/vsu.14008

10. Yap FW, Dunn AL, Farrell M, Calvo I. Trans-iliac pin/bolt/screw internal fixation for sacroiliac luxation or separation in cats: six cases. *J Feline Med Surg*. (2014) 16:354–62. doi: 10.1177/1098612X13503650

11. Borer LR, Voss K, Montavon PM. Ventral abdominal approach for screw fixation of sacroiliac luxation in clinically affected cats. *Am J Vet Res*. (2008) 69:549–56. doi: 10.2460/ajvr.69.4.549

12. Raffan PJ, Joly CL, Timm PG, Miles JE. A tension band technique for stabilisation of sacroiliac separations in cats. *J Small Anim Pract*. (2002) 43:255–60. doi: 10.1111/j.1748-5827.2002.tb00068.x

13. Burger M, Forterre F, Brunnberg L. Surgical anatomy of the feline sacroiliac joint for lag screw fixation of sacroiliac fracture-luxation. *Vet Comp Orthop Traumatol*. (2004) 17:146–51. doi: 10.1055/s-0038-1632803

14. Shales CJ, White L, Langley-Hobbs SJ. Sacroiliac luxation in the cat: defining a safe corridor in the dorsoventral plane for screw insertion in lag fashion. *Vet Surg*. (2009) 38:343–8. doi: 10.1111/j.1532-950X.2009.00509.x

15. Philp H, Durand A, Vicente F. Use of computed tomography to define a sacral safe corridor for placement of 2.7 mm cortical screws in feline sacroiliac luxation. *J Feline Med Surg*. (2018) 20:487–93. doi: 10.1177/1098612X17716847

16. Shales C, Moores A, Kulendra E, White C, Toscano M, Langley-Hobbs S. Stabilization of sacroiliac luxation in 40 cats using screws inserted in lag fashion. *Vet Surg*. (2010) 39:696–700. doi: 10.1111/j.1532-950X.2010.00699.x

17. Frizon LA, Shao J, Maldonado-Naranjo AL, Lobel DA, Nagel SJ, Fernandez HH, et al. The safety and efficacy of using the O-arm intraoperative imaging system for deep brain stimulation Lead implantation. *Neuromodulation*. (2018) 21:588–92. doi: 10.1111/ner.12744

18. van de Kelft E, Costa F, van der Planken D, Schils F. A prospective multicenter registry on the accuracy of pedicle screw placement in the thoracic, lumbar, and sacral levels with the use of the O-arm imaging system and StealthStation navigation. *Spine (Phila Pa 1976)*. (2012) 37:E1580–7. doi: 10.1097/BRS.0b013e318271b1fa

19. Schouten R, Lee R, Boyd M, Paquette S, Dvorak M, Kwon BK, et al. Intra-operative cone-beam CT (O-arm) and stereotactic navigation in acute spinal trauma surgery. *J Clin Neurosci*. (2012) 19:1137–43. doi: 10.1016/j.jocn.2012.01.020

20. Theologis AA, Burch S, Pekmezci M. Placement of iliosacral screws using 3D image-guided (O-arm) technology and stealth navigation: comparison with traditional fluoroscopy. *Bone Joint J*. (2016) 98-B:696–702. doi: 10.1302/0301-620X.98B5.36287

21. Ghisla S, Napoli F, Lehoczky G, Delcogliano M, Habib N, Arigoni M, et al. Posterior pelvic ring fractures: intraoperative 3D-CT guided navigation for accurate positioning of sacro-iliac screws. *Orthop Traumatol Surg Res*. (2018) 104:1063–7. doi: 10.1016/j.otsr.2018.07.006

22. Lee DJ, Kim S-B, Rosenthal P, Panchal RR, Kim KD. Stereotactic guidance for navigated percutaneous sacroiliac joint fusion. *J Biomed Res*. (2016) 30:162–7. doi: 10.7555/JBR.30.20150090

23. Claeys I, van der Vekens E, Kümmerle J, De PM, Koch C. Computer-assisted surgery for placing toggle constructs across the coxofemoral joints of small equids using a minimally invasive approach-a proof-of-concept cadaveric study. *Vet Surg*. (2023) 52:994–1008. doi: 10.1111/vsu.14004

24. De PM, Klopfenstein Bregger MD, Brünisholz HP, van der Vekens E, Schweizer-Gorgas D, Koch C. Clinical use of computer-assisted orthopedic surgery in horses. *Vet Surg*. (2020) 49:1075–87. doi: 10.1111/vsu.13486

25. Gygax D, Lischer C, Auer JA. Computer-assisted surgery for screw insertion into the distal sesamoid bone in horses: an in vitro study. *Vet Surg*. (2006) 35:626–33. doi: 10.1111/j.1532-950X.2006.00200.x

26. Guevar J, Samer ES, Precht C, Rathmann JMK, Forterre F. Accuracy and safety of Neuronavigation for minimally invasive stabilization in the thoracolumbar spine using Polyaxial screws-rod: a canine cadaveric proof of concept. *Vet Comp Orthop Traumatol*. (2022) 35:370–80. doi: 10.1055/s-0042-1750056

27. Samer ES, Forterre F, Rathmann JMK, Stein VM, Precht CM, Guevar J. Accuracy and safety of image-guided freehand pin placement in canine cadaveric vertebrae. *Vet Comp Orthop Traumatol*. (2021) 34:338–45. doi: 10.1055/s-0041-1731808

28. Piazza AM, McAnulty JF, Early P, Guevar J. Craniectomies for dogs with skull multilobular Osteochondrosarcoma using the Misonix bone scalpel: cadaveric evaluation and retrospective case series. *Top Companion Anim Med*. (2023) 53-54:100772. doi: 10.1016/j.tcam.2023.100772

29. Meneses F, Maiolini A, Forterre F, Oevermann A, Schweizer-Gorgas D. Feasability of a frameless brain biopsy system for companion animals using cone-beam CT-based automated registration. *Front Vet Sci*. (2021) 8:779845. doi: 10.3389/fvets.2021.779845

30. Johnson KA. Piermattei's atlas of surgical approaches to the bones and joints of the dog and cat. *5th* ed. St. Louis, Mo: Elsevier (2014).

31. Frewein J, Vollmerhaus B, Amselgruber W. Anatomie von Hund und Katze. Berlin: Blackwell Wissenschafts-Verlag (1994).

32. Kendoff D, Citak M, Gardner MJ, Stübig T, Krettek C, Hüfner T. Improved accuracy of navigated drilling using a drill alignment device. *J Orthop Res*. (2007) 25:951–7. doi: 10.1002/jor.20383

33. Dyce SB. Sack, and Wensing's textbook of veterinary anatomy. *5th revised* ed. S.l.: Saunders (2017).

34. Anderson MA, Mann FA, Wagner-Mann C, Hahn AW, Jiang BL, Tomlinson JL. A comparison of nonthreaded, enhanced threaded, and Ellis fixation pins used in type I external skeletal fixators in dogs. *Vet Surg*. (1993) 22:482–9. doi: 10.1111/j.1532-950X.1993.tb00425.x

35. Daley BJ, Cecil W, Clarke PC, Cofer JB, Guillamondegui OD. How slow is too slow? Correlation of operative time to complications: an analysis from the Tennessee surgical quality collaborative. *J Am Coll Surg*. (2015) 220:550–8. doi: 10.1016/j.jamcollsurg.2014.12.040

frontiers | Frontiers in Veterinary Science

TYPE Original Research
PUBLISHED 27 February 2025
DOI 10.3389/fvets.2025.1528345

OPEN ACCESS

EDITED BY
Ozan Gündemir,
Istanbul University Cerrahpasa, Türkiye

REVIEWED BY
Caner Bakici,
Ankara University, Türkiye
Ebru Eravci Yalin,
Istanbul University-Cerrahpasa, Türkiye

*CORRESPONDENCE
Nicole Diana Wolf
✉ nicole.wolf@unibe.ch

RECEIVED 14 November 2024
ACCEPTED 10 February 2025
PUBLISHED 27 February 2025

CITATION
Wolf ND, Kleiner L, Precht C, Guevar J, de Preux M, Forterre F and Duever P (2025) Minimally invasive computer-assisted repair of feline sacroiliac luxation—a cadaveric study. *Front. Vet. Sci.* 12:1528345. doi: 10.3389/fvets.2025.1528345

Minimally invasive computer-assisted repair of feline sacroiliac luxation—a cadaveric study

Nicole Diana Wolf[1]*, Lukas Kleiner[2], Christina Precht[3], Julien Guevar[4], Mathieu de Preux[5], Franck Forterre[1] and Pia Duever[1]

[1]Division of Small Animal Surgery, Department of Clinical Veterinary Medicine, Vetsuisse-Faculty, University of Bern, Bern, Switzerland, [2]Divison of Small Animal Surgery, Department of Clinical Veterinary Medicine, Tierklinik Marigin, Feusisberg, Switzerland, [3]Divison of Clinical Radiology, Department of Clinical Veterinary Medicine, Vetsuisse-Faculty, University of Bern, Bern, Switzerland, [4]Divison of Small Animal Neurology, Department of Clinical Veterinary Medicine, Anicura Tierklinik Thun, Thun, Switzerland, [5]Swiss Institute of Equine Medicine (ISME), Department of Clinical Veterinary Medicine, Vetsuisse-Faculty, University of Bern, Bern, Switzerland

Introduction: The delicate anatomy of the feline sacrum presents challenges for surgeons to perform a safe and accurate surgery without risking to damage vital neurovascular structures. In this context computer-assisted surgery represents an attractive minimally invasive surgical solution to increase the accuracy and safety of the intervention. This cadaveric study evaluates the feasibility and safety of a minimally invasive approach by a novice surgeon using computer navigation compared to traditional fluoroscopy as well as a new method for patient reference array positioning.

Material and methods: Eleven cats' cadavers were used to simulate sacroiliac joint luxation whereas one had to be excluded due to a sacral fracture. Sides were randomly assigned to two groups: (1) minimally invasive computer-assisted drilling group (MICA group); (2) fluoroscopy-controlled group (FC group). All surgeries were performed by a first-year ECVS resident. After positioning of the reference array, cone beam computer tomography scans were conducted for planning of the temporary and final fixation of the sacroiliac luxation. Final fixation was achieved through a minimally invasive approach via computer-assisted drilling of the iliac wing and the sacral body for the placement of a positional screw (2.4 mm). The other side was operated on via an open dorsal, fluoroscopy-controlled approach. Comparison between the two groups for surgical time, accuracy of screw placement, radiologic safety and the learning curve was recorded. Statistical analysis consisted of Fisher's exact test to compare the assigned radiological safety grades and the Wilcoxon signed-rank test for total surgery time and accuracy.

Results: Mean total time for MICA and FC groups were 44 min and 45 s and 19 min and 54 s, respectively. The mean total time for the first five cases was 53 min and 30 s in the MICA group and 20 min and 15 s in the FC group and improved to a mean total time of 36 min and 15 s in the MICA group and to 18 min and 40 s in the FC group in the second five cadavers. Accuracy aberration of surgery in the MICA group improved from a mean deviation on the target point, the end of the drill tract, from 4.2 mm in the first five to 0.9 mm in the second five cats. This criterion was only applicable in the MICA group. Evaluation for radiologic safety was assessed with three radiologic categories (I-III) and four subcategories (a-d). Additionally, the surgery was classified into radiographically

safe implant placement (yes/no). The first five cats of the MICA as well as the FC group received a lower safety grade compared to the second five cats. The novel method for placement of the patient reference array was categorized as grade I without violating any vital structures in all 10 cats.

Discussion: The computer-assisted surgery for minimal invasive surgical fixation of sacroiliac luxation seems to be a safe procedure with a steep learning curve. Compared to previous study using the same technical set-up, the safety of the computer-assisted surgical procedure was improved by changing the smooth to the negative threaded pin to have better bone purchase for sufficient anchoring in the spinous process alone and therefore minimizing the risk for violation of the spinal canal.

KEYWORDS

minimally invasive, computer-assisted orthopedic surgery (CAOS), sacroiliac luxation, feline, Stealth Station S8, cadaveric study

1 Introduction

Sacroiliac luxation is a common injury in cats, especially after high velocity trauma like road traffic accident or high-rise trauma. Sacroiliac luxation occurred in 59.2% of cats with pelvic injuries and accounted for 27% of all pelvic fractures. Sacroiliac separation was the second most common injury after pelvic floor fractures (1, 2). Treatment options are either conservative or surgical. If displacement is minimal or the luxation is unilateral with no concurrent pelvic fractures it might be treated conservatively with analgesics, cage rest and monitoring of urination and defecation (3). Surgical stabilization of sacroiliac luxation is indicated if there are signs of severe pain, inability to ambulate, neurologic deficits attributable to the luxation, severe instability or displacement (>50%) of one or both hemipelvises, pelvic outlet obstruction and/or concurrent orthopedic injuries (1, 4, 5).

The method of choice for surgical fixation is a cortical screw in lag fashion, or alternatively in a positional fashion (1, 2). Furthermore, a single transiliosacral pin in cats or a transiliosacral rod in dogs as well as transiliosacral toggle sutures, transileac pin/bolt/screw and tension band technique are described for successful stabilization (6–10). The fixation can be achieved through an open, dorsal or ventral, or closed, minimally invasive, approach with or without the help of fluoroscopy (3, 4, 11–16).

Since the sacral body of cats is very small, penetrating vital structures like the spinal canal dorsally, the intervertebral disc cranially and important nervous and vascular structures ventrally while placing the lag screw into the sacral body is a feared complication. Therefore, accurate positioning is essential, best at the first attempt (17, 18).

The correct position of the screw can be secured either through fluoroscopic control or as shown by the study of Kleiner et al. with computer-assisted surgery using an optical tracking system, the StealthStation (12, 16, 19, 20). However, this study showed, that placement of the patient tracker pin could increase the risk of complications by penetrating the spinal canal to achieve enough stability of the patient tracker. Open reduction techniques are invasive and correct screw placement can be challenging.

Previous studies showed that closed reduction and stabilization provided more accurate and consistent screw placement along safe corridors and optimal sacral purchase with minimal tissue dissection (12, 16, 20–24). Further documented benefits in human surgery are reduced blood loss, shorter surgical and hospitalization times, improved pain scores, faster weight bearing, lower complication rates and lower costs (25–32).

To the authors knowledge there is no study demonstrating the feasibility and safetiness of a minimal invasive approach for the fixation of the sacroiliac joint by computer-assisted drilling with any surgical navigation system. The hypothesis of this study is that minimal invasive computer-assisted surgery is more accurate than fluoroscopy-controlled drilling for the repair of sacroiliac joint luxation and that the procedure might be conducted by an unexperienced surgeon.

2 Material and methods

2.1 Preparation of cadavers

The study considered cadavers of 11 skeletally mature cats with an intact pelvic region that died or were euthanized for reasons unrelated to this study. Exclusion criteria were all pelvic or sacral pathologies like pelvic fractures, sacroiliac luxation, lumbosacral (sub) luxation and sacral fractures. Therefore, all cadavers underwent examination with a cone beam computed tomography (CBCT) scan beforehand. One cat had to be excluded due to an accidentally induced sacral fracture while manually luxating the sacroiliac joint during preparation which resulted in 10 cats included in the study.

The cat cadavers were donated to our institution by the owners who gave consent to use them for research purposes.

All images (Fluoroscopic and CBCT) were generated remotely without exposing personnel to radiation.

The first side was operated with the new computer-assisted technique through a minimal invasive approach (minimal invasive computer-assisted surgery, MICA). The second side of each cat was operated using an open dorsal, fluoroscopy controlled, approach

(fluoroscopy-controlled surgery, FC). As a result, a total of 20 surgeries were carried out. The sides with which to start with (right or left sacroiliac joint) were randomized.

All joints of all cats were luxated manually with a Freer periosteal elevator through a ventral abdominal approach as described by Borer et al. (3, 11) and Montavon et al. (39).

For comparable stability during the surgeries, the first sacroiliac joint was luxated and surgically stabilized with the positional screw before the second side was luxated and fixated. Using a ventral abdominal approach, the pelvic symphysis was separated by an oscillating saw to imitate additional pelvic fractures (Colibri II; DePuy Synthes, West Chester, PA). Following this, only one side was luxated during each surgery.

2.2 Technical equipment, orthopedic equipment, implants

Images for the minimally invasive computer-assisted surgical repair of sacroiliac luxation were acquired with a mobile cone beam computed tomography unit (CBCT; O-Arm; Medtronic, Louisville, Colorado), which was coupled to a surgical navigation system equipped with an optical tracking system, the StealthStation S8 (Medtronic). Specific instrumentation for the navigated procedure included a patient reference array, a navigated pointer (Passive Planar Marker, Medtronic) and an instrument tracker (SureTrak II clamps and tracker, Medtronic) mounted on a battery-powered surgical drill (Colibri II, DePuy Synthes, West Chester, PA) (Figure 1). Every instrument and tracker that had to be detected by the localizer camera of the optical tracking system was mounted with infrared reflecting spheres, also called fiducials. Furthermore, a radiolucent carbon fiber table (Opera Swing; General Medicale Merate SPA, Seriate, Italy) was used.

A lighter, custom-made copy of the original patient reference array was 3D printed to avoid excessive lever arm on the small feline sacral bone. The patient reference array was a modification of the version used by Papacella-Beugger et al. (33), printed out of Formlabs Tough 1500 and weighted 9 g. The array was equipped with six holes through the middle segment to press fit a 1.4 mm negative threaded stainless-steel pin for the fixation into the sacral spinous process.

Further surgical instruments included a Backhaus clamp and a kern bone holding forceps, a 1-0 Kirschner (K)-wire, tap sleeves of the according size, 1.1 and 1.8 mm drill bit, a 2.4 mm self-tapping cortical screw, a screwdriver and a pin cutter.

2.3 Surgical procedure

All surgeries were performed by a first year European College of Veterinary Surgery (ECVS) resident without significant experience in orthopedic surgical procedures. For both procedures (i.e., the computer-assisted and the fluoroscopic guided drilling) the cats were placed in lateral recumbency on the carbon fiber table whereas the correct positioning with superimposition of the transverse processus of the seventh lumbar vertebra was evaluated through fluoroscopy.

2.3.1 Image acquisition, surgical planning, patient registration, and instrument calibration

One latero-lateral fluoroscopic projection was performed to confirm the correct positioning of the sacroiliac region of the cadaveric specimen in the isocenter of the gantry of the O-arm. A navigated 3D CBCT-scan (high resolution scan of 192 images during one tube rotation with an exposure of 120 kV and 20 mA and a voxel size of $0.4 \times 0.4 \times 0.8$ mm^3) was then acquired. During the scan acquisition, the camera of the StealthStation S8 had to detect simultaneously the tracker of the O-arm gantry and the patient reference array. The acquired CBCT data set was automatically transferred to the navigation system.

Preoperative surgical planning of the drill corridor was performed using the planning function of the Stealth Station S8. The entry point was set on the lateral aspect of the ilial wing whereas the target point marked the end of the drill hole at 50% of the depth in the sacral body. The planning of the drill corridor was done on the axial and coronal view and verified with probe's eye view.

The O-arm was then moved away from the surgical area to provide unrestricted access to the surgical site. To start the navigated surgical procedure, patient registration (32) was performed by touching the divot of the patient reference array with the tip of the navigated pointer. Instrument calibration was performed by following consecutive steps instructed by the StealthStation S8 for the identification of the plane, tip and long axis of the instrument. Calibration was repeated whenever a drill bit of different length was used, in order to display the correct length on the screen of the navigation system. For intraoperative, real-time orientation, the "navigation" mode was selected, and the trajectory 1 and 2 as well as the guidance function were displayed on the screen (Figure 2).

2.3.2 Minimally invasive computer-assisted drilling

The location of the spinous process of the first and second sacral vertebra was determined by percutaneous palpation. Decision to use S1 or S2 was made individually depending on the size of S1 or S2 on each cadaver, whereas the larger spinous process was selected for patient reference array placement.

A stab incision to the cortex of the spinous process was performed using a #11 scalpel blade. A negative threaded 1.4 mm pin with the pre-positioned reference array and its fiducials was drilled at a 45-degree angle from ipsilateral through the spinous process and, in contrast to the study of Kleiner et al., not anchored into the roof of the sacrum (19). The reference array was moved away from the surgical site by bending the anchoring pin to prevent spatial interference with the navigated instruments and ensure continuous detection by the localizer camera throughout the procedure.

The first CBCT scan was conducted to plan the location in the caudal part of sacrum for the temporary fixation pin to hold the reduction in place. Reduction of the sacroiliac luxation was achieved with the help of a Backhaus clamp in the ischial tuberosity to facilitate movement of the bone while manually pushing the wing of the ilium in its desired place. Assessment of reduction was

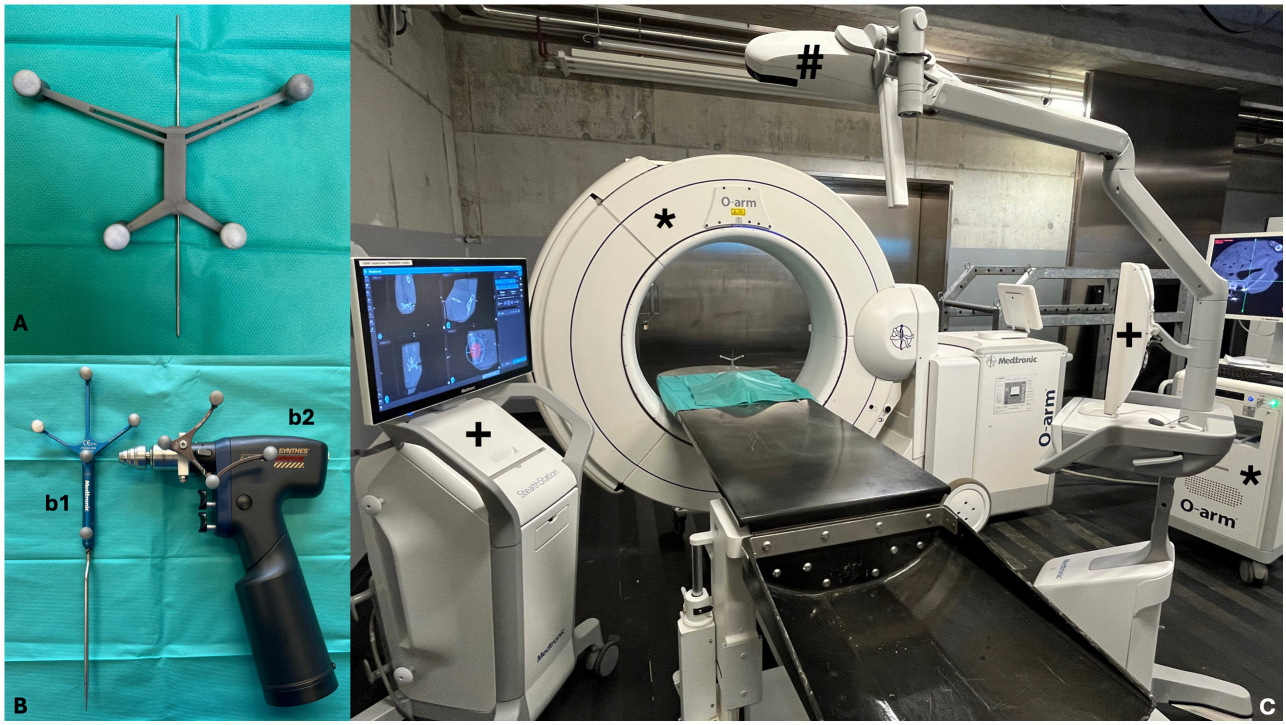

FIGURE 1
(A) 3D printed patient reference array with its reflecting spheres and pre-positioned 1.4 mm negative threaded pin. **(B)** Specific instrumentation for the navigated procedure: (b1) Navigated Pointer (Passive Planar Marker); (b2) Instrument tracker on a battery-powered drill (SureTrakII clamps and tracker on Colibri II). **(C)** Set-up for the computer-navigated drilling: O-arm with screen (*), Stealth Station S8 with its two screens (+), infrared camera for optical tracking (#).

estimated with the symmetrical palpation of the iliac wings in its cranial and dorsal plane.

The navigated pointer was used to determine the location of the entry point according to the predefined plan on the StealthStation 8. A stab incision was then performed with a #11 scalpel blade onto the near cortex of the ilium in the correct location as seen on the screen for temporary fixation pin placement. A 1.1 mm tap sleeve was placed and the location and direction of the pin placement was verified again with the help of the navigated pointer and the 1-0 K-wire was drilled through the tap sleeve in the desired direction to temporarily keep the ilium to the sacrum.

Another CBCT scan was made to assess the reduction and create the plan for the computer-assisted drilling of a hole through the ilium and sacrum for correct screw placement in the center of the sacral body, as described by Burger et al. (17). If the reduction was not accurate, the previously described procedure had to be repeated.

After planning and calibration of the instruments, the hole in the ilium and sacrum was drilled under surgical navigation guidance. Stability of the patient reference array and thus accuracy of the navigation system was verified before each drilling by touching the entry point of the patient reference array pin with the navigated pointer and by simultaneously assessing the virtual images displayed on the screen of the navigation system.

The first three cats were directly drilled with a 1.8 mm drill bit of 100 mm in length. As slippage of the drill bit on the iliac wing as well as bending of the drill was evident, the following seven cats were predrilled with a smaller 1.1 mm drill bit of 37 mm in length and the use of a 2.0 mm tap sleeve to protect the soft tissues. The first hole was enlarged with a 1.8 mm drill bit. A 2.4 mm self-tapping positional cortical screw of appropriate length was placed.

The conducted drill holes aimed to reach only 50% of the width of the sacral body to not interfere with the subsequent contralateral procedure.

2.3.3 Fluoroscopy controlled drilling

A conventional open dorsal approach to the sacroiliac joint was chosen. To allow good visualization of the sacral wing the iliac wing was retracted caudoventrally by an assistant. A surgical power drill (Colibri II) was used to place a 0.8 mm K-wire in the sacral wing to facilitate the correct screw placement through the sacral body according to Burger et al. (17) via fluoroscopic control. The K-wire placement was targeted at the center of the first sacral body. Fluoroscopic control was performed after every new pin positioning. Once the correct positioning of the pin was achieved, the pin was removed and the hole within the sacral body was sequentially overdrilled with a 1.1 mm and a 1.8 mm drill bit. Reduction of the luxation was carried out under visualization and held in place by the assistant until the equivalent hole in the wing of the ilium was drilled with a 1.8 mm drill bit and the 2.4 mm self-tapping positional cortical screw of appropriate length was placed.

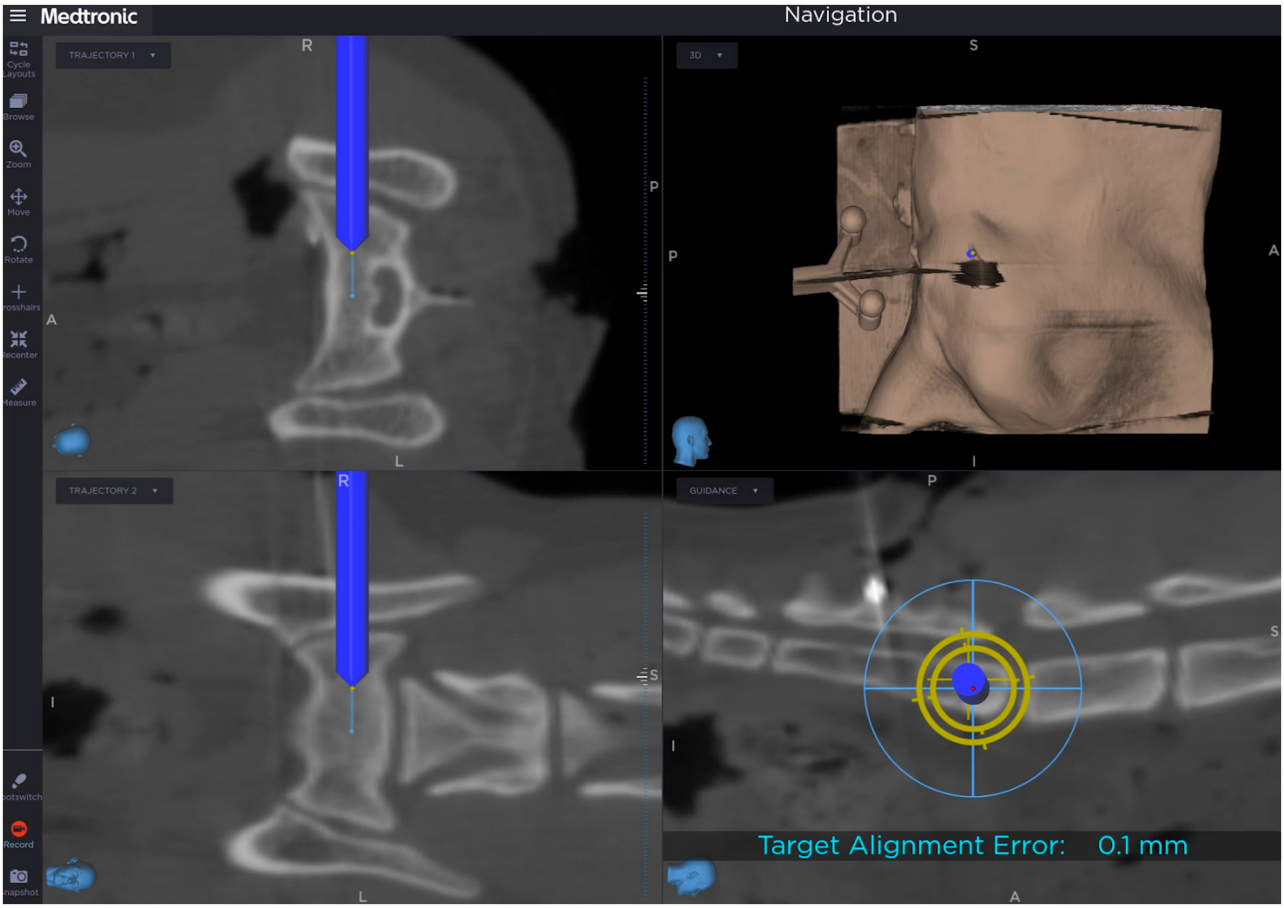

FIGURE 2
Screen view during computer-assisted drilling in trajectory 1 and 2 as well as guidance view. The dark blue cylinder represents the drill bit following the planned drill corridor (light blue line).

2.4 Time

For all procedures "total time" was noted and split into "time on patient" and "time off patient". "Total time" started with the placement of the patient reference array (MICA group) or the manipulation of the previously luxated sacroiliac joint (FC group). It ended in both groups after the placement of the 2.4 mm positional screw. "Time on patient" was defined as time needed for the surgical procedures which includes surgical approach, placement of the reference array, reduction and temporary fixation of the luxation, the drilling process itself and placement of the screw. "Time off patient" was defined as time needed for the imaging procedures in both groups (CBCT scans and fluoroscopy) and the planning of temporary fixation and the drill hole in the MICA group.

The additional control CBCT scans taken only for radiologic evaluation were not included in any of the time measurements.

2.5 Accuracy

The accuracy of the drilling was evaluated for the MICA group where the initial plan and the actual drill hole could be compared via CBCT images (Figure 3). Entry and target points for the conducted drill hole were defined on postoperative CBCT images using Stealth Navigation software (Medtronic). To compare the initial plan and the actual drill hole, pre- and postoperative CBCT images had to be manually merged to achieve superimposition of the images so that 3D coordinates could be extracted. To calculate the deviation in millimeters between the initial plan and the actual drill hole, the coordinates of the entry and target points were described by the Euclidean distance formula

$$\sqrt{(X2-X1)^2+(Y2-Y1)^2+(Z2-Z1)^2}$$

to calculate the deviation in millimeters to compare the initial plan and the actual drill hole (33, 34).

2.6 Radiologic evaluation

To ensure an optimal radiologic evaluation, five additional CBCT scans were conducted after drilling the hole in the sacral body. These included: one scan after completing the computer-assisted drill hole, one scan with the screw placed on the first side, one scan following the fluoroscopy guided freehand drill hole with the first screw still in place, one scan with the first and second screw

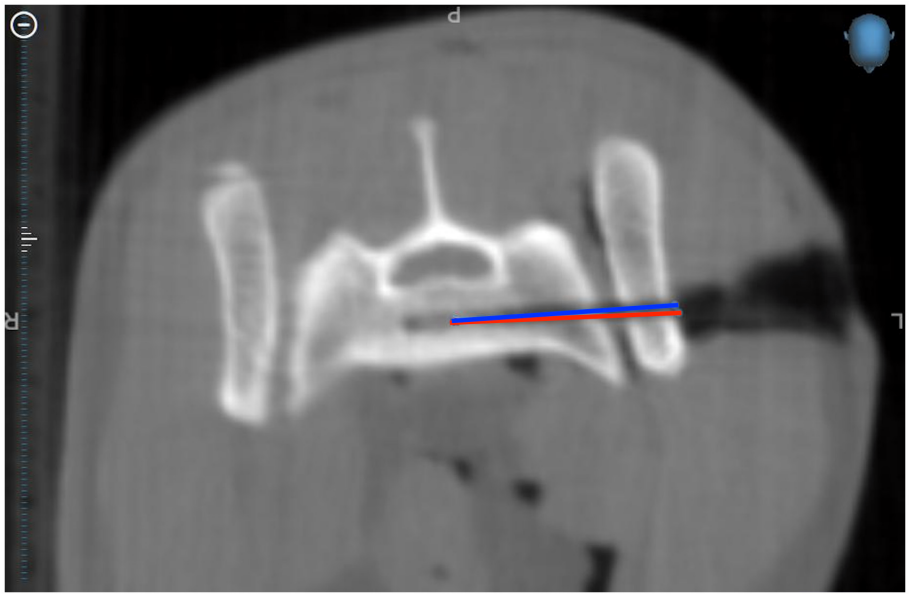

FIGURE 3
Merged CBCT images where you can see the planned drill corridor (red) and the actual drill corridor (blue) in Cat 10.

in place, and the final scan without any implants, showing only the two drill holes.

The postoperative CBCT images were evaluated by a Diplomate of the European College of Veterinary Diagnostic Imaging (DECVDI), C.P. The primary focus was the course of the drill hole in the 20 surgical procedures and the positioning of the patient reference array in the 10 cats in the MICA-group. Radiologic safety was assessed using three categories (I–III) and four directional subcategories (a–d) (Table 1). Additionally, surgeries were classified based on radiographic safety of implant placement (yes/no). Category I represented a drill hole entirely within the vertebral body, category II was assigned if the screw was in contact or eroding the sacral cortex, and category III indicated a violation of the cortex. Categories I and II were considered radiographically safe, whereas category III was classified as radiographically unsafe. The subcategory described the direction of deviation: a = dorsally, b = ventrally, c = cranially, d = caudally. As the drill holes only penetrated 50% of the sacral body to avoid contralateral interference, radiologic evaluation extended to 60% of bone purchase, as recommended for fixation of sacroiliac luxation.

The safety of the patient reference array was categorized into grade I, IIIa, or IIIb. Grade I was assigned if the patient reference array was located within the dorsal spinous process of S1 or S2. Grade III indicated sacral cortex penetration, with IIIa specifying intrusion into the vertebral canal and IIIb indicating direction toward the soft tissues ventral to the sacrum.

TABLE 1 Safety grade drilling corridor.

Safety grade	Safety name	Description
I	Well IN (optimal placement)	Trajectory within the vertebra, intact cortex of the vertebral canal floor and the ventral aspect of the sacrum
IIa	Just, IN	Trajectory within the vertebra, in contact or eroding the cortex of the vertebral canal floor
IIIa	Too far, IN	Trajectory violating the cortex of the vertebral canal floor or within the vertebral canal
IIb	Just, OUT	Trajectory within the vertebra, in contact or eroding the ventral aspect of the sacrum
IIIb	Too far, OUT	Trajectory violating the ventral cortex of the sacrum or ventrally outside of the sacrum
IIc	Just, CRAN	Trajectory within the vertebra, in contact or eroding the cranial endplate of S1
IIIc	Too far, CRAN	Trajectory violating the cranial endplate of SI or within the IVDS L7/S1
IId	Just, CAUD	Trajectory within the vertebra, in contact or eroding the caudal endplate of S1
IIId	Too far, CAUD	Trajectory violating the caudal endplate of SI or within S2

2.7 Statistical analysis

The learning curve was analyzed by comparing the first five to the last five surgeries. Wilcoxon signed-rank test was used to compare the two groups concerning the total surgery time. More insight was gained by dividing the total time between the time spent on the cadaver and the time spent planning the surgery. The same method was used to compare the deviation from the target for the screw entry and target sites. Fisher's exact test was performed to compare the frequency of the assigned radiological safety grades. The analysis was performed using the statistical software R (version 4.3.1) in Rstudio (Posit Software, version 2023.09.1.494).

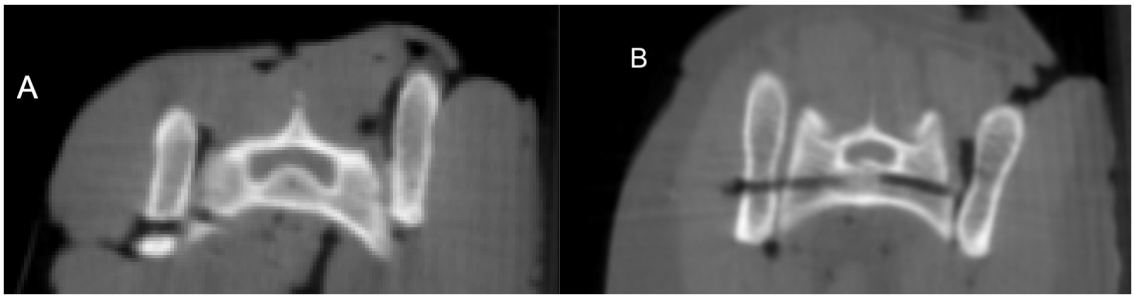

FIGURE 4
Final CBCT scans for radiologic evaluation without implants. **(A)** Drill corridor graded as IIIb where it ended ventrally outside of the sacrum and was categorized as radiographically unsafe (Cat 2, MICA procedure). **(B)** Drill corridor graded as I where it runs within the vertebrae and was categorized as radiographically safe (Cat 9, MICA procedure on the left side of the image and FC procedure on the right side of the image).

3 Results

The cadavers of 10 mature domestic shorthair cats were included in the study, seven males and three females with a median weight of 3.88 kg (range 2.1–6.3 kg).

Comparison of the first five procedures to the second five showed an improvement in total time, accuracy and safety, especially in the MICA group.

Inadequate reduction of the sacroiliac luxation was detected on preprocedural CBCT scan and had to be corrected in two cases (Cat 1 and Cat 3). Reduction was adequate in the remaining 8 cats.

3.1 Time

The MICA group showed a significantly slower "total time" ($p = 0.002$) with a mean of 44 min 45 s ± 11 min 53 s compared to the mean "total time" of 19 min 54 s ± 6 min 58 s in the FC group.

For the MICA group the mean "time on patient" was 23 min 50 s ± 8 min 55 s and the "time off patient" was 20 min 40 s ± 5 min 43 s. For the FC group, both, time on-and off-patient were shorter, with the "time on patient" being 14 min 40 s ± 4 min 42 s and "time off patient" of 4 min 40 s ± 3 min 40 s.

In the MICA group, although not statistically significant ($p = 0.056$), the mean "total time" decreased from 53 min 30 s ± 8 min 20 s to 36 min 15 s ± 8 min 40 s in the first vs. the second five procedures. A less pronounced improvement was seen in the FC group from the first five cases with a mean "total time" of 20 min 30 s ± 3 min 45 s to 18 min 50 s ± 9 min 20 s in the second five procedures, this was also not statistically significant ($p = 0.31$).

When comparing "time on patient" between the first five and the second five procedures, neither the MICA group ($p = 0.222$) nor the FC group ($p = 0.69$) resulted in a statistically significant difference. The "time on patient" decreased in the MICA group from 28 min 20 s ± 10 min 30 s to 19 min 36 s ± 6 min 10 s whereas the FC group showed a minimal improvement in "time on patient" from 15 min 15 s ± 4 min to 14 min 16 s ± 5 min 43 s.

The reduction from the mean "time off-patient" of 24 min 55 s ± 3 min 40 s in the first five procedures to a mean "time off-patient" of 16 min 30 s ± 3 min 35 s in the second five procedures in the MICA group was statistically significant ($p = 0.032$). This comparison in the FC group did not show a significant improvement ($p = 0.222$) with a mean "time off-patient" of 5 min 10 s ± 7 min 42 s in the first five compared to the "time off-patient" of 4 min 34 s ± 4 min 40 s in the second five cases.

3.2 Accuracy

This criterion was only measurable in the MICA group.

The 10 cases in the MICA group showed a mean deviation of 2 mm at the entry point and a mean deviation of 2.5 mm at the target point. Although not statistically significant ($p = 0.063$), there was an improvement in the accuracy aberration when comparing the first five to the second five procedures.

The mean deviation on the entry point decreased from 2.4 to 1.6 mm and on the target point from 4.2 to 0.9 mm in the first five compared to the second five procedures.

3.3 Radiologic evaluation

In all cats, the safety grade for placement of the patient reference array was categorized as I, with a trajectory running correctly within the dorsal spinous process of S1 or S2.

Inferior safety grade for the screw placement was assigned to the first three cadavers of both groups with a IIIb in the MICA and IIb in the FC group compared to grade I in the remaining seven cadavers.

The safety grade in the MICA group was worse in the first five trials compared to the last five ones. Three cadavers (3/10) were categorized a IIIb, whereas the trajectory was violating the ventral cortex of the sacrum or was even ventrally outside of the sacrum and therefore rated as radiographically unsafe implant placement. The following seven cadavers (7/10) were classified in category I and fulfilled the criterion for radiographically safe implant placement (Figures 4A, B).

In the FC group the first and third cat were categorized as IIb with the trajectory being in contact or eroding the ventral cortex of the sacrum (2/10). All the other were evaluated as category I (8/10), which means the procedures on all 10 cadavers achieved radiographically safe implant placement.

The radiologic grading wasn't statistically significant when performing the Fisher's exact test due to a small sample size (count range 2–7 for the different grades).

4 Discussion

Computer-assisted surgery for minimally invasive surgical fixation of feline sacroiliac luxation seems to be a safe procedure with a steep learning curve for a novice surgeon. Several cadaver surgeries were needed to get comfortable with the handling of the technical instruments and the navigation software. In our experimental set-up, the reduction and surgical fixation of sacroiliac luxation via an open dorsal, fluoroscopy-controlled approach also resulted in safe implant placement in most of the cadaveric specimens. Although the minimally invasive procedure was associated with a significantly longer surgical time, it avoids the creation of a large surgical approach and improves intraoperative control of implant placement.

Compared to the study of Kleiner et al. (19) the safety of the computer-assisted surgery was improved by changing the smooth to the negative threaded pin to have better bone purchase for sufficient anchoring in the spinous process alone and therefore minimizing the risk of violation of the spinal canal.

The technical equipment used from Medtronic is very user-friendly. The only downside was the recognition of the custom-made 3D printed patient reference array by the Stealth Station Navigation system in some trials. In one case (Cat 6) it took 15 min and several adjustments in position of the infrared camera for the Stealth Station to recognize the patient reference array and to conduct a computer navigated scan. In other trials, one of the four reflecting spheres had to be removed for the infrared camera to recognize the patient reference array. These challenges did prolong the "time off patient" but did not interfere with the accuracy. As previously described, the patient reference array was a modification to the version used by Papacella-Beugger et al. (33) Our patient reference array was out of Formlabs Tough 1500 and weighted 9 g whereas the one from Papacella-Beugger is out of polyactide with a weight of 12 g compared to the original patient reference array by Medtronic with 59 g. Modification included the fixation with a press fit negative-threaded pin going through the patient reference array compared to a pre-printed fixation method with variable adapters by Papacella-Beugger. Challenges in recognition of the custom-made patient reference array by the Stealth Station Navigation system were not described in their study and we assume it to be due to a slight deviation in the geometry of the arms of the patient reference array resulting from 3D printing.

The positioning of the patient reference array is a critical point in computer-assisted surgery. An accurate correlation between the CBCT images and therefore the plan and the anatomical structures in the surgical field are only given, if the patient reference array is securely anchored to the target bone throughout the whole procedure, in an angle-stable manner. If any alteration of the spatial relationship between the array and the target bone occurs, the CBCT scans must be redone and a new plan according to the new reference has to be made. In the study of Kleiner et al. the reference array was fixated with a smooth pin which was drilled through the spinous process of S1 or S2 and anchored in the roof of the sacrum (19). As in some of the first cases the pin penetrated the spinal canal, the fixation of the reference array was changed for our study. We used a negative threaded pin to improve stability and eliminating the need for a second anchoring point into the roof of the sacrum due to better bone purchase of the threaded version. As a result, positioning in the spinous process was sufficiently stable and the safety of the procedure was increased. None of the pins in the present study violated any important structures. Furthermore, by placing the patient reference array in the same bony structure as the target bone (Spinous process of S1 or S2 for surgeries on the sacral body), a potential error in surgical accuracy aberration was minimized. As described in other studies (35, 36), applying pressure on the bone during surgical manipulation can alter its imaged position if the patient reference array is fixed to a different structure than the target structure. If the patient reference array is fixed to the same structure where the surgery takes places, movement of it correlates with the image due to a similar movement of the reference array. Nevertheless, movement and manipulation of the imaged position should be minimized.

As demonstrated in previous studies, a minimally invasive approach for the repair of sacroiliac joint luxation led to more accurate screw placement and less soft tissue damage and therefore a reduction of patient morbidity might be anticipated (12, 16, 20, 23, 24). The control for screw placement was usually done by fluoroscopy. The safety of screw placement in sacroiliac luxation with the help of computer navigation was proven in a study by Kleiner et al. (19), which lead to a combination of a minimally invasive approach with the guidance of computer navigation. The basics of the minimal invasive computer-assisted surgical procedure are similar to the minimal invasive approach described by Tomlinson et al. (12). The advantage of this new technique is the control of reduction via CBCT before fixation and the precise planning of the drill corridor through the ilium and sacral body while sparing the soft tissue. However, for cases with a longer duration from trauma to surgical repair, the surgeon should be prepared to convert to an open approach if a closed approach is not amenable for adequate reduction screw placement.

Due to the CBCT scans, planning process and set up of the technical equipment of the surgical navigation, the total time is doubled in the MICA group compared to the FC group, but with training a clear reduction in time is anticipated as seen when comparing the first five to the second five trials. Thus, training and practice are essential to optimize time when using computer navigation. Similar results were seen in the study of Kleiner et al. (19) with a mean duration of 23 min and 37 s for the computer navigated group and 9 min and 47 s in the FC group with improvement of time in both groups with training. However, a team approach should be considered when applying this technique in clinical cases to optimize the workflow of the navigated procedure in order to shorten the overall surgery time and minimize the associated complications (37).

The observed surgical accuracy aberration from the planned to the actual drilled corridor of 2 mm at the entry point and 2.5 mm at the target point were similar to the results with an open approach computer-assisted surgery shown by Kleiner et al. with a deviation of 2 mm at the entry point and 1.6 mm at the target point in the same anatomical location (19). Comparable results were achieved using the same CBCT-based computer-assisted

drilling procedure in other anatomical locations (33, 34). Papacella-Beugger had a median entry point deviation of 1.8 mm (range: 0.3–3.7 mm) and median exit point deviation of 1.6 mm (range: 0.6–5 mm) in lumbar plate fixation (33). In the study by Guevar et al. for minimally invasive stabilization in the thoracolumbar spine the overall mean deviations for the entry points were 2.2 mm for the experienced surgeon and 3.7 mm for the novice surgeon. For the exit points, deviations were 3.0 and 5.0 mm, respectively. Significant difference was found in accuracy between the experienced and novice surgeon for the deviations overall (34). An accuracy aberration of 2 and 2.5 mm in entry and target point matches the accuracy expectations when applying an optical tracking system (like the Stealth Station) for a computer-assisted orthopedic surgical procedure (38). Overall, a deviation in the close range of 2 mm meets the high standards in precision required when working on a bony structure as small as a feline sacrum. Comparison of drill hole accuracy between an experienced surgeon vs. a lesser experienced surgeon in this anatomical location was performed by Kleiner et al. and did not show a significant difference (19). Therefore, this study was carried out by novice first year ECVS resident surgeon only.

The first three cadavers with the highest deviation on entry as well as target point and the poorest radiology safety grade (IIIb in MICA Group/IIb in FC Group) were drilled with a 1.8 mm drill bit. As slippage of the drill bit on the iliac wing was evident, the following 7 cats where predrilled with a smaller 1.1 mm drill bit and showed less deviation from the initial plan and scored a better radiological safety grade. The 1.1 mm drill bit was shorter than the 1.8 mm drill bit (35 vs. 100 mm). It was found that longer drill bits tend to bend more easily and therefore the actual position of the drill tip does not match with the fiducials on the handpiece and the drilling is not accurate to the planned procedure on the screen. Similar observations with bending of the drill were made in equine computer-assisted surgeries, whereas recommendation to use a shorter drill bit was expressed (35). Nevertheless, the lack of surgical experience in drilling uneven, slippery surface on the iliac wing as well as first using a longer drill bit is hypothesized to have influenced the results more than the lack of experience with the navigation system as demonstrated by improvement of accuracy with the transition to a shorter drill bit and more training.

To facilitate radiologic evaluation, account for possible artifacts due to the metal implants and avoid interference between the bilateral drill holes, additional CBCT scans were performed after the surgical procedures with the implants in place and after removal. In a clinical setting, only one CBCT scan would typically be required for temporary fixation without computer navigation, or two scans if computer navigation is used, as opposed to the seven CBCT scans performed in this study. Since time measurement was paused for the additional CBCT scans, total time could only be reduced by omitting the scan for the temporary fixation pin planning. Since there are no critical structures located directly ventral to the vertebra, a previous study by Shales et al. (18, 21) did not consider screws penetrating the ventral cortex as mispositioned. Nevertheless, we did categorize our first three cadavers as a radiographically unsafe implant placement because there was not enough bone purchase before violating the ventral cortex and stability of the fixation could not be ensured as well as neurologic deficits could not be excluded in this *ex vivo* study. We did consider Category I and II as radiographically safe implant placement where the cortex was not violated, and a good surgical outcome would be expected. Due to possible neurological deficits and screw loosening and therefore unsatisfactory surgical outcome, category III was classified as radiographically unsafe implant placement. Depending on the direction of deviation (a = dorsally, b = ventrally, c = cranially, d = caudally) in category III a revision would be needed or even a fatal outcome could be anticipated.

4.1 Limitations

One of the main limitations of the study is its cadaveric nature with artificially induced unilateral sacroiliac luxation which does not provide an accurate imitation of a clinical case as muscle trauma and additional pelvic fractures are not identical. The feasibility has to be tested for the closed reduction of the sacroiliac luxation in an *in vivo* study where muscle contracture is present or if a bilateral luxation, and therefore change in known landmarks, complicates the surgery. Furthermore, both sides of each cat were used for this study, this could cause a bias in anatomical landmarks when doing the second procedure. Cautious extrapolation of the results of this experimental study to clinical cases is warranted, and the potential for screw loosening and neurological deficits should be assessed in an *in vivo* study, particularly in cats that were categorized in group IIIb where the trajectory violated the ventral cortex.

Different surgical approaches (minimally invasive vs. open approach) were used for the two different groups and therefore limited an exact comparison concerning time and visualization of anatomical structures. As all surgeries were performed by a first-year surgery resident without major orthopedic experience, some initial problems were evident, like slippage of the drill bit on the bony surface. On the other hand, a steep learning curve was observed. Results could differ if a more experienced surgeon had performed the surgeries.

To allow direct comparison of the plan and the actual drillhole the pre- and postoperative CT images were manually merged using Stealth Station software and could therefore lead to an error in accuracy.

The effect of increased exposure to radiation of patients treated by MICA in comparison to those of the FC group should also be taken in consideration but was not estimated in the present study. This has yet to be tested.

5 Conclusion

Computer-assisted surgery for minimally invasive sacroiliac luxation in cats can be considered as a safe alternative procedure with a high accuracy for correct screw positioning. The time needed for surgery is increased compared to fluoroscopy controlled freehand surgery but a steep learning curve positively affecting accuracy and duration of the procedure was observed, leading to the assumption that with more experience the observed results might be further improved and further emphasize the advantages of not performing a large open approach, especially regarding intra- and postoperative morbidity.

Data availability statement

The original contributions presented in the study are included in the article/supplementary material, further inquiries can be directed to the corresponding author.

Ethics statement

Ethical approval was not required for the study involving animals in accordance with the local legislation and institutional requirements because the study only included cadavers of client owned cats who gave consent to use them for research purposes. No alive animals were included in the study.

Author contributions

NW: Conceptualization, Data curation, Formal analysis, Methodology, Writing – original draft, Writing – review & editing. LK: Conceptualization, Data curation, Formal analysis, Methodology, Writing – review & editing. CP: Data curation, Formal analysis, Resources, Writing – review & editing. JG: Writing – review & editing, Resources, Validation. MP: Writing – review & editing, Conceptualization, Software. FF: Conceptualization, Supervision, Writing – review & editing. PD: Conceptualization, Supervision, Writing – review & editing.

Funding

The author(s) declare financial support was received for the research, authorship, and/or publication of this article. Open access funding by University of Bern.

Conflict of interest

The authors declare that the research was conducted in the absence of any commercial or financial relationships that could be construed as a potential conflict of interest.

Generative AI statement

The author(s) declare that no Gen AI was used in the creation of this manuscript.

Publisher's note

References

1. Bookbinder PF, Flanders JA. Characteristics of pelvic fracture in the cat. *Vet Comp Orthop Traumatol.* (1992) 5:122–7.

2. Moens NMM, DeCamp CE. Fractures of the pelvis (Ch. 56). In: Tobias KM, Johnston SA, editors. *Small Animal Veterinary Surgery sl*. St Louis, MO: Elsevier (2018).

3. Borer LR, Voss K, Montavon PM. Ventral abdominal approach for screw fixation of sacroiliac luxation in clinically affected cats. *Am J Vet Res.* (2008) 69:549–56. doi: 10.2460/ajvr.69.4.549

4. Tomlinson JL. Fractures of the pelvis. In: Douglas S, editor. *Textbook of Small Animal Surgery*. 3rd ed. Philadelphia, PA: WB Saunders Co. (2003). p. 1989–2001.

5. Brinker WO, Piermattei DL, Flo GL. *Sacroiliac Fracture-Luxation*. Philadelphia, PA: WB Saunders Co. (1997). p. 398–403.

6. Parslow A, Simpson DJ. Bilateral sacroiliac luxation fixation using a single transiliosacral pin: surgical technique and clinical outcomes in eight cats. *J Small Anim Pract.* (2017) 58:330–6. doi: 10.1111/jsap.12659

7. Leasure CS, Lewis DD, Sereda CW, Mattern KM, Jehn CT, Wheeler JL. Limited open reduction and stabilization of sacroiliac fracture-luxations using fluoroscopically assisted placement of a trans-iliosacral rod in five dogs. *Vet Surg.* (2007) 36:633–43. doi: 10.1111/j.1532-950X.2007.00315.x

8. Froiedefond B, Moinard M, Caron A. Outcomes for 15 cats with bilateral sacroiliac luxation treated with transiliosacral toggle suture repair. *Vet Surg.* (2023) 52:983–93. doi: 10.1111/vsu.14008

9. Yap FW, Dunn AL, Farell M, Calvo I. Trans-iliac pin/bolt/screw internal fixation for sacroiliac luxation or separation in cats: six cases. *J Feline Med Surg.* (2014) 16:354–62. doi: 10.1177/1098612X13503650

10. Raffan PJ, Joly CL, Timm PG, Miles JE. A tension band technique for stabilisation of sacroiliac separations in cats. *J Small Anim Pract.* (2002) 43:255–60. doi: 10.1111/j.1748-5827.2002.tb00068.x

11. Borer LR, Voss K, Montavon PM. Ventral abdominal approach for screw fixation of sacroiliac luxation in cadavers of cats and dogs. *Am J Vet Res.* (2008) 69:542–8. doi: 10.2460/ajvr.69.4.542

12. Tomlinson JL. Minimally invasive repair of sacroiliac luxation in small animals. *Vet Clin North Am Small Anim Pract.* (2012) 42:1069–77. doi: 10.1016/j.cvsm.2012.06.005

13. Jourdain M, Fernandes D, Védrine B, Gauthier O. Fluoroscopically-assisted closed reduction and percutaneous fixation of sacroiliac luxations in cats using 2.4mm headless cannulated compression screws: description, evalutation and clinical outcome. *Vet Surg.* (2024) 53:603–12. doi: 10.1111/vsu.14070

14. Permattei DL, Johnson KA. Approacht to the ventral aspect of the sacrum. In: Permattei DL, Johnson KA, editors. *Permattei's Atlas of Surgical Aproaches to the Bones and Joints of the Dog and Cat. s.l.* St Louis, MO: WB Saunders Co. (2014). p. 320–1.

15. Alexander JE, Archibald J, Cawley AJ. Approach to the wing of the ilium and dorsal aspect of the sacrum. In: Johnson KA, editor. *Permattei's Atlas of Surgical Approaches to the Bones and Joints of the Dog and Cat. s.l.* St Louis, MO: WB Saunders Co. (2014). p. 312–5.

16. Tomlinson JL, Cook JL, Payne JT, Anderson CC, Johnson JC. Closed reduction and lag screw fixation of sacroiliac luxations and fractures. *Vet Surg.* (1999) 28:188–93. doi: 10.1053/jvet.1999.0188

17. Burger M, Forterre F, Brunnberg L. Surgical anatomy of the feline sacroiliac joint for lag screw fixation of sacroiliac fracture-luxation. *Vet Compar Orthop Traumatol.* (2004) 17:146–51. doi: 10.1055/s-0038-1632803

18. Shales CJ, White L, Langley-Hobbs SJ. Sacroiliac luxation in the cat: defining a safe corridor in the dorsoventral plane for screw insertion in lag fashion. *Vet Surg.* (2009) 38:343–8. doi: 10.1111/j.1532-950X.2009.00509.x

19. Kleiner L, Wolf ND, Precht Ch, Haenssgen K, Forterre F, Duever P. Feline saroiliac luxation: comparison of fluoroscopy-controlled freehand vs. computer-navigated drilling in the sacrum—a cadaveric study. *Front Vet Sci.* (2024) 11:1510253. doi: 10.3389/fvets.2024.1510253

20. Tonks CA, Tomlinson JL, Cook JL. Evaluation of closed reduction and screw fixation in lag fashion of sacroiliac fracture-luxations. *Vet Surg.* (2008) 37:603–7. doi: 10.1111/j.1532-950X.2008.00414.x

21. Shales CJ, Moores A, Kulendra E, White C, Toscano M, Langley-Hobbs S. Stabilization of sacroiliac luxation in 40 cats using screws inserted in lag fashion. *Vet Surg.* (2010) 39:696–700. doi: 10.1111/j.1532-950X.2010.00699.x

22. DeChamp CE, Braden TD. Sacroiliac fractures-separation in the dog: a study of 92 cases. *Vet Surg.* (1985) 14:127–30. doi: 10.1111/j.1532-950X.1985.tb00841.x

23. Déjardin LM, Marturello DM, Guiot LP, Guillou RP, DeCamp CE. Comparison of open reduction versus minimally invasive surgical approaches on screw position in canine sacroiliac lag-screw fixation. *Vet Compar Orthop Traumatol*. (2016) 29:290–7. doi: 10.3415/VCOT-16-02-0030

24. Rollins A, Balfour R, Szabo D, Chesvick CM. Evaluation of fluoroscopic-guided closed reduction versus open reduction of sacroiliac fracture-luxations stabilized with a lag screw. *Vet Compar Orthop Traumatol*. (2019) 32:467–74. doi: 10.1055/s-0039-1693471

25. Sciulli RL, Daffner RH, Altman DT, Altman GT, Sewecke JJ. CT-guided iliosacral screw placement: technique and clinical experience. *Am J Roentgenol*. (2007) 188:W181–92. doi: 10.2214/AJR.05.0479

26. Smith AG, Capobianco R, Cher D, Rudolf L, Sachs D, Gundanna M, et al. Open versus minimally invasive sacroiliac joint fusion: a multi-center comparison of perioperative measures and clinical outcomes. *Ann Surg Innov Res*. (2013) 7:1–14. doi: 10.1186/1750-1164-7-14

27. Ledonio CG, Polly DW, Swiontkowski MF. Minimally invasive versus open sacroiliac joint fusion. Are they similarly safe and effective? *Clin Orthop Relat Res*. (2014) 472:1831–8. doi: 10.1007/s11999-014-3499-8

28. Heiney J, Capobianco R, Cher D. A systematic review of minimally invasive sacroiliac joint fusion utilizing a lateral transarticular technique. *Int J Spine Surg*. (2015) 9:40. doi: 10.14444/2040

29. Pieske O, Landersdorfer C, Trumm C, Greiner A, Wallmichtrath J, Gottschalk O, et al. CT-guided sacroiliac percutaneous screw placement in unstable posterior pelvic ring injuries: accuracy of screw position, injury reduction and complications in 71 patients with 136 screws. *Injury*. (2015) 46:333–9. doi: 10.1016/j.injury.2014.11.009

30. Tonetti J, Carrat L, Lavalleé St, Pittet L, Merloz Ph, Chirossel JP. Percutaneous iliosacral screw placement using image guided techniques. *Clin Orthop Relat Res*. (1998) 354:103–10. doi: 10.1097/00003086-199809000-00013

31. Wang H, Wang F, Leong APY, Xu L, Chen X, Wang Q. Precision insertion of percutaneous sacroiliac screws using a novel augmented reality-based navigation system: a pilot study. *Int Orthop*. (2016) 40:1941–7. doi: 10.1007/s00264-015-3028-8

32. Cher DJ, Frasco MA, Arnold RJG, Polly DW. Cost-effectiveness of minimally invasive sarcroiliac joint fusion. *ClinicoEcon Outcom Res*. (2016) 8:1–14. doi: 10.2147/CEOR.S94266

33. Papacella-Beugger A, Forterre F, Samer E, Guevar J, Müller A, Planchamp B, et al. Spinal neuronavigation for lumbar plate fixation in miniature breed dogs. *Vet Compar Orthop Traumatol*. (2024) 37:279–85. doi: 10.1055/s-0044-1787707

34. Guevar J, Samer ES, Precht C, Rathmann JMK, Forterre F. Accuracy and safety of neuronavigation for minimally invasive stabilization in the thoracolumbar spine using polyaxial screws-rod: a canine cadaveric proof of concept. *Vet Compar Orthop Traumatol*. (2022) 35:370–80. doi: 10.1055/s-0042-1750056

35. de Preux M, Vidono B, Koch Ch. Influence of a purpose-built frame on the accuracy of computer-assisted orthopedic surgery of equine extremities. *Vet Surg*. (2020) 49:1367–77. doi: 10.1111/vsu.13484

36. Kim TT, Johnson JP, Pashman R, Drazin D. Minimally invasive spinal surgery with intraoperative image-guided navigation. *Biomed Res Int*. (2016) 2016:16235. doi: 10.1155/2016/5716235

37. Windhagen H, Thorey F, Ostermeier S, Emmerich J, Wirth CJ, Stukenborg-Colsman C. Das Navigatorkonzept—Prozessoptimierung in der navigierten Knieendprothetik. *Orthopäde*. (2005) 34:1125–26. doi: 10.1007/s00132-005-0853-2

38. Medtronic. *StealthStation S8 Cranial Optical Kurzhandbuch*. Louisville, CO: Medtronic Navigation. (2019).

39. Montavon MP, Boudrieau RJ, Hohn RB. Approach to the ventral aspect of the sacrum. In: Permattei DL, Johnson KA, editors. *Permattei's Atlas of Surgical Aproaches to the Bones and Joints of the Dog and Cat. s.l.* St. Louis, MO: WB Saunders Co. (2014). p. 320–1.

frontiers | Frontiers in Veterinary Science

TYPE Original Research
PUBLISHED 12 March 2025
DOI 10.3389/fvets.2025.1521684

OPEN ACCESS

EDITED BY
Sokol Duro,
Agricultural University of Tirana, Albania

REVIEWED BY
Howard Dobson,
Invicro, United States
Germain Arribarat,
INSERM U1214 Centre d'Imagerie Neuro Toulouse (ToNIC), France

*CORRESPONDENCE
Lena Bunzendahl
✉ lena.bunzendahl@uni-goettingen.de
Susann Boretius
✉ sboretius@dpz.eu

RECEIVED 02 November 2024
ACCEPTED 10 February 2025
PUBLISHED 12 March 2025

CITATION
Bunzendahl L, Moussavi A, Bleyer M, Neumann S and Boretius S (2025) Magnetisation transfer, T1 and T2* relaxation in canine menisci of elderly dogs—an *ex vivo* study in stifle joints.
Front. Vet. Sci. 12:1521684.
doi: 10.3389/fvets.2025.1521684

Magnetisation transfer, T1 and T2* relaxation in canine menisci of elderly dogs—an *ex vivo* study in stifle joints

Lena Bunzendahl[1,2]*, Amir Moussavi[2,3], Martina Bleyer[4], Stephan Neumann[1] and Susann Boretius[2]*

[1]Small Animal Clinic, Institute of Veterinary Medicine, Georg-August University of Göttingen, Göttingen, Germany, [2]Functional Imaging Laboratory, German Primate Center, Leibniz Institute for Primate Research, Göttingen, Germany, [3]Fachhochschule Südwestfalen, University of Applied Sciences, Hagen, Germany, [4]Pathology Unit, German Primate Center, Leibniz Institute for Primate Research, Göttingen, Germany

Magnetic resonance imaging (MRI) is widely used in human medicine, offering multiple contrast mechanisms to visualise different tissue types. It is also gaining importance in veterinary medicine, including diagnosing joint disorders. The menisci of the stifle joint play a crucial role in the development of osteoarthritis (OA), and multi-parameter MRI of the menisci may aid in early OA diagnosis, potentially improving therapeutic outcomes. In a previous *ex vivo* study, we measured T2 relaxation times in menisci of elderly dogs with mild histological signs of degeneration but no clinical symptoms of lameness. As no significant changes in T2 relaxation times were observed in relation to histological scores, the present study extends this investigation by exploring more advanced MR parameters—including T1 relaxation time, T2* relaxation time, magnetisation transfer ratio (MTR), and magnetisation transfer saturation (MTsat)—to assess their potential for detecting early microstructural changes in the menisci. While T2* relaxation times and MTR showed no significant variation across histological scores, MTsat values increased with higher proteoglycan staining. In contrast, the apparent T1 relaxation time (T1app) was lower in menisci with elevated proteoglycan scores and increased with higher cellularity scores. The correlation between MTsat and proteoglycan content suggests that MTsat, along with T1app, could be a promising parameter for characterising the extracellular matrix. However, further research is needed to validate these findings.

KEYWORDS

multi-parameter MRI, T2* mapping, T1 mapping, magnetisation transfer, canine menisci, osteoarthritis, stifle joint, proteoglycans

1 Introduction

Osteoarthritis (OA) of the canine stifle joint is a predominantly degenerative joint disease, especially common in older dogs. OA frequently develops in the context of cranial cruciate ligament disease (1) and is closely associated with damage or degeneration of the menisci. These fibrocartilaginous structures play a critical role in absorbing compressive loads and maintaining joint stability, which helps to protect the articular cartilage from excessive wear (2–4). As OA progresses, it leads to structural changes in all joint components, including the medial and lateral menisci, making meniscal degeneration a key factor in OA onset and progression.

Magnetic resonance imaging (MRI) is the gold standard for diagnosing knee disorders in humans, offering high-resolution, non-invasive imaging of soft tissues and bone structures. It is routinely employed to detect meniscal tears, ligament injuries, and cartilage degeneration (5–12). In veterinary medicine, although traditionally less common, the use of MRI is steadily increasing (13, 14). In addition to identifying macroscopic injuries (10, 11, 15), MRI is gaining importance in characterising tissue microstructures. Recent advances in quantitative and semi-quantitative techniques have proven particularly useful for assessing microscopic changes in humans (9, 16–18) and animals (1, 19–21).

The menisci are composed of fibrochondrocytes embedded in an extracellular matrix primarily consisting of water, collagen, and proteoglycans (22–25). The collagen fibres, primarily type I with smaller amounts of type II and III, are arranged in radial and circumferential patterns, allowing the menisci to resist multidirectional stresses. Proteoglycans, mainly aggrecan, make up 1–2% of the meniscal dry weight and contain glycosaminoglycan (GAG) chains such as chondroitin sulphate and keratan sulphate (22).

In osteoarthritic menisci, alterations in the extracellular matrix commonly lead to increased water content and mobility, which in turn influences the T2 relaxation time. Elevated T2 relaxation times have been documented in human meniscus degeneration (9, 10). In a previous *ex vivo* study, we measured T2 relaxation times in menisci from elderly dogs with mild histological degeneration but without clinical signs of lameness. The results showed no significant changes in T2 relaxation times with higher histological scores, suggesting that these early degenerative changes did not markedly affect the T2 values (26). We have now expanded our investigation to include T1 and T2* relaxation times, as well as magnetisation transfer (MT) techniques and the derived parameters, including magnetisation transfer ratio (MTR) and magnetisation transfer saturation (MTsat).

These advanced MR parameters are not yet part of routine clinical diagnostics in human or veterinary medicine, partly due to longer acquisition times and the complexity of data interpretation (27, 28). However, these techniques are gaining significance in medical imaging (27), and *post mortem* studies may help to identify promising candidates for future clinical applications. In the following, we will briefly address the potential advantages and added value of these techniques for the microtissue characterization of the menisci.

Given the observed increase in water content during meniscal degeneration, T2* relaxation times may behave similarly to T2 relaxation times. Nebelung et al. reported higher T2* relaxation values correlating with increasing histological scores in humans, though primarily at the extreme ends of the spectrum (29). Furthermore, Lee et al. found a positive correlation between contact strain and T2* relaxation times in the articular cartilage of cattle (6). Although T2 and T2* are related, T2* is more sensitive to magnetic field inhomogeneities, potentially providing additional insights into subtle tissue changes such as variation in fiber density and orientation. However, this heightened sensitivity poses challenges for data acquisition and interpretation, limiting its current clinical use.

T1 relaxation time, another parameter sensitive to water content, is valuable for assessing cartilage and soft tissues (8, 18, 30, 31), but its application to the meniscus remains largely in the research phase.

MT techniques have been widely applied to indirectly assess macromolecular content in various biological tissues (32–36). These methods exploit the interaction between free water protons and protons bound to macromolecules. By selectively saturating the bound protons, magnetisation is transferred to the free water protons, resulting in a reduction in signal intensity. The MTR quantifies the degree of this signal loss by comparing it to a data set acquired without the saturating radiofrequency pulse. Higher MTR values typically indicate denser macromolecular structures (12). Several studies have measured MTR in articular cartilage and menisci, reporting lower MTR values in tissues with reduced collagen and proteoglycan content (12, 30, 32).

A limitation of MTR is its lack of specificity. Various factors, such as inflammation and oedema, can influence the results. Additionally, MTR is susceptible to B0 (main magnetic field) and B1 (radiofrequency) field inhomogeneities and highly sensitive to acquisition parameters, such as the choice of saturation pulse, which can lead to inconsistent values and makes standardisation across different studies or clinical environments challenging. To address these limitations, quantitative magnetisation transfer (qMT) methods have been developed. These techniques provide more specific and reproducible macromolecular parameters, such as the macromolecular pool size fraction and the exchange rate between free and bound protons. However, the advantages of qMT come at the cost of longer acquisition times and more complex data processing, limiting its availability in clinical practice.

Helms et al. (37) introduced a technique called MTsat that bridges the gap between the simplicity of MTR and the complexity of full qMT imaging. MTsat incorporates corrections for B1 inhomogeneities and T1 relaxation times, providing more accurate data but with shorter acquisition times compared to full qMT. MTsat is increasingly used in research settings, particularly for studying neurological disorders (38–41). To our knowledge, this technique has not yet been applied to examine musculoskeletal structures. We hypothesize that MTsat may be suitable for quantifying the macromolecular content of the meniscus, thereby offering more detailed insights into the remodeling processes of menisci during degeneration.

In this study, we determined the T1 and T2* relaxation times, along with MTR and MTsat, in menisci from elderly dogs as previously described. Our goal was to evaluate the sensitivity of these MR parameters in detecting relatively mild degenerative tissue changes in mostly normally aged menisci and to determine whether and how these parameters can identify specific types of tissue alterations. If successful, these early markers could enhance the understanding of osteoarthritis pathogenesis and pave the way for more effective treatment strategies.

2 Materials and methods

2.1 Study samples

The stifle joints used in this study have been described previously (26). One joint had to be excluded from the original cohort of 16 joints from 8 dogs due to image artefacts. In total, 30 menisci from 15 joints (15 medial, 15 lateral) were included. Only elderly dogs, aged between 10 and 17 years, were selected for the study. None of the dogs had a history of hindlimb lameness or stifle instability. The reasons for the required euthanasia were unrelated to this study. Additional patient information can be found in Bunzendahl et al. (26).

Based on the results of X-ray scoring using the modified Kellgren-Lawrence scale (42, 43), 29% of the joints showed no radiographic evidence of osteoarthritis (score 0). The remaining 71% exhibited mild signs of osteoarthritis, corresponding to a score of 1.

Histological scoring was based on a system adapted from Sun et al. (44) and Pauli et al. (45), which includes individual scores for meniscus cellularity (0 to 3), collagen content (0 to 2), collagen organisation (0 to 3), and proteoglycan content (0 to 2). Additionally, a total score was calculated by summing up all the individual scores, resulting in a maximum possible total score of 10. Among the 30 menisci, one was classified with a total score of 0, while the highest total score observed was 6 ($n = 2$).

2.2 MR imaging

Before MRI, the stifle joints were dissected from the surrounding tissue and fixed in 10% neutral-buffered formaldehyde. The joints, submerged in the formaldehyde solution were positioned in a flexible 16-channel receive-coil (Variety, NORAS MRI products GmbH, Höchberg, Germany). All MR measurements were performed using a 3 Tesla whole-body MR system (MAGNETOM Prisma, Siemens Healthineers, Erlangen, Germany).

Maps of T2-relaxation time* were estimated from 3D multi-echo gradient echo (GRE) images acquired with the following parameters: TR = 75 ms, TE = 5–64.5 ms in 8.5 ms increments (8 echos), flip angle $\alpha = 25°$, and an isotropic resolution of 300 µm. The total acquisition time was 1 h and 14 min. The T2*-maps were calculated using an in-house pixel-wise mono-exponential fitting routine (MATLAB R2021a, Math Works, Natick, MA, United States).

To estimate *MTR and MTsat*, 3D single-echo GRE images (TR = 27 ms, TE = 4 ms and 300 µm isotropic resolution) with varying weightings were acquired. Weightings were achieved by applying an off-resonance saturation pulse (MT-weighted: MT flip angle = 500° and MT offset = 1,500 Hz) or by modifying the flip angle α (proton density (PD)-weighted: $\alpha = 7°$; T1-weighted: $\alpha = 20°$). The total acquisition time was 27 min per acquisition. MTsat and T1 relaxation time were calculated as described in Helms et al. (37). Since the measured T1 relaxation time reflects both intrinsic tissue properties and the effects of the imaging technique, it is referred to as the *apparent T1 relaxation time (T1app)*. T1app, T2*-relaxation time, MTR and MTsat were extracted from manually defined regions of interest (ROIs) that segmented the medial and lateral menisci. All segmentations were consistently performed by the same experienced observer on T2-weighted images using the software program ITK-SNAP.[1] The segmentation process utilized sagittal, transverse, and coronal planes as previously described (26). An example of the segmentation is shown in Supplementary Figure 1.

2.3 Statistical analysis

Statistical analyses were conducted using the Python libraries statsmodels (version 0.14.1, www.statsmodels.org), scipy (version 1.10.1, www.scipy.org), and scikit-learn (version 1.3.0, http://scikit-learn.org). To assess differences in MR parameters across the three values (0, 1, 2) of each histological score, a one-way ANOVA was performed using statsmodels.stats.anova. Given the limited sample size and deviations from normality assumptions for some parameters (scipy.stats.shapiro), the ANOVA results should be interpreted with caution and are presented here primarily for orientation purposes. To ensure transparency, individual data points are displayed in the corresponding figure, enabling readers to assess the data distribution and variability within and across groups.

Additionally, a linear regression analysis was conducted using sklearn.linear_model, and the Pearson correlation coefficient was calculated with scipy.pearsonr. The normality of the residuals from the regression analysis was evaluated using scipy.stats.shapiro.

A paired *t*-test was applied to compare findings between the medial and lateral menisci using scipy.ttest_rel. A *p*-value of less than 0.05 was considered statistically significant.

3 Results

3.1 Delineation of menisci on differently weighted images and their derived maps

Figures 1–3 illustrate the achieved image quality, all derived from the same joint. The T2*-weighted images (Figure 1, GRE) clearly separate bone from softer tissues, including muscles and cartilage. As the echo time increases, the fibrous cartilage of the menisci (red arrow) becomes progressively better delineated from the hyaline articular cartilage (blue arrow), although the signal-to-noise ratio decreases. In the *post mortem* specimen, the best contrast was observed at TE = 22 ms. The improved delineation at longer TE is attributed to the shorter T2* relaxation time of fibrous cartilage compared to hyaline articular cartilage, as further confirmed by the calculated T2* relaxation time map (Figure 1, right).

Interestingly, the macromolecule-based contrast of magnetisation transfer-weighted imaging also clearly delineates fibrous and hyaline cartilage, whereas proton density-weighted (PDw-GRE) and T1-weighted (T1w-GRE) images show very little difference (Figure 2). The higher MT in fibrous cartilage is particularly evident on the calculated maps of MTR and MTsat (Figure 3). Notably, the T1-corrected MTsat map provides even better results than MTR, offering enhanced contrast and more precise tissue delineation.

3.2 Relationship between histological scores and MR parameters

The menisci included in this study exhibited histological scores for cellularity, proteoglycan content, collagen content, and collagen organisation ranging from 0 to 2. To assess whether these mild histological alterations were reflected in the MR parameters, the measured values were initially categorised according to the corresponding histological scores for each staining (Figure 4). A one-way ANOVA was performed primarily as an exploratory tool to provide an initial overview of potential differences in the MR parameters across the three scores. Additionally, the Pearson

1 www.itksnap.org

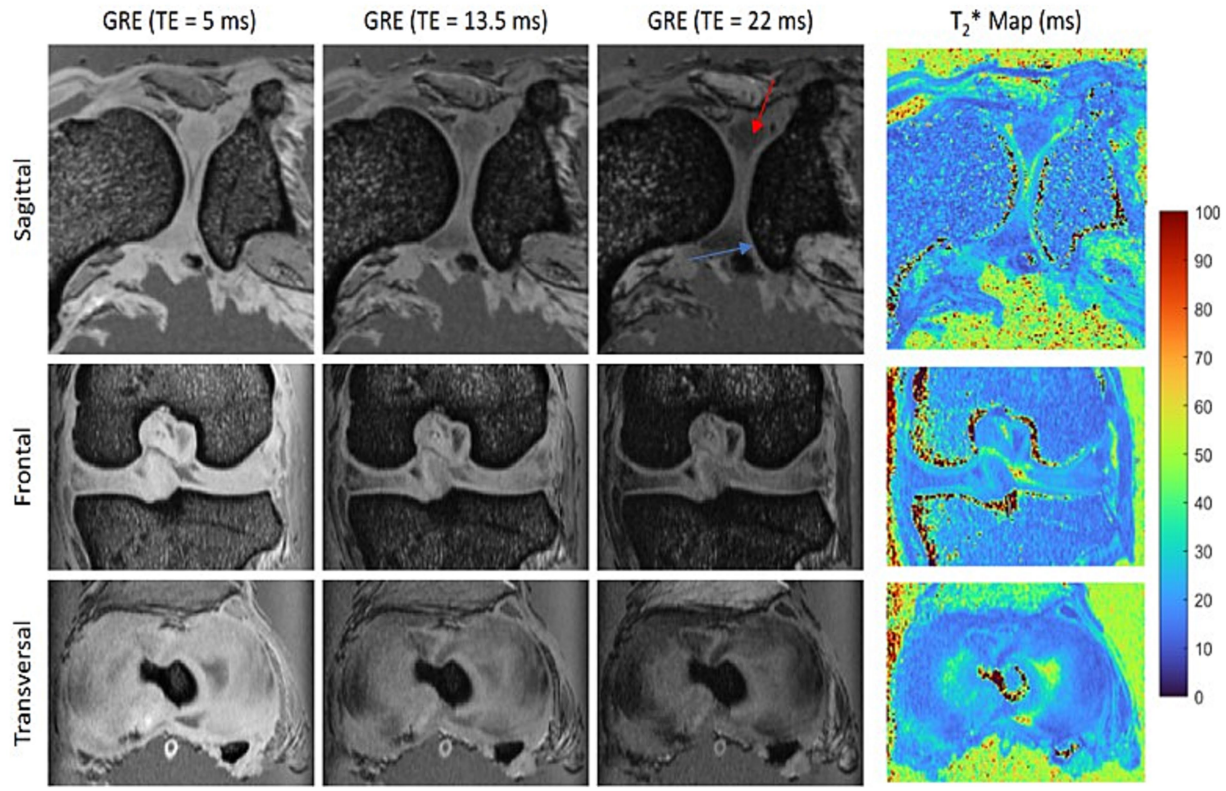

FIGURE 1
Orthogonal slices acquired with a 3D multi-gradient echo (GRE) sequence show the best contrast between the fibrous cartilage of the menisci (red arrow) and the hyaline articular cartilage (blue arrow) at an echo time (TE) of 22 ms. The corresponding T2* maps confirm the shorter T2* relaxation time of the menisci compared to the articular cartilage.

correlation coefficient was calculated to assess the relationship between each histological score and the corresponding MR parameter.

While most MR parameters did not show significant differences across individual scores, T1app decreased with increasing proteoglycan staining (ANOVA: $p < 0.003$; Pearson correlation: $r = -0.54$, $r < 0.003$) and increased with higher cellularity scores (ANOVA, $p < 0.05$, $r = 0.37$, $p < 0.05$). In contrast, MTsat values were higher in menisci with elevated proteoglycan scores (ANOVA, $p < 0.0003$, Pearson correlation: $r = 0.63$, $p < 0.0003$).

Interestingly, collagen and proteoglycan content appeared to have opposite effects on MTsat. To explore this further, we calculated the ratio of the collagen and proteoglycan scores, adjusting all values by adding one to avoid division by zero. The results are shown in Figure 5, where MTsat significantly decreased with a higher collagen-to-proteoglycan ratio ($r = -0.56$, $p < 0.002$).

To investigate a potential correlation between the severity of changes and the MRI parameters, we summarised, as previously described (26), all individual histological scores into a total score and performed a correlation analysis between the total score and the MRI parameters. When analysing the lateral and medial menisci together, none of the parameters showed a significant correlation with the total score. A separate analysis of the lateral and medial menisci indicated a potential mild negative correlation between MTR and the total score in the medial menisci, though this trend did not reach statistical significance ($r = -0.48$, $p = 0.08$, Supplementary Figure 2).

3.3 Comparison of lateral and medial menisci

Due to their restricted mobility, medial menisci are more prone to injury and may be more susceptible to degenerative changes over time (46). The histological analysis of the menisci included in this study revealed no statistically significant difference between the medial and lateral menisci (Supplementary Table 1), except for the proteoglycan score. On average, the medial menisci exhibited more intense proteoglycan staining (higher score), with greater variability between samples (paired t-test, $p = 0.006$) (Figure 6, left). To determine whether these histological differences are reflected in any of the MR parameters, the values for T2*, T1, MTR, and MTsat were analysed separately for lateral and medial menisci. None of the investigated parameters showed a significant difference, although MTR displayed a trend toward lower levels in the medial menisci (paired t-test, $p = 0.059$), as shown in Figure 6. The mean and standard deviation for each MR parameter, separated by lateral and medial menisci, are summarised in Table 1.

4 Discussion

In this *ex vivo* study, we evaluated the detectability of mild, histologically confirmed degeneration in the menisci of elderly dogs with no history of hindlimb lameness using MRI. None of the

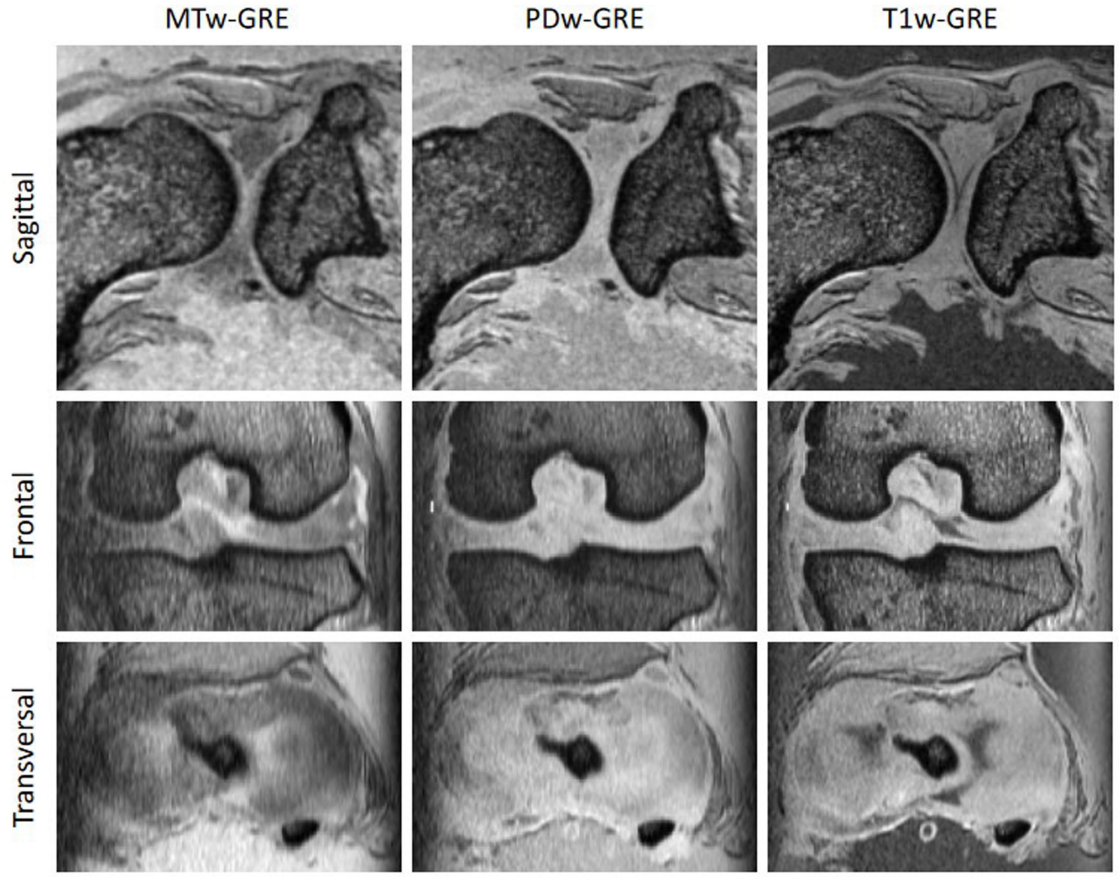

FIGURE 2
Comparison of images acquired with a 3D multi-gradient echo (GRE) proton-density weighted (PD) sequence with (MTw-GRE) and without (PDw-GRE) magnetisation transfer preparation, as well as the corresponding T1 weighted images (T1w-GRE). The macromolecule-based contrast of MTw-GRE provided the clearest delineation of fibrous and hyaline cartilage across all three orthogonal slices.

included dogs showed signs of meniscal tears or other macroscopically visible injuries. Therefore, the samples can be considered representative of canine menisci from essentially normally aged dogs. Building on our previous study, which primarily investigated T2 relaxation times (26), we broadened our analysis to include T2* and T1 relaxation times, MTR, and MTsat. Our aim was to explore the suitability of these MR parameters for identifying mild changes in tissue microstructure associated with age-related degradation. Previous MRI studies on dog stifles have mainly concentrated on T2 and T2* weighted images or the corresponding relaxation time maps (1, 20, 21). To our knowledge, this is the first study on canine menisci that has additionally incorporated magnetisation transfer techniques.

Compared to hyaline cartilage, MRI of the menisci can be more challenging. Their lower water content, dense collagen network, and restricted proton mobility lead to rapid signal attenuation due to their short T2 and T2* relaxation times (29, 47). This also applies to *post mortem* imaging, as demonstrated in this study. Increasing the echo time of a gradient echo sequence, thereby enhancing T2* weighting, improved the delineation between hyaline cartilage and the menisci. However, excessively long echo times resulted in insufficient signal intensity. Furthermore, the MTR and MTsat values of the menisci were higher than those of hyaline cartilage, likely due to their dense collagen structure, offering a promising contrast mechanism for improved delineation.

The menisci analysed in this study exhibited relatively mild degenerative changes. The highest score observed in any histological staining did not exceed 2, and the highest total score was 6 (in 2 out of 30 menisci), with 10 being the maximum possible score. Our goal was to determine whether any of the tested MR parameters could reflect these subtle structural alterations. In summary, T2* relaxation times and MTR showed no significant differences across histological scores, while T1app and MTsat correlated with certain scores. These findings will be discussed in more detail below.

T2* relaxation time has been reported to increase following meniscal tears and other injuries. For instance, Koff et al. (48) observed prolonged T2* and T2 values in menisci after surgical repair in an ovine model. However, in the case of milder alterations, the results are less clear.

Nebelung et al. (29), for example, found no significant correlation between T2* values and histological degeneration in human menisci using the Williams grading system, which considers properties such as cellularity, matrix organisation and matrix staining intensity—a finding that aligns with our observations. A

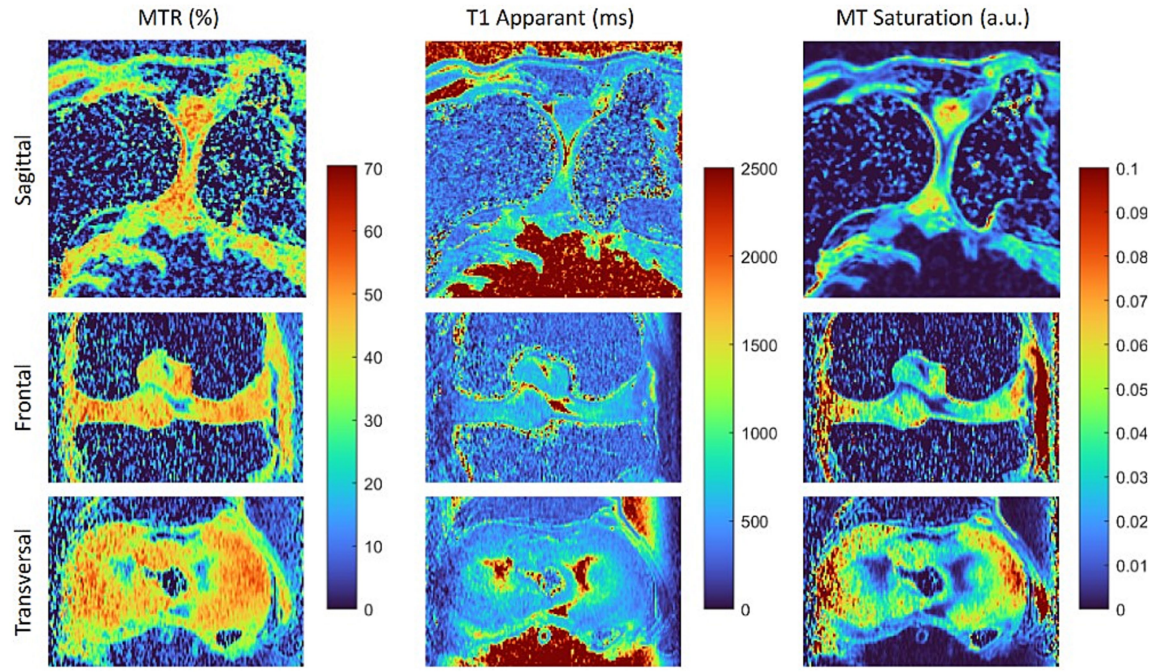

FIGURE 3
Maps of the magnetisation transfer ratio (MTR), apparent T1 relaxation time and magnetisation transfer saturation (MT saturation) calculated from the data sets shown in Figure 2. Both magnetisation transfer maps reveal differences between fibrous and hyaline cartilage, with the T1-corrected MTsat map offering enhanced contrast.

relatively mild increase in extracellular water, as opposed to the pronounced changes seen in acute injuries, combined with almost preserved fiber density and orientation, may render T2* less sensitive to detecting mild, age-related alterations. Furthermore, T2* relaxation is highly susceptible to magnetic field inhomogeneities. For example, differences in tissue fixation post mortem may overlay the effects of mild degeneration, contributing to increased standard deviation.

Interestingly, Powndner et al. (47) reported longer T2* values in the caudal horn of the medial, histologically normal menisci of healthy beagles. We did not observe any significant differences between lateral and medial menisci, although we did not analyse the horns separately. A possible reason for these differing observations could be the MR sequences used. The ultrashort echo time (UTE) imaging employed by Powndner et al. is more prone to the magic angle effect. This effect occurs when collagen fibres are orientated at approximately 55 degrees to the main magnetic field (B0), resulting in an artificially increased signal due to the decreased dipolar interaction of protons in collagen-rich tissues. The longer echo times used in our study may have minimised this effect.

Degeneration of the menisci is often accompanied by changes in collagen content and collagen organisation, making MT techniques a promising candidate for early detection. Zhang et al. reported significantly decreased MTR values in menisci from human patients with severe osteoarthritis. However, quantitative MT techniques appear to be more effective in detecting milder alterations (12). MTR can be affected by several confounding factors, including B1 inhomogeneity and T1 relaxation. It reflects both the exchange rate between free and bound protons and the recovery of longitudinal magnetisation of saturated spins. Consequently, when T1 relaxation times are shorter, the MT effect—and thus the apparent macromolecular content—may be underestimated, and vice versa (49).

The absence of significant changes in MTR in our study may be due to the relatively mild alterations in tissue properties. Additionally, the observed changes in T1 relaxation time could counterbalance the MT effect, potentially masking any detectable variations. Quantitative MT techniques aim to separate the effects of T1 relaxation from the MT effect, enabling parameters that more accurately reflect macromolecular content, such as the macromolecular fraction (MMF) or bound proton fraction (BPF).

Interestingly, Li et al. reported an increase in BPF associated with higher GAG levels in engineered cartilage (32), which aligns with our findings. The toluidine blue, which we used in this study to assess the amount of proteoglycans semi-quantitively, binds to the acidic GAGs within the proteoglycans. We found that menisci with increased proteoglycan staining showed higher MTsat values, a marker for magnetisation transfer that is corrected for T1 relaxation (37).

The role of GAGs in the pathobiology of meniscal tissue remains debated, especially in dogs, with limited data available. Inflammatory processes may increase enzymes like matrix metalloproteinases (MMPs) and aggrecanase, leading to a reduction in proteoglycan content. Conversely, there may be an initial rise in proteoglycan synthesis as the tissue attempts to repair, accompanied by the inhibition of degrading enzymes to support recovery (50, 51).

Notably, T1 relaxation time decreased with more intense proteoglycan staining and increased with higher cellularity scores, suggesting its potential for distinguishing between degenerative (reduced proteoglycan content, fibroblast-like cells) and regenerative processes (increased cellular activity and proteoglycan production) in the meniscus. Another promising diagnostic parameter may be the

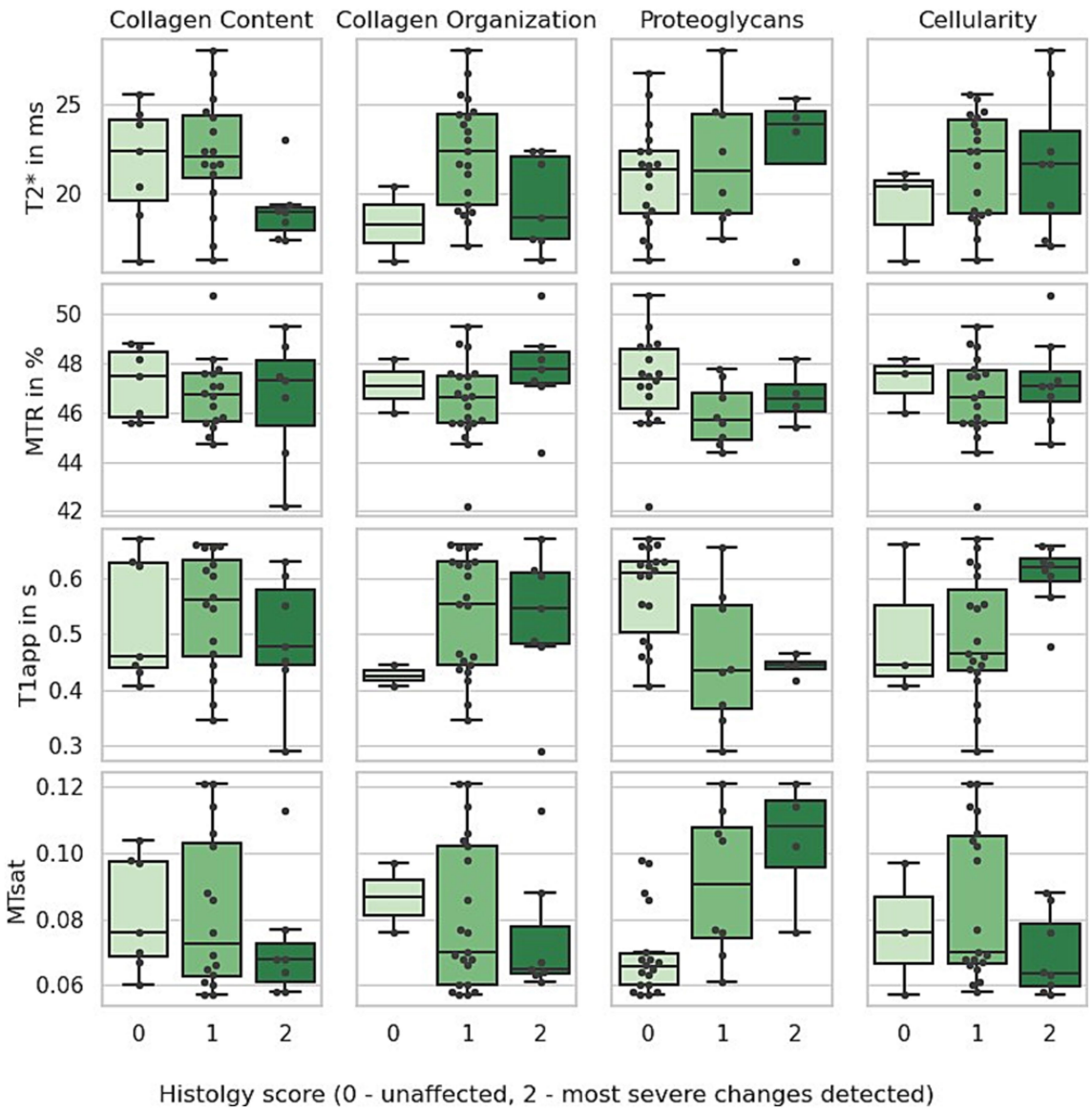

FIGURE 4
Boxplot of MRI parameters across different histological scores. The apparent T1 relaxation time (T1app) is shorter in menisci with increased proteoglycan staining and longer in those with increased cellularity score. In contrast, MTsat values (magnetisation transfer saturation) are higher in menisci with elevated proteoglycan scores.

collagen-to-proteoglycan ratio, as a decrease in this ratio was linked to lower MTsat values. However, further studies involving menisci with a broader range of pathological lesions are needed to validate these findings. Future research should also compare MTsat and T1app directly with T1ρ in relation to the collagen-to-proteoglycan ratio, given T1ρ's sensitivity to proteoglycan loss.

Besides the limitation of including only menisci with relatively mild changes and not having either healthy or severely affected menisci involved, the applied histological scoring system may also limit the correlation between MRI and histological findings. More quantitative, continuous readouts would be preferable. Further studies aim to address these limitations by including a broader range of pathological changes, a larger sample size, additional histological methods and separate analyses of the meniscal body and horns.

Another limitation of this study is that all measurements were conducted *post mortem* on formalin-fixed tissue. Formalin affects the tissue's hydration state and thereby influences relaxation times (26, 29, 52). Additionally, measurements were performed at room temperature, which is lower than body temperature and impacts several MRI-relevant properties, such as exchange rate, diffusivity, and T1 relaxation time (53). On the other hand, *post mortem* MRI studies offer the advantage of longer measurement times, allowing for higher spatial resolution and the simultaneous use of multiple contrast mechanisms. So, this approach can be used to test a wide range of MR contrasts, with the most promising ones then applied and validated *in vivo*.

Finally, it should be noted that MR parameters are influenced by various factors, leading to limited overall specificity when

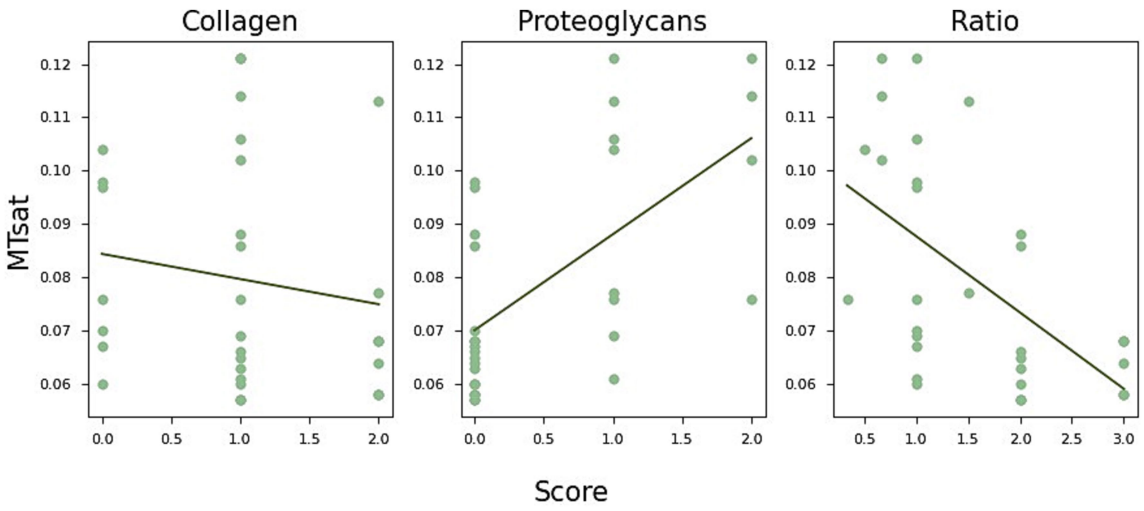

FIGURE 5
MTsat (magnetisation transfer saturation) values in relation to collagen and proteoglycan content. Collagen and proteoglycan scores appear to have opposite effects on MTsat. Specifically, MTsat tends to decrease with lower collagen content ($r = -0.16$, $p = 0.43$), while it increases with increased proteoglycan staining ($r = 0.62$, $p < 0.0003$). This relationship is further reflected in lower MTsat values associated with a reduced collagen-to-proteoglycan ratio (left, $r = -0.56$, $p < 0.002$).

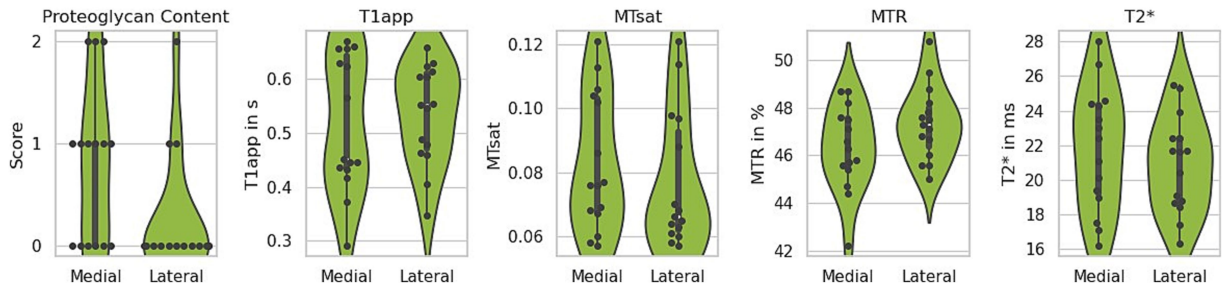

FIGURE 6
Comparison of lateral and medial menisci. The medial menisci exhibited more intense proteoglycan staining (higher score) and greater variability between the analysed samples. Among the quantitative MRI parameters, only the magnetisation transfer ratio (MTR) indicated a potential difference, showing a trend toward lower values in the medial menisci. T1app – apparent T1 relaxation time, MTsat – magnetisation transfer saturation.

TABLE 1 Mean values and standard deviations (SD) of the respective magnetic resonance (MR) parameters (MTR – magnetisation transfer ratio, T1app – apparent T1 relaxation time, MTsat – magnetisation transfer saturation) in the medial and lateral menisci.

MR parameter	Medial menisci (mean ± SD)	Lateral menisci (mean ± SD)	*p*-value
MTR	46.3 ± 1.7 ms	47.4 ± 1.5 ms	0.06
T1app	517 ± 121 ms	536 ± 88 ms	0.56
MTsat	0.08 ± 0.02 ms	0.08 ± 0.02 ms	0.24
T2*	21.8 ± 3.4 ms	20.9 ± 0.7 ms	0.27

A paired *t*-test was applied to assess significant differences, and the corresponding *p*-values are provided.

detecting subtle or complex tissue changes. To achieve a more comprehensive characterization of meniscal degeneration—an essential factor in guiding therapeutic decisions—future studies should not only assess multiple MR parameters but also investigate their combined use. This integration could significantly enhance diagnostic specificity and precision. Based on our results, MTsat and T1app emerge as particularly promising parameters for future in vivo studies, which should encompass a broad spectrum of meniscal alterations, extending beyond age-related changes in canine menisci.

5 Conclusion

In summary, none of the investigated contrast mechanisms showed high sensitivity or specificity for detecting mild changes in the

tissue microstructure of canine menisci, as assessed by histological analyses using the modified scoring systems of Pauli (45) and Sun (44). However, the observed correlation between MTsat and proteoglycan content may be a promising candidate for characterising the extracellular matrix, though further studies are needed to validate this effect.

Data availability statement

The raw data supporting the conclusions of this article will be made available by the authors, without undue reservation.

Ethics statement

Ethical approval was not required for this study involving animals in accordance with local legislation and institutional requirements, as only cadaver dogs were used. These dogs were euthanised in our clinic due to incurable diseases to prevent further suffering, not for scientific purposes. Written informed consent was not obtained as the dogs were provided by their owners for disposal.

Author contributions

LB: Conceptualization, Data curation, Methodology, Visualization, Writing – original draft, Resources. AM: Conceptualization, Formal analysis, Methodology, Visualization, Software, Supervision, Writing – review & editing, Validation. MB: Methodology, Software, Supervision, Writing – review & editing, Project administration. SN: Writing – review & editing, Project administration, Resources. SB: Conceptualization, Formal analysis, Methodology, Writing – original draft, Investigation, Software, Supervision, Writing – review & editing, Resources.

Funding

The author(s) declare that financial support was received for the research and/or publication of this article. We acknowledge support for publication by the Open Access Publication Funds of the Göttingen University.

Conflict of interest

The authors declare that the research was conducted in the absence of any commercial or financial relationships that could be construed as a potential conflict of interest.

Generative AI statement

The author(s) declare that no Generative AI was used in the creation of this manuscript.

Publisher's note

Supplementary material

The Supplementary material for this article can be found online at: https://www.frontiersin.org/articles/10.3389/fvets.2025.1521684/full#supplementary-material

References

1. Powndner SL, Hayashi K, Caserto BG, Breighner RE, Norman ML, Potter HG, et al. Quantitative magnetic resonance imaging and histological comparison of Normal canine menisci. *Vet Comp Orthop Traumatol.* (2018) 31:452–7. doi: 10.1055/s-0038-1668115

2. McDermott I. Meniscal tears, repairs and replacement: their relevance to osteoarthritis of the knee. *Br J Sports Med.* (2011) 45:292–7. doi: 10.1136/bjsm.2010.081257

3. Hu J, Xin H, Chen Z, Zhang Q, Peng Y, Jin Z. The role of menisci in knee contact mechanics and secondary kinematics during human walking. *Clin Biomech (Bristol, Avon).* (2019) 61:58–63. doi: 10.1016/j.clinbiomech.2018.11.009

4. Fox AJS, Wanivenhaus F, Burge AJ, Warren RF, Rodeo SA. The human meniscus: a review of anatomy, function, injury, and advances in treatment. *Clin Anat.* (2015) 28:269–87. doi: 10.1002/ca.22456

5. Zarins ZA, Bolbos RI, Pialat JB, Link TM, Li X, Souza RB, et al. Cartilage and meniscus assessment using T1rho and T2 measurements in healthy subjects and patients with osteoarthritis. *Osteoarthr Cartil.* (2010) 18:1408–16. doi: 10.1016/j.joca.2010.07.012

6. Lee W, Miller EY, Zhu H, Luetkemeyer CM, Schneider SE, Neu CP. High frame rate deformation analysis of knee cartilage by spiral dualMRI and relaxation mapping. *Magn Reson Med.* (2023) 89:694–709. doi: 10.1002/mrm.29487

7. Welsch GH, Apprich S, Zbyn S, Mamisch TC, Mlynarik V, Scheffler K, et al. Biochemical (T2, T2* and magnetisation transfer ratio) MRI of knee cartilage: feasibility at ultra-high field (7T) compared with high field (3T) strength. *Eur Radiol.* (2011) 21:1136–43. doi: 10.1007/s00330-010-2029-7

8. Mittal S, Pradhan G, Singh S, Batra R. T1 and T2 mapping of articular cartilage and menisci in early osteoarthritis of the knee using 3-tesla magnetic resonance imaging. *Pol J Radiol.* (2019) 84:549–e564. doi: 10.5114/pjr.2019.91375

9. Eijgenraam SM, Bovendeert FAT, Verschueren J, van Tiel J, Bastiaansen-Jenniskens YM, Wesdorp MA, et al. T2 mapping of the meniscus is a biomarker for early osteoarthritis. *Eur Radiol.* (2019) 29:5664–72. doi: 10.1007/s00330-019-06091-1

10. Hofmann FC, Neumann J, Heilmeier U, Joseph GB, Nevitt MC, McCulloch CE, et al. Conservatively treated knee injury is associated with knee cartilage matrix degeneration measured with MRI-based T2 relaxation times: data from the osteoarthritis initiative. *Skeletal Radiol.* (2018) 47:93–106. doi: 10.1007/s00256-017-2759-6

11. Banjar M, Horiuchi S, Gedeon DN, Yoshioka H. Review of quantitative knee articular cartilage MR imaging. *Magn Reson Med Sci.* (2022) 21:29–40. doi: 10.2463/mrms.rev.2021-0052

12. Zhang X, Ma Y-J, Wei Z, Wu M, Ashir A, Jerban S, et al. Macromolecular fraction (MMF) from 3D ultrashort echo time cones magnetization transfer (3D UTE-cones-MT) imaging predicts meniscal degeneration and knee osteoarthritis. *Osteoarthr Cartil.* (2021) 29:1173–80. doi: 10.1016/j.joca.2021.04.004

13. Labruyère J, Schwarz T. CT and MRI in veterinary patients: an update on recent advances. *In Pract.* (2013) 35:546–63. doi: 10.1136/inp.f6720

14. Gavin PR. Growth of clinical veterinary magnetic resonance imaging. *Vet Radiol Ultrasound.* (2011) 52:S2–4. doi: 10.1111/j.1740-8261.2010.01779.x

15. Arno S, Bell CP, Xia D, Regatte RR, Krasnokutsky S, Samuels J, et al. Relationship between meniscal integrity and risk factors for cartilage degeneration. *Knee.* (2016) 23:686–91. doi: 10.1016/j.knee.2015.11.004

16. Mosher TJ, Liu Y, Torok CM. Functional cartilage MRI T2 mapping: evaluating the effect of age and training on knee cartilage response to running. *Osteoarthr Cartil.* (2010) 18:358–64. doi: 10.1016/j.joca.2009.11.011

17. Mamisch TC, Hughes T, Mosher TJ, Mueller C, Trattnig S, Boesch C, et al. T2 star relaxation times for assessment of articular cartilage at 3 T: a feasibility study. *Skeletal Radiol*. (2012) 41:287–92. doi: 10.1007/s00256-011-1171-x

18. Li X, Han ET, Ma CB, Link TM, Newitt DC, Majumdar S. In vivo 3T spiral imaging based multi-slice T(1rho) mapping of knee cartilage in osteoarthritis. *Magn Reson Med*. (2005) 54:929–36. doi: 10.1002/mrm.20609

19. Hontoir F, Pirson R, Simon V, Clegg P, Nisolle J-F, Kirschvink N, et al. Age-related morphometric changes of the tidemark in the ovine stifle. *Anat Histol Embryol*. (2019) 48:366–74. doi: 10.1111/ahe.12449

20. Pownder SL, Hayashi K, Caserto BG, Norman ML, Potter HG, Koff MF. Magnetic resonance imaging T2 values of stifle articular cartilage in Normal beagles. *Vet Comp Orthop Traumatol*. (2018) 31:108–13. doi: 10.3415/VCOT-17-03-0093

21. Harper TAM, Jones JC, Saunders GK, Daniel GB, Leroith T, Rossmeissl E. Sensitivity of low-field T2 images for detecting the presence and severity of histopathologic meniscal lesions in dogs. *Vet Radiol Ultrasound*. (2011) 52:428–35. doi: 10.1111/j.1740-8261.2011.01818.x

22. McDevitt CA, Webber RJ. The ultrastructure and biochemistry of meniscal cartilage. *Clin Orthop Relat Res*. (1990) 252:8???18. doi: 10.1097/00003086-199003000-00003

23. AufderHeide AC, Athanasiou KA. Mechanical stimulation toward tissue engineering of the knee meniscus. *Ann Biomed Eng*. (2004) 32:1163–76. doi: 10.1114/b:abme.0000036652.31658.f3

24. Aidos L, Modina SC, Millar VRH, Peretti GM, Mangiavini L, Ferroni M, et al. Meniscus matrix structural and biomechanical evaluation: age-dependent properties in a swine model. *Bioengineering (Basel)*. (2022) 9:117. doi: 10.3390/bioengineering9030117

25. Abraham AC, Edwards CR, Odegard GM, Donahue TLH. Regional and fiber orientation dependent shear properties and anisotropy of bovine meniscus. *J Mech Behav Biomed Mater*. (2011) 4:2024–30. doi: 10.1016/j.jmbbm.2011.06.022

26. Bunzendahl L, Moussavi A, Bleyer M, Dehnert J, Boretius S, Neumann S. Histological findings and T2 relaxation time in canine menisci of elderly dogs-an ex vivo study in stifle joints. *Vet Sci*. (2023) 10:182. doi: 10.3390/vetsci10030182

27. Berg RC, Leutritz T, Weiskopf N, Preibisch C. Multi-parameter quantitative mapping of R1, R2*, PD, and MTsat is reproducible when accelerated with compressed SENSE. *NeuroImage*. (2022) 253:119092. doi: 10.1016/j.neuroimage.2022.119092

28. Tofts P. Quantitative MRI of the brain: measuring changes caused by disease. John Wiley & Sons (2003) doi: 10.1002/0470869526

29. Nebelung S, Tingart M, Pufe T, Kuhl C, Jahr H, Truhn D. Ex vivo quantitative multiparametric MRI mapping of human meniscus degeneration. *Skeletal Radiol*. (2016) 45:1649–60. doi: 10.1007/s00256-016-2480-x

30. Regatte RR, Akella SVS, Wheaton AJ, Lech G, Borthakur A, Kneeland JB, et al. 3D-T1rho-relaxation mapping of articular cartilage: in vivo assessment of early degenerative changes in symptomatic osteoarthritic subjects. *Acad Radiol*. (2004) 11:741–9. doi: 10.1016/j.acra.2004.03.051

31. Brandt KD, Radin EL, Dieppe PA, van de Putte L. Yet more evidence that osteoarthritis is not a cartilage disease. *Ann Rheum Dis*. (2006) 65:1261–4. doi: 10.1136/ard.2006.058347

32. Li W, Hong L, Hu L, Magin RL. Magnetization transfer imaging provides a quantitative measure of chondrogenic differentiation and tissue development. *Tissue Eng Part C Methods*. (2010) 16:1407–15. doi: 10.1089/ten.tec.2009.0777

33. Mehta RC, Pike GB, Enzmann DR. Improved detection of enhancing and nonenhancing lesions of multiple sclerosis with magnetization transfer. *AJNR Am J Neuroradiol*. (1995) 16:1771–8.

34. Ropele S, Fazekas F. Magnetization transfer MR imaging in multiple sclerosis. *Neuroimaging Clin N Am*. (2009) 19:27–36. doi: 10.1016/j.nic.2008.09.004

35. Gray ML, Burstein D, Lesperance LM, Gehrke L. Magnetization transfer in cartilage and its constituent macromolecules. *Magn Reson Med*. (1995) 34:319–25. doi: 10.1002/mrm.1910340307

36. Olsson H, Andersen M, Wirestam R, Helms G. Mapping magnetization transfer saturation (MTsat) in human brain at 7T: protocol optimization under specific absorption rate constraints. *Magn Reson Med*. (2021) 86:2562–76. doi: 10.1002/mrm.28899

37. Helms G, Dathe H, Kallenberg K, Dechent P. High-resolution maps of magnetization transfer with inherent correction for RF inhomogeneity and T1 relaxation obtained from 3D FLASH MRI. *Magn Reson Med*. (2008) 60:1396–407. doi: 10.1002/mrm.21732

38. Grabher P, Callaghan MF, Ashburner J, Weiskopf N, Thompson AJ, Curt A, et al. Tracking sensory system atrophy and outcome prediction in spinal cord injury. *Ann Neurol*. (2015) 78:751–61. doi: 10.1002/ana.24508

39. Lema A, Bishop C, Malik O, Mattoscio M, Ali R, Nicholas R, et al. A comparison of magnetization transfer methods to assess brain and cervical cord microstructure in multiple sclerosis. *J Neuroimaging*. (2017) 27:221–6. doi: 10.1111/jon.12377

40. Leutritz T, Seif M, Helms G, Samson RS, Curt A, Freund P, et al. Multiparameter mapping of relaxation (R1, R2 *), proton density and magnetization transfer saturation at 3 T: a multicenter dual-vendor reproducibility and repeatability study. *Hum Brain Mapp*. (2020) 41:4232–47. doi: 10.1002/hbm.25122

41. Weiskopf N, Suckling J, Williams G, Correia MM, Inkster B, Tait R, et al. Quantitative multi-parameter mapping of R1, PD*, MT, and R2* at 3T: a multi-center validation. *Front Neurosci*. (2013) 7:95. doi: 10.3389/fnins.2013.00095

42. Diekmann H.U. Analysis of the pathogenesis and progression of osteoarthritis in canine stifle joints considering three bone healing markers [Internet]. [Hannover]: Tierärztliche Hochschule Hannover. (2018) Available at: https://nbn-resolving.org/urn:nbn:de:gbv:95-111906.

43. Kellgren JH, Lawrence JS. Radiological assessment of osteo-arthrosis. *Ann Rheum Dis*. (1957) 16:494–502. doi: 10.1136/ard.16.4.494

44. Sun Y, Mauerhan DR, Kneisl JS, James Norton H, Zinchenko N, Ingram J, et al. Histological examination of collagen and proteoglycan changes in osteoarthritic menisci. *Open Rheumatol J*. (2012) 6:24–32. doi: 10.2174/1874312901206010024

45. Pauli C, Grogan SP, Patil S, Otsuki S, Hasegawa A, Koziol J, et al. Macroscopic and histopathologic analysis of human knee menisci in aging and osteoarthritis. *Osteoarthr Cartil*. (2011) 19:1132–41. doi: 10.1016/j.joca.2011.05.008

46. Flo GL. Meniscal injuries. *Vet Clin North Am Small Anim Pract*. (1993) 23:831–43. doi: 10.1016/s0195-5616(93)50085-2

47. Williams A, Qian Y, Golla S, Chu CR. UTE-T2∗ mapping detects sub-clinical meniscus injury after anterior cruciate ligament tear. *Osteoarthr Cartil*. (2012) 20:486–94. doi: 10.1016/j.joca.2012.01.009

48. Koff MF, Shah P, Pownder S, Romero B, Williams R, Gilbert S, et al. Correlation of meniscal T2* with multiphoton microscopy, and change of articular cartilage T2 in an ovine model of meniscal repair. *Osteoarthr Cartil*. (2013) 21:1083–91. doi: 10.1016/j.joca.2013.04.020

49. Henkelman RM, Stanisz GJ, Graham SJ. Magnetization transfer in MRI: a review. *NMR Biomed*. (2001) 14:57–64. doi: 10.1002/nbm.683

50. López-Franco M, Gómez-Barrena E. Cellular and molecular meniscal changes in the degenerative knee: a review. *J Exp Orthop*. (2018) 5:11. doi: 10.1186/s40634-018-0126-8

51. Krupkova O, Smolders L, Wuertz-Kozak K, Cook J, Pozzi A. The pathobiology of the Meniscus: a comparison between the human and dog. *Front Vet Sci*. (2018) 5:73. doi: 10.3389/fvets.2018.00073

52. Son M, Goodman SB, Chen W, Hargreaves BA, Gold GE, Levenston ME. Regional variation in T1ρ and T2 times in osteoarthritic human menisci: correlation with mechanical properties and matrix composition. *Osteoarthr Cartil*. (2013) 21:796–805. doi: 10.1016/j.joca.2013.03.002

53. Noeske R. Anwendung der Hochfeld-(3-Tesla)-NMR-Tomographie Freie Universität Berlin (2000). Available at: http://www.diss.fu-berlin.de/2000/126/index.html

frontiers | Frontiers in Veterinary Science

TYPE Original Research
PUBLISHED 13 March 2025
DOI 10.3389/fvets.2025.1521986

OPEN ACCESS

EDITED BY
Ozan Gündemir,
Istanbul University Cerrahpasa, Türkiye

REVIEWED BY
Howard Dobson,
Invicro (United States), United States
Dominic Gascho,
University of Zurich, Switzerland

*CORRESPONDENCE
Manon Mikić
✉ Manon.mikic@tiho-hannover.de

†These authors have contributed equally to this work

RECEIVED 03 November 2024
ACCEPTED 26 February 2025
PUBLISHED 13 March 2025

CITATION
Mikić M, Lietz P, Dierig J-A, Meller S, Pees M and Merhof K (2025) Evaluation of virtual non-contrast detector-based spectral CT images in comparison to true unenhanced images in 20 rabbits.
Front. Vet. Sci. 12:1521986.
doi: 10.3389/fvets.2025.1521986

Evaluation of virtual non-contrast detector-based spectral CT images in comparison to true unenhanced images in 20 rabbits

Manon Mikić[1*†], Philipp Lietz[1†], Julie-Ann Dierig[2], Sebastian Meller[1], Michael Pees[2] and Kristina Merhof[1]

[1]Clinic for Small Animals, University of Veterinary Medicine, Hannover, Germany, [2]Department of Small Mammal, Reptile and Avian Medicine and Surgery, University of Veterinary Medicine, Hannover, Germany

Introduction: Spectral detector Computed Tomography (SDCT) enables generation of virtual non-contrast (VNC) images derived from a post-contrast scan, as previously investigated in healthy dogs. This technique is especially promising for awake scanned rabbits where motion between the pre- and the post-contrast scans makes comparison challenging. This study aimed to determine the reliability of VNC images for assessing abdominal organs in 20 rabbits by evaluating their qualitative and quantitative parameters compared to true unenhanced (TUE) images. Our hypothesis were that the VNC series would be comparable to TUE series and that the quality of the VNC images would be equal to or even superior to the native images.

Methods: Attenuation values of VNC and TUE series were assessed using a two one-sided t-test (TOST) and the signal-to-noise ratio was calculated for each ROI in the different series. Additionally, a qualitative assessment of the VNC images relative to TUE images was performed in consensus by a board-certified radiologist and a second year diagnostic imaging resident by evaluating the iodine subtraction, image quality and noise of VNC images based on a 5-point Likert scale.

Results: A total of 219 regions of interest (ROIs) where drawn in abdominal organs. 72.1% of the ROIs displayed differences of less than 15 Hounsfield Units (HU) between TUE and VNC images. The differences in attenuation values of TUE and VNC were statistically significant ($p < 0.05$) for ≤ 5 HU in the spleen, for ≤ 10 HU and ≤ 15 HU additionally in the liver, musculature and renal cortices. These findings support the equivalence between VNC and TUE images. An average score of 4.4 was achieved for iodine subtraction across all patients, which encompasses all organ values, with no individual patient scoring below 4.0.

Discussion: VNC images present a promising alternative to TUE images for abdominal organs without pathology in rabbits with the benefit of eliminating motion between the compared series and reducing examination time and radiation exposure by replacing pre-contrast scans. Further research is necessary to demonstrate the applicability of the technique to morphologically diseased organs.

KEYWORDS

virtual non-contrast (VNC), computed tomography, rabbits, detector-based spectral CT, true unenhanced images

1 Introduction

In recent years, a significant increase in the number of pet rabbits in European households has been noted (1). In the United Kingdom, rabbits constitute approximately 2% of the total pet population, including dogs, cats, rabbits and other species (2). Correspondingly, there has been a noted rise in the frequency of veterinary visits and the amount of diagnostic procedures performed (3). The use of computed tomography (CT) of various diseases for these patients is becoming the standard of care due to the ability to produce multiplanar reconstructions, to evaluate structures without superimposition and due to the high spatial resolution (1, 3–9). The scans can be performed while the patient is conscious which is especially interesting for rabbits as their anesthetic risk is higher compared to our canine patients (10). However, due to the low soft tissue contrast of true unenhanced images (TUE), iodinated contrast medium is frequently administered and offers a higher diagnostic value (11, 12). The use of intravenous iodinated contrast medium is well-tolerated and safe in rabbits (13). Potential movement during the scans can lead to streak artefacts but movement between the pre- and post-contrast scans often poses an additional challenge, potentially limiting the comparability of the scans (14). Dual-energy CT (DECT) has the ability to differentiate materials of different effective atomic numbers with comparable Hounsfield units (HUs) in conventional CT studies by a separate assessment of low and high-energy attenuation profiles (11, 15). Technically, this concept can be achieved in different ways. In the case of detector-based spectral DECT technology, two different layers of scintillator detectors are employed. The upper layer of the detector exhibits absorptive properties regarding low-energy photons while exhibiting permeability to high-energy photons, which are absorbed by the lower layer. This results in the generation of low- and high-energy images, and through weighted summation, full-spectrum images are calculated. The spectral data are automatically generated with each scan without the need to modify the scan parameters (16). With the aid of post-processing algorithms, iodine-containing voxels can be identified to create virtual non-contrast (VNC) images. In case the quality of VNC images proves to be sufficient in the future, pre-contrast scans could potentially be omitted (12, 15). The limitations caused by motion artefacts between the pre and post-contrast scan could thus be eliminated and the radiation dose and examination time for patients could be reduced by 50% due to the absence of the pre-contrast scan. Various studies in human medicine (11, 12, 16–18), as well as one veterinary study (19), have demonstrated good to excellent comparability between VNC and TUE images. These studies employed various comparison methods, including subjective assessments of the series and objective analyses of spectral detector computed tomography (SDCT) quality parameters such as signal-to-noise ratio (SNR), contrast-to-noise ratio, edge sharpness, and equivalence of Hounsfield Units (HUs) of identical regions of interest (ROIs) in congruent image material. The authors are not aware of any studies that have applied this technique to rabbits.

The objective of this study therefore was to assess the comparability of TUE and VNC images based on measurements in various abdominal organs and to assess the reliability of VNC images. We hypothesized that (a) the calculated VNC series would not significantly differ from the TUE series, and (b) that the quality of the VNC images would be equal or superior to that of the TUE images.

2 Materials and methods

This was a retrospective, single-institutional study. Institutional and medical image archives were searched from March 2023 to April 2024 for rabbits that had undergone a full body or at least abdominal CT study at the Clinic for Small Animals of the University of Veterinary Medicine Hannover, Germany, using a spectral dual-energy CT scanner (Philips IQon Spectral CT, Philips Healthcare Germany). Rabbits were included in the study if (a) a standardized SDCT protocol with complete pre-and post-contrast scans of the patients were obtained, (b) the CT study was of diagnostic quality and (c) a complete signalment including age, sex, neuter status, body weight, and reason for presentation was available. All patients were scanned consciously and placed into a device designed to minimize movement. Patients with incomplete abdominal CT scans, lacking post-contrast studies or severe motion artefacts were excluded. Additionally, patients with pathological imaging findings in the liver, spleen, kidneys, paraspinal musculature, aorta, caudal vena cava, abdominal fat, or within the urinary bladder were excluded. Patients were also excluded if a corresponding region of interest (ROI) with a minimum size of five square millimetres could not be drawn. All cases were collected by a second-year resident of diagnostic imaging (M.M.) and confirmed in consensus with a board-certified veterinary radiologist (K.M.).

2.1 SDCT protocol

All examinations included an initial true unenhanced (TUE) series, followed by a venous phase with the conscious patient positioned head first in prone recumbency. SDCT scans were acquired using an automated adapted tube current, a tube potential of 120–140 kV, a pitch of 0.4, a gantry rotation time of 1 s, a slice thickness of 0.9 mm, and a 512 × 512 image matrix. The volume computed tomography dose index ($CTDI_{vol}$) of the scans ranged between 36.6 and 51.9 mGy, while the scan size of the rabbits varied from 11.2 to 26.4 cm. Scans were performed following a standardized abdominal protocol, employing both soft tissue (HB) and bone kernels (YC) with appropriate bone window settings (window length: 800; window width: 2000) and soft tissue window settings (window length: 60; window width: 350). Post-contrast CT scans were obtained approximately 60 s after the manual intravenous administration of non-ionic contrast media into the auricular vein. Each patient received 700 mg iopamidol/kg bodyweight [2.3 mL/kg of Solutrast®300, Bracco Imaging Deutschland GmbH, Konstanz, Germany].

2.2 Quantitative image analysis

All images were analyzed by a second-year diagnostic imaging resident (M.M.) on a computer workstation equipped with system-associated software (IntelliSpace Portal Version 11.x/Philips Healthcare) and a calibrated flat-panel Retina display monitor (HP Deutschland GmbH, Boeblingen, Germany) certified for image analysis. In the first step, VNC images were reconstructed from the provided spectral data using system-specific software. The image series of conventional TUE, conventional post-contrast and VNC images of the abdomen were then linked and synchronized to allow

for an exact comparison of the sections. In cases where synchronization of the series failed due to patient movement between scans, manual adjustment of the image pairing was performed. The images were examined exclusively in a soft tissue window (window level: 60; window width: 350). Adjustments to the windowing were permitted for the reviewer. In the subsequent phase of the process, multiple circular regions of interest were drawn in the TUE images in seven different organs. Wherever feasible, ROIs were sized at 100 $mm^2 \pm 2$ mm^2. If this size was not applicable to an organ to avoid including extraneous structures (such as in the spleen, aorta and renal cortex), the largest possible circular ROI was selected. The ROIs needed to have a minimum of five square millimetres. The ROIs were then transferred to the paired post-contrast and VNC images using copy/paste, ensuring that both the location and size of the ROIs were identical (Figure 1). The following locations were selected for analysis:

1 Liver (2 ROIs, avoiding larger vessels: in right and left liver lobes).
2 Spleen (2 ROIs).
3 Renal cortex bilaterally (1 ROI each).
4 Abdominal aorta (1 ROI) at the level of the diaphragm.
5 Paravertebral muscles (1 ROI each right and left, at the level of the transition between the 13th thoracic and first lumbar vertebrae).
6 Intra-abdominal fat (1 ROI).
7 Urinary bladder (1 ROI).

The different average HUs were documented for each paired ROI measurement in the VNC and TUE images, whereby the HUs of the ROIs were automatically averaged. Based on a categorization derived from medical studies (11, 16, 17) and a preceding study by the authors (19), the data were classified into four distinct groups.

1 Difference between VNC_{HU} and TUE_{HU} = ≤ 5 HU
2 Difference between VNC_{HU} and TUE_{HU} = ≤ 10 HU
3 Difference between VNC_{HU} and TUE_{HU} = ≤ 15 HU
4 Difference between VNC_{HU} and TUE_{HU} = > 15 HU

2.3 Qualitative image analysis

The qualitative analysis included the assessment of image quality and noise, as well as the efficiency of iodine subtraction. The analysis was performed in consensus by a board-certified veterinary radiologist (K.M.) and a second-year diagnostic imaging resident (M.M.). Image quality was assessed by comparing the overall appearance of the gastrointestinal tract, hepatic and splenic parenchyma, kidneys, paraspinal musculature, urinary bladder and major vessels (aorta and caudal vena cava) in paired TUE and VNC images using a 5-point Likert scale (Table 1).

The efficiency of iodine subtraction in VNC images was evaluated by direct comparison with the paired conventional pre- and post-contrast images using a modified 5-point Likert scale (Table 2).

2.4 Statistical methods

Dedicated software was used for statistical data evaluation and visualization (Microsoft® Excel, GraphPad Prism 10). VNC and TUE images of each organ or tissue were grouped and compared by subtracting the HU of every ROI in VNC from the corresponding ROI in the TUE images. If multiple ROIs per organ were used, the differences between values in VNC and TUE images were averaged. The equivalence between the VNC and TUE series was tested using a two-one-sided t-test (TOST) with an opposing null hypothesis. This null hypothesis assumed a difference between VNC and TUE images, with deviation limits of ≤5, ≤10, or ≤ 15 HUs. If this hypothesis was significantly rejected ($p \leq 0.05$), equivalence between both techniques within the specific deviation limit was assumed, thereby confirming the original study hypothesis. The distribution of animals with HU differences within the corresponding limits was also calculated for each organ system or tissue as a percentage. Additionally, a qualitative analysis of the VNC and TUE data was conducted by documenting the mean values for each patient and individual organs by two observers (M.M. and K.M.) in consensus, as described in the section of qualitative analysis. To investigate relationships between the weight of animals and the differences between TUE and VNC values, Pearson correlations

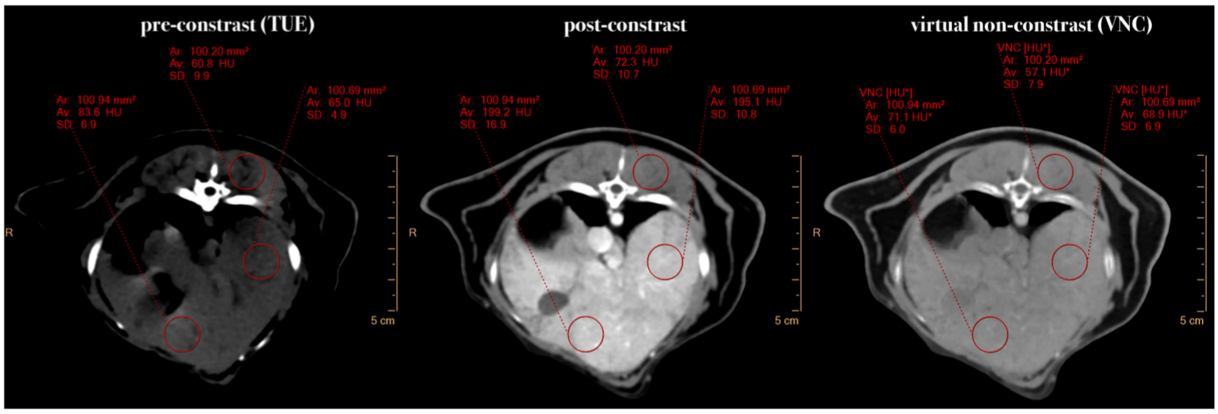

FIGURE 1
Comparative presentation of synchronized pre-contrast (TUE), post-contrast, and virtual non-contrast (VNC) images in the transverse plane. If it was not possible to draw a ROI of 100mm^2, the ROI size was chosen to be "as large as possible." Note the HU differences of ≤15 HU in the liver and ≤10 HU in the musculature between TUE and VNC images.

TABLE 1 Modified five-point-likert-scale for assessment of image noise and quality in VNC compared to TUE images.

Image noise and quality: VNC vs. TUE images	
1	VNC markedly worse than TUE images
2	VNC mildly worse than TUE images
3	VNC equivalent to TUE images
4	VNC mildly better than TUE images
5	VNC markedly better than TUE images

TABLE 2 Modified five-point-Likert-scale for assessing the iodine subtraction from VNC images in comparison with TUE images.

Iodine subtraction in VNC images	
1	Insufficient subtraction of iodine
2	Partly sufficient subtraction of iodine with larger, incomplete areas in the parenchyma
3	Moderately sufficient subtraction of iodine with incomplete areas in parts of the parenchyma
4	Almost complete subtraction of iodine
5	Complete subtraction of iodine

were applied for each organ system or tissue. Tests were two-sided and a p-value of ≤ 0.05 was considered significant. To investigate the normal distribution of the dara, a Shapiro–Wilk test was performed.

3 Results

3.1 Study population

A total of 20 CT scans met the inclusion criteria, based on a total of 87 abdominal or full-body CT scans from client-owned rabbits which were identified and reviewed during the study period from February 2023 to April 2024. As post-contrast scans were traditionally not performed as a standard procedure in our institution by the time the data was collected, 66 studies had to be excluded. One additional study was excluded due to excessive motion artefacts, which made a comparison of the pre- and post-contrast scans impossible. The presenting complaint of the patients included one or more of the following symptoms: inappetence, apathy, chronic or acute weight loss, respiratory distress, hypothermia, polyuria, stanguria, trauma, ocular discharge, previously by ultrasound diagnosed nephrolithiasis, precardial mass, liver cysts or cardiomyopathy. The most commonly reported clinical complaint was weight loss despite normal food intake. The study population included 10 female and 10 male rabbits, with 9 (45%) neutered males, 1 (5%) sexually intact male, 6 (30%) female neutered and 4 (20%) sexually intact females. The average age was 5.8 years, with a range from 1 to 11 years (SD: ± 2.56). The rabbits ranged from 1.27 kg to 6.48 kg in body weight (mean and SD: 2.81 ± 1.61).

3.2 Quantitative analysis

A total of 219 ROIs were drawn. In one patient, the right kidney was absent due to a prior nephrectomy, so only the cortex of the left kidney could be measured in this case. The difference between TUE and VNC attenuation values was ≤ 15 HU in 72.1%, ≤ 10 HU in 60% and ≤ 5 HU in 30.7% of all compared ROIs. All measured ROIs of each organ or tissue were found to be normally distributed and averaged ROIs showed a Gaussian distribution according to the Shapiro–Wilk test.

The differences in attenuation values of TUE and VNC were statistically significant ($p < 0.05$) for ≤ 5 HU in the spleen, for ≤ 10 HU and ≤ 15 HU additionally in the liver, musculature and renal cortices. No statistically significant differences in attenuation values ≤ 15 HU were detected in the aorta, urinary bladder and intraabdominal fat. Table 3 summarizes the TOST results.

The smallest differences in HUs between TUE and VNC images were observed in the liver, spleen, and paraspinal musculature. In these cases, 80, 75, and 95% of the measurements, respectively, fell within the threshold of ≤10 HU difference. The most notable discrepancy in the HUs between VNC and TUE was observed in the assessments of intra-abdominal fat and the aorta. Consequently, only 35 and 55% of the measurements were within the acceptable range of ≤ 15 HU. It is important to note that these results are not statistically significant as shown in Table 3. As shown in Table 3, it is also evident that for liver, spleen, and muscle measurements, only 6, 4, and none of the 40 measured ROIs, respectively, exceeded the threshold of 15 HUs. In contrast, 10 out of 40 ROIs in the renal cortex, 7 out of 20 in the urinary bladder, 9 out of 20 in the aorta, and even more than half of the measurements (13) in intra-abdominal fat were above this threshold.

The average HU value difference between TUE and VNC was ≤10 HU in the majority of measurements in the liver, muscle, and spleen, and ≤ 15 HU in the renal cortex. For all regions, the values are summarized and displayed with the range of the standard deviation using a box-and-whisker plot in Figure 2.

Correlations between the weight of animals and the distances of the difference between VNC and TUE images to 0 were negative in each organ system or tissue except for the bladder. A significant correlation ($r = -0.6723$; $p = 0.0012$) with a moderate fit ($R^2 = 0.5$) was found only for the kidneys.

3.3 Qualitative analysis

An average score of 4.4 was achieved for iodine subtraction across all patients, which encompasses all organ values, with no individual patient scoring below 4.0. This indicates that there has been a nearly complete subtraction of iodine on average. However, smaller intraparenchymal vessels were in general not sufficiently suppressed and therefore not included in the assessment. Scores of at least 4.6 were achieved for the liver, spleen, caudal vena cava, aorta, and musculature. Iodine subtraction values for the bladder, gastrointestinal tract, and renal cortices were at least 3.8, 3.9, and 3.5, respectively. The detailed values from this evaluation are presented in Table 4.

The mean image quality score was 4.2 on the 5-point Likert scale. A single patient was assigned a rating of "3" on the five-point Likert scale, which represents the lowest rating in the study.

4 Discussion

The calculated VNC values for the liver, spleen, renal cortices, and musculature were equivalent to the measurements in the TUE series which confirmed our first hypothesis.

10.3389/fvets.2025.1521986

TABLE 3 Two one-sided *t*-test (TOST) for assessment of equivalence between VNC and TUE images (*p*-values).

Region of interest (ROI)	≤ 5 HU	≤ 10 HU	≤ 15 HU
Liver (mean out of two measurements); *n* = 40	0.1212 (*n* = 20)	**0.0006** (*n* = 32)	**<0.0001** (*n* = 34)
Spleen (mean out of two measurements); *n* = 40	**0.038** (*n* = 20)	**0.0001** (*n* = 30)	**<0.0001** (*n* = 36)
Musculature (mean out of two measurements – left and right); *n* = 40	0.1029 (*n* = 14)	**<0.0001** (*n* = 38)	**<0.0001** (*n* = 40)
Renal cortex (mean out of two measurements – left and right); *n* = 39	0.7005 (*n* = 8)	**0.0498** (*n* = 24)	**0.0004** (*n* = 30)
Aorta; *n* = 20	0.9979 (*n* = 6)	0.9367 (*n* = 9)	0.4765 (*n* = 11)
Urinary Bladder; *n* = 20	0.9931 (*n* = 6)	0.9953 (*n* = 9)	0.802 (*n* = 13)
Intraabdominal Fat; *n* = 20	1 (*n* = 0)	0.9998 (*n* = 4)	0.9757 (*n* = 7)

A *p*-value ≤ 0.05 shows equivalence within the specified HU-delta (tolerance limits ≤ 5, ≤ 10, ≤ 15 HU difference of VNC towards TUE). Significant values are marked in bold. *n* = number of ROIs.

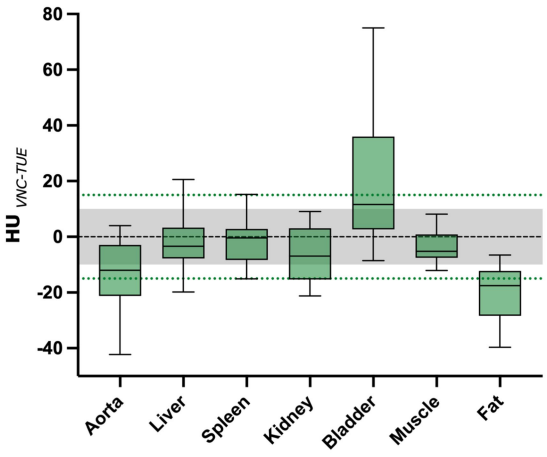

FIGURE 2
The mean difference between VNC and TUE for all ROIs is illustrated. The threshold of 10 HU difference, which is considered "negligible," is indicated by the grey shaded area, while the threshold of 15 HU difference, which is considered "acceptable," is represented by the green dashed line. The lower and upper margins of each box represent the 25th and 75th percentiles, respectively. The median is marked by a black line within the plots.

Under favourable conditions, human observers can distinguish between 700 and 900 shades of grey displayed simultaneously across the available brightness range of the medical display. The human eye is capable of detecting only a 6% change in grayscale (20). In practical terms, this means that in a reconstructed soft tissue window with a greyscale range of 290 Hounsfield Units, a discrimination of a difference of about 17 HUs is possible for the human eye.

Based on this, previous studies have established a negligible threshold of ≤ 10 HU between VNC and TUE images. Additionally, an acceptable threshold of ≤ 15 HUs has been established (16, 17).

The highest discrepancies in HU values were observed in the aorta, urinary bladder and intra-abdominal fat. This finding is consistent with those of previous studies. It should be noted that, in contrast to the liver, musculature, spleen, and renal cortex, which exhibited averaged ROI values, these organs displayed only a single ROI, which could have increased the measurement bias. Sauter et al. (16) sought to elucidate this phenomenon by postulating that the exceedingly high iodine concentrations within the aorta might lead to disproportionately elevated iodine subtraction rates through the algorithm. Another study attributed the incomplete subtraction of motion artefacts of the aorta, which resulted in a minimal spatial difference between the two tubes and, consequently, an impact on the output of the VNC algorithm (21).

Rabbits are distinctive in their calcium utilization, exhibiting a markedly elevated absorption rate from the digestive tract. This hyperabsorption of dietary calcium can result in excessive calcium excretion in the urine, leading to the formation of a typical sludge in the bladder (22). The distinction between contrast medium and calcium or calcified tissue depends on the CT density of the tissues and is limited when the CT attenuation is low (23). Suppression of iodine-like attenuation might interfere with calcium-like attenuation (24) which may result in normal calcium or calcium sludge within the bladder and renal parenchyma being subtracted, thereby limiting the comparability of TUE and VNC images in this region (Figure 3). This observation was also partially noted in the renal cortices, where smaller mineralizations were sometimes removed by the VNC algorithm during the study. If this pitfall poses a source of relevant errors in clinical interpretation in diseased patients needs to be evaluated in future studies.

In addition, the calculation of the VNC images is based on the measurement of water and iodine, which are in turn based on the photoelectric effect and Compton scattering. In contrast to the parenchymal organs, the intraabdominal fat is not situated on the water line as a reference point, but rather beneath it (19). This may explain the reduced accuracy of the algorithm in adipose tissue. If this weak point of the algorithm has a clinically relevant impact on certain pathologies like for example the fatty infiltration of the liver, needs to be evaluated in further studies.

The second hypothesis regarding the superior image quality of VNC images compared to the conventional TUE images was also confirmed. Similar improvements in image quality with VNC images have been demonstrated in both human medical studies (16, 17) and a veterinary study (19). In 72.1% of the measured ROIs, a discrepancy of ≤15 HUs between VNC and TUE images was observed. A difference of ≤ 15 HUs was deemed acceptable given that the human eye is only capable of discerning differences of approximately 17 HUs within a specified soft tissue window with a grayscale range of approximately 290 HUs (20). This result is in accordance with the findings of previous studies. Lietz et al. addressed the same question in a cohort of clinically healthy Beagle dogs, and their findings indicated that 91.61% of the measured ROIs exhibited a difference of less than or equal to 15 HUs. In human medicine studies, values of 72% (12), 98% (17), and over 90% (16) have been reported. Similarly, Laukamp et al. achieved good results in their study comparing TUE

TABLE 4 Iodine subtraction score for 20 rabbits.

Location	Rabbits																				Average score location
	1	2	3	4	5	6	7	8	9	10	11	12	13	14	15	16	17	18	19	20	
Liver	5	5	4	5	5	3	5	5	4	5	5	5	4	5	3	4	5	5	5	5	4.6
Spleen	5	5	5	5	5	5	5	5	5	5	5	5	5	5	5	5	5	5	5	5	5.0
Kidneys	4	4	3	5	4	3	4	3	3	4	4	4	3	3	3	3	4	4	3	2	3.5
GIT	3	4	3	5	4	4	4	3	3	5	5	4	4	4	3	4	4	4	4	4	3.9
CVC	4	5	5	5	5	5	4	4	5	5	5	5	5	5	5	5	5	4	4	5	4.8
Aorta	5	5	5	5	5	5	5	5	5	5	5	5	5	5	5	5	4	5	4	5	4.9
Urinary bladder	5	4	4	4	4	2	5	4	5	3	5	4	4	2	3	3	3	4	5	2	3.8
Musculature	5	5	5	5	5	5	5	5	5	5	5	5	5	5	5	5	5	5	5	5	5.0
Average score patient	4.5	4.6	4.3	4.9	4.6	4.0	4.6	4.3	4.4	4.6	4.9	4.6	4.4	4.3	4.0	4.3	4.4	4.5	4.4	4.1	4.4

Note the complete iodine subtraction in spleen and musculature and almost complete subtraction in aorta, caudal vena cava (CVC) and liver. The iodine subtraction score for the gastrointestinal tract (GIT), urinary bladder and kidneys is still ≥ 3.5. 1: insufficient subtraction of iodine, 2: Partly sufficient subtraction of iodine with larger, incomplete areas in the parenchyma, 3: Moderately sufficient subtraction of iodine with incomplete areas in parts of the parenchyma, 4: almost complete subtraction of iodine, 5: complete subtraction of iodine.

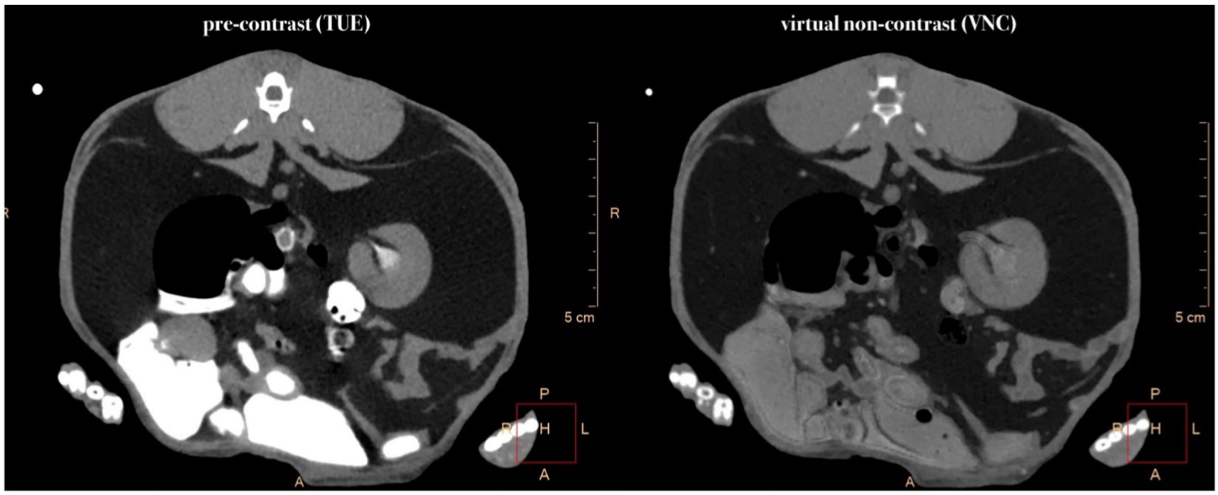

FIGURE 3
Comparative presentation of synchronized pre-contrast (TUE) and virtual non-contrast (VNC) images in the transverse plane. Note the partly subtraction of iodine in the region of the renal pevis and the almost complete subtraction of mineral-attenuating structures within the intestinal tract.

and VNC images of the liver (25). In this study, the difference between VNC and true unenhanced images was below 10 HUs in 92.3% of the comparative liver measurements. Several factors, including patient size, voxel size, beam hardening artefacts and high iodine concentrations, have been suggested as potential influences on the accuracy of iodine subtraction (17). Given that the patients included in this study were exclusively rabbits, the impact of body size is of particular interest. However, a correlation between weight and ROIs was only observed in renal measurements ($r = -0.6723$; $p = 0.0012$), with a moderate fit ($R^2 = 0.5$). A possible explanation for this error might be the generally small size of patients included in the study.

Our study had several limitations. Firstly, due to the small number of animals in this study, the power of our statistical analysis was limited. A second limitation was the retrospective nature and the resulting selection of patients. As the patients were selected based on specific criteria from the CT studies, the study did not only include clinically healthy animals. Although the described measurements were performed in radiologically normal organs, this does not exclude pathology. We could not prove our findings by pathology or histopathology as our study included clinical patients. Further studies with histopathologically or cytologically confirmed diseased organs could confirm the reliability of the VNC algorithm and test its constraints. Another limitation was that the rabbits were scanned consciously. This occasionally resulted in movement between the native and post-contrast scans, which in turn might have led to inaccuracies in the alignment of the images for the simultaneous ROI placements, necessitating exclusion in case of significant movement or manual adjustments when minor movement was present. However, the

movement was primarily affecting the head, and therefore the impact on the region of interest was minimal. Furthermore, scanning the rabbits consciously represents the normal clinical routine. In this study, the administration of contrast medium was performed manually, as the utilisation of our contrast injector was not compatible with rabbits due to the high injection pressure. Consequently, minor discrepancies were observed in the timing of the post-contrast scans, which, given the physiological characteristics of the rabbits, could have resulted in different contrast phases. Further research could investigate the influence of the contrast phase on the comparability of VNC and TUE images.

5 Conclusion

In conclusion, the VNC images demonstrated an acceptable discrepancy from the TUE images in 76% of the ROIs when a minimal cutoff of ≤10 HU was applied, and in 61% of the ROIs when a minimal cutoff of ≤10 HUs was utilized. The most favourable outcomes were observed in the spleen, liver, paraspinal musculature, and renal cortex. Further research is required to ascertain whether VNC algorithms can be employed in the analysis of pathologically affected organs and whether the resulting images are comparable to those obtained using TUE data. This technique has significant potential, particularly for patients undergoing conscious scans, as it substantially reduces the radiation exposure, possible motion artifacts in between the scans and the stress associated with the scan by halving the scan time.

Data availability statement

The original contributions presented in the study are included in the article/supplementary material, further inquiries can be directed to the corresponding author.

Ethics statement

A direct, written consent of the animal owners for the use of the patient data in this certain study was not obtained, as the anonymized use of the data in general is approved by signature during the admission of the patients in the registration certificate.

Author contributions

MM: Conceptualization, Data curation, Formal analysis, Funding acquisition, Investigation, Methodology, Project administration, Resources, Validation, Visualization, Writing – original draft, Writing – review & editing. PL: Conceptualization, Methodology, Project administration, Visualization, Writing – review & editing. J-AD: Data curation, Writing – review & editing. SM: Data curation, Software, Writing – review & editing. MP: Writing – review & editing. KM: Conceptualization, Investigation, Methodology, Supervision, Validation, Writing – review & editing.

Funding

The author(s) declare financial support was received for the research and/or publication of this article. We acknowledge financial support by the Open Access Publication Fund of the University of Veterinary Medicine Hannover, Foundation.

Conflict of interest

The authors declare that the research was conducted in the absence of any commercial or financial relationships that could be construed as a potential conflict of interest.

Generative AI statement

The author(s) declare that no Gen AI was used in the creation of this manuscript.

Publisher's note

References

1. Mullhaupt D, Wenger S, Kircher P, Pfammatter N, Hatt JM, Ohlerth S. Computed tomography of the thorax in rabbits: a prospective study in ten clinically healthy New Zealand white rabbits. *Acta Vet Scand*. (2017) 59:72. doi: 10.1186/s13028-017-0340-x

2. Sanchez-Vizcaino F, Noble PM, Jones PH, Menacere T, Buchan I, Reynolds S, et al. Demographics of dogs, cats, and rabbits attending veterinary practices in Great Britain as recorded in their electronic health records. *BMC Vet Res*. (2017) 13:218. doi: 10.1186/s12917-017-1138-9

3. Kwan V, Quesenberry K, Le Roux AB. Mensuration of the rabbit pituitary gland from computed tomography. *Vet Radiol Ultrasound*. (2020) 61:322–8. doi: 10.1111/vru.12852

4. Artiles CA, Sanchez-Migallon Guzman D, Beaufrere H, Phillips KL. Computed tomographic findings of dental disease in domestic rabbits (*Oryctolagus cuniculus*): 100 cases (2009-2017). *J Am Vet Med Assoc*. (2020) 257:313–27. doi: 10.2460/javma.257.3.313

5. Daggett A, Loeber S, Le Roux AB, Beaufrere H, Doss G. Computed tomography with Hounsfield unit assessment is useful in the diagnosis of liver lobe torsion in pet rabbits (Oryctolagus cuniculus). *Vet Radiol Ultrasound*. (2021) 62:210–7. doi: 10.1111/vru.12939

6. Richardson J, Longo M, Liuti T, Eatwell K. Computed tomographic grading of middle ear disease in domestic rabbits (Oryctolagus cuniculi). *Vet Rec*. (2019) 184:679. doi: 10.1136/vr.104980

7. Longo M, Thierry F, Eatwell K, Schwarz T, Del Pozo J, Richardson J. Ultrasound and computed tomography of sacculitis and appendicitis in a rabbit. *Vet Radiol Ultrasound*. (2018) 59:E56–60. doi: 10.1111/vru.12602

8. Lye G, Dittmer K, Pemberton S, Lockhart K, Pollard R. Osteosarcoma with widespread metastasis in a 1-year-old crossbred rabbit. *Vet Radiol Ultrasound*. (2024) 65:518–22. doi: 10.1111/vru.13385

9. Di Girolamo N, Tollefson C. Computed tomographic diagnosis and clinical outcomes of small intestinal obstruction caused by trichobezoars in client-owned rabbits. *Vet Radiol Ultrasound*. (2024) 65:264–74. doi: 10.1111/vru.13349

10. Brodbelt DC, Blissitt KJ, Hammond RA, Neath PJ, Young LE, Pfeiffer DU, et al. The risk of death: the confidential enquiry into perioperative small animal fatalities. *Vet Anaesth Analg*. (2008) 35:365–73. doi: 10.1111/j.1467-2995.2008.00397.x

11. Holz JA, Alkadhi H, Laukamp KR, Lennartz S, Heneweer C, Pusken M, et al. Quantitative accuracy of virtual non-contrast images derived from spectral detector computed tomography: an abdominal phantom study. *Sci Rep*. (2020) 10:21575. doi: 10.1038/s41598-020-78518-5

12. Niehoff JH, Woeltjen MM, Laukamp KR, Borggrefe J, Kroeger JR. Virtual non-contrast versus true non-contrast computed tomography: initial experiences with a photon counting scanner approved for clinical use. *Diagnostics (Basel)*. (2021) 11. doi: 10.3390/diagnostics11122377

13. Isaac I, Richardson J, Liuti T, Longo M. Safety of intravenous iodinated contrast medium injection in rabbits undergoing conscious computed tomography. *Vet Rec Open*. (2022) 9:e31. doi: 10.1002/vro2.31

14. Greco A, Meomartino L, Gnudi G, Brunetti A, Di Giancamillo M. Imaging techniques in veterinary medicine. Part II: computed tomography, magnetic resonance imaging, nuclear medicine. *Eur J Radiol Open*. (2023) 10:100467. doi: 10.1016/j.ejro.2022.100467

15. McCollough CH, Leng S, Yu L, Fletcher JG. Dual- and multi-energy CT: principles, technical approaches, and clinical applications. *Radiology*. (2015) 276:637–53. doi: 10.1148/radiol.2015142631

16. Sauter AP, Muenzel D, Dangelmaier J, Braren R, Pfeiffer F, Rummeny EJ, et al. Dual-layer spectral computed tomography: virtual non-contrast in comparison to true non-contrast images. *Eur J Radiol*. (2018) 104:108–14. doi: 10.1016/j.ejrad.2018.05.007

17. Jamali S, Michoux N, Coche E, Dragean CA. Virtual unenhanced phase with spectral dual-energy CT: is it an alternative to conventional true unenhanced phase for abdominal tissues? *Diagn Interv Imaging*. (2019) 100:503–11. doi: 10.1016/j.diii.2019.04.007

18. Durieux P, Gevenois PA, Muylem AV, Howarth N, Keyzer C. Abdominal attenuation values on virtual and true unenhanced images obtained with third-generation dual-source dual-energy CT. *AJR Am J Roentgenol*. (2018) 210:1042–58. doi: 10.2214/AJR.17.18248

19. Lietz P, Bruntgens M, Wang-Leandro A, Volk HA, Meller S, Merhof K. Virtual non-contrast images of detector-based spectral computed tomography in dogs: a promising alternative to true non-contrast images in veterinary medicine. *Front Vet Sci*. (2023) 10:1251535. doi: 10.3389/fvets.2023.1251535

20. Kimpe T, Tuytschaever T. Increasing the number of gray shades in medical display systems—how much is enough? *J Digit Imaging*. (2007) 20:422–32. doi: 10.1007/s10278-006-1052-3

21. Lehti L, Soderberg M, Hoglund P, Nyman U, Gottsater A, Wasselius J. Reliability of virtual non-contrast computed tomography angiography: comparing it with the real deal. *Acta Radiol Open*. (2018) 7:2058460118790115. doi: 10.1177/2058460118790115

22. Clauss M, Burger B, Liesegang A, Del Chicca F, Kaufmann-Bart M, Riond B, et al. Influence of diet on calcium metabolism, tissue calcification and urinary sludge in rabbits (*Oryctolagus cuniculus*). *J Anim Physiol Anim Nutr (Berl)*. (2012) 96:798–807. doi: 10.1111/j.1439-0396.2011.01185.x

23. Tran DN, Straka M, Roos JE, Napel S, Fleischmann D. Dual-energy CT discrimination of iodine and calcium: experimental results and implications for lower extremity CT angiography. *Acad Radiol*. (2009) 16:160–71. doi: 10.1016/j.acra.2008.09.004

24. Fervers P, Fervers F, Weisthoff M, Rinneburger M, Zopfs D, Reimer RP, et al. Dual-energy CT, virtual non-calcium bone marrow imaging of the spine: an AI-assisted, volumetric evaluation of a reference cohort with 500 CT scans. *Diagnostics (Basel)*. (2022) 12. doi: 10.3390/diagnostics12030671

25. Laukamp KR, Lennartz S, Ho V, Grosse Hokamp N, Zopfs D, Gupta A, et al. Evaluation of the liver with virtual non-contrast: single institution study in 149 patients undergoing TAVR planning. *Br J Radiol*. (2020) 93:20190701. doi: 10.1259/bjr.20190701

Frontiers in Veterinary Science

Transforms how we investigate and improve animal health

The third most-cited veterinary science journal, bridging animal and human health with a comparative approach to medical challenges. It explores innovative biotechnology and therapy for improved health outcomes.

Discover the latest Research Topics

See more →

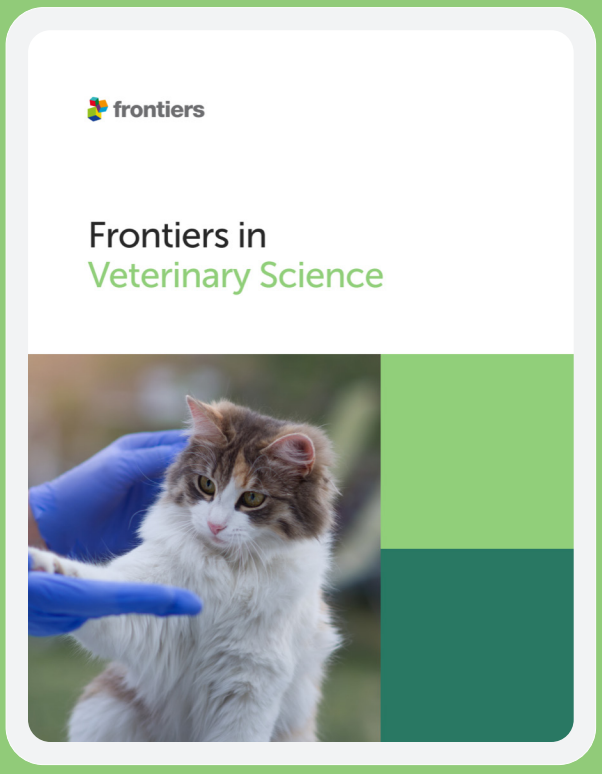

Frontiers

Avenue du Tribunal-Fédéral 34
1005 Lausanne, Switzerland
frontiersin.org

Contact us

+41 (0)21 510 17 00
frontiersin.org/about/contact